Title
Energy Transfer via Solar Wind Driven Ultra Low Frequency Waves in the Earth's Magnetosphere

Author
Hartinger, Michael David

Publication Date
2012

Peer reviewed|Thesis/dissertation

University of California
Los Angeles

Energy Transfer via Solar Wind Driven Ultra Low Frequency Waves in the Earth's Magnetosphere

A dissertation submitted in partial satisfaction
of the requirements for the degree
Doctor of Philosophy in Geophysics and Space Physics

by

Michael David Hartinger

2012

Abstract of the Dissertation

Energy Transfer via Solar Wind Driven Ultra Low Frequency Waves in the Earth's Magnetosphere

by

Michael David Hartinger

Doctor of Philosophy in Geophysics and Space Physics

University of California, Los Angeles, 2012

Professor Vassilis Angelopoulos, Chair

Ultra Low Frequency (ULF) waves are an important mechanism for energy transfer in the Earth's magnetosphere, interacting with a variety of different plasma populations and other plasma wave modes. The solar wind is an important energy source for ULF waves, and there are many pathways through which solar wind energy can drive wave activity. In this thesis, two case studies and two statistical studies are presented to demonstrate the manner in which energy is transferred from the solar wind to magnetospheric ULF waves. These studies demonstrate the viability of both the field line resonance paradigm and global fast (cavity/waveguide) modes as pathways for energy transfer from the solar wind to various sinks of wave energy in the magnetosphere. They also show that the plasmasphere plays an important role in suppressing electromagnetic energy transfer via ULF waves from the solar wind to the inner magnetosphere in the Pc5 frequency band.

The first case study demonstrates the conversion from isotropic to perpendicular energy flux at the field line resonance (FLR) location, providing further validation for the FLR paradigm. The second case study demonstrates that solar wind dynamic pressure fluctuations with a broadband frequency spectrum provide energy to drive a monochromatic global (cavity/waveguide) mode, which in turn provides energy to drive shear Alfvén waves through FLR; this is the first direct observation of energy transfer via a global mode in the Pc5 (2-7 mHz) frequency band outside of the plasmasphere. The first statistical study demonstrates

that Pc5 electric and magnetic field perturbations have significantly lower amplitude in the plasmasphere compared to the low density region outside the plasmasphere; this suggests that ULF wave electromagnetic energy incident from the outer magnetosphere is not easily transferred across the plasmapause boundary in the Pc5 frequency range. The second statistical study characterizes global mode waves and provides a lower bound for the occurrence rate, or total time that global modes are observed divided by total observation time, of 1.0%.

The dissertation of Michael David Hartinger is approved.

Richard M. Thorne

Robert L. McPherron

Margaret G. Kivelson

Mark B.S. Moldwin

Vassilis Angelopoulos, Committee Chair

University of California, Los Angeles

2012

This thesis is dedicated to my mother, Jeanne, my sister, Laura, and my girlfriend, Beth Ann.

Table of Contents

List of Figures

Acknowledgments

The work in this thesis would not have been possible without the time and effort of many other people. I am sincerely thankful for all of the help and support that I received from my advisors, professors and researchers at UCLA, fellow graduate students at UCLA, and collaborators from other universities and organizations. I am also grateful to my mother, Jeanne, my sister, Laura, and my girlfriend, Beth Ann, for their love and support.

There are many people who contributed significantly to the work in this thesis. First, I am extremely thankful for the help, advice, and support from my two advisors, Mark Moldwin and Vassilis Angelopoulos. I worked with Mark for the first three years of my graduate career, before he moved to the University of Michigan. He was very supportive in allowing me to try several research projects before settling on ULF waves, providing extremely useful advice on each. I am inspired by his commitment to education and public outreach, and he has strongly influenced my decision to become more engaged in both areas. I am looking forward to working with Mark as a postdoc.

After Mark left, I was lucky enough to become one of Vassilis's graduate students. Like Mark, Vassilis was extremely supportive in allowing me to pursue several research projects before settling on my final thesis project. His advice has changed the way I construct scientific arguments. I aspire to be as adept as Vassilis at succinctly expressing the main points of a scientific argument, exposing any flaws in the argument, and strengthening the argument with appropriate tests. I have learned so much from Vassilis's impressive breadth of knowledge in space plasma physics research as well as mission planning and engineering, and I plan on collaborating with him for many years to come.

I am also extremely thankful for the time, effort, and advice from my first advisor in space plasma physics research, Reiner Friedel. Without my experiences working with him at Los Alamos National Laboratory when I was an undergraduate, I would not currently be studying space plasmas. I hope to continue collaborating with him throughout my career.

I have benefited from the knowledge and expertise of several professors at UCLA. I was able to learn from Margaret Kivelson both in class and as a collaborator on the work

presented in Chapter 4. She has provided much useful advice on ULF wave phenomena. I took my first space plasma physics class with Robert Mcpherron, and I have since bounced several ideas for ULF wave studies off him. I also learned from Ray Walker in class, and I greatly appreciate his help while preparing for my first exam. Finally, the classes I took with Chris Russell, Richard Thorne, and George Morales were extremely beneficial for examining the basic properties of wave growth and wave-particle interactions in plasmas and for data analysis in space plasmas.

Throughout my graduate studies, I have benefited from the experience and advice of several researchers at UCLA. Yukitoshi Nishimura helped me process and diagnose the electric field data used in Chapters 2, 3, and 4, and he has provided many useful suggestions regarding ULF wave analysis and phenomena. Drew Turner helped determine the location and role of the ion foreshock in driving ULF waves in Chapter 4. He also also provided very useful advice in many aspects of data processing and analysis of energetic particle data, particularly from the THEMIS-SST instrument, and I have been lucky enough to collaborate with him on several projects. Ferdinand Plaschke provided much useful advice on ULF wave phenomena and signal processing. I also benefited from discussions with Yuri Shprits and Binbin Ni in the UCLA AOS department, who I have collaborated with on several projects.

There are many graduate students in both the UCLA Earth and Space Science and UCLA Atmospheric Science departments who helped make this research possible. I first need to thank all of the graduate students in Mark's old group at UCLA, Dave Berube, Megan Cartwright, and David Galvan, for all of their advice, support, and help with research. I especially thank David Galvan for his help using LaTex for this thesis. I also thank my current office mates, Xiangning Chu and Jenni Kissinger, for their advice and support. Finally, there are many other graduate students, both in space plasma physics and with other concentrations, whose friendship, support, and advice have helped me in so many different ways. I feel truly lucky to have been exposed to such a diverse group of interesting people during my graduate studies at UCLA.

I received significant help and advice from scientists located at other institutes. Kazue Takahashi provided the electric field, magnetic field, and electron density data used in Chap-

ter 2. He also provided useful advice on these data as well as on signal processing and ULF wave analysis. Karl-Heinz Glassmeier provided THEMIS magnetic field data used in Chapters 3, 4, and 5. He also also provided useful advice on signal processing and ULF wave analysis. John Bonnell supplied THEMIS electric field data and helped in diagnosing and understanding those data.

Howard J. Singer (NOAA) provided the original data from the CRRES fluxgate magnetometer and information for its use in Chapter 2. Howard also provided information for analyzing magnetometer data from the NOAA GOES spacecraft. John R. Wygant (University of Minnesota) provided the original data from the CRRES Langmuir probe/electric field instrument and information for its use in Chapter 2. Roger R. Anderson (University of Iowa) provided the original data from the CRRES plasma wave experiment used for obtaining electron density and information for its use in Chapter 2. Robert Lauchlan Scott provided help and advice with CRRES data analysis.

I am thankful to many different scientists for providing the THEMIS data used in Chapters 3, 4, and 5. First, I acknowledge NASA contract NAS5-02099 and Vassilis Angelopoulos for use of data from the THEMIS Mission. I thank John W. Bonnell and Forrest S. Mozer for use of the THEMIS EFI data. I thank Davin Larson and Robert P. Lin for use of THEMIS SST data. I thank Charles W. Carlson and James P. McFadden for use of ESA data. I thank Karl-Heinz Glassmeier, Uli Auster and Wolfgang Baumjohann for the use of FGM data provided under the lead of the Technical University of Braunschweig and with financial support through the German Ministry for Economy and Technology and the German Center for Aviation and Space (DLR) under contract 50 OC 0302.

I am also thankful to many different scientists and organizations for providing other sources of data and software tools used in Chapters 3, 4, and 5. I thank the NASA Space Science Data facility for use of solar wind data and geomagnetic activity indices. I thank D. Boscher, S. Bourdarie, Paul O'Brien, and T. Guild for providing the ONERA library V4.2. I thank the institutes that maintain the IMAGE magnetometer array. I thank Stephen Mende and Christopher T. Russell for use of the THEMIS ground magnetometer data. I thank Ian R. Mann, D.K. Milling and the rest of the CARISMA team for use of GMAG data

(CARISMA is operated by the University of Alberta, funded by the Canadian Space Agency). I thank Martin Connors and Christopher T. Russell for use of ground magnetometer data. I thank Erik Steinmetz, Augsburg College for the use of GMAG data. I thank Tromsø Geophysical Observatory, University of Tromsø, Norway for use of the Greenland and Norway magnetometer data. I thank the Geophysical Institute, University of Alaska for data from the Geophysical Institute Magnetometer Array. I thank Claudia Stolle and Jürgen Matzka for providing ground magnetometer data from the Technical University of Denmark as well as instructions for use of these data.

Chapter 2 is a version of Hartinger, M., M. B. Moldwin, V. Angelopoulos, K. Takahashi, H. J. Singer, R. R. Anderson, Y. Nishimura, and J. R. Wygant (2010), Pc5 wave power in the quiet-time plasmasphere and trough: CRRES observations, Geophys. Res. Lett., 37, L07107, doi:10.1029/2010GL042475.

Chapter 3 is a version of Hartinger, M., V. Angelopoulos, M. B. Moldwin, K.-H. Glassmeier, and Y. Nishimura (2011), Global energy transfer during a magnetospheric field line resonance, Geophys. Res. Lett., 38, L12101, doi:10.1029/2011GL047846.

Chapter 4 is a version of Hartinger, M., V. Angelopoulos, M. B. Moldwin, K.-H. Glassmeier, Y. Nishimura, D. Turner, K.-H. Glassmeier, M.G. Kivelson, J. Matzka, and C. Stolle (2012), Observations of a Pc5 global (cavity/waveguide) mode outside the plasmasphere by THEMIS, J. Geophys. Res., (in press).

Financial support for this thesis has been made possible through the NASA THEMIS contract NAS5-02099, NASA Geospace science grant NNX09A162G, the NSF Measure II grant ATM-0348398, and the NSF GK12 teaching fellowship.

Vita

2005-2006	NASA Undergraduate Student Research Program Los Alamos National Laboratory, Los Alamos, New Mexico.
2006	B.A. Physics Physics Department, College of Arts and Sciences, Cornell University.
2006-2012	Graduate Student Researcher Earth and Space Sciences Department, UCLA.
2007	Heliophysics Summer School University Corporation for Atmospheric Research, Boulder, Colorado.
2008	M.S. Geophysics and Space Physics UCLA.
2009-2010	National Science Foundation GK12 Fellow UCLA.
2009-2011	AVID tutor Culver City High School, California.
2009-2011	Curriculum Committee Earth And Space Sciences Department, UCLA.
2010	American Geophysical Union Outstanding Student Paper Award.
2011	American Geophysical Union Outstanding Student Paper Award.

Publications

Hartinger, M., M. B. Moldwin, V. Angelopoulos, K. Takahashi, H. J. Singer, R. R. Ander-

son, Y. Nishimura, and J. R. Wygant (2010), Pc5 wave power in the quiet-time plasmasphere and trough: CRRES observations, *Geophys. Res. Lett., 37*, L07107, doi:10.1029/2010GL042475.

Ni, B., Y. Shprits, **M. Hartinger**, V. Angelopoulos, X. Gu, and D. Larson (2011), Analysis of radiation belt energetic electron phase space density using THEMIS SST measurements: Cross-satellite calibration and a case study, *J. Geophys. Res., 116*, A03208, doi:10.1029/2010JA016104.

Hartinger, M., V. Angelopoulos, M. B. Moldwin, K.-H. Glassmeier, and Y. Nishimura (2011), Global energy transfer during a magnetospheric field line resonance, *Geophys. Res. Lett., 38*, L12101, doi:10.1029/2011GL047846.

Ni, B., R. Thorne, J. Liang, V. Angelopoulos, C. Cully, W. Li, X.J. Zhang, **M. Hartinger**, O. Le Contel, A. Roux, (2011), Global Distribution of electrostatic electron cyclotron harmonic waves observed on THEMIS, *Geophys. Res. Lett., 38*, L17105, doi:10.1029/2011GL048793.

Turner, D.L., Y. Shprits, **M. Hartinger**, and V. Angelopoulos, (2012), Explaining sudden losses of outer radiation belt electrons during geomagnetic storms, *Nature Phys., 8*, 3, doi:10.1038/NPHYS2185.

Tian, A.M., Q.G. Zong, T.L. Zhang, R. Nakamura, A.M. Du, W. Baumjohann, K.H. Glassmeier, M. Volwerk, **M. Hartinger**, Y.F. Wang, J. Du, B. Yang, X.Y. Zhang, and E. Panov (2012), Dynamics of long-period ULF waves in the plasma sheet: Coordinated space and ground observations, *J. Geophys. Res., 117*, A03211, doi:10.1029/2011JA016551.

Hartinger, M., V. Angelopoulos, M. B. Moldwin, K.-H. Glassmeier, Y. Nishimura, D. Turner, K.-H. Glassmeier, M.G. Kivelson, J. Matzka, and C. Stolle (2012), Observations of a Pc5 global (cavity/waveguide) mode outside the plasmasphere by THEMIS, J. Geophys. Res., (in press)

CHAPTER 1

Introduction

1.1 ULF waves

Ultra Low Frequency (ULF) plasma waves in the Earth's magnetosphere are named for their observed frequencies. They have been observed on the ground for well over two centuries using a variety of instruments, including compass needles and magnetographs (*Kangas et al.*, 1998). Observers recognized the connection between magnetic perturbations observed by ground instruments and the aurora as early as 1741, although it was not understood until much later that the origin of these waves was rooted in the interaction between plasma and magnetic fields in the Earth's magnetosphere (*Stewart*, 1861; *Alfvén*, 1945). Two of the earliest and most important contributors to our understanding of ULF waves in the Earth's magnetosphere were Hannes Alfvén and Jim Dungey. Hannes Alfvén described the excitation and propagation of what we now refer to as Alfvén waves in plasmas, while Jim Dungey showed how the Earth's inhomogeneous magnetic field and high conductivity ionosphere would affect ULF waves (e.g., *Alfvén*, 1945; *Dungey*, 1963).

A series of studies by Jim Dungey first showed how the magnetosphere and ionosphere can together act to trap Alfvén waves, creating a continuum of standing wave frequencies throughout the radial extent of the magnetosphere (e.g., *Dungey*, 1955, 1963). *Tamao* (1965) later showed that a resonant mode coupling could occur between fast and shear Alfvén MHD waves in the Earth's magnetosphere. *Chen and Hasegawa* (1974) and *Southwood* (1974) elaborated on this theory, relating it to ground based ULF wave observations and showing how surface waves at the magnetopause could drive shear Alfvén waves through resonant mode coupling, or field line resonance (FLR - Figure 1.1). FLR has since become one of

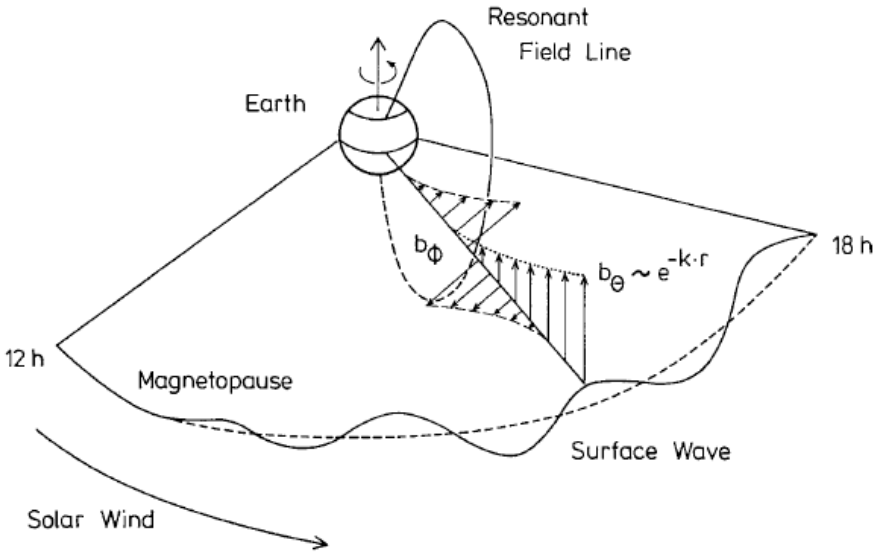

Figure 1.1: A schematic of resonant mode coupling between an evanescent magnetopause surface wave and shear Alfvén waves. The horizontal arrows represent the amplitude of compressional magnetic field perturbations associated with the surface wave. The vertical arrows represent shear Alfvén waves, which have peak amplitude at the field line resonance location. From *Glassmeier et al.* (1999).

the most important paradigms for explaining energy transfer via ULF waves in the Earth's magnetosphere.

There are many different types of ULF waves, and they can be classified using a number of schemes (e.g., polarization, driver of wave activity). Perhaps the most often used and well accepted scheme is from *Jacobs et al.* (1964), a study which classified ULF waves in the Earth's magnetosphere according to their frequency and the character of their pulsations. ULF waves were classified as either continuous, for steady oscillation, or irregular, for oscillations only lasting a few wave periods (*Jacobs et al.*, 1964). ULF waves were further subdivided by frequency, and the upper frequency for referring to oscillations as ULF was set at 5 Hz (Figure 1.2). This classification scheme has proved useful for quickly referring to different types of ULF waves, as the character and frequency of oscillation is often enough to associate a ULF wave with different regions of the magnetosphere or source mechanisms. However, there are notable limitations. For example, oscillations that have frequencies close

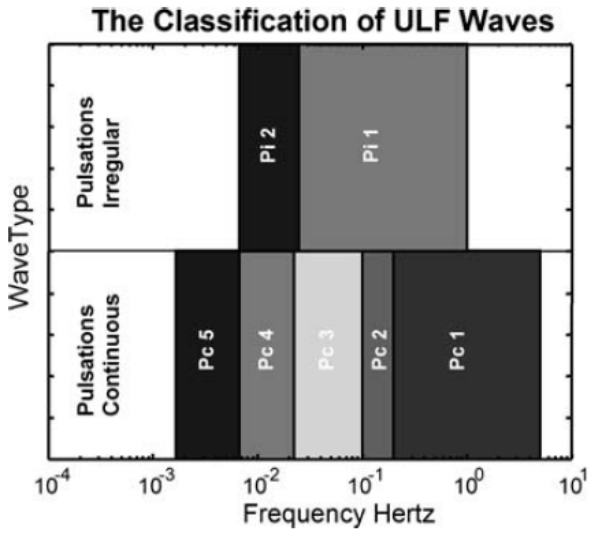

Irregular Pulsations

Class	Low edge Period (s)	High edge Period (s)
Pi 2	150	45
Pi 1	45	1

Continuous Pulsations

Class	Low edge Period (s)	High edge Period (s)
Pc 5	600	150
Pc 4	150	45
Pc 3	45	10
Pc 2	10	5
Pc 1	5	0.2

Figure 1.2: *Jacobs et al.* (1964) used the frequency and character (continuous or irregular) of pulsations to classify ULF waves. From *McPherron* (2005).

to the local ion cyclotron frequency will behave much differently than oscillations far below it. However, both types of oscillations are labeled as ULF in this scheme. Since this study will be dealing exclusively with ULF waves that can be well described mathematically by magnetohydrodynamics (MHD), we note now that when we refer to ULF waves in these studies, we are referring to MHD waves, excluding waves that are affected by ion cyclotron resonance. We shall discuss the applicability of MHD as a mathematical description of ULF waves in Section 1.4.

Understanding the dynamics of ULF waves in the Earth's magnetosphere is important for a variety of reasons. Due to their large wavelengths and fast propagation times, ULF waves can be used to remote sense distant magnetospheric processes. For example, the arrival of Pi2 pulsations at ground stations can be used to infer a substorm's onset time (*Olson*, 1999; *Hsu and McPherron*, 2007). The properties of certain types of ULF waves can also be used to remote sense plasma mass density from either the ground or in space, through a technique known as magneto-seismology (e.g., *Obayashi and Jacobs*, 1958; *Takahashi et al.*, 2006).

ULF waves interact with both low energy (plasmasphere) and high energy (radiation belt,

ring current) plasma populations in the Earth's magnetosphere. The effect of ULF waves on the radiation belts is a particularly important area of research, as energetic electrons in the outer radiation belts can seriously damage satellite electronics (*Baker et al.*, 1994). ULF waves are thought to be able to facilitate radial diffusion of radiation belt electrons through a variety of interactions related to an electron's drift orbit (*Elkington et al.*, 2003). The energetic electrons that can damage satellites have energies on the order of 1 MeV. To get an estimate of the range of wave frequencies of interest for accelerating radiation belt electrons to energies greater than 1 MeV, one can consider 1 MeV electrons. At a distance of 6 Re, these electrons have a drift frequency of approximately 2 mHz. Waves that have frequencies that are low integer multiples of 2 mHz will interact with 1 MeV electrons. These frequencies are common to ULF waves generated by the solar wind, and they are of primary interest in the studies contained in this thesis.

1.2 Energy sources for ULF waves

There are several important energy sources for ULF waves at Earth. Perhaps the most important is the solar wind, which may drive ULF wave activity through a variety of mechanisms. Dynamic pressure fluctuations in the solar wind may drive magnetopause boundary oscillations causing compressions and rarefactions in the magnetic field inside the magnetopause (e.g., *Kepko et al.*, 2002). Enhanced solar wind velocity or convection can drive magnetopause surface waves on the flanks of the magnetosphere through the Kelvin-Helmholtz instability (e.g., *Hasegawa et al.*, 2004). The bow shock and ion foreshock are also a source of ULF waves that may enter the Earth's magnetosphere for preferred orientations of the cone angle of the solar wind magnetic field relative to the Earth-Sun line (e.g., *Troitskaya et al.*, 1971; *Takahashi et al.*, 1981; *Chi and Russell*, 1998).

ULF waves may also be generated through several processes that are internal to the Earth's magnetosphere. One example is compressional waves generated by substorm processes in the magnetotail (e.g., *Olson*, 1999; *Hsu and McPherron*, 2007). Another example is waves generated through a drift-bounce resonance with ring current ions (*Southwood et al.*,

1969). The drift-mirror instability is also an important way of driving ULF waves in the Earth's magnetosphere (*Hasegawa*, 1969). Finally, standing Alfvén waves may be driven by compressional MHD waves through the field line resonance (FLR) mechanism (e.g., *Southwood*, 1974).

1.3 Energy sinks for ULF waves

There are several important energy sinks for ULF waves in the Earth's magnetosphere. Two of the most important regions of energy loss are located in the ionosphere or just outside the topside ionosphere. Two mechanisms act to damp standing Alfvén waves in this region: Joule dissipation and the field-aligned acceleration of electrons. Joule dissipation in the ionosphere has often been considered the most important energy loss mechanism for standing Alfvén waves (*Greenwald and Walker*, 1980). However, the acceleration of electrons needed to carry the field-aligned currents associated with Alfvén waves can also rapidly damp Alfvén waves (*Damiano et al.*, 2007), with the region of largest acceleration and energy loss being located above and within 2 Earth radii of the topside ionosphere. Figure 1.3 shows a schematic with the locations of these two energy loss mechanisms.

Additional energy loss mechanisms can be found in the form of boundaries throughout the Earth's magnetosphere, with energy from ULF waves which transfer energy across these boundaries being lost from the system. Examples of these types of sinks include the Earth's nightside magnetosphere (where wave energy can exit the magnetosphere via the magnetotail) (*Samson et al.*, 1992), the plasmapause (*Zhu and Kivelson*, 1989), and the magnetopause (*Mann et al.*, 1999).

Finally, wave-wave and wave-particle interactions can act as both a source and a sink for ULF wave energy. One of the most well-known wave-wave interactions is the resonant mode coupling between compressional and shear Alfvén MHD waves through the FLR mechanism; just as FLR is a source of energy for shear Alfvén waves, it is also a sink of energy for compressional waves (*Southwood*, 1974). ULF waves can also transfer energy to particles through a variety of mechanisms and at a range of particle energies. For example, ULF

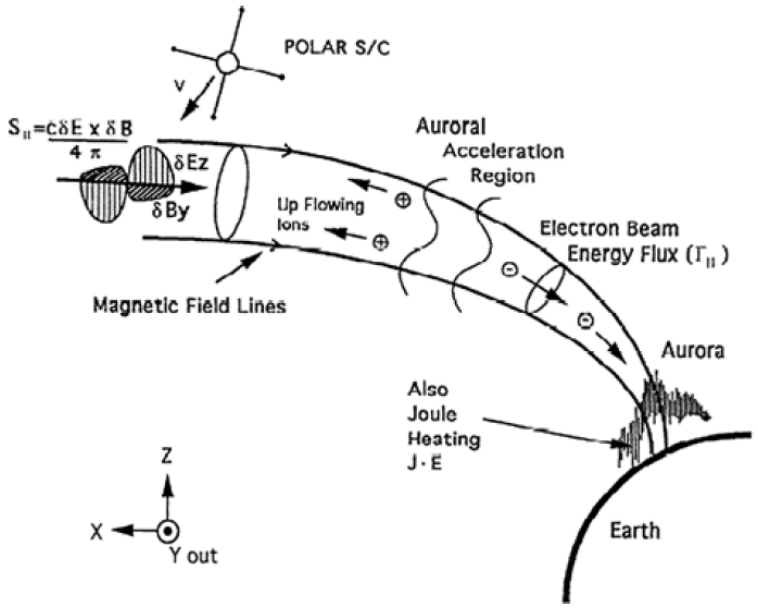

Figure 1.3: Two of the most important energy sinks for shear Alfén waves in the Earth's magnetosphere are Joule dissipation, which occurs primarily in the ionosphere, and field--aligned acceleration of electrons, which occurs above the topside ionosphere. From *Wygant et al.* (2000).

waves can interact with low energy particles, providing energy for the growth of plasmapause surface waves (*Daly and Hughes*, 1985). They can also interact with higher energy ring current particles through a drift-bounce resonance which may act as a source or sink of wave energy (*Southwood et al.*, 1969). Finally, radial diffusion and drift resonance with radiation belt electrons can act as a sink of wave energy (*Elkington et al.*, 2003).

1.4 Modeling energy transfer via solar wind driven ULF waves

1.4.1 The ideal MHD approximation

There are a number of mathematical descriptions possible for waves in space plasmas. These include fully kinetic descriptions where single particle motion is considered and fluid descriptions where only the collective behavior of particles is considered. Not every description is useful or leads to mathematically tractable descriptions of phenomena of interest. Here, we discuss the advantages and disadvantages of different approximations; in particular, we jus-

tify our use of ideal MHD as a description for ULF waves in this thesis, noting the required assumptions.

A fully kinetic approach that accounts for interactions between fields and each particle in the system, while the most accurate, is the least tractable mathematical description of ULF waves. In such approaches, the distribution function of each particle species must be known and accounted for, leading to considerable complexity (*Boyd and Sanderson*, 2003). Some attempts have been made to study ULF wave phenomena in specific situations using kinetic theory and simulations (e.g., *Damiano et al.*, 2007). However, this approach is not required in most regions of the magnetosphere.

Describing the plasma as a fluid assumes that the phenomena of interest vary on timescales that are long compared to timescales of significant microscopic particle motion (e.g., the cyclotron period and the inverse plasma frequency) and spatial scales much larger than the Debye length and particle gyroradius (*Kivelson, M. G. & Russell, C. T.*, 1995). The length scales of interest to justify the fluid description of ULF waves in the Earth's magnetosphere are the typical wavelengths for ULF waves, which are on the order of an Earth radius (6371 km), and the typical ion gyroradius (which is much larger than the Debye length of ~ 100 m), which is on the order of 10 to 100 km for protons at geosynchronous orbit in the Earth's magnetosphere. Since typical ULF wavelengths are much larger than typical ion gyroradii, a fluid description of ULF waves is valid for most regions of the Earth's magnetosphere, and the kinetic approach is not required. In the fluid description of magnetospheric plasma waves, it is also standard practice to neglect sources and losses of particles, except in the ionosphere where they may be significant (*Kivelson, M. G. & Russell, C. T.*, 1995).

In the two fluid approximation, where ions of a given species and electrons are treated as separate fluids, there is a large variety of plasma wave modes possible. This is true even when many simplifying assumptions are made. For example, in a homogeneous, unbounded, cold (thermal speed much less than wave phase speed) plasma, when wave propagation is along a background magnetic field, there are two approximate dispersion relations that arise from the two fluid approximation, leading to the two dispersion curves shown in Figure 1.4. The waves described by these relations are often referred to as the R (Figure 1.4A) and L

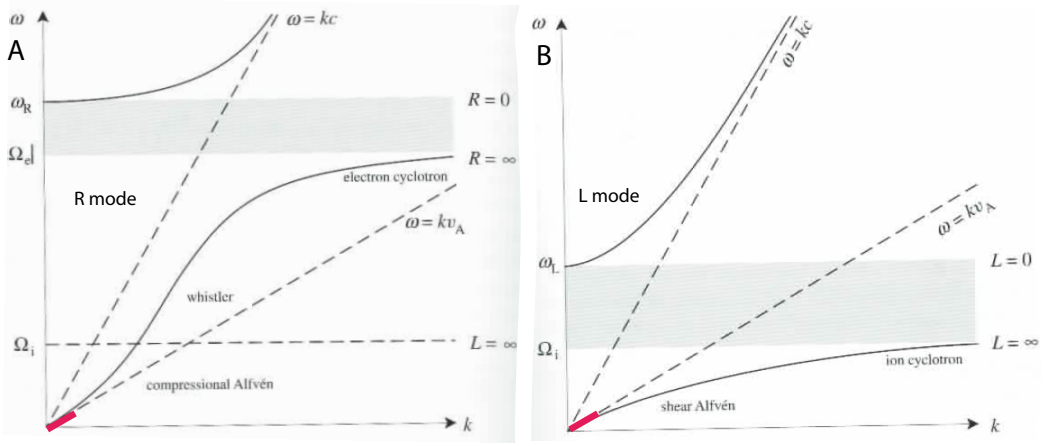

Figure 1.4: A) Dispersion curve for the R mode. B) Dispersion curve for the L mode (*Boyd and Sanderson*, 2003).

(Figure 1.4B) modes. The behavior of the R and L modes change as the frequency changes, and there are certain frequency ranges, or stop bands, where no wave activity is possible. Above and below certain characteristic frequencies, such as the ion cyclotron frequency, the wave behavior changes markedly, leading to different names for wave modes in these different regimes, such as the compressional Alfvén wave below the ion cyclotron frequency and the whistler wave above the ion cyclotron frequency for the R mode dispersion curve. It is important to note while referencing these curves that the frequencies of the ULF waves that we shall consider lie well below the ion cyclotron frequency, as indicated by the pink lines in each panel, where the dispersion curve is approximately linear. The R and L mode at these frequencies are equivalent to the fast and shear Alfvén modes in ideal MHD.

In the two fluid approximation, it is not straightforward to arrive at a simple solution even when restricting to propagation along or perpendicular to the background magnetic field in an unbounded, uniform medium; thus, studies attempting to describe ULF waves in the inhomogeneous magnetosphere where boundary conditions are important require a simpler description. Moving to a single fluid approximation requires additional assumptions, but greatly simplifies the problem. Using the MHD approximation, one assumes that the electric and magnetic fields change on timescales comparable to changes in plasma variables (e.g., electron and ion density). In this case, the displacement current and electrostatic force

can be neglected. For the purpose of describing ULF waves, one must assume that the wave phase velocity is much less than the speed of light (*Kivelson, M. G. & Russell, C. T.*, 1995; *Boyd and Sanderson*, 2003); the ratio of these two parameters in the Earth's magnetosphere is typically on the order of 0.001, so this assumption is justified. In ideal MHD, electrons and ions are treated as the same fluid and the conductivity of the fluid is very large while the collision frequency is small but finite; these are good approximations for the Earth's magnetosphere (*Schunk and Nagy*, 2004). Ideal MHD is often referred to as the large scale length limit (*Boyd and Sanderson*, 2003). With regard to ULF wavelengths, large means much greater than the local ion gyroradius; as previously stated, wavelengths are typically a factor of 10 or more larger than ion gyroradii in the Earth's magnetosphere, making this a good assumption.

The ideal MHD assumption has been used in a wide range of space physics applications. It is the most mathematically tractable approximation for describing ULF waves in the Earth's magnetosphere while accounting for the presence of significant inhomogeneities. The descriptions that have resulted from the MHD approximation have been validated in most regions of the Earth's magnetosphere through a considerable amount of observational evidence spanning more than 40 years (e.g., *Tamao*, 1965; *Southwood*, 1974; *Kokubun et al.*, 1976; *Kivelson and Southwood*, 1985; *Lee and Lysak*, 1989; *Glassmeier et al.*, 1999; *McPherron*, 2005, and the references therein).

1.4.2 Energy transfer via MHD waves

The dispersion relation for ideal MHD waves in cold plasma, assuming plane waves of the form $e^{i(kx-\omega t)}$ in a homogeneous medium (magnetic field and plasma mass density do not vary), is given by

$$(\frac{\omega}{k})^2 = v_a^2 \cos(\theta)^2 \tag{1.1}$$

$$(\frac{\omega}{k})^2 = v_a^2 \tag{1.2}$$

$$v_a^2 = \frac{B^2}{\mu_0 \rho} \tag{1.3}$$

where B represents the background magnetic field magnitude, ρ is the background plasma mass density, θ is the angle between the background magnetic field and the wave vector, and v_a is the Alfvén speed (e.g., *Kivelson, M. G. & Russell, C. T.*, 1995; *Boyd and Sanderson*, 2003). Equations 1.1 and 1.2 represent two different wave modes, the shear mode (1.1) and the compressional mode (1.2). The phase velocity of the shear mode depends on θ and the phase velocity of the fast mode does not. The shear mode can only carry energy along the direction of the background magnetic field, whereas the fast mode can carry energy both along the background field and perpendicular to it.

The Earth's magnetosphere is not a homogeneous medium, and it is not necessarily composed of cold plasma. This can lead to several important modification of the above equations. For example, when solving the linearized MHD equations in a dipole magnetic field geometry (still assuming cold plasma), the fast and shear Alfvén modes are nearly always coupled to some extent (*Radoski*, 1971). There are also instabilities that can generate ULF perturbations that become important when plasma temperature is finite (*Hasegawa*, 1969). However, despite these and other complications, the fast and shear Alfvén modes described in equations 1.2 and 1.1 are useful starting points for understanding how energy is transferred via ULF waves in the Earth's magnetosphere.

There is still much debate on how various energy sources from the solar wind ultimately transfer their energy to ULF waves. For example, field line resonance, a resonant coupling between the fast and shear Alfvén wave modes, is a well established paradigm for energy transfer from the solar wind, as evidenced by numerous models, simulations, ground observations, and in situ observations (e.g., *Southwood*, 1974; *Rae et al.*, 2005; *Claudepierre et al.*, 2010). However, all steps of the energy transfer process via FLR have not been directly observed simultaneously, leading some authors to conclude that the FLR mechanism should be regarded as a "well argued conjecture, but not as a proven phenomenon" (*Glassmeier et al.*, 1999). Sufficient proof of the operation of FLR would include consideration of the Poynting vector in the region of strong mode coupling between the compressional and shear Alfvén

modes; in particular, conversion from isotropic to field-aligned energy transfer (*Glassmeier et al.*, 1999).

Compressional MHD wave modes known as global modes, a type of standing fast mode wave, may be important for energy transfer via ULF waves through FLR, although their importance relative to other energy transfer mechanisms is an open question. Even in the presence of a broadband driver, they may select out certain discrete frequencies or frequency ranges; this frequency selection will in turn affect the location of FLR and peak energy transfer to shear Alfvén waves (*Wright and Rickard*, 1995). The term global mode may refer to cavity modes, waveguide modes, or trapped/tunneling modes (*Kivelson and Southwood*, 1985; *Zhu and Kivelson*, 1989; *Samson et al.*, 1992). These three wave modes share many similarities. One important similarity is that they are all affected by the radial Alfvén speed profile and, in particular, the sharp plasma density gradient at the plasmapause (*Zhu and Kivelson*, 1989). Despite the important role the plasmapause is suspected to play in modulating global modes and other ULF wave activity, there has been no attempt to systematically quantify the effect of the plasmasphere and plasmapause on ULF wave energy transfer using in situ observations.

Finally, there is debate as to whether standing Alfvén waves are typically directly driven by, for example, solar wind dynamic pressure fluctuations or through an intermediate step with a global mode (*Kivelson and Southwood*, 1985; *Kepko et al.*, 2002). There is evidence for both paradigms, but it is not clear which occurs most often, or whether certain regions of the magnetosphere or frequency bands are favored for one mechanism or the other (although waves directly driven by solar wind density fluctuations have been shown to occur preferentially at frequencies $\leq 5mHz$, (*Viall et al.*, 2009)). The same question (directly driven versus intermediate wave mode) has also been presented with regard to other ULF wave energy sources, such as magnetopause surface waves and substorms (*Mann et al.*, 1999; *Takahashi et al.*, 2001).

1.5 Outline of Study

In this thesis, two case studies and two statistical studies are presented to demonstrate the manner in which energy is transferred from the solar wind to magnetospheric ULF waves. Chapter 2 discusses a statistical study examining the effect of the plasmasphere on ULF wave energy transfer. We conclude in this chapter that the plasmasphere has an important effect on ULF wave energy transfer in the Pc5 frequency band; in particular, we quantify the difference in wave power spectral density inside and outside the plasmasphere, finding it to be as much as an order of magnitude for both electric and magnetic field perturbations. These observations complement models that have shown the importance of the plasmasphere in modulating ULF wave activity (e.g., *Zhu and Kivelson*, 1989). We propose that the difference in power spectral density is caused by the reflection of fast mode waves incident on the plasmapause from the outer magnetosphere or the fact that the range of frequencies accessible to standing Alfvén is typically above the Pc5 frequency range in the plasmasphere. Determining which of these reasons best explains these differences by comparing with models and making more detailed observations of wave polarization is a topic for future work.

Chapter 3 discusses a field line resonance case study. This is the first study to make an observation of the electromagnetic energy flux near the magnetic equator and at the FLR location, and we conclude that FLR is a viable mechanism for converting isotropic electromagnetic energy transfer to field-aligned electromagnetic energy transfer, meeting the criteria for the validation of the FLR paradigm described by *Glassmeier et al.* (1999). We also estimate the energy flux into the ionosphere and the Joule dissipation rate, which we find to be comparable. Future work could include better quantifying the energy transfer from the magnetic equator to the ground by including incoherent scatter radar (to better estimate energy lost through Joule dissipation) and low Earth orbiting satellites (to estimate energy lost through the field-aligned acceleration of electrons).

Chapter 4 discusses a global mode case study. In this study, we observe a global mode in the Pc5 frequency band outside of the plasmasphere; the global mode converts energy from solar wind dynamic pressure fluctuations with a broadband frequency spectrum to

monochromatic ULF wave activity in the magnetosphere, and it drives standing Alfvén waves at the plasmapause. This study is the first to show this conversion and energy transfer; we conclude that global modes are a viable mechanism for driving monochromatic shear Alfvén waves outside the plasmasphere in the Pc5 frequency band in the presence of an external energy source with a broadband frequency spectrum.

Chapter 5 discusses a statistical study of global modes. In this chapter, we use electric field data, magnetic field data, plasma data, and multi-point in situ and ground observations to identify an ensemble of 72 global mode events. We use this ensemble to estimate a lower bound for the normalized occurrence rate of global modes of 1%, and to identify the typical spatial locations, frequencies, and driving conditions for global modes. This is the first time a statistical study of global modes has been attempted using in situ data, and it is an important first step in quantifying the importance of global modes relative to other ULF wave modes in the context of energy transfer. Future work will include case studies drawn from this ensemble that are similar to the one presented in Chapter 4, but for different driving mechanisms and in different locations of the magnetosphere, to better understand what factors affect the spatial extent, duration, and amplitude of global modes.

Finally, in the sixth chapter, the results of this thesis are summarized.

CHAPTER 2

Pc5 wave power in the quiet-time plasmasphere and trough

The Combined Release and Radiation Effects Satellite (CRRES) mission provides an opportunity to study the distribution of MHD wave power in the inner magnetosphere both inside the high-density plasmasphere and in the low-density trough. We present a statistical survey of Pc5 power using CRRES magnetic field, electric field, and plasma wave data separated into plasmasphere and trough intervals. Using a database of plasmapause crossings, we examined differences in power spectral density between the plasmasphere and trough regions. These differences were typically a factor of 3 or 4 but could be as much as an order of magnitude and could be seen in both electric and magnetic field data. Our study shows that determining the plasmapause location is important for understanding and modeling the MHD wave environment in the Pc5 frequency band.

2.1 Introduction

The effectiveness different energy sources in driving ULF waves is determined in part by the presence of a significant population of cold plasma ($\leq 1eV$) in the inner magnetosphere known as the plasmasphere. The plasmasphere is a cold, dense plasma torus in the inner magnetosphere supplied by the ionosphere. The outer edge of the plasmasphere, known as the plasmapause, can be a smooth or a sharp cold plasma density gradient, depending on geomagnetic activity. Typical plasma density gradients at the plasmapause are a factor of five to ten decrease over half an L shell (from inside to outside). The plasmapause boundary has been observed at a wide range of radial distances from the Earth, anywhere from $L = 2$

to $L = 8$, and often overlaps with the more energetic ring current and radiation belt particle populations (*Lemaire and Gringauz*, 1998).

The presence of cold plasma can affect ULF waves in a variety of ways, including wave growth and energy transfer. For example, the drift-mirror instability that drives the growth of mirror mode waves occurs in high beta plasma (*Hasegawa*, 1969); the presence of a large population of cold plasma lowers the plasma temperature, making the plasma stable to the growth of drift-mirror waves. In the plasmasphere, $\beta \ll 1$, and mirror mode waves cannot grow there.

Drift-bounce resonance with ring current ions is also less likely to be effective in generating waves in the plasmasphere. These interactions require a substantial population of ring current ions to supply energy for wave growth (*Southwood et al.*, 1969), and they are often associated with enhancements in the dusk sector ring current (*Anderson*, 1993). Although it is possible for ring current ions to be present inside the plasmasphere, they are usually less likely to occur there and are only present near the plasmaspause boundary due to loss processes in the plasmasphere that include charge exchange and the generation of ion cyclotron waves near the plasmapause (*Williams*, 1983; *Fok et al.*, 1991). Primarily for this reason, waves driven by drift-bounce resonance with ring current ions are typically observed in regions outside the nominal plasmapause location (*Anderson*, 1993).

The plasmasphere can also affect energy transfer from sources of wave energy at the magnetopause to the inner magnetosphere. In some cases, the plasmapause will reflect wave energy incident on the plasmapause from the outer magnetosphere, whereas in others it will allow it to penetrate into the plasmasphere (*Zhu and Kivelson*, 1989; *Lee et al.*, 2002).

Despite theoretical expectations for the role of the plasmasphere in modulating Pc5 ULF waves, there have not been direct observations of this role other than in case studies. Statistical studies have typically not differentiated between the high-density plasmasphere and low-density trough region. For example, (*Hudson et al.*, 2004) found occurrence rates of Pc5 FLRs using CRRES magnetometer data, but they did not specify whether the observed FLRs occurred in the plasmasphere or trough region. (*Brautigam et al.*, 2005) obtained

radial profiles of electric field power spectral densities (PSDs) using CRRES, but they did not make comparisons between the plasmasphere and trough.

In this chapter, we present a statistical comparison of Pc5 wave power between the trough and plasmasphere using fluxgate magnetometer, electric field instrument, and sweep frequency receiver data from CRRES. We compare power in both regions to examine the plasmasphere's role in modulating Pc5 wave activity.

2.2 Methodology

2.2.1 Instrumentation

CRRES (Combined Release and Radiation Effects Satellite) operated from 25 July 1990 to 12 October 1991 in a geosynchronous transfer orbit. The orbit was designed so the local time at apogee changed by 2.5 minutes per day for complete local time coverage over 19 months. Since the mission ended in less than 15 months, there is a gap in coverage at higher L on the dayside. CRRES had a spin period of about 30 seconds (*Johnson and Kierein*, 1992).

The CRRES plasma wave experiment included an electric dipole antenna and sweep frequency receiver. The upper hybrid resonance frequency and electron plasma frequency are obtained from plasma wave spectra. These frequencies can then be used to calculate electron density (*Anderson et al.*, 1992).

The CRRES triaxial fluxgate magnetometer was sensitive to magnetic field variations greater than 0.43 nT in high-gain mode and 22 nT in low-gain mode. For the present MHD wave study, only the high-gain data are useful. The gain mode switched when the magnetic field strength exceeded 850 nT, which occurs near 3.5 Re (*Singer et al.*, 1992). The CRRES magnetometer data used in this study were transformed from spacecraft coordinates into spin resolution data in a modified GSE coordinate system (MGSE), where x points along the CRRES spin axis, which is approximately parallel to the x-axis in GSE, y intersects the ecliptic and spin planes and points towards dusk, and z completes the set (*Brautigam et al.*, 2005). These coordinates are similar to GSE because the CRRES spin axis points

approximately nine degrees from the Earth-Sun line.

The CRRES electric field instrument (EFI) measured the electric potential differences between two spherical probes and two cylindrical probes (*Wygant et al.*, 1992). Both measurements were made in the spin plane of CRRES and yielded electric field measurements with a sensitivity of 0.1 mV/m. The third component along the spin axis was obtained by assuming E dot B = 0. The spin-fit electric field data, like the magnetic field data, were transformed into MGSE. CRRES EFI data were previously used for statistical studies of electric field PSD in the Pc5 frequency band (*Brautigam et al.*, 2005). We follow the same procedure as *Brautigam et al.* (2005) in selecting electric field data that can be used in the present study. Because of several restrictions on the CRRES EFI data, coverage is very limited (*Brautigam et al.*, 2005).

2.2.2 Data Processing

Small gaps in the magnetometer and electric field data were filled through interpolation. A digital filter designed to pass frequencies below 2 mHz was applied. The low-pass filtered data were subtracted from the original data to remove the background field. The unprocessed and detrended data were both visually inspected for large spikes and unphysical wave activity, which were flagged. Step changes in any component, possibly due to current sheet crossings, were also flagged because they could be mistaken for Pc5 wave power in the statistical study.

A running 32 point (16 minute) Fast Fourier Transform (FFT) with a half window overlap was applied to compute PSD (see Appendix C.2 for FFT normalization convention); we average this PSD over the 2 to 8 mHz frequency band to examine Pc5 wave activity. Software available through the CRATERRE project (http://craterre.onecert.fr/home.html, funded by CNES, the French Space Agency) was used to compute CRRES's location in a Tsyganenko 1989 model field (*Tsyganenko*, 1989). The Tsyganenko 1989 L value, magnetic local time, and magnetic latitude for the time at the center of each FFT window were recorded.

Moldwin et al. (2002) used electron density inferred from the CRRES sweep frequency receiver and the following criteria to identify the plasmapause boundary: the plasmapause

occurs at the innermost location where there is at least a factor of five change in electron density within 0.5 L. Using these criteria, two plasmapause boundaries could be identified for each CRRES orbit. We compared the database of crossing times with the times at the center of each FFT window. If an FFT window occurred within eight minutes of a crossing, it was identified as being at the plasmapause. If CRRES was outbound and an FFT window occurred 8.5 minutes or more before a crossing, it was flagged as the plasmasphere; if it was outbound and an FFT window occurred 8.5 minutes or more after a crossing, it was flagged as the trough. Similar criteria were used when CRRES was inbound. If there was no crossing identified on the inbound or outbound part of CRRES's orbit, the data were excluded. Only data flagged as plasmasphere or trough were used in the study.

One limitation of the present study is the lack of data coverage in certain regions. In particular, there are large data gaps on the dayside because of the early termination of the CRRES mission. Also, CRRES spends more time at higher L values because of its lower radial velocity near the apogee. Finally, CRRES preferentially samples high magnetic latitudes at high L. Since some standing waves may have nodes in either the electric or magnetic field at certain latitudes, we use both electric and magnetic field data in the present study. However, the fluxgate magnetometer and EFI have unique limitations in data coverage. The magnetic field is poorly sampled for L less than 3.5 because only high-gain magnetometer data can be used. EFI also has many data coverage limitations (*Brautigam et al.*, 2005).

Figure 2.1 is an example interval from an orbit used in this study. In the top panel, regions flagged as trough and plasmasphere are indicated. Electron density was used as a proxy for the plasma mass density when identifying the plasmapause. However, it is worth noting that trends in the electron density will not always track the plasma mass density, because the relative concentration of heavy ions may change in different regions. These changes will modify the Alfvén speed and play an important role in modulating MHD wave activity (*Fraser et al.*, 2005).

The second panel in Figure 2.1 shows the sunward component of the detrended electric field, and the third panel shows the dynamic power spectrum. The fourth and fifth panels are

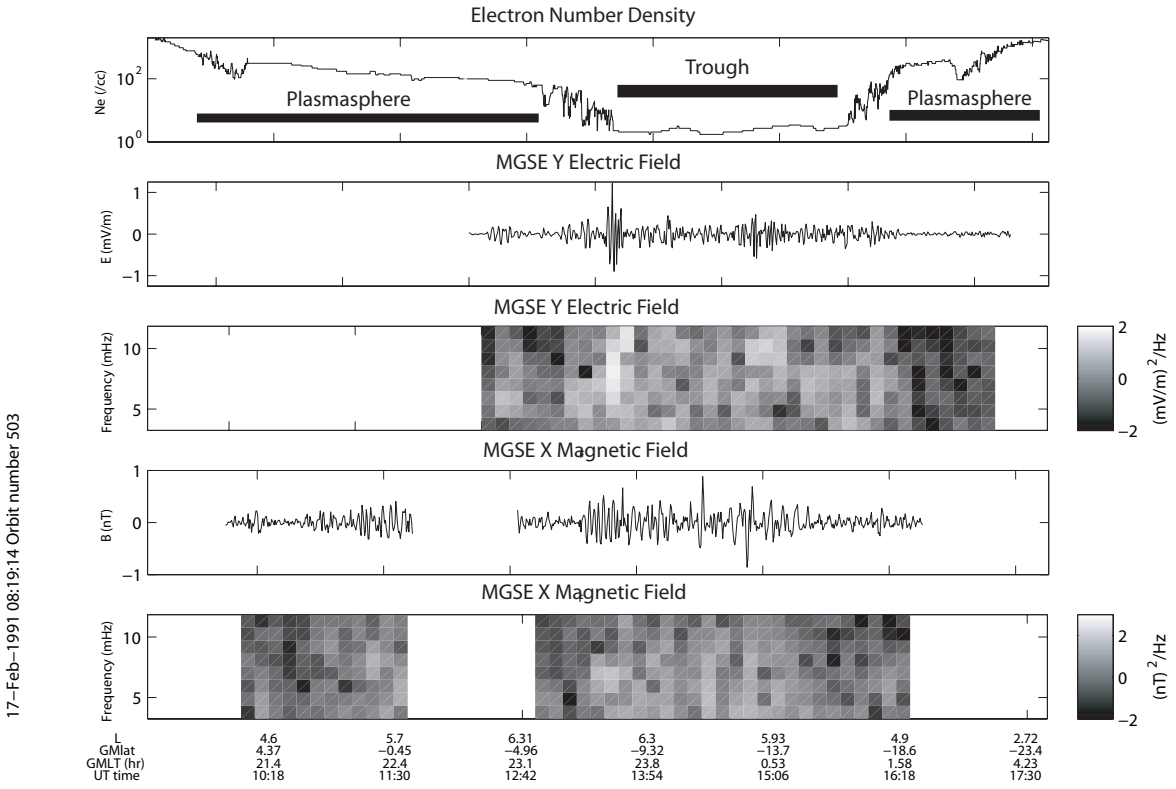

Figure 2.1: Orbit 503, 17 February 1991. An example of one orbit of CRRES data used in the statistical study. From top to bottom, electron density with plasmasphere and trough intervals indicated, MGSE x detrended electric field followed by corresponding dynamic power spectrum, MGSE x detrended magnetic field followed by corresponding dynamic power spectrum. From *Hartinger et al.* (2010).

for the sunward component of the magnetic field. There is an enhancement in Pc5 activity visible in both the electric and magnetic field data beginning at 13:30 UT that appears to coincide with CRRES crossing the plasmapause and moving into the trough. In the present study, we used electric and magnetic field data from many such orbits to determine whether the plasmasphere plays a statistically significant role in modulating Pc5 wave activity.

2.3 Results

The final data product used in this study is the total PSD, the sum of the PSD computed for all components in each FFT window, averaged over the 2 to 8 mHz frequency band. The data is binned by the Tsyganenko 1989 L value. Some power data are below the noise threshold of the electric ($10^{-0.75}(mV/m)^2/Hz$) and magnetic ($10^{\cdot 52}nT^2/Hz$) field instruments.

We further bin the data by Kp and separate between quiet ($Kp \leq 3$) and active times ($Kp > 3$). Previous studies have shown that increased Kp is correlated with increased ULF wave power (*Takahashi and Anderson*, 1992). Kp is also correlated with the most probable location of the plasmapause (*Moldwin et al.*, 2002). There is a strong potential source of bias when measuring Pc5 wave power if we do not consider geomagnetic activity. For example, when Kp is low, the plasmapause is likely to be located at high L. Thus, CRRES is more likely to be inside the plasmasphere at high L for low Kp. Similarly, when Kp is high, the plasmapause is likely located at low L. Thus, CRRES is more likely to be in the trough at high L for high Kp. During strong geomagnetic storms, the inner magnetosphere can also become severely distorted, impacting field-line mapping and modulating field-line resonance frequencies, producing another source of bias related to Kp (*Berube et al.*, 2006). Finally, there is a local time Kp bias on the spacecraft orbit due to the short duration of the CRRES mission. There was more geomagnetic activity during the latter part of the CRRES mission, when the apogee was in the dusk and midnight sectors. Because these sources of bias were most evident for active times, we focus on results obtained for $Kp \leq 3$.

Shown in Figure 2.2 are scatter plots of the logarithm of the Pc5 electric (left panel) and magnetic (right panel) field PSD (PSD that was averaged over the 2 to 8 mHz frequency

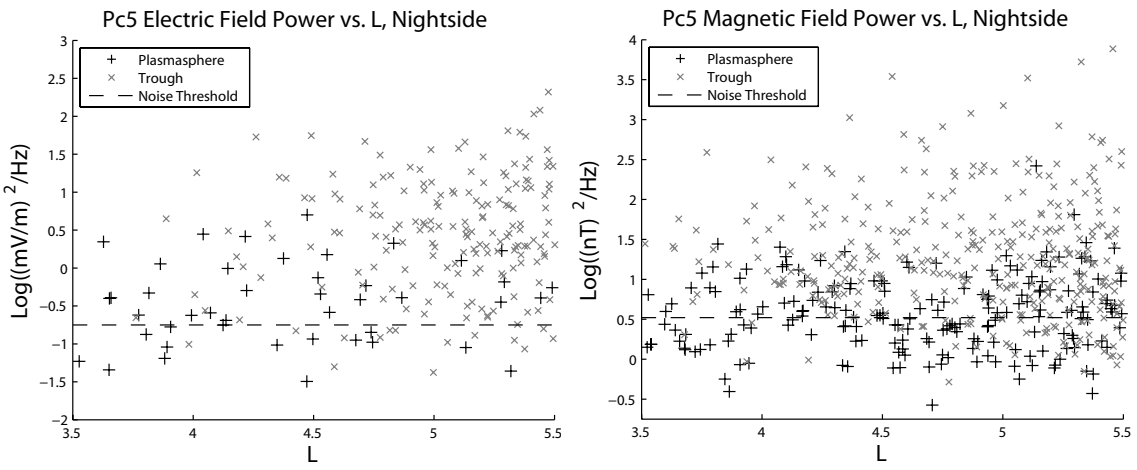

Figure 2.2: Scatter plots of total Pc5 power for each FFT window in the midnight sector (21 to 3 MLT) as a function of L. The left panel is electric field data with the + symbol indicating plasmasphere data, the x symbol indicating trough data, and the dashed line indicating the noise threshold for the data. The same symbols are used for magnetic field data in the right panel. From *Hartinger et al.* (2010).

band); we plot the total PSD, or the sum of the power computed for each component. Each point corresponds to a measurement of the Pc5 PSD for one FFT window, or time step. All measurements of the Pc5 PSD made in the midnight sector and during quiet times are shown. We chose the midnight sector for this figure because of the good electric and magnetic field data coverage in both the plasmasphere and trough. The data are divided by region, with +'s representing plasmasphere data and x's representing trough data.

A significant fraction of both the electric and magnetic field data recorded in the plasmasphere lie below the noise threshold of the instrument. The data also have a wide range, spanning more than three orders of magnitude for electric field data and four orders of magnitude for magnetic field data. In the present study, we will use median rather than mean values for comparisons, because the mean values can be strongly influenced by a few extreme events and a significant number of measurements below the noise threshold. The median electric field power value for all points in the plasmasphere is $10^{-0.41}(mV/m)^2/Hz$ compared to $100^{.47}(mV/m)^2/Hz$ in the trough. The median magnetic field power value for all points in the plasmasphere is $10^{0.57}(nT)^2/Hz$ compared to $10^{1.18}(nT)^2/Hz$ in the trough. In both panels, the data in the plasmasphere are clustered at lower power values than the trough for

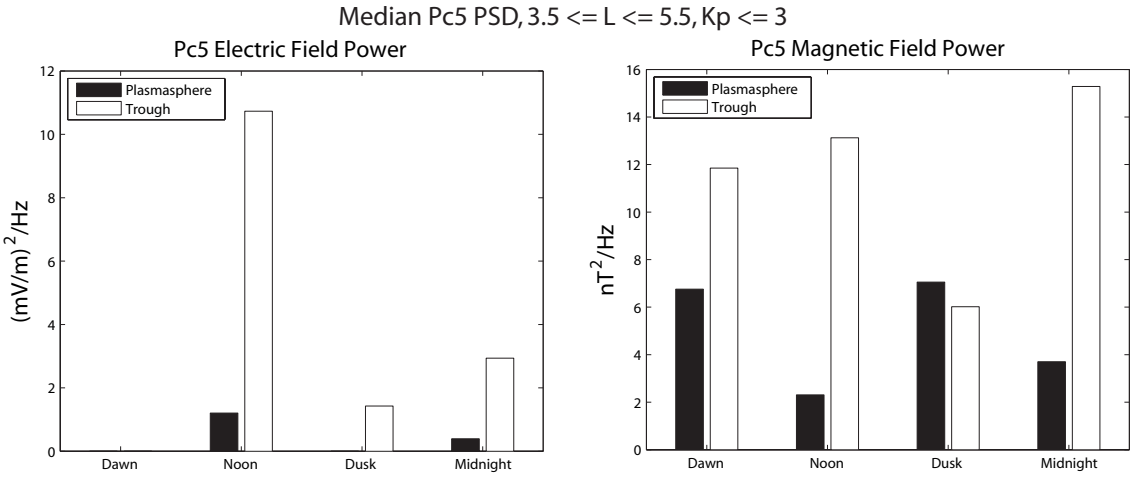

Figure 2.3: Median values of electric and magnetic field power in the plasmasphere and trough in different MLT regions for intervals where Kp = 3 and 3.5 = L = 5.5. From *Hartinger et al.* (2010).

all L.

In Figure 2.3, we display the median power values for the electric (left panel) and magnetic (right panel) fields for different MLT sectors on a linear scale. Dawn is from 3 to 9 MLT, noon is from 9 to 15, dusk is from 15 to 21, and midnight is from 21 to 3. The data are further restricted to $Kp \leq 3$ and $3.5 \leq L \leq 5.5$, a particularly well sampled region for both electric and magnetic field data in the plasmasphere and trough.

The only MLT sectors that allow comparisons between the plasmasphere and trough for both the electric and magnetic fields are noon and midnight. At midnight, the median power is roughly 8 times larger in the trough compared to the plasmasphere for the electric field and 4 times larger for the magnetic field. At noon, the median power is roughly 9 times larger in the trough compared to the plasmasphere for the electric field and 6 times larger for the magnetic field.

In the dawn and dusk sectors, only magnetic field data is available for comparison. In the dawn sector, the total magnetic field PSD is roughly twice as large in the trough compared to the plasmasphere. The dusk sector is the only local time sector where no significant difference in the magnetic field PSDs is observed between the plasmasphere and trough.

We performed similar comparisons for $L > 5.5$ and $Kp > 3$ and observed similar results. However, there was only adequate data for a comparison with both electric and magnetic field data in the midnight sector for $L > 5.5$. For both $Kp \leq 3$ and $Kp > 3$, we found that the trough had higher power than the plasmasphere by roughly an order of magnitude.

2.4 Discussion

The most prominent feature in Figure 2.3 is the difference in the median PSDs between the trough and the plasmasphere. PSD may be lower in the plasmasphere because solar wind driven waves in the Pc5 band do not penetrate into the plasmasphere effectively. It is also possible that nominal conditions in the plasmasphere are not conducive to MHD resonance in the Pc5 band. If the fundamental FLR frequency and the fundamental cavity resonance frequency do not typically occur in the Pc5 band in the plasmasphere, one would expect a much lower average PSD.

We find that the difference in PSDs between the plasmasphere and trough depends on local time sector. For example, we do not observe as significant a difference in the median magnetic field PSDs in the dusk sector compared to other sectors. There are a few possibilities for this local time dependence. It is possible that solar wind driven MHD waves in the Pc5 frequency band cannot penetrate into the plasmasphere effectively. Internally generated waves, however, may be more likely to occur inside the plasmasphere than previously expected. This would explain the negligible difference in PSDs at dusk, as internally generated Pc5 waves are more likely to occur at dusk (*Hudson et al.*, 2004). The distribution of the plasma mass density in the plasmasphere and the sharpness of the plasmapause density gradient also depend on local time and may play a role in determining the difference in PSDs. For example, the dusk region is more structured due to the presence of plumes and the plasmapause boundary at dusk tends to be smoother and less well defined (*Moldwin et al.*, 2002). This could affect the transmission of wave energy from the trough to the plasmasphere, perhaps making it easier for wave energy to penetrate deeper into the plasmasphere in the dusk sector (*Zhu and Kivelson*, 1989).

2.5 Summary

We have presented a statistical comparison of Pc5 wave power between the plasmasphere and trough regions and demonstrated that the plasmasphere plays a significant role in modulating Pc5 wave activity. For quiet times, the median total PSD in the electric and magnetic fields is higher in the trough compared to the plasmasphere. However, the difference in power depends on local time, with the largest differences of about an order of magnitude occurring at noon and midnight and almost no difference at dusk.

Our observations and several previous observations and models have demonstrated the importance of constraining properties of the plasmasphere and plasmapause when studying MHD wave propagation and resonance in the inner magnetosphere. Persistent spatial features that are unique to the plasmasphere or trough could be examined in future statistical studies of the global distribution of MHD wave power if data from each region are studied separately. For example, *Brautigam et al.* (2005) found that electric field Pc5 PSDs decreased with decreasing radial distance. Our results suggest that part of this decrease is due to the presence of the plasmasphere at low L. In other words, the decrease at low L would not be as large if only trough data were studied.

This study also suggests that radiation belt models that use empirical averages of Pc5 wave power should consider the location of the plasmapause. Radiation belt models that incorporate MHD waves as a source of radial diffusion could be improved by constraining the location of the plasmapause, since radial diffusion coefficients are affected by MHD wave power (e.g., *Elkington et al.*, 2003). For example, an average for Pc5 power that included both trough and plasmasphere data would underestimate the average power in the trough and overestimate the average power in the plasmasphere. The effects of radial diffusion due to Pc5 waves would then be underestimated in the trough region and overestimated in the plasmsphere.

CHAPTER 3

Global energy transfer during a magnetospheric field line resonance

Field line resonances (FLRs) are important for transferring energy from fast mode waves to shear Alfvén waves in the Earth's magnetosphere. Using simultaneous multi-satellite observations from THEMIS and the IMAGE ground magnetometer array, we report on the transfer of energy from compressional magnetopause undulations through an FLR to the ionosphere. Energy diversion from the magnetosphere to the ionosphere took place at the FLR: we find net energy flux there to have comparable values in the radial and the field-aligned directions. The field-aligned energy flux, when mapped to the ionosphere, was 0.70 mW/m^2 and consistent with the inferred Joule dissipation rate at that time. IMAGE's regional monitoring of wave activity reveals that the temporal evolution of the FLR wave power and energy transfer were correlated with the amplitude profile of magnetopause undulations, confirming these waves to be the FLR driver.

3.1 Introduction

The Earth's magnetosphere is an inhomogeneous medium. This facilitates energy transfer between different plasma wave modes at plasma boundaries. Early models of magnetohydrodynamic (MHD) wave propagation in the Earth's magnetosphere suggested that the shear and compressional MHD wave modes could couple via a field line resonance (FLR) mechanism (*Tamao*, 1965).

General features of field line resonance can be obtained through an analogy with a series of damped, driven simple harmonic oscillators in a steady state. They each have a different

spring constant, k. They all have the same mass, m, damping constant, γ, and are all being driven at the same frequency and amplitude, ω_d and A. The equation of motion for any of the oscillators is given by

$$m\frac{d^2x(t)}{dt^2} + kx(t) + \gamma\frac{dx(t)}{dt} = Ae^{i\omega_d t} \tag{3.1}$$

Taking the Fourier transform of both sides of the above equation, solving for $X(\omega)$, the Fourier transform of $x(t)$, and finally taking the inverse Fourier transform of $X(\omega)$ yields the following solution

$$x(t) = \frac{-1}{2\pi}\frac{A}{m}\frac{1}{\omega_d^2 - \omega_0^2 - i\frac{\gamma\omega_d}{m}}, \omega_0^2 = \frac{k}{m} \tag{3.2}$$

where ω_0 is the natural frequency of the simple harmonic oscillator. The phase of each oscillator's motion, neglecting the sinusoidal time dependence, is

$$\frac{\pi}{2} - \arctan\frac{\gamma\omega_d}{m(\omega_d^2 - \omega_0^2)}, \omega_d > 0, \omega_d > \omega_0 \tag{3.3}$$

$$-\frac{\pi}{2} - \arctan\frac{\gamma\omega_d}{m(\omega_d^2 - \omega_0^2)}, \omega_d > 0, \omega_d < \omega_0 \tag{3.4}$$

The amplitude of each oscillator's motion is given by

$$|x| = \frac{A}{m\sqrt{2\pi[(\omega_d^2 - \omega_0^2)^2 + (\frac{\gamma\omega_d}{m})^2]}} \tag{3.5}$$

Inspecting the above equation for the amplitude, it is clear that the maximum displacement for the oscillator occurs when the driving frequency matches the natural frequency of the harmonic oscillator. Examination of the expression for phase shows that there is a rotation of 180 degrees when comparing oscillators that have natural frequencies just below the driving frequency to oscillators that have natural frequencies just above the driving frequency.

The above model can explain many of the features expected for field line resonance in the Earth's magnetosphere. Standing, shear Alfvén waves have frequencies that are determined by the Alfvén speed along a field line and the length of the field line. The local Alfvén frequency varies as a function of radial distance. Fast mode waves with a particular frequency

will couple to standing Alfvén waves most strongly at the location where the fast mode frequency matches the local standing Alfvén wave frequency (*Southwood*, 1974). Just as the simple harmonic oscillator with the frequency that matched the driving frequency in the example above had the peak displacement, the field line at this location will have the maximum displacement, or wave amplitude.

If the standing Alfvén wave frequency is a monotonically increasing or decreasing function of radial distance, the standing Alfvén wave frequency will be lower on one side of the location of maximum displacement and higher on the other side. This will lead to a 180 phase difference between displacements on either side of the location of peak displacement, just as the simple harmonic oscillators with lower natural frequencies were 180 degrees out of phase with the oscillators with higher natural frequencies.

Energy transfer near an FLR has been modeled in several studies (e.g., *Junginger*, 1985; *Kouznetsov and Lotko*, 1995). If the FLR is being driven by a source in the solar wind or a surface wave at the magnetopause, net energy flux directed earthward into the resonance region is expected. This energy flux is both kinetic and electromagnetic (Poynting vector). Electromagnetic energy transfer will be the focus of this study; however, it should be noted that kinetic energy flux can significantly alter the expected behavior of the MHD wave modes associated with field line resonance (*Kouznetsov and Lotko*, 1995). In the FLR region, the earthward energy flux is converted to net field-aligned energy flux, as the FLR loses energy to the ionosphere through Joule dissipation (*Newton et al.*, 1978; *Glassmeier et al.*, 1984). It is expected that earthward energy flux (perpendicular to the background magnetic field) should be larger near the magnetic equator, as models and observations show that compressional MHD waves are confined to this region (*Zhu and Kivelson*, 1991; *Lee*, 1996).

Junginger et al. (1985) examined the Poynting vector for Pc5 pulsations, finding values from 10^{-10} to $10^{-5}\frac{W}{m^2}$ that were often directed radially inward and tailward. *Rae et al.* (2005) identified a specific FLR that was steady over several hours and using ground and satellite measurements they examined the associated Poynting vector averaged over several wave cycles. They found that the radial Poynting vector component was smallest, followed by a significant azimuthal (tailward) and a dominant field-aligned component. *Rae et al.*

(2007) examined the energy balance between the average field-aligned Poynting vector and Joule dissipation rate in the ionosphere, finding that they were nearly equal.

The goal of this chapter is to examine the energy transfer associated with a shear Alfvén mode generated through the FLR mechanism. We present simultaneous observations of an FLR near the magnetic equator (i.e., where compressional-to-shear Alfvén wave coupling is strong), at the magnetopause boundary (i.e., where the solar wind driver imparts energy) and on the ground, where a network of stations removes the space-time ambiguity associated with single spacecraft crossings of a resonant L-shell. The fortuitous conjunction occurred on 31 October 2008 near the dawn terminator.

3.2 Instrumentation

We use magnetospheric data from the five-satellite Timed History of Events and Macroscale Interactions (THEMIS) mission, solar wind data from OMNIweb that have been time-referenced to the subsolar magnetopause, and ground magnetometer data from the International Monitor for Auroral Geomagnetic Effects (IMAGE) array (*Sibeck and Angelopoulos*, 2008). Observations from the five THEMIS satellites are particularly useful for ULF wave studies (e.g., *Agapitov et al.*, 2009; *Sarris et al.*, 2009). Each satellite has a 3 second spin period and is equipped with a fluxgate magnetometer (FGM, (*Auster et al.*, 2008)), an electric field instrument (EFI, (*Bonnell et al.*, 2008)), and an ion and electron electrostatic analyzer (ESA, (*McFadden et al.*, 2008a)). EFI provides its highest-quality low frequency measurements in the spin-plane. The third component of the electric field is obtained by assuming $E \cdot B = 0$ when the normal of the spacecraft spin plane is sufficiently far from the background magnetic field direction. ESA measures the three-dimensional particle distributions and moments (electrons: 5 eV - 30 keV, ions 5eV - 25 keV) once per spin.

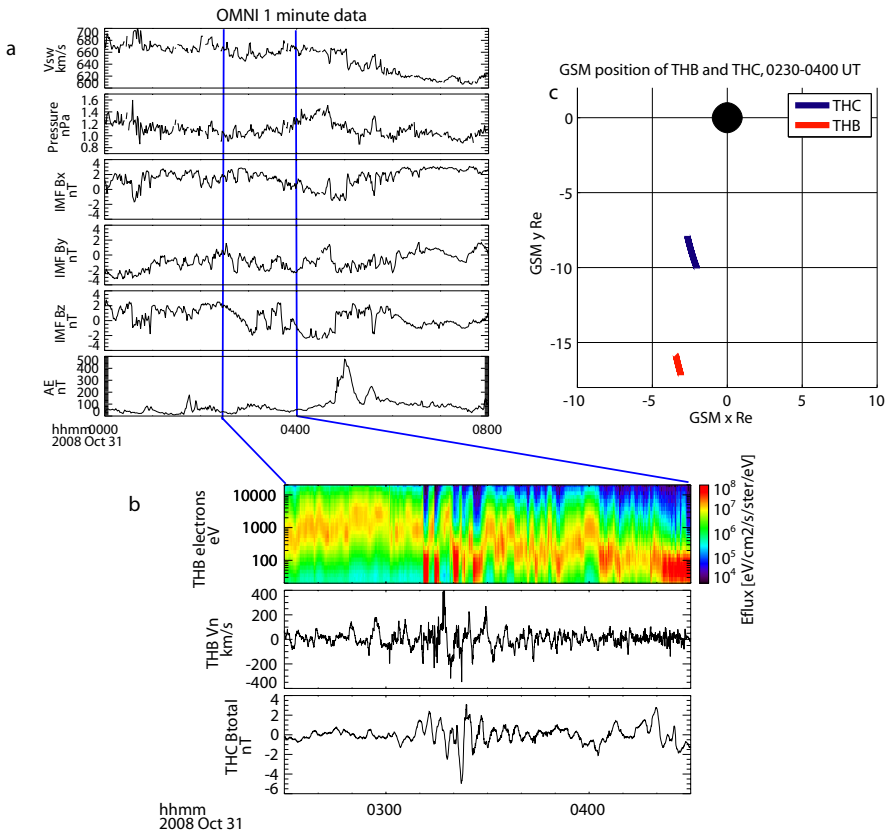

Figure 3.1: a) From top to bottom, solar wind velocity, dynamic pressure, IMF Bx (GSE/GSM), IMF By (GSM), IMF Bz (GSM), and the AE index from OMNIweb. b) From top to bottom, a dynamic energy flux spectrogram from TH-B (electrons), the plasma velocity component normal to the magnetopause inferred from TH-B ESA ion measurements, and detrended total magnetic field from TH-C. c) The orbits of TH-B and TH-C in the GSM equatorial plane during the interval from 0230 to 0400 UT. From *Hartinger et al.* (2011).

3.3 Observations

The FLR event occurred during a period of quiet geomagnetic activity, elevated ($\sim 650 \frac{km}{s}$) solar wind velocity, weak dynamic pressure, and some IMF fluctuations (see top panel of Figure 3.1a). The high value of the solar wind speed suggests that the magnetopause was most probably Kelvin-Helmholtz unstable (e.g., *Engebretson et al.*, 1998). Magnetopause undulations were observed by THEMIS-B (TH-B, P1) between 0230 to 0400 UT near the magnetopause boundary, as shown in 3.1b: The energy-time spectrogram from ESA data (Fig. 3.1b top panel) shows the characteristic signatures of alternating hot (1 keV) magnetospheric and cold (100 eV) magnetosheath electrons, consistent with multiple magnetopause cross-

ings. We follow *Liu et al.* (2008) and compute the component of the ion velocity (from ESA on board moments) normal to the nominal magnetopause. Several strong negative/positive excursions in the normal velocity occur inside the magnetopause just before/after sheath crossings in (Figure 3.1b, panel 2). These magnetopause velocity undulations have an approximate frequency of 5 mHz (as determined by the spacing between negative excursions) and clearly increase in amplitude from 0310 to 0330 UT. TH-C is located several Earth Radii (RE) inside of the magnetopause (Fig. 3.1c). The high-pass filtered (> 0.5 mHz) total magnetic field at TH-C is shown on the third panel of Figure 3.1b. ULF waves of about 5 mHz frequency, consistent with the velocity perturbations observed by TH-B, are evident there.

Similarly high-pass filtered electric and magnetic field vectors observed at TH-C were rotated into a field-aligned coordinate system in which y points eastward, z is along the background magnetic field (direction obtained from low pass filtered data, frequency < 0.5 mHz), and x completes the orthogonal set pointing approximately radially outward. In Panel 1 of Figure 3.2, the x component of the electric field is shown, and Panel 2 is for the corresponding dynamic power spectrum. A large enhancement in wave activity occurred from 0310 to 0340 UT. The frequency of the enhanced wave activity was 5 mHz, with several harmonics at higher frequencies. Panels 3 and 4 show the y component of the detrended magnetic field and corresponding dynamic power spectrum; an enhancement is also seen there at ~ 5 mHz.

To examine the phase relations amongst various components we next band pass filter these data and plot the radial electric and east-west magnetic field components in Panel 5. Both the surface wave frequency and the wave activity observed at TH-C had a frequency of ~ 5 mHz; we found that a band pass filter with an upper and lower cutoff of 3 and 6 mHz, respectively, best captured this wave activity (i.e., did not introduce changes in the phase or amplitude of the signal) while removing weaker wave activity that was present with lower and higher frequencies. It is evident from the filtered data that the electric and magnetic field were approximately 90 degrees out of phase during the period of enhanced wave activity. We next employ the method of the analytic signal to determine the instantaneous amplitude and

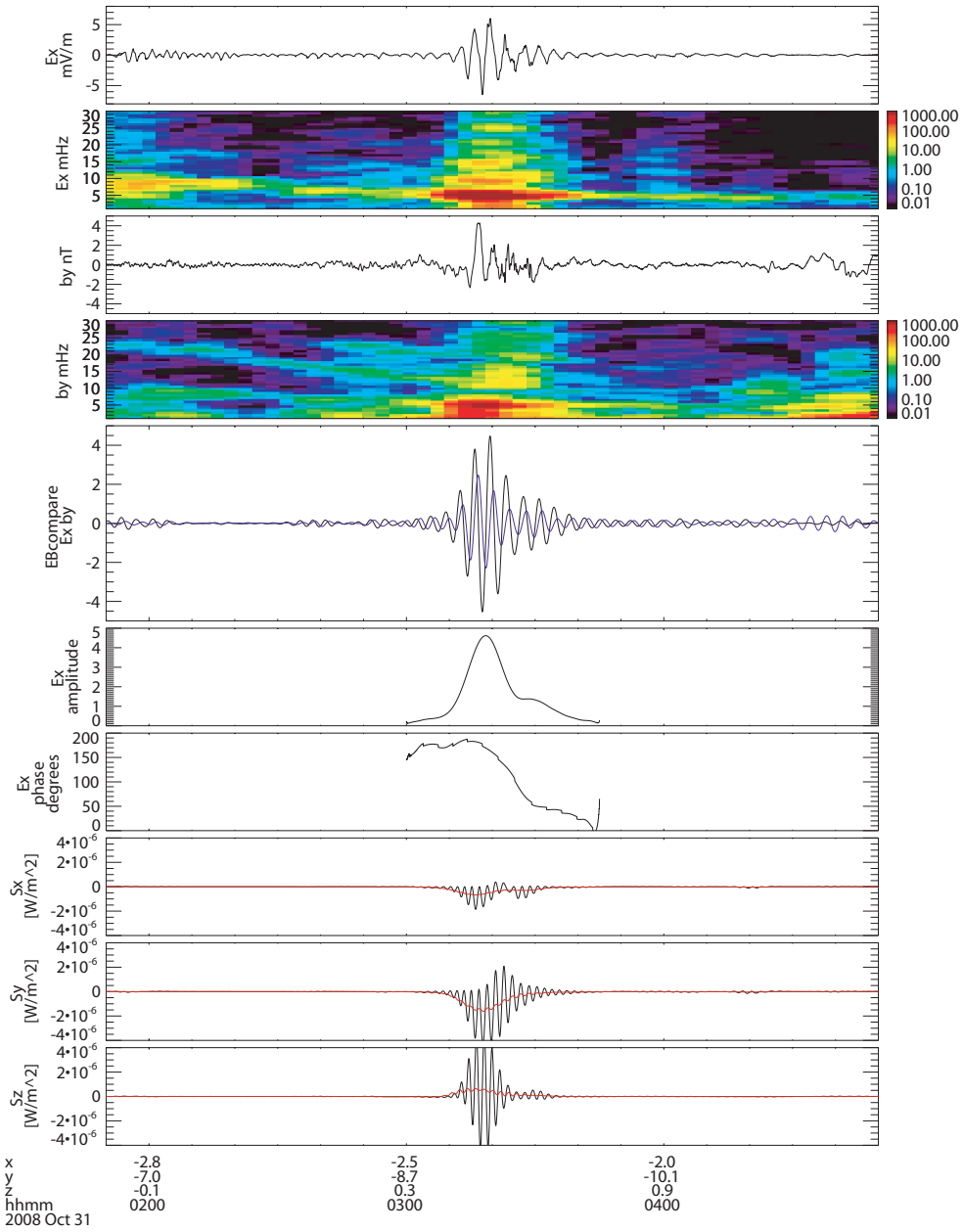

Figure 3.2: From top to bottom, radial electric field, radial electric field dynamic power spectra, east-west magnetic field, east-west magnetic field spectra, band pass filtered (3-6 mHz) radial electric (black) and east-west magnetic field (blue) data, instantaneous amplitude of radial electric field, instantaneous phase of radial electric field, radial Poynting vector (black) and time averaged radial Poynting vector (red), east-west Poynting vector, field-aligned Poynting vector. The time average is computed with a running 10 minute boxcar window. From *Hartinger et al.* (2011).

phase of the x component of the electric field during the period of enhanced wave activity (*Glassmeier*, 1980). Panels 6 and 7 show a clear change in phase of about 180 degrees across the amplitude peak. All of the observations presented in panels 1-7 are therefore consistent with a toroidal wave mode associated with an FLR: there was a localized peak in amplitude in both the radial electric and east-west magnetic field; the two field components were 90 degrees out of phase; there was a clear jump in phase of approximately 180 degrees across the FLR; and harmonics were observed. Finally, the frequency of 5 mHz is expected for a toroidal mode in this region (*Lee and Lysak*, 1989).

Panels 8 - 10 show, in black lines, the Poynting flux components computed using the band-pass filtered data in a field aligned coordinate system. Red lines are component running averages (10 minute window), showing the net energy transfer over several wave cycles. It is clear that the strongest energy flux in all three directions occurred at 0310-0330 UT. Panel 8 shows the radial component, with a net energy flux towards Earth. The east-west component, in Panel 9, shows a net energy flux westward, i.e., towards the magnetotail, given the spacecraft location at the dawn terminator. The field-aligned component, in Panel 10, shows a net energy flux towards the northern ionosphere, as expected for a damped standing wave.

Finally, we examine 10 sec magnetic field data from the IMAGE magnetometer array. The IMAGE magnetometers were in the same local time sector as TH-C at the time the FLR was observed. In Figure 3.3, the component of the magnetic field that points towards magnetic north, or X component, is shown after detrending (frequency $> 0.5mHz$). Like TH-C, the stations see an increase in wave activity at 0310. Figure 3.4 shows the dynamic power spectrum for these data, and the frequency of the wave activity is peaked at 5 mHz, like at TH-C.

To more closely compare with TH-C observations, we overplot lines of constant L parameter (*McIlwain*, 1966), calculated at time 0315 UT using software from the French National Aerospace Research Center (ONERA), on a map of the magnetometer station locations (Fig. 3.5a). This McIlwain parameter, L, is a proxy of the equatorial distance of a ground point. We chose to use the *Mead and Fairfield* (1975) external magnetic field model, combined

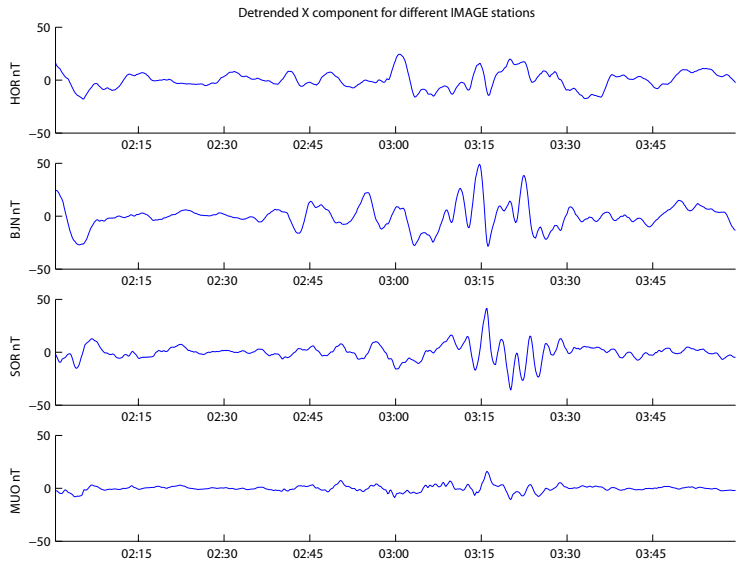

Figure 3.3: Ground magnetometer data (H component) from four IMAGE stations is shown after high pass filtering (frequency $> 0.5mHz$). From top to bottom, HOR ($L \sim 16$), BJN ($L \sim 11$), SOR ($L \sim 9$), and MUO ($L \sim 5$). From *Hartinger et al.* (2011).

with an International Geomagnetic Reference Field (IGRF), to compute these constant-L lines, because this combination provides the best match of the magnetic field at TH-B and TH-C during this interval. In Fig. 3.5a, a red line shows the ground track of TH-C between 0300-0345 UT, mapped using the same model and software. The detrended (hourly mean subtracted) X component of the magnetic field is shown on a smaller timescale in Fig. 3.5b. Data from two stations are overplotted in each panel. The top panel is for the two stations at the highest magnetic latitudes, HOR and BJN, the next for intermediate latitudes, BJN and SOR, and the bottom for lowest latitudes, SOR and MUO. A 5 mHz signal is most clearly seen in the stations that map to locations close to THC (BJN and SOR), but this signal is also visible at other stations. A black line indicates a time when a 180 degree phase difference between BJN and SOR is clearly visible, whereas the other station pairs have signals that are in phase. This phase jump at 5 mHz between BJN and SOR is apparent for several wave cycles and provides further confirmation that TH-C crossed through the center of an FLR, even though the FLR was evolving in time. This phase reversal is seen more clearly in cross phase spectrograms.

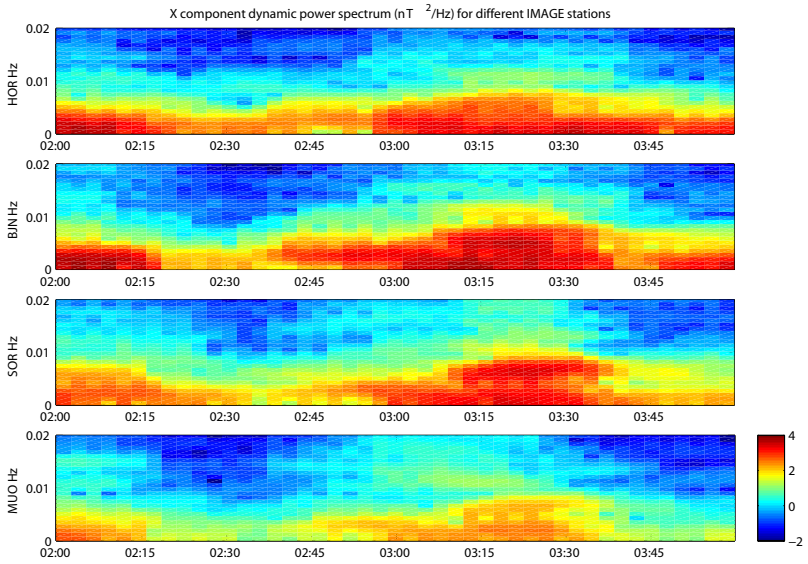

Figure 3.4: Dynamic power spectrum for the X traces shown in Figure 3.5. Units are in nT^2/Hz, and the frequency range is from 0 to 20 mHz. From top to bottom, HOR ($L \sim 16$), BJN ($L \sim 11$), SOR ($L \sim 9$), and MUO ($L \sim 5$). Note the power enhancement at frequencies of about 5 mHz at 0310 UT. This is most clearly seen at SOR and MUO, where the power is less broadband. From *Hartinger et al.* (2011).

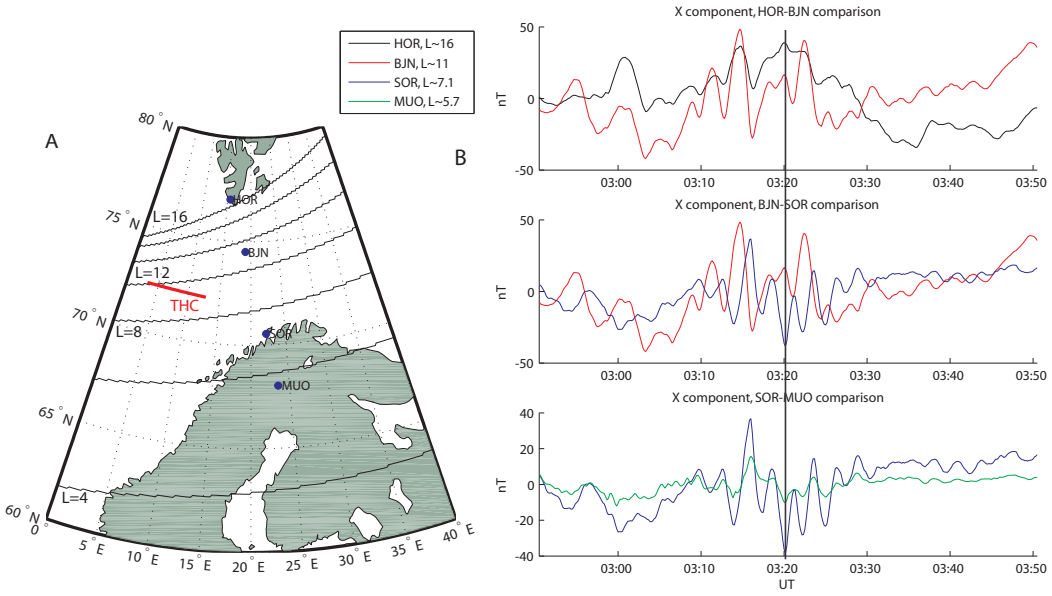

Figure 3.5: a) The positions of IMAGE magnetometer stations are plotted on a geographic grid (dotted lines) and solid black lines of constant McIlwain L parameter are overplotted in steps of 2 Re. The red line is the ground track of TH-C, mapped from TH-C's position using field line tracing in the *Mead and Fairfield* (1975) magnetic field model. b) In each panel, the X component of the magnetic field with hourly means subtracted is plotted for pairs of stations. From top to bottom, the X component of the magnetic field observed at HOR and BJN, BJN and SOR, and SOR and MUO is shown. A black line indicates a time when a 180 degree phase difference between BJN and SOR is particularly clear, whereas the other stations are in phase. From *Hartinger et al.* (2011).

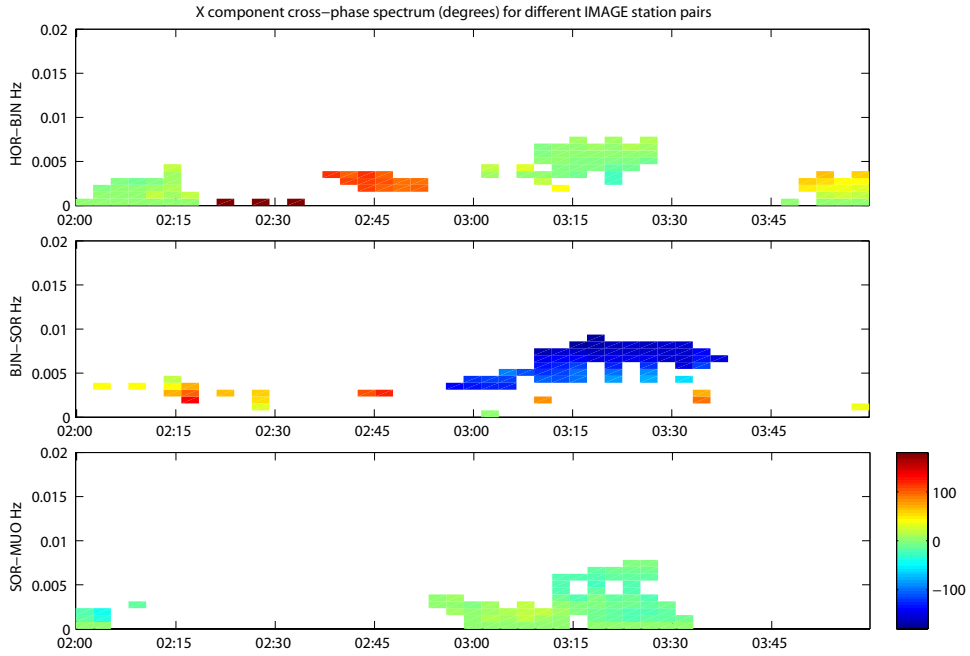

Figure 3.6: Masked dynamic cross phase spectrum for different IMAGE station pairs, using the X traces shown in Figure 3.3. Points where either a) the PSD observed at either station is less than 100 nT^2/Hz, or b) the coherence is less than 0.7, are not displayed. Units are in degrees and the frequency range is from 0 to 20 mHz. From top to bottom, the cross phase between HOR ($L \sim 16$) and BJN ($L \sim 11$), BJN and SOR ($L \sim 7$), SOR and MUO ($L \sim 5$). Only signals with high coherence and PSD are shown, and the FLR is clearly observed using these three station pairs. The two stations at higher latitudes than the FLR (HOR, BJN) are in phase (~ 0 degrees phase difference), the two at lower latitudes (SOR, MUO) are in phase (0 degrees phase difference), and the two on either side are ~ 180 degrees out of phase (BJN, SOR). From *Hartinger et al.* (2011).

In Figure 3.6, the masked dynamic cross phase spectrograms are shown for the same station pairs as in Figure 3.5. Points where either the PSD is less than 100 nT^2/Hz or the coherence is less than 0.7 are not displayed. The points with the highest PSD and coherence correspond to the increased wave activity beginning at 0310. The middle station pair (BJN, SOR), with stations on either side of the FLR, shows a 180 degree phase difference, whereas the other station pairs are in phase.

3.4 Discussion

The FLR and associated wave activity observed by TH-C and ground magnetometers beginning at 0310 UT appears to be strongly linked to the change in the character of the boundary undulations that occurred from $0310 - 0330$ UT. We conclude that the increase in amplitude of the magnetic field perturbations observed by TH-C beginning at 0310 UT was the result of the temporal evolution of the driver rather than the spatial motion of TH-C through the FLR. However, the rotation in phase of the radial electric field at TH-C (3.2, panel 7) and the phase variation observed by the ground magnetometers (Figure 3.5b, 3.6), argue that TH-C also fortuitously passed through the center of the FLR at approximately 0325 UT, i.e., approximately near the time of FLR absolute peak power.

The average Poynting vector (from band pass filtered electric and magnetic field data, 3 to 6 mHz) observed by TH-C from 0310-0330 UT was $-4.3*10^{-7}\frac{W}{m^2}$ for the radial component (earthward), $-8.6 * 10^{-7}\frac{W}{m^2}$ for the azimuthal component (tailward), and $3.3 * 10^{-7}\frac{W}{m^2}$ for the field-aligned component (towards the northern ionosphere). Net field-aligned energy flux was comparable to radial energy flux, suggesting that strong coupling was occurring between the driving wave and the Alfvén waves via FLR.

Our results differ from *Rae et al.* (2005), who observed "very small radial, significant azimuthal, and dominant field-aligned" Poynting vector near an FLR. In our case, the azimuthal component of the Poynting vector was the strongest for both net and instantaneous energy transfer. Additionally, the net radial Poynting vector was larger than the net field-aligned Poynting vector. Finally, the instantaneous radial Poynting vector was about 3 times larger relative to the instantaneous field-aligned Poynting vector in this study compared to *Rae et al.* (2005). One potential explanation for these differences is the different positions of the satellites used in each study; *Rae et al.* (2005) used observations from POLAR, which was located between 4 and 15 degrees magnetic latitude, whereas TH-C was within 3 degrees of the magnetic equator (location determined using the *Mead and Fairfield* (1975) model). Compressional MHD waves propagate near the magnetic equatorial plane, leading to higher perpendicular Poynting vectors in this region (*Zhu and Kivelson*, 1989; *Lee*, 1996). Our

observations suggest that TH-C is directly observing strong coupling between fast mode and shear Alfvén waves via FLR because of its location near the magnetic equator, as the observed radial and field-aligned energy transfer is comparable.

Another explanation for the differences between this study and *Rae et al.* (2005) is that the present observation was made on October 31, closer to equinox than the case study of *Rae et al.* (2005), which was made on November 25. In the *Rae et al.* (2005) study, the conductivity at the northern and southern footpoints of the field line where the resonance was observed would have been more asymmetric than the present case study, with the conductivity lower in the northern ionosphere. This would shift the null point for energy transfer, or the point at which there is no net energy transfer in the field-aligned direction, below the magnetic equator (*Allan*, 1982). POLAR may thus have been further from the null point, the expected region of strongest coupling between the fast and shear Alfvén modes, than the magnetic latitude suggests in the *Rae et al.* (2005) study, leading to the weak (compared to parallel Poynting vector) perpendicular Poynting vector observation. In the present study, this effect would be less pronounced since the ionospheric conductivities are less asymmetric near equinox.

Finally, the difference between the Poynting vector observations in this study and the *Rae et al.* (2005) study may be due to the location of the probes in magnetic local time. In the present study, TH-C was located near the dawn flank at 5 MLT whereas POLAR was located near 20 MLT in the *Rae et al.* (2005) study (an hour further from the dayside). TH-C was closer to the magnetopause location, where the surface waves driving the FLR were generated, when compared to POLAR. Thus, the energy flux associated with the evanescently decaying wave may have been easier to observe in the present study when compared to *Rae et al.* (2005).

The energy contained in the FLR region in this study was gradually lost to the ionosphere through Joule dissipation (*Newton et al.*, 1978), manifested by the time-averaged energy flux towards the ionosphere. A positive net flux towards the northern ionosphere is expected near the magnetic equator when the conductivity is lower in the northern ionosphere (compared to the southern one) and the fundamental standing wave has a magnetic node at southern

latitudes (*Allan*, 1982). The Poynting flux from the FLR into the ionosphere should be comparable to Joule dissipation rates, if Joule dissipation is the primary damping mechanism for the shear Alfvén wave.

It is possible to estimate the Joule dissipation rate in the ionosphere using

$$W_{JD} = \Sigma_p |E_i|^2 \tag{3.6}$$

where Σ_p is the Pedersen conductivity (*Greenwald and Walker*, 1980). Using the technique of *Ozeke et al.* (2009), we map the ground magnetic perturbation to an electric field in the ionosphere, E_i. This technique requires a few additional parameters and assumptions, including assuming the ground perturbations are caused by a toroidal mode ULF wave; this is a reasonable assumption in this case, given that these stations map to THC, which observes a toroidal mode. The equation to obtain the electric field is

$$E_i = \frac{b_g}{\mu_0} \frac{1}{sin(x)} \frac{1}{H} e^{(m^2 L + \frac{4\pi^2}{d\theta^2})^{\frac{1}{2}} \frac{h}{Re}} \tag{3.7}$$

where E_i is the ionospheric electric field perturbation, b_g is the magnetic field perturbation observed on the ground, μ_0 is the permeability of free space, x is the magnetic field dip angle, H is the Hall conductivity, m is the azimuthal wave number, L is the McIlwain L parameter for the location of peak amplitude, $d\theta$ is the latitudinal (CGM) thickness of the toroidal mode in radians, h is the altitude of the E region ionosphere, and Re is an Earth radius (*Ozeke et al.*, 2009).

To obtain $d\theta$, we used a latitudinal chain of five IMAGE ground magnetometers, fitting a Gaussian to the square root of the power spectral density, which is proportional to the root mean square amplitude (RMS). We used the full width at half the maximum of the fitted Gaussian as the estimate for $d\theta$, finding it to be 5.5 degrees (Figure 3.7).

We used two longitudinally spaced IMAGE magnetometers to estimate the m-number using the phase difference between perturbations in the Y, or east-west, component at each station at 5 mHz (Figure 3.8). We found the m-number to be 6 ± 2, where we estimated the

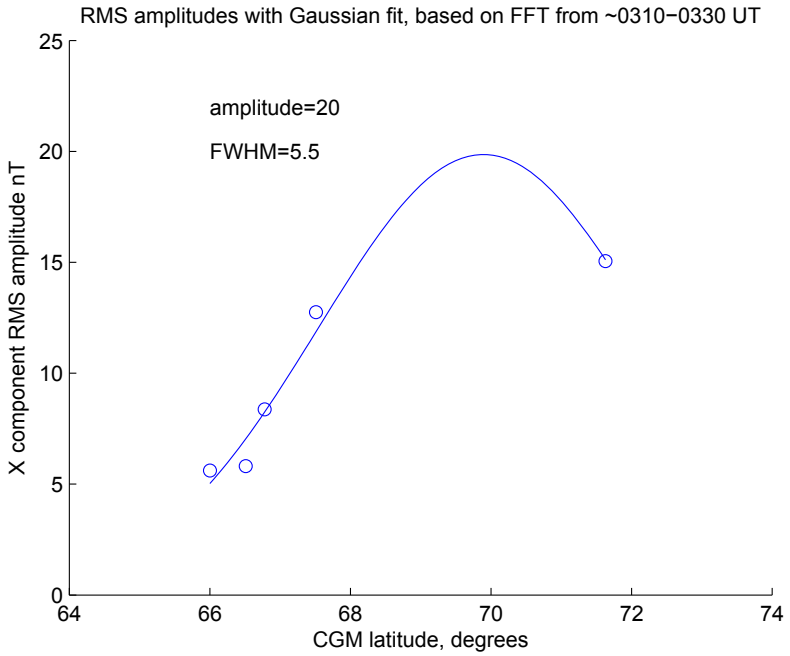

Figure 3.7: RMS amplitude (from power spectral density) vs. Corrected Geomagnetic (CGM) latitude for a latitudinal chain of IMAGE ground magnetometers. The stations used in this figure include KIL ($L \sim 6.3$), KEV ($L \sim 6.5$), TRO ($L \sim 6.7$), SOR ($L \sim 7.1$), and BJN ($L \sim 11$) for the ~ 20 minute FFT window centered at 0320 UT. A Gaussian is fit to the data from all stations in order to estimate the thickness in CGM latitude of the FLR (5.5 degrees), the peak RMS amplitude (20 nT), and the location of the peak (L=9.4). From *Hartinger et al.* (2011).

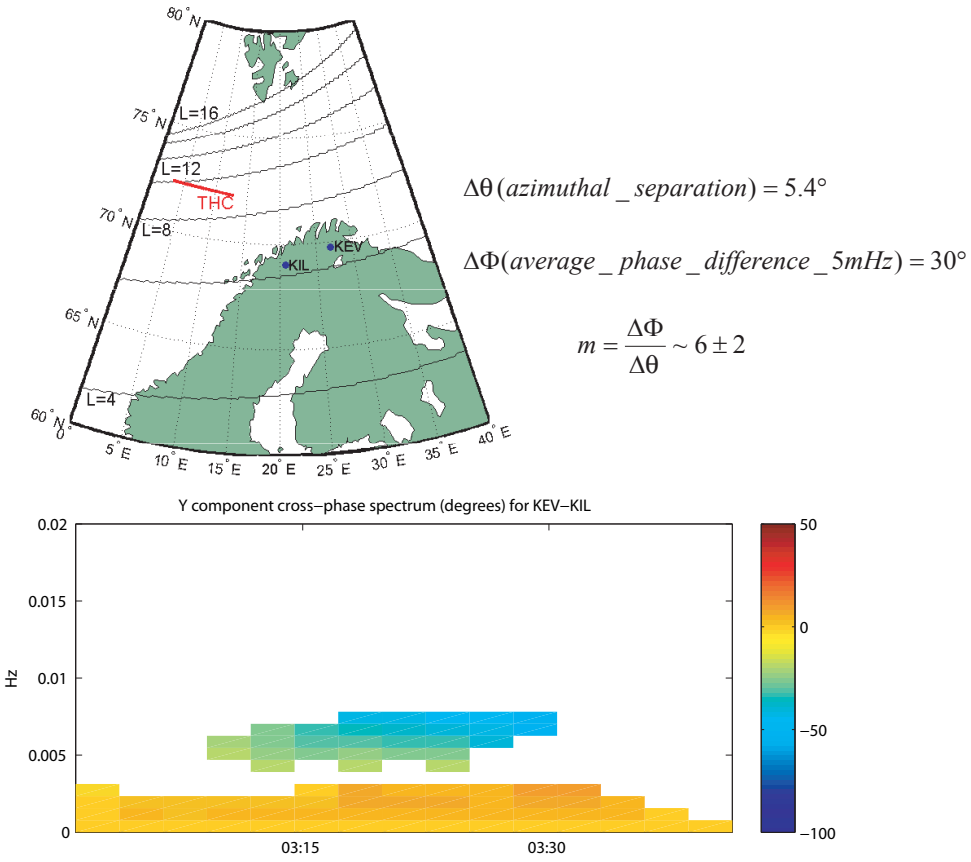

Figure 3.8: At top, a map of the two IMAGE magnetometers used for the m-number calculation. At bottom, the dynamic cross-phase spectrum for the Y component for these stations. From *Hartinger et al.* (2011).

error using the following equation from *Mathie and Mann* (2000)

$$Error = \frac{360dt}{Td\theta} \tag{3.8}$$

where dt is half the sampling rate of the IMAGE magnetometers, 5 seconds, T is the period of the wave, 200 seconds, and $d\theta$ is the longitudinal separation between stations, 5.4 degrees. Using data from the IMAGE magnetometers, the *Hardy et al.* (1987) statistical study of ionospheric conductivity, and the technique of *Ozeke et al.* (2009), we map the ground magnetic perturbation to an electric field in the ionosphere, E_i, and calculate the Joule dissipation rate using Equation 3.6. We estimate the Joule dissipation rate using a range of assumptions for ionospheric Hall and Pedersen conductivities, ionosphere E region peak

density heights, and m-numbers, finding it to be from $0.16 - 1.0 mW/m^2$, in good agreement with rates obtained from radar data in previous studies (*Greenwald and Walker*, 1980; *Rae et al.*, 2007).

With regards to the Poynting flux, since TH-C passes through the center of the FLR between 0310 - 0330 UT, we use the time-averaged field-aligned Poynting vector from that interval to map to the ionosphere and compare it with estimates of the Joule dissipation rate. Assuming that the cross-sectional area of a flux tube is inversely proportional to the magnetic field strength we have:

$$\frac{S_2}{|B_2|} = \frac{S_1}{|B_1|} \tag{3.9}$$

where $|B_2|$ is the magnetic field strength observed on the ground, 53000 nT, $|B_1|$ is the magnetic field strength at TH-C, 25 nT, and S_1 is the time averaged Poynting vector observed from 0310 to 0330 UT by TH-C, $3.3 * 10^{-7} \frac{W}{m^2}$. We thus find the energy flux into the ionosphere is $S_2 = 0.7 \frac{mW}{m^2}$. Evidently, the Joule dissipation rate obtained is between 23% and 150% of the energy flux into the ionosphere, both measured near the center of the FLR, implying that Joule dissipation is an important damping mechanism.

3.5 Summary

The simultaneous, fortuitous crossing of a clearly identifiable FLR center by an equatorial THEMIS spacecraft, observation of the magnetopause by another spacecraft, and observation of the FLR on the ground by a regional network of magnetometers provides an opportunity to study the transfer of wave energy from compressional waves, to shear Alfvén waves via FLR, and on to the ionosphere. The simultaneous observations of the solar wind, the magnetopause, and the FLR enable us to conclude that magnetopause surface waves are the source of energy for the FLR. A comparison of the energy balance between the field-aligned energy flux observed by TH-C and the Joule dissipation rate in the ionosphere shows that Joule dissipation is an important damping mechanism.

The radial trajectory of TH-C near the magnetic equator allows us to quantify the energy

transfer associated with the FLR in the radial ($-4.3 * 10^{-7} \frac{W}{m^2}$) and field-aligned ($3.3 * 10^{-7} \frac{W}{m^2}$) direction. These observations suggest a strong coupling between the fast mode waves driven at the magnetopause and the shear Alfvén waves via the FLR mechanism. Ground magnetometer observations demonstrate that TH-C crossed through the center of the FLR near the time that magnetopause undulations were the most pronounced and had the same frequency as the magnetospheric ULF waves. These observations complement many previous ground and in situ observations that showed that FLR is an important mechanism for energy transfer in the Earth's magnetosphere (e.g., *Walker et al.*, 1979; *Rae et al.*, 2007). Unlike previous studies, this study included global observations in the solar wind, magnetosheath, at the resonance location (and, importantly, near the magnetic equator), and on the ground, tracing the energy driving the Alfvén waves from the source at the magnetopause, through the FLR region, and, finally, to the ionosphere. This is the first study to show the conversion from isotropic electromagnetic energy flux to field-aligned electromagnetic energy flux near the magnetic equator and at the FLR location, meeting the criteria for the validation of the FLR paradigm described by *Glassmeier et al.* (1999).

CHAPTER 4

Observations of a global (cavity/waveguide) mode outside the plasmasphere

Standing fast mode waves known as global modes, or cavity/waveguide modes, have been extensively studied as a potential driver of monochromatic shear Alfvén waves in the Earth's magnetosphere via the field line resonance (FLR) mechanism. However, their existence outside of the plasmasphere remains controversial. In this chapter we present a global mode observation outside the plasmasphere, using simultaneous multi-spacecraft observations in the solar wind, the magnetosheath and the outer magnetosphere, as well as ground magnetometer data. Broadband solar wind dynamic pressure fluctuations are the most likely drivers of the Pc5 frequency range (2-7 mHz) global mode. The global mode transfers energy towards the plasmapause, where it drives localized shear Alfvén wave activity in the Pc5 frequency range. Global modes are thus a viable mechanism for converting broadband energy sources to monochromatic, radially localized shear Alfvén waves in the Pc5 frequency range.

4.1 Introduction

4.1.1 Monochromatic ULF waves

Ultra Low Frequency (ULF) waves are often observed on the ground in the Pc5 frequency range ($\sim 2-7$ mHz) at mid to high latitudes. The wave activity is often monochromatic and in many cases localized in latitude (*Walker et al.*, 1979). Sometimes the same frequency is observed at a wide range of latitudes (*Samson and Rostoker*, 1972). Several mecha-

nisms could provide a source of energy for these waves: wave-particle interactions with ring current ions (*Southwood et al.*, 1969), the drift-mirror instability (*Hasegawa*, 1969), magnetopause surface waves driven by the Kelvin-Helmholtz instability (*Southwood*, 1974; *Chen and Hasegawa*, 1974; *Fujita et al.*, 1996), quasi-monochromatic fluctuations in the solar wind (*Kepko et al.*, 2002), and global (or cavity/waveguide) modes (*Kivelson et al.*, 1984; *Kivelson and Southwood*, 1985). Observational evidence for the operation of the first four driver mechanisms exists; however, definitive evidence in the data for the operation of the global mode mechanism in the outer magnetosphere has been lacking, despite significant modeling efforts demonstrating its viability (e.g., *Allan et al.*, 1986a,b; *Lee and Lysak*, 1989; *Claudepierre et al.*, 2009).

4.1.2 Global mode mechanism

Global modes are standing fast mode waves trapped between different magnetospheric boundaries, such as the magnetopause, the plasmapause and/or the equatorial ionosphere (e.g., *Kivelson and Southwood*, 1986). The global mode frequency is set by the transit time of fast mode waves, which in turn depends on the locations of the boundaries and the plasma environment within them. Global modes are expected to have perturbations in the east-west electric field and parallel magnetic field with a $\sim$ 90 degree phase difference in time and nodal structure throughout their radial extent (*Waters et al.*, 2002).

An example of the radial amplitude profile and phase for the compressional magnetic field perturbation associated with a cavity mode, a type of global mode, is shown in Figure 4.1, using the numerical model of *Zhu and Kivelson* (1989). Details of the implementation of this model are given in Appendix A. In this particular example, the Alfvén speed is assumed to vary monotonically as the inverse of the distance from the inner boundary. There are multiple nodes, or local amplitude minima, throughout the radial extent and there is a 180 degree rotation in phase of the perturbation on either side of each node, characteristic of global modes. The 360 degree jump seen at $L \sim 7$ is not related to the spatial structure of the cavity mode; it occurs because the phase decreased below -180 degrees, causing it to

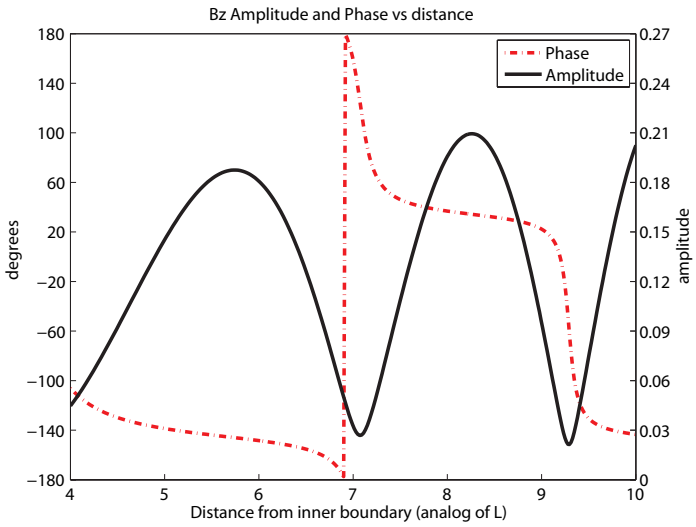

Figure 4.1: The model amplitude (black line) and phase (red dashed line) of the magnetic field perturbation along the background field as a function of radial distance, generated using the *Zhu and Kivelson* (1989) numerical model. In the model, the Alfvén speed varies as the inverse of the distance from the inner boundary; only one harmonic (eigenfrequency) is shown.

wrap around to +180 degrees. Other numerical models have shown that significantly more structured global modes are possible and that non-monotonic Alfvén speed profiles and sharp density gradients play important roles in determining the behavior of global modes (e.g., *Zhu and Kivelson*, 1989; *Waters et al.*, 2002).

The term global mode can refer to a number of different types of standing, fast mode waves, including cavity modes and waveguide modes (*Kivelson and Southwood*, 1985; *Samson et al.*, 1992). Both of these wave modes exhibit the features described above (e.g., nodal structure). The term cavity mode refers to a global mode in a closed magnetosphere; in other words, the only sink of energy is the ionosphere. The closely related waveguide mode has similar observational features to the cavity mode, but exhibits spatial and temporal dispersion as energy is allowed to leak into the magnetotail (*Wright*, 1994). The differences between these two types of global modes are not important for the main results of this study.

There are a number of potential drivers of global modes, including but perhaps not limited to dynamic pressure fluctuations (e.g. *Claudepierre et al.*, 2009), magnetosheath flows (*Mann et al.*, 1999; *Mills et al.*, 1999, 2000), fluctuations in the ion foreshock (e.g., *Takahashi et al.*,

2010), and Kruskal-Schwarzschild modes (*Plaschke et al.*, 2009). *Wright and Rickard* (1995) showed that in the case of boundary motion with a broadband frequency spectrum, global modes can be excited when the frequencies for standing fast mode waves lie within the spectrum of the driver; *Claudepierre et al.* (2009) demonstrated that continual buffeting by broadband dynamic pressure fluctuations can effectively drive cavity modes in this manner. *Wright and Rickard* (1995) also showed that Alfvén waves can be excited if the standing fast mode frequencies lie within the range of accessible standing Alfvén wave frequencies in the magnetosphere cavity; in these cases, Alfvén waves will be excited at locations where the standing Alfvén wave frequency matches the global mode, or standing fast mode, frequency.

4.1.3 Alternative mechanisms

There are a few other sources of ULF waves with fluctuations parallel to the background magnetic field in the Pc5 frequency range. We note some of the properties of waves driven by these sources that are unique and can be used to differentiate them from global modes. Wave-particle interactions with ring current ions can generate ULF waves with antinodes (maximum amplitudes) in the radial magnetic field perturbation near the magnetic equator through a drift bounce resonance (*Southwood et al.*, 1969). Waves driven by drift-bounce resonance are often associated with enhancements in hot ($> 1keV$) ions during the recovery phase of geomagnetic storms or during substorms (e.g., *Yang et al.*, 2010), which would cause an increase in the plasma β (ratio of thermal pressure to magnetic pressure). A spacecraft located where the wave is being driven ought to observe ion fluxes varying with the wave frequency at energies corresponding to drift and bounce frequencies that satisfy the resonance condition with the wave; furthermore, there should be a 180 degree phase difference between flux variations observed above and below the resonant energy (*Southwood and Kivelson*, 1981).

The drift-mirror instability is another mechanism for generating Pc5 ULF waves with parallel magnetic field perturbations. It occurs in high β plasmas and is associated with transverse magnetic field perturbations at the equator (*Cheng and Lin*, 1987). Waves gen-

erated by the drift-mirror instability may also have compressional perturbations that are a harmonic of the transverse perturbations (*Hasegawa*, 1969; *Takahashi et al.*, 1990).

There are also energy sources for ULF fluctuations in the Pc5 frequency range in the magnetosheath and solar wind, such as the Kelvin-Helmholtz instability (which drives magnetopause surface modes) or fluctuations in the solar wind dynamic pressure (e.g., *Fujita et al.*, 1996; *Kepko et al.*, 2002). In the event that these sources of wave energy do not excite cavity or waveguide modes, they ought to directly drive parallel magnetic field perturbations that have amplitude monotonically decaying with increasing distance from the magnetopause, where the waves are being driven.

4.1.4 Previous global mode observations and observational difficulties

Substantial evidence has been presented for the existence of global modes in the plasmasphere, typically at frequencies above the Pc5 range (e.g., *Takahashi et al.*, 2010). However, there have been few direct observations of global modes outside of the plasmasphere. *Kivelson et al.* (1997) reported observations of a compressional, quasi-monochromatic (24 mHz) perturbation of the magnetic field in the dayside magnetosphere, contrasted it to broadband fluctuations in the magnetosheath, and interpreted it as a cavity mode. *Mann et al.* (1998) used magnetic field data to identify compressional perturbations in the dawn and pre-noon sectors. Using two spacecraft and ground observations, they determined that significant spatial and temporal dispersion occurred, consistent with a waveguide mode. *Rickard and Wright* (1995) proposed that few cavity modes have been observed because dispersion, expected for regions that are better described as cavities than waveguides, would preclude the observation of a monochromatic signal. One would then expect broadband observations similar to *Mann et al.* (1998) rather than monochromatic observations similar to *Kivelson et al.* (1997). Finally, *Eriksson et al.* (2006) identified perturbations on the dayside as being associated with a tailward propagating waveguide mode that was strongly coupled to locally standing Alfvén waves.

Kivelson et al. (1997) noted several possible reasons why so few cavity modes have been observed; these reasons apply to other global modes:

1. The quality factor of the magnetospheric resonator is low and cavity modes damp quickly.

2. The energy sources (drivers) for cavity modes are rarely steady for long enough for a spacecraft to identify the global structure of the cavity mode.

3. To sustain a cavity mode, the cavity must be stable in size and configuration. This means that, for example, there cannot be large changes in the solar wind dynamic pressure that significantly change the location of the magnetopause on a timescale similar to or less than one wave period. Additionally, the geomagnetic activity should be low, since processes internal to the Earth's magnetosphere can also alter its configuration.

4. Amplitudes of compressional fluctuations associated with fast mode waves are small because the wave energy can rapidly spread out in all directions, unlike Alfvén wave modes. This suggests that other sources of ULF wave activity could often obscure cavity modes and that they might often be below the detection threshold of electric and magnetic field instruments.

5. A spacecraft must be located close to the magnetic equator to identify a cavity mode, since that is where most of the wave energy is confined (*Zhu and Kivelson*, 1991; *Lee*, 1996). It must also be moving radially, or be in a radial alignment with other spacecraft, to identify the global structure of the cavity mode.

4.1.5 Overview of study

The above list provides guidelines for finding intervals that are ideal for determining whether ULF wave activity is consistent with the presence of global modes. Such intervals should occur when:

1. A particular driver of ULF waves provides a continual source of energy over several

wave cycles.

2. There are no large fluctuations in solar wind dynamic pressure or other phenomena that could cause a rapid (timescale less than a few wave periods) change in the size of the magnetosphere

3. Geomagnetic activity is low and there are no other major sources of ULF wave activity.

4. Several radially separated observations are available near the magnetic equator.

We used these guidelines to identify intervals where conditions were ideal for global mode identification. To find such intervals, we required periods when multi-point observations are available in the magnetosphere near the magnetic equator, in the magnetosheath, and in the solar wind. Once such intervals were identified, we used the electric and magnetic field data from probes in the magnetosphere to identify intervals where the wave polarization was consistent with global modes and inconsistent with other wave modes. The search for intervals was conducted by visually inspecting overview plots of satellite data during intervals with ideal spacecraft conjunctions, and only 3 or perhaps 4 global mode events were found. In Chapter 5, we will discuss more systematic search for global mode events.

The purpose of this chapter is to identify global mode oscillations during one such interval in the dawn sector in the region outside of the plasmasphere on 13 Nov 2008. Using observations in the solar wind, magnetosheath, magnetosphere, and on the ground, we determine that broadband dynamic pressure fluctuations in the solar wind are converted into a monochromatic global mode with Pc5 frequency (6.5 mHz). We also observe energy flux directed earthward from the location of the global mode observation and towards the plasmapause; at the plasmapause, we find that standing Alfvén wave activity is occurring in the same frequency range as the global mode.

We present our results in the next five sections. In the second section of this chapter, we describe the instrumentation used in this study. In the third section, we provide an overview of the event and the criteria we used to select a short interval when the global mode is observed. In the fourth section, we describe wave polarization, energy transfer, time

evolution, spatial structure, and the relationship between electron density and wave activity during this shorter interval. In the fifth section, we describe how these wave properties are inconsistent with several mechanisms that have previously been shown to drive waves in the Pc5 frequency range. In the sixth section, we describe how the wave properties are consistent with the global mode mechanism and further characterize the global mode. Finally, we summarize our results in the seventh section.

4.2 Instrumentation

For magnetosphere, magnetosheath, and solar wind observations we use data from the five-satellite Time History of Events and Macroscale Interactions (THEMIS) spacecraft (*Sibeck and Angelopoulos*, 2008). Each spinning satellite (3 second spin period) is equipped with a fluxgate magnetometer (FGM, *Auster et al.*, 2008), an electric field instrument (EFI, *Bonnell et al.*, 2008), an ion and electron electrostatic analyzer (ESA, *McFadden et al.*, 2008a), and ion and electron solid state telescopes (SST, e.g., *Ni et al.*, 2011).

EFI measures ULF fluctuations best in the spin plane of the spacecraft; we obtain the component along the spin axis using the $E \cdot B = 0$ approximation when the normal of the spin plane is at a large angle to the background magnetic field direction; in this study, the angle was always larger than 20 degrees. The measurement of the amplitude and phase of ULF waves by EFI is affected by several sources of contamination. In Appendix B, we describe these sources of contamination, how they can be routinely identified and removed, and how we determined which THEMIS EFI data were useable for the present study. ESA measures the three-dimensional particle distributions and moments (electrons: 5 eV - 30 keV, ions 5eV - 25 keV) once per spin. SST also measures the three-dimensional particle distributions and moments once per spin and is sensitive to energies above 25 keV; however, calibration of the SST instrument is ongoing and the highest quality data for this study is only available at $\sim$ 5 minute resolution. We obtained all THEMIS data directly from the THEMIS website (http://themis.ssl.berkeley.edu/index.shtml) and applied the latest calibrations and corrections using the software package distributed by the THEMIS science team. For ground

magnetometer observations, we use 1 second data from Greenland magnetometers from DTU Space at the Technical University of Denmark.

4.3 Event overview and selection

4.3.1 Overview of geomagnetic activity and solar wind conditions

The global mode event occurred on 13 Nov 2008 during a prolonged period of low geomagnetic activity. Solar wind data and geomagnetic activity indices (obtained from the NASA Space Science Data Facility through OMNIweb - http://omniweb.gsfc.nasa.gov/) for several days leading up to the event are shown in Figure 4.2, with the interval of interest highlighted in pink. The *Kp*, *Dst*, and *AE* indices all indicate quiet geomagnetic activity levels (top 3 panels). The event occurred during an interval of solar wind flow speed of $\sim 310\frac{km}{s}$ (fifth panel from top) and typical number density of $\sim$ 6 protons per cubic centimeter (fourth panel from top).

4.3.2 Solar Wind and Magnetosheath data during the event

More detailed, higher time resolution information from the solar wind and magnetosheath are given in Figure 4.3. Figure 4.3a shows the positions of the THEMIS probes in the GSM xy plane, along with the statistical location of the magnetopause and bow shock derived from the *Shue et al.* (1997) and *Fairfield* (1971), respectively. Selected solar wind, magnetosheath, and ground magnetometer observations are shown in Figure 4.3b from THEMIS-B (THB), THEMIS-C (THC), and the Tasiilaq (code AMK, former name Ammassalik) and Nuuk (code GHB, former name Godthaab) ground magnetometers for the period from 0600-0820 UT. AMK is located at 65.60^o geographic north and 322.37^o east and GHB is located at 64.17^o geographic north and 308.27^o east. We used field line tracing software from the French National Aerospace Research Center (ONERA) with the *Tsyganenko* (1989) model to determine that AMK mapped to THEMIS-D's (THD) location during the period from 0600-0820 UT, whereas GHB mapped to a location $\sim$ 1.5 Earth radii (Re) further away from

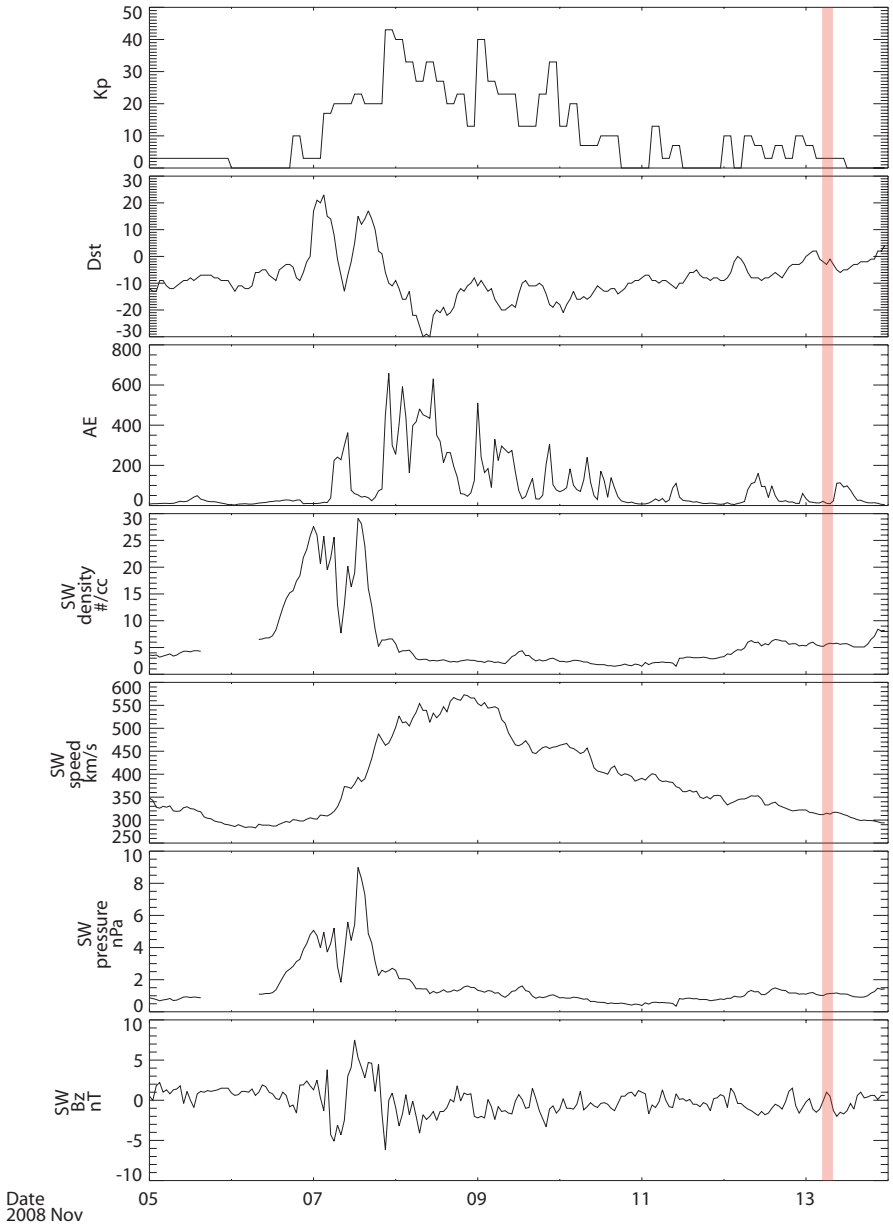

Figure 4.2: From top to bottom, Kp*10, Dst, AE, solar wind density, solar wind speed, solar wind pressure, and the GSM z component of the interplanetary magnetic field, obtained from OMNIweb (http://omniweb.gsfc.nasa.gov/). The shaded pink region indicates the interval of interest for this study.

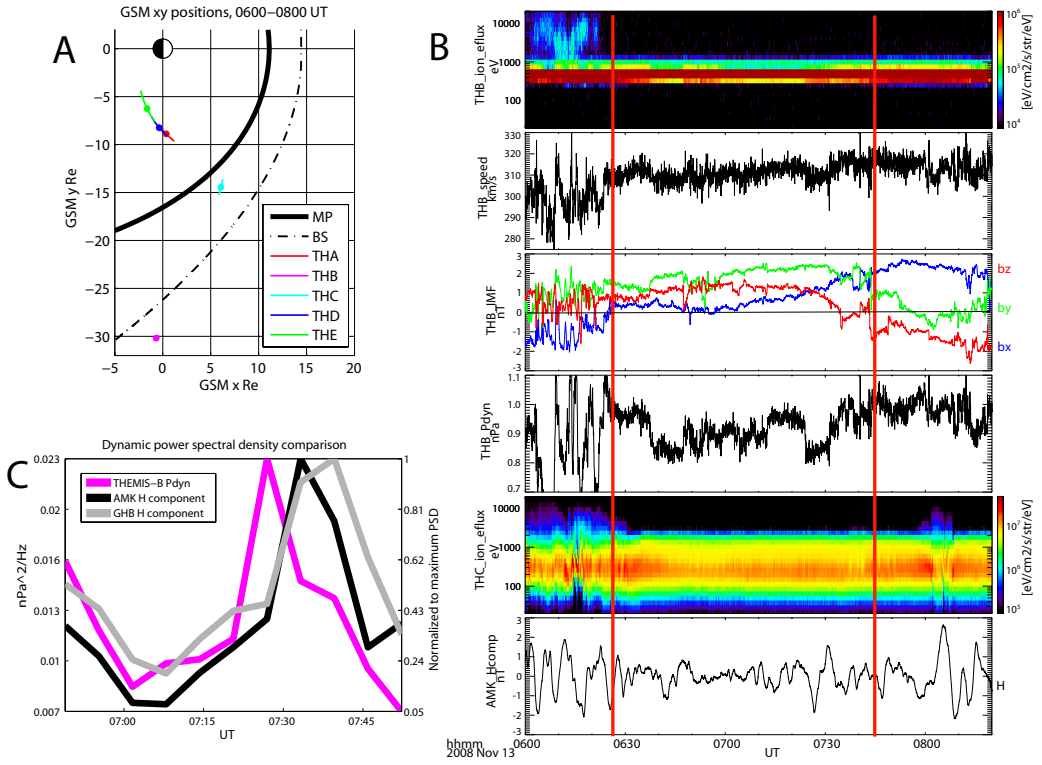

Figure 4.3: A: The GSM xy plane showing the orbits of 5 THEMIS probes from 0600 to 0800 UT (lines) and their position at 0700 UT (dots), with the location of the magnetopause as a solid black line and the location of the bow shock as a dot-dashed line. B: From top to bottom, (1) ion energy flux spectrogram from THB, (2) plasma speed at THB calculated using ESA electrons, (3) the GSM components of the magnetic field at THB, (4) the dynamic pressure at THB calculated using ESA electrons, (5) the ion energy flux spectrogram from THC, (6) the H component of the high pass filtered (> 0.5 mHz) magnetic field at the Tasiilaq (AMK) ground magnetometer, which maps to a region very close to THD. C: The power spectral density averaged over the 1 to 50 mHz frequency band during the interval from 0630 to 0800 UT (marked by red lines in B) for dynamic pressure fluctuations (pink) and ground magnetic field fluctuations at AMK (black) and Godthaab (GHB); GHB maps to a region ~ 1.5 Re outside and ~ 3 Re tailward of THD's location.

the Earth and ~ 3 Re tailward of AMK's location. The *Tsyganenko* (1989) model predicted the magnetic field magnitude to within 9% and the magnetic field direction to within 9^o at 0700 UT at all THEMIS probes in the magnetosphere, suggesting that it is suitable for mapping the magnetometers' locations.

Figure 4.3b, panel 1 shows the solar wind ion energy flux spectrogram. Reflected ions with energies ≥ 1 keV ions are seen at the beginning of the interval, when the ion foreshock is located in the dawn sector. After 0625 UT, the interplanetary magnetic field (panel 3) reorients, the ion foreshock moves away from the dawn sector, and THB measures the pristine solar wind. The IMF GSM z component is primarily positive until 0745 UT, the solar wind velocity is $\sim$ 310 km/s (panel 2), and small dynamic pressure fluctuations are seen with a maximum amplitude of about 0.15 nPa (panel 4). The lower than nominal solar wind speed and the steady, positive IMF z component suggest that neither flux transfer events (FTEs) nor magnetopause surface waves driven by the Kelvin-Helmholtz instability will be present between 0625 and 0745 UT. The absence of these features is confirmed by THEMIS-C (THC), which is located in the magnetosheath; in panel 5 an ion energy flux spectrogram shows no significant transient features or surface wave activity. The IMF begins to turn southward at 0735 UT and turns sharply southward at 0745 UT (panel 3); these changes likely caused a flux transfer event that THC observes at 0800 UT (panel 5). This southward turning could have produced a change in the magnetopause location (*Shue et al.* (1997)) as well as transient ULF wave activity in the magnetosphere before 0800 UT, as THC is located close to the dawn flank and there is a time delay between the initial interaction at the bow shock nose and the arrival of the flux transfer events or other changes at THC's location.

4.3.3 ULF wave drivers

We used ground based observations from AMK and GHB for initial examination of the ULF wave activity and its relationship with conditions in the solar wind and magnetosheath. Unlike spacecraft moving near the magnetic equator, ground magnetometers such as AMK map to positions near the magnetic equator that change little over time (their mapped

position changes slightly due to stretching on the nightside and compression on the dayside). The power in magnetic fluctuations at a ground station can be interpreted without concern for the ambiguity that would arise, for example, in interpreting spacecraft data that could not distinguish between a global increase in wave power and a local increase arising from approach to an antinode of a standing wave. Thus, for the present study, ground based observations are more useful for examining temporal changes in ULF wave activity and their relationship with time variable driving conditions than in situ observations.

ULF wave activity is seen on the ground in the high-pass filtered (frequency > 0.5 mHz) H component at AMK (Figure 4.3b, panel 6). We shifted the solar wind dynamic pressure data from THB by 310 seconds, accounting for the solar wind propagation time from the bow shock nose to THB's downstream location, to study the response of the magnetosphere to solar wind fluctuations at the bow shock nose. We then applied a running, 512 point (26 minute) Fast Fourier Transform (FFT) to the solar wind dynamic pressure and ground magnetometer H component quantities at AMK and GHB during the interval when the IMF was predominately northward (indicated by the red lines in Figure 4.3b). For each FFT window, we computed the average power spectral density (PSD) in the range from 1 to 50 mHz.

We normalized the PSD from AMK and GHB to the maximum value observed at each magnetometer in order to show the time evolution of the PSD rather than differences in the absolute value of the PSD between the two stations. We used the 1 to 50 mHz frequency range for two reasons. One was to facilitate comparisons of the time evolution of wave power between the two stations. The local resonant field line frequency is different at the two stations, and examination of the time evolution of wave power would be difficult if a narrower frequency range was chosen that overlapped with the fundamental or harmonics of standing Alfvén waves at one station and not the other. We are interested in the global dependence of ULF wave activity on solar wind dynamic pressure fluctuations, so we chose a larger frequency range to remove these regional differences. Another reason we chose the 1 to 50 mHz frequency range was to examine whether dynamic pressure fluctuations are an important source of energy for ULF waves over a large frequency range. It is possible for

different mechanisms to drive ULF waves at different frequencies. However, if the magnetic field perturbations observed at ground stations are correlated with dynamic pressure fluctuations in the solar wind over a broad frequency range, it suggests that dynamic pressure fluctuations are the most important energy source for ULF waves.

The running averages for all three quantities are shown in Figure 4.3c. ULF wave power variations at two different stations on the ground appear to follow well the ULF wave power in the solar wind dynamic pressure. Since the ground stations map to locations near the THEMIS probes in the magnetosphere, we conclude that broad band solar wind dynamic pressure fluctuations are the main driver of ULF wave activity in the region near these THEMIS probes after the ion foreshock moved away from the dawn sector but before the IMF turned sharply southward ($\sim$ 0625 to 0745 UT).

4.3.4 Location of probes relative to magnetic equator

THEMIS-A (THA), THEMIS-D (THD), and THEMIS-E (THE) are located in the magnetosphere in the dawn sector during this interval (Figure 4.3a). All probes were very close to the magnetic equator where fast mode wave energy is expected to be confined, as shown in Figure 4.4 (*Zhu and Kivelson*, 1991; *Lee*, 1996). We used two methods to determine the location relative to the magnetic equator: inspection of magnetometer observations and magnetic field models of the location of the magnetic equator. In Figure 4.4a, we show magnetometer data from each THEMIS probe in GSM coordinates. Near the dawn meridian, the GSM y component ought to be small compared to the other components if a probe is near the magnetic equator, and this is indeed the case. In Figure 4.4b, we show the probe locations in the GSM yz plane, confirming that they are close to the geomagnetic equator (since the GSM z coordinate is small for all probes). To account for the fact that the position of the magnetic equator in a distorted magnetic field may differ from the position of the dipole magnetic equator to varying degrees at different magnetic local times, we used the ONERA software package to determine the location of the magnetic equator as a function of time using the *Tsyganenko* (1989) magnetic field model, which we have already validated

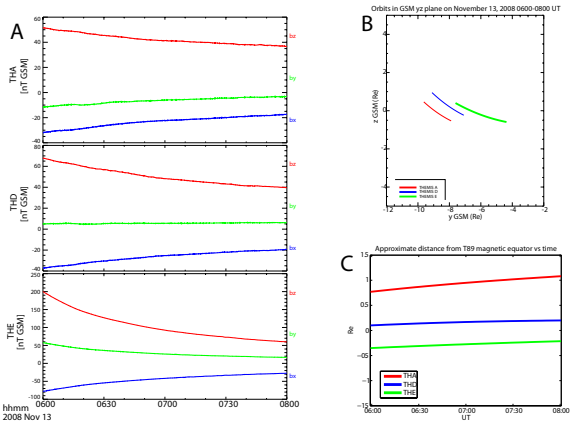

Figure 4.4: A: From top to bottom, magnetometer data from THA, THD, and THE in GSM coordinates. In each panel, red is for the GSM z component, green is for the GSM y component, and blue is for the GSM x component. If a probe is near the magnetic equator and on the dawn meridian, the GSM y component of the magnetic field ought to be small compared to the other components. B: The orbits of THA (red), THD (blue), and THE (green) from 0600 to 0800 UT projected onto the GSM yz plane. C: The approximate distance from the geomagnetic equator, as computed with the *Tsyganenko* (1989) model, for THA (red), THD (blue) and THE (green).

as a reliable model for this interval (when mapping AMK to THD's location - see Section 4.3.2). The software determines the location of the magnetic equator by tracing along a field line from each satellite's position to the magnetic equator at each instant in time. In Figure 4.4c, we plot the approximate distance from the geomagnetic equator using the GSM z separation between each probe's position and the magnetic equator position as a function of time. All probes are within ~ 1 Re of the geomagnetic equator during this interval, or have geomagnetic latitudes of less than ~ 3 degrees.

4.3.5 Overview of ULF wave activity observed in situ

The probes in the region of primary interest are THA and THD. ULF wave activity observed by THA and THD from 0545 to 0825 UT is shown at the top of Figure 4.5, with panels for smaller time intervals at the bottom. For analysis of the wave data, we use a field-aligned coordinate (FAC) system in which z is along the background magnetic field, y points eastward, and x completes the right-hand orthogonal set pointing radially outward.

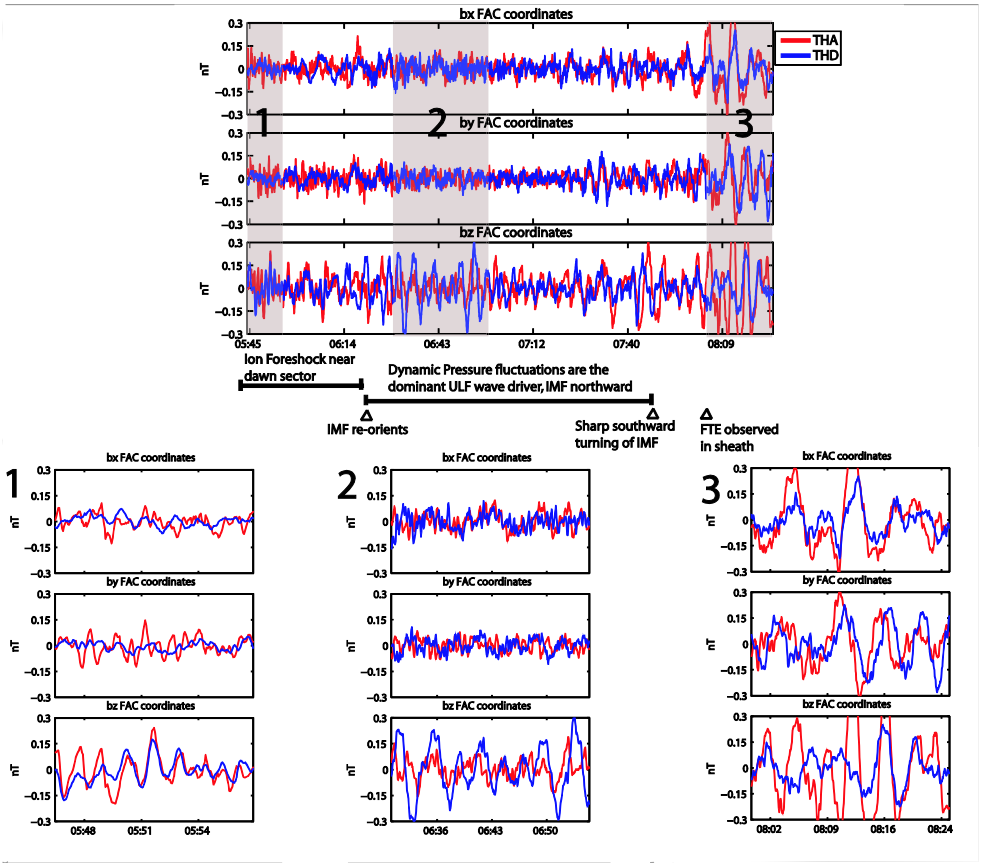

Figure 4.5: On the top, traces for each field-aligned coordinate (FAC) component are shown for THA (red) and THD (blue). The z component is on the top, y in the middle, and x on the bottom. The solid black lines indicate the interval of interest for this study. The three numbered, grey shaded areas correspond to the three insets on the bottom, displayed in the same manner as on the top. They show the same data as on the top, but for smaller time intervals.

From top to bottom, the high pass filtered (frequency $> 2mHz$) magnetic field x, y, and z components are shown; red is for THA, blue is for THD. Throughout much of the interval, the z component perturbations are larger than those for the x and y components for both probes, indicating that compressional waves dominate.

Since THA and THD are separated by less than one Earth radius during this interval, propagating fast mode waves originating from a source remote from this region (e.g., the magnetopause) ought to arrive at nearly the same time, since the transit time is comparable to the magnetic field sampling rate. Inspection of a shorter time interval from 0547 to 0557 UT in inset 1 shows that this is indeed the case; compressional waves with ~ 1 minute period are seen by both probes with similar amplitude and with no phase difference evident. The ion foreshock was located in the dawn local time sector during this interval and was likely the dominant source of wave activity in this region of the magnetosphere (see Figure 4.3).

A later time interval is shown in Figure 4.5, inset 2, during a period when the ion foreshock is no longer present in the dawn sector and dynamic pressure fluctuations are the main source of wave activity. As in inset 1, compressional perturbations dominate. However, the wave period is 3 times larger than before (~ 3 minutes) and is only noticeable at THD (blue), despite the fact that THD is further from the magnetopause than THA. Finally, in inset 3 we examine an interval after the IMF turned southward and at about the same time that THC observed a flux transfer event in the magnetosheath in the dawn sector; compressional perturbations no longer dominate, the perturbations of all components are generally larger than before, and the z perturbations have longer period than before ($\sim 4 - 5$ minute) and are more irregular.

4.3.6 Summary of event overview and selection

To summarize, we have identified an interval where the geomagnetic activity was low and several probes were in a favorable radial alignment near the geomagnetic equator in the dawn sector of the magnetosphere. Using one probe in the solar wind, one in the magnetosheath, and two ground magnetometers we determined that dynamic pressure fluctuations were the

dominant driver of ULF wave activity in the dawn sector magnetosphere and the IMF was steady and primarily northward from $\sim$ 0625 to $\sim$ 0745 UT with no large changes in the overall dynamic pressure. Finally, using two probes separated by less than 1 Re in the magnetosphere, we drew several distinctions between ULF wave activity observed before 0625 UT, from 0625 to 0745 UT, and after 0745 UT.

We conclude that the interval from 0625 to 0745 UT is ideal for investigating whether the fluctuations observed are consistent with the presence of a global mode, as there is one dominant driver of ULF waves (dynamic pressure) with no significant transient sources of wave activity, the size of the magnetospheric cavity is expected to be stable as the IMF GSM z component is positive and there are no large changes in dynamic pressure (*Shue et al.*, 1997), and there is a favorable alignment of several probes near the geomagnetic equator. These criteria are consistent with the guidelines motivated by *Kivelson et al.* (1997) that were described in the Section 4.1.4. We next turn our attention to the wave activity during this shorter interval.

4.4 ULF wave properties

4.4.1 Multi-spacecraft power spectral density comparisons

From top to bottom in Figure 4.6, the dynamic power spectrum for the x, y, and z components (FAC system) of the high pass filtered magnetic field (frequency $>$ 2 mHz) are shown for THA (top 3 panels) and THD (bottom 3 panels) for the same interval as in Figure 4.3b, with the frequency range extending from 2 to 11 mHz in each panel. We also show a dynamic power spectrum for the solar wind dynamic pressure measured at THB in the bottom panel of Figure 4.6, where we have whited out time intervals when THB is located in the ion foreshock and not in the pristine solar wind (and thus cannot directly measure the solar wind dynamic pressure). We used a 1024 point ($\sim$ 50 minute) FFT window, applied a Hanning window before computing the power spectrum, and smoothed the data in the frequency domain to reduce noise.

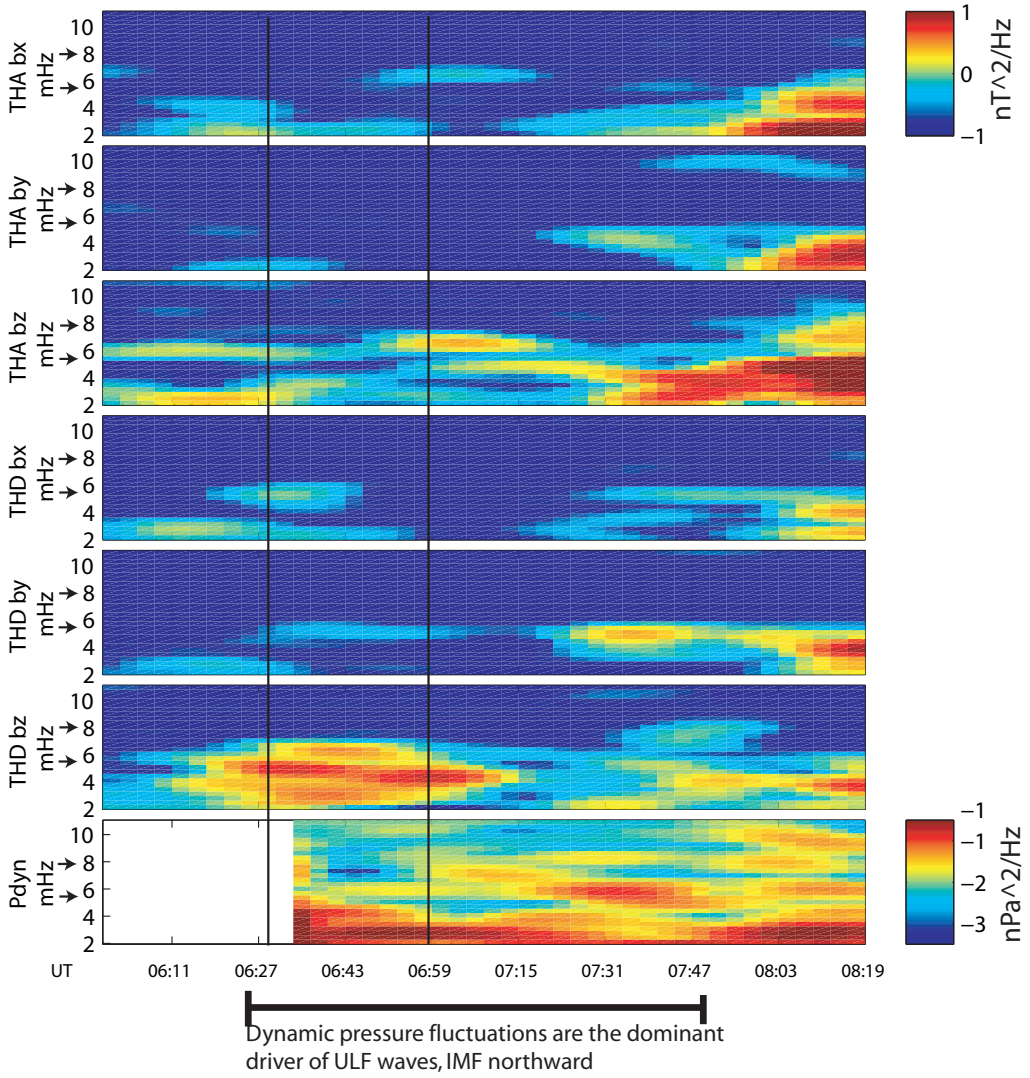

Figure 4.6: From top to bottom, the dynamic power spectrum for the x, y, and z components (field-aligned coordinates) for THA magnetic field data, the x, y, and z components for THD magnetic field data, and for the solar wind dynamic pressure fluctuations measured at THB. The solid black lines indicate the interval shown in Figure 7. The black arrows on the frequency axes demarcate the 5.5 to 8 mHz frequency band.

For much of the interval shown in Figure 4.6, compressional magnetic field perturbations (z component) are dominant at both probes. There is enhanced wave power at several frequencies. For example, in panel 3 at 0700 UT, there are perturbations at 6.5 mHz and 4 mHz observed by THA. These frequencies are also evident at THD during the interval between the black lines. We focus on the 6.5 mHz power enhancements by demarcating the 5.5 to 8 mHz frequency band with black arrows on the frequency axis in each panel. For the entire interval, there are perturbations only in the z, and to a lesser extent x, components in this frequency band. Enhancements in power at 6.5 mHz do not occur at the same time at both probes suggesting that the probes are moving through a spatial structure.

The dynamic power spectrum for the solar wind dynamic pressure shows enhanced wave power at a broader band of frequencies than observed at the THEMIS probes. Notably, the strongest enhancements in power in the 6.5 mHz frequency band (e.g., at 0730 UT) do not coincide with enhancements in power at the THEMIS probes. If broadband dynamic pressure fluctuations are the source of energy for the 6.5 mHz fluctuations at the THEMIS probes, as is suggested by the correlation between broadband dynamic pressure fluctuations and ULF wave power observed on the ground (Figure 4.3c), this suggests that the amplitude of the ULF waves is changing primarily due to passage through spatial structures rather than the temporal variation of the driver. Such a scenario was proposed by *Wright and Rickard* (1995); they demonstrated that a driver with a broadband frequency spectrum could excite global modes with discrete frequencies. These global modes can act as reservoirs of energy, storing energy from the driver and exhibiting persistent spatial structure even if the energy supplied by the driver varies in time.

4.4.2 Wave Polarization

For the remainder of the Section 4.4, we will focus on the 6.5 mHz signal, because observations shown in Figure 4.6 suggest that it exhibits spatial structure as expected for a global mode. We examine both the electric and magnetic field data from THD during the interval marked by the black lines in Figure 4.6. This interval is best suited to examining the

wave polarization properties because both the electric and magnetic field perturbations are finite and measurable in the 6.5 mHz frequency band and are distinguishable from other frequencies. We use THD because electric field measurements on THA are contaminated throughout its entire outbound trajectory (see appendix B and B.1).

The high pass filtered (frequency > 0.5 mHz) magnetic field z and electric field y components, respectively, are shown in Figure 4.7 as black traces. A ~ 3 min period (~ 6.5 mHz) signal is seen between 0635 and 0650 UT, with an amplitude of ~ 200 pT in the magnetic field and $\sim 0.8\frac{mV}{m}$ in the electric field. Overplotting the band-pass filtered (5 to 8 mHz) signal in panels 1 and 2 (red traces) shows that the raw ~ 6.5 mHz signal phase has not been altered by our processing. In panel 3, the band pass filtered electric field y component (red) and magnetic field z component (blue) are overplotted. In panel 4, we use a Hilbert transform technique adapted from *Glassmeier* (1980) to compute the cross phase; a phase difference close to 90^o is seen in panels 3 and 4, as expected for a global mode.

The electric field x, magnetic field y, and magnetic field x components do not have appreciable amplitudes, as shown in panel 5 of Figure 4.7. Perturbations in these components are often associated with standing Alfvén waves and were present in all previous observations of cavity or waveguide modes outside of the plasmasphere. Their absence in this case suggests that no other wave modes were present in the observation region. When the fast and shear Alfvén modes are weakly coupled and a global mode observation is made near the magnetic equator and remote from any field line resonances, perturbations in the electric field x and magnetic field y components should be very weak (*Lee and Lysak*, 1989).

4.4.3 Electromagnetic energy transfer

The Poynting vector computed from the band pass filtered data in the FAC system is shown in Figure 4.7, panels 6 to 8. Blue lines correspond to the instantaneous Poynting vector and red lines to the time average computed with a 10 minute boxcar window. The instantaneous energy transfer associated with the radial Poynting vector (panel 6) is on the order of 50 $\frac{nW}{m^2}$, with a radially inward (Earthward) average energy transfer on the order of 10

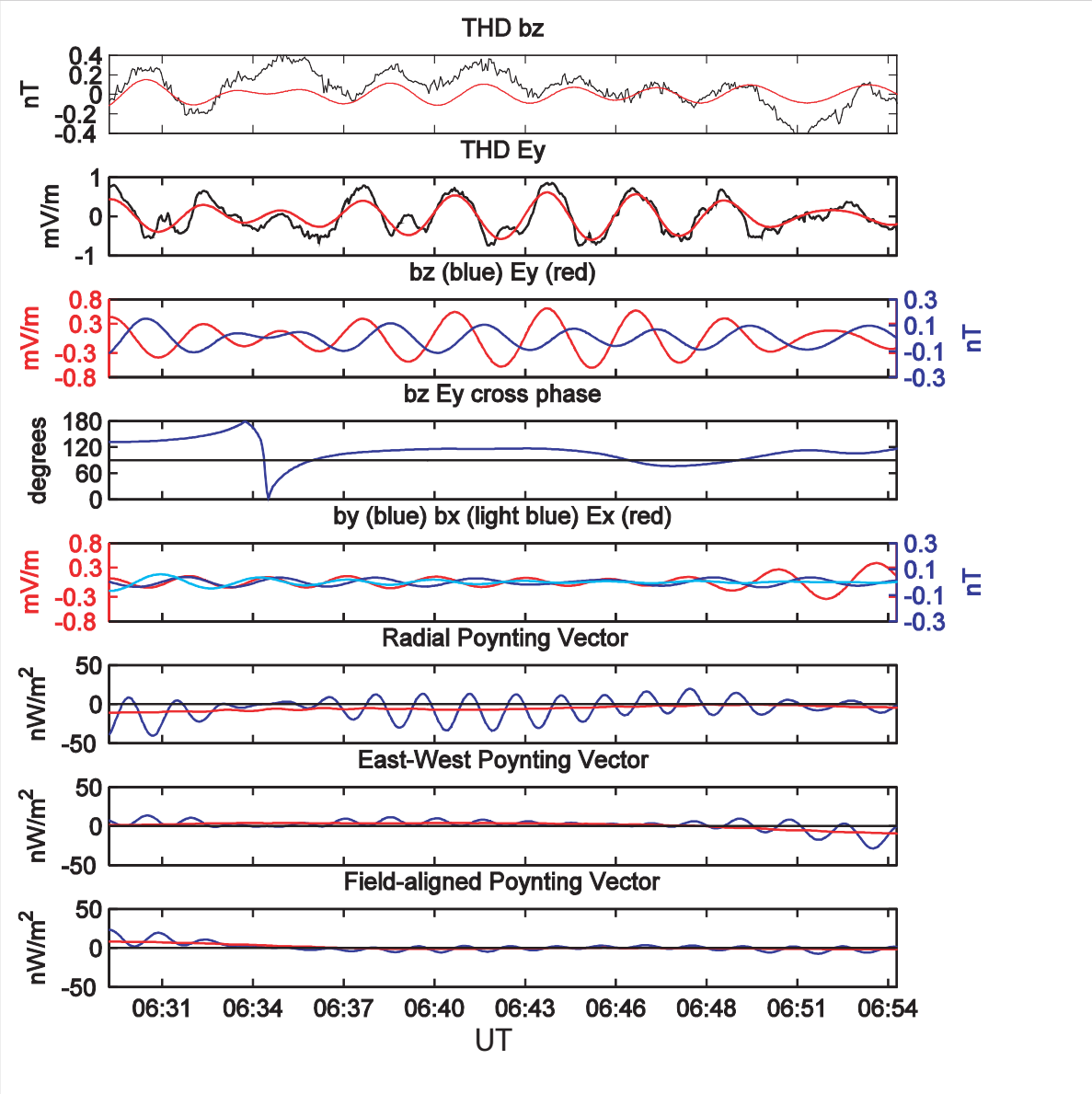

Figure 4.7: From top to bottom, (1) the z component (field-aligned coordinates) of the high pass filtered (frequency $>$ 0.5 mHz) magnetic field (black) and the band pass filtered (5 $<$ frequency $<$ 8 mHz) magnetic field (red), (2) the same for the electric field y component, (3) band pass filtered magnetic field z (blue) and electric field y (red) components, (4) cross phase of magnetic field z component and electric field y component, (5) band pass filtered magnetic field y (blue), magnetic field x (light blue), and electric field x (red) components, (6) x component of Poynting vector from band pass filtered fields (blue) and time average (red), (7) the same for the y component of the Poynting vector, (8) the same for the z component of the Poynting vector.

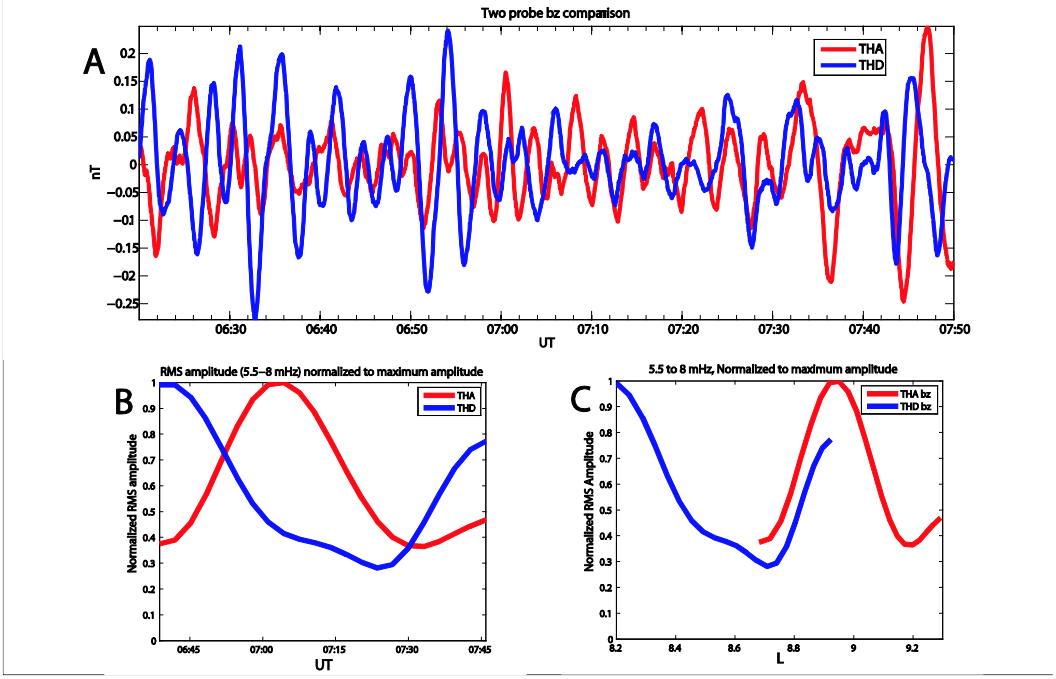

Figure 4.8: A: The z component of the high pass filtered (frequency $>$ 2 mHz) magnetic field for THA (red) and THD (blue). B: The normalized root mean square amplitude of the z component of the magnetic field for THA (red) and THD (blue) in the 5.5 to 8 mHz frequency band. C: The same data as in B ordered by L (radial distance).

$\frac{nW}{m^2}$. The Poynting vector, both instantaneous and average, is negligible for the y and z components when compared to the x component (panels 7 and 8). These observations differ from observations of the Poynting vector associated with standing Alfvén waves, where the z component (field-aligned) is significant (e.g., *Hartinger et al.*, 2011). We note that these estimates are lower bounds for the overall energy transfer rate, as we have not estimated the kinetic energy transfer rate (*Kouznetsov and Lotko*, 1995).

4.4.4 Time evolution and spatial structure

We examine the z component of the magnetic field observed at THA and THD in more detail in Figure 4.8. The traces of both probes are plotted in Figure 4.8a, applying a 20 point (one minute) smoothing window to reduce digitization noise and high pass filtering (frequency $>$ 2 mHz). We verified that neither process significantly altered the phase or

amplitude of the 6.5 mHz signal by comparing to the original data, as in Figure 4.7. THA observes the 6.5 mHz signal clearly from $\sim$ 0650 to $\sim$ 0730 UT. THD observes the 6.5 mHz signal intermittently throughout the interval, but a clear observation over a long period of time is made difficult by the presence of lower frequency waves seen clearly at 0630-0638 UT and 0650-0658 UT (also seen in Figure 4.6, panel 6). Both probes observe these lower frequency signals, but they have lower amplitudes when THA observes the 6.5 mHz signal, making the observation of that signal clearer.

The amplitude of the 6.5 mHz signal varies for both probes throughout the interval. We examine the temporal variation of the 6.5 mHz signal by using the power spectral density from Figure 4.6 averaged over the frequency band from 5.5 to 8 mHz (demarcated by the black arrows in Figure 4.6). We compute the square root of the averaged PSD for each probe and normalize it to the maximum value observed by both probes during the interval (i.e., only one number is used for the normalization of both probes for the entire interval); this quantity is equivalent to the normalized root mean squared (RMS) amplitude. In Figure 4.8b, we show the normalized RMS amplitude of the z component of the perturbation magnetic field as a function of time for THA and THD. The maximum values observed by both probes are nearly equal, so the maximum value both probes observe after normalization equals or is very close to one. The amplitude of the z component perturbations at 6.5 mHz observed at THD is higher than THA at the beginning of the interval, then becomes higher at THA at $\sim$ 0650 UT, and then becomes higher again at THD at the end of the interval.

We next investigate whether the amplitude of the 6.5 mHz signal is changing due to spatial variations as well as temporal variations. For each PSD data point, we use the ONERA software to compute the radial distance of the magnetic equatorial crossing of the field line that the THEMIS probe is located on, which we refer to as L. The data are ordered by L in Figure 4.8c and have been normalized in the same manner as Figure 4.8b. Both probes pass through minima in amplitude at an L of 8.7 Re and subsequently see an increase in amplitude as they continue outward, suggesting there is a persistent minima in amplitude there. THD sees increased amplitude at the beginning of the interval, followed by decreased amplitude, and then increased amplitude again. These observations are consistent with a

radial standing wave structure, such as a global mode, which could have multiple maxima (anti-nodes) and minima (nodes) throughout the radial extent. The structure is very stable, as THD observes almost the same RMS amplitude as THA when it passes through the same region $\sim$ 50 minutes later (note that observations from THD and THA are normalized to the same value). *Wright and Rickard* (1995) have previously shown that global modes can act as reservoirs for energy supplied by a time variable driver. In this case, even if the energy supplied by a driver with a broadband frequency spectrum is varying in time, a stable standing wave structure is still possible.

One of the expected features of a global mode is a 180 degree phase difference across a node, or minima, in amplitude. Inspecting the traces in Figure 4.8a reveals that the phase relationships between THA and THD are complicated by the presence of lower frequency waves (also seen in Figure 4.6). The only interval we can identify where both probes are primarily observing the 6.5 mHz signal is between 0710 and 0730 UT, where the traces appear to be in phase. This implies that THD had crossed a node at 0710 UT. Prior to 0710 UT, we cannot identify as long an interval where the 6.5 mHz signal is the main signal being observed by both THA and THD; however, there are a few shorter intervals where this is the case, such as 0626-0632 UT, where a 180 degree phase difference is observed.

We note that we cannot compare the phases of these two signals using band pass filtered data and a Hilbert transform as in Figure 4.7, nor can we conduct cross phase analysis between the two spacecraft for the perturbations in the z component as suggested by, for example, *Waters et al.* (2002), because of the close spacing of these two frequencies and the rapid motion of the two probes through spatial structures. This exemplifies a difficulty in observing a 180 degree rotation in phase across a node of a global mode using two spacecraft. There may be other frequencies present, such as a harmonic of the global mode, that require data from a long time interval to isolate in the frequency domain. However, both spacecraft may move a significant radial distance during the longer time interval, with one or both spacecraft perhaps crossing one or more nodes of the global mode. In this particular case, we required at least a $\sim$ 50 minute FFT window to separate the signals with frequencies below 4 mHz from the 6.5 mHz signal. In Figure 4.8b, one can see that both probes are on

either side of the nodal structure for only $\sim$ 15 minutes; this is far too short a time to isolate the 6.5 mHz frequency and observe a 180 degree phase difference in the frequency domain using typical forms of cross-phase analysis (e.g., Fourier or wavelet analysis). It is also too short for filtering that could effectively separate a 6.5 mHz signal from a 4 mHz signal.

4.4.5 Relationship between wave activity and electron density

We finally investigate the relationship between ULF wave activity and electron density using observations from THA (red), THD (blue) and THE (green). In Figure 4.9a, we show electron density inferred from spacecraft potential as a function of L, or radial distance, from the three probes. All three probes are on nearly the same orbit, with THA leading THD by about 50 minutes, and THD leading THE by about 90 minutes. The plasmapause moved outward and became more structured between the time that THD and THE observed it. The time interval that the global mode was observed is indicated on this plot using bolded lines; THA and THD were outside the plasmasphere when the global mode was observed, while THE was inside the plasmasphere or at the highly structured plasmpause region.

The plasmapause moved outward between the time that THD and THE observed it, as shown in Figure 4.9a. The timescale for this change is $\sim$ 2 hours, too short to be explained by typical plasmaspheric refilling rates (*Darrouzet et al.*, 2009). However, the timescale is consistent with an azimuthally structured plasmapause. In particular, if the plasmapause was more structured and located at a higher L shell at a pre-dawn local time when THA and THD observed the plasmapause at dawn, it could then drift into the dawn sector by the time that THE observed the plasmapause (*Darrouzet et al.*, 2009). The structure, both azimuthal and radial, of the plasmapause can play a role in determining which, if any, global modes are established in the magnetosphere (*Lee and Takahashi*, 2006). It is thus important to determine the role that the structure of the outer plasmasphere played in establishing the global mode observed by THD and THA. Unfortunately, the observations of the plasmapause structure that THD and THE make are widely separated in time ($\sim$ 0510 and $\sim$ 0720, respectively), and there are several other important changes that occur during this time

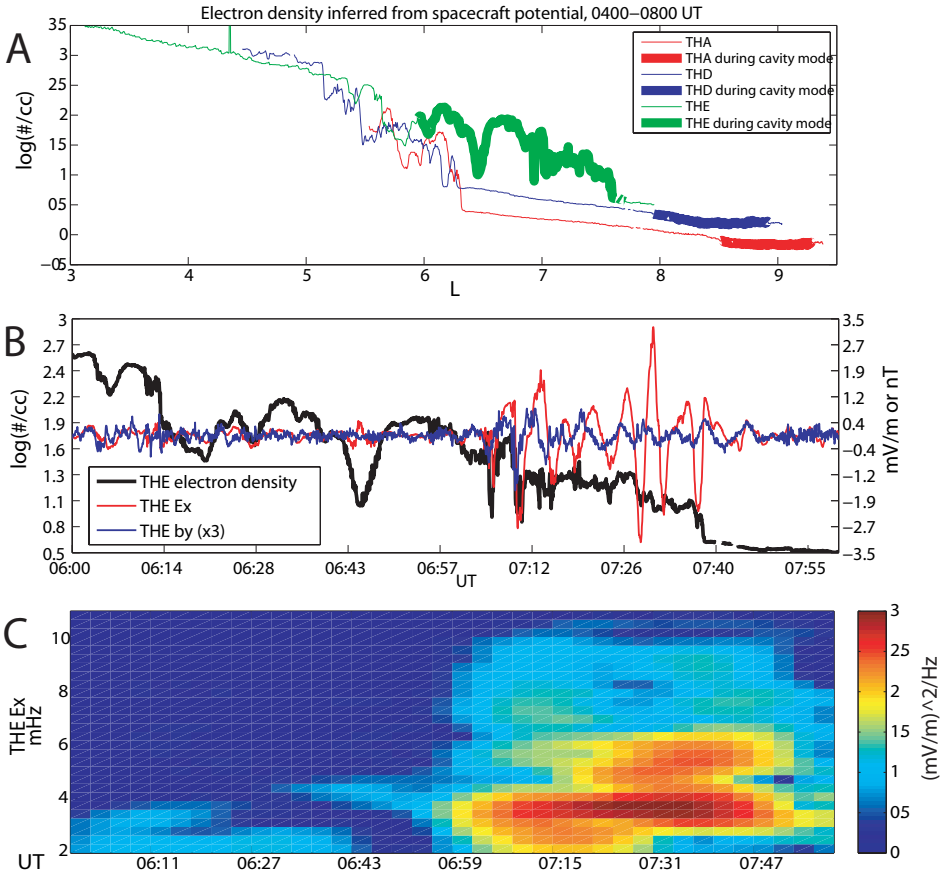

Figure 4.9: A: The electron density (inferred from spacecraft potential) observed by THA (red), THD (blue), and THE (green), plotted versus L. The bolded intervals indicate observations from the period when the global mode was observed, 0625-0745 UT. B: The electron density observed by THE (black line), the high-pass filtered (frequency $>$ 2 mHz) east-west magnetic field perturbation observed by THE (blue), and the high-pass filtered (frequency $>$ 2 mHz) radial electric field perturbation observed by THE, all plotted versus time. Note that the magnetic field perturbation has been multiplied by a factor of 3 to better see the phase difference with the radial electric field. C: Dynamic power spectrum for the radial electric field perturbations observed by THE.

interval that likely played a role in establishing the global mode; most importantly, the change in the dominant driver of ULF waves and the change in the orientation of the IMF (Figures 4.3, 4.5). Without more detailed information about the time evolution and global structure of the outer plasmasphere, we cannot separate the effects of the plasmapause structure from these other effects. It is thus beyond the scope of the present study to determine the role of these changes in the plasmapause in setting up the global mode. However, we can at least say that the plasmapause structure that THE observed was conducive to setting up global modes, as THA and THD observed the signature of the global mode at the same time that THE observed the plasmapause at approximately the same magnetic local time sector.

In Figure 4.9b, we show the high-pass filtered (frequency $>$ 2 mHz) magnetic field y component (blue) and electric field x component (red) in the FAC system observed by THE on the same plot as electron density (black) as a function of time for the interval from 0600 to 0800 UT. The magnetic field perturbation has been scaled up by a factor of 3 to better show the time dependence of wave activity and relationship with the electric field. The amplitude of wave activity is very small inside the high density region but increases sharply at $\sim$ 0710 UT near the plasmapause, which we define as the point after which the electron density decreases monotonically (apart from small scale variations). We note that these are the relevant perturbations for standing Alfvén waves driven by global modes (*Kivelson and Southwood*, 1985). In Figure 4.9c, we show the dynamic power spectra for the x component of the electric field; the perturbations cover a broad range of frequencies that overlap with the global mode frequency (6.5 mHz) but are peaked at lower frequencies. Further investigation of Figure 4.9b shows that the perturbations with largest amplitude exhibit a 90 degree phase difference between the x component of the electric field and y component of the magnetic field, as expected for standing shear Alfvén waves.

We note here that there are several ways that the observed frequency of Alfvén waves can be shifted in the spacecraft frame relative to the stationary frame when a spacecraft is moving through a phase-mixed Alfvén wave structure. These frequency shifts are separate from Doppler shift, which is negligible for both the global mode and Alfvén waves in this study because the spacecraft velocity is significantly less than the wave phase velocity (whether

Alfvén or fast magnetosonic). They depend on the radial velocity of the spacecraft and the rate of change of the frequency of standing Alfvén waves with radial distance (*Anderson et al.*, 1989). These frequency shifts should not be significant, even near the plasmapause where the rate of change of the standing Alfvén wave frequency ought to be largest. The reason is that the Alfvén waves are being continually excited by the global mode, and they do not have time to phase mix significantly. However, even if a large phase-mixing timescale is assumed, these shifted frequencies should not deviate from the stationary frame by more than about 10% when THE crosses the structured (compared to THA and THD observations) plasmapause (*Anderson et al.*, 1989). Even if such shifts, which would only apply to Alfvén waves and not the global mode, are present, they would not affect the main conclusions of this study.

4.4.6 Summary of wave properties

To summarize, using two probes we have identified wave activity outside of the plasmapause at 6.5 mHz that exhibits radial-nodal spatial structure, dominant perturbations in the east-west electric and field-aligned magnetic field, and a 90 degree phase difference between the electric and magnetic field perturbation. Furthermore, this wave activity is associated with net earthward electromagnetic energy transfer. At the same time, using a probe first located in the plasmasphere and then crossing out a highly structured plasmapause, we identify no significant wave activity in the plasmasphere followed by an abrupt increase at the plasmapause. This wave activity is spread over a large frequency range that overlaps the global mode frequency. Finally, this wave activity includes perturbations with phase relationships expected for standing Alfvén waves driven by energy transferred earthward from the global mode.

4.5 ULF wave modes that are inconsistent with observations

In the following sections, we compare our observations between 0625 and 0745 UT with previous observations and theory pertaining to wave modes which may be driven in the Pc5

frequency range in this region of the magnetosphere, excluding global modes. We focus on the following drivers of ULF waves that may have a compressional magnetic field perturbation, as they could operate in this region of the magnetosphere: drift-bounce resonance with ring current ions (*Southwood et al.*, 1969), the drift-mirror instability (*Hasegawa*, 1969), magnetopause surface waves driven by the Kelvin-Helmholtz instability (*Chen and Hasegawa*, 1974), and monochromatic fluctuations in the solar wind (*Kepko et al.*, 2002).

4.5.1 Compressional waves driven by drift-bounce resonance

Drift-bounce resonance can occur when a significant population of hot ions is available to supply energy to ULF waves that have appropriate frequencies for the resonance. *Southwood et al.* (1969) showed that waves generated through the resonance would most likely have odd symmetry about the magnetic equator with regard to field line displacement and be associated with a strong radial magnetic field perturbation at the magnetic equator. In the event presented in this paper, the radial magnetic field perturbation is significantly weaker than the field-aligned magnetic field perturbation at the magnetic equator (Figures 4.6 and 4.7), inconsistent with theory.

Ion fluxes ought to rise and fall at the wave frequency for energies close to the drift-bounce resonant energy. Furthermore, there ought to be a 180 degree phase difference between flux observations above and below the resonant energy (*Southwood and Kivelson*, 1981). Finally, overall enhancements or decreases in wave energy ought to be associated with significant changes in the ion population, as would occur during a substorm injection or the recovery phase of a geomagnetic storm (e.g., *Yang et al.*, 2010). In the top panel of Figure 4.10, we show an ion energy flux spectrogram generated by the ESA and SST instruments on THD that includes energy ranges typically considered for drift bounce resonance (e.g., *Korotova et al.*, 2009). We find that there is a general decrease in the ion energy flux with time, with one peak occurring at ~ 4 keV. We do not find any modulation of fluxes at the wave frequency of 6.5 mHz at any energy range, nor do we observe a 180 degree phase difference across any energy range. However, we do not stress this as definitive evidence against the drift-

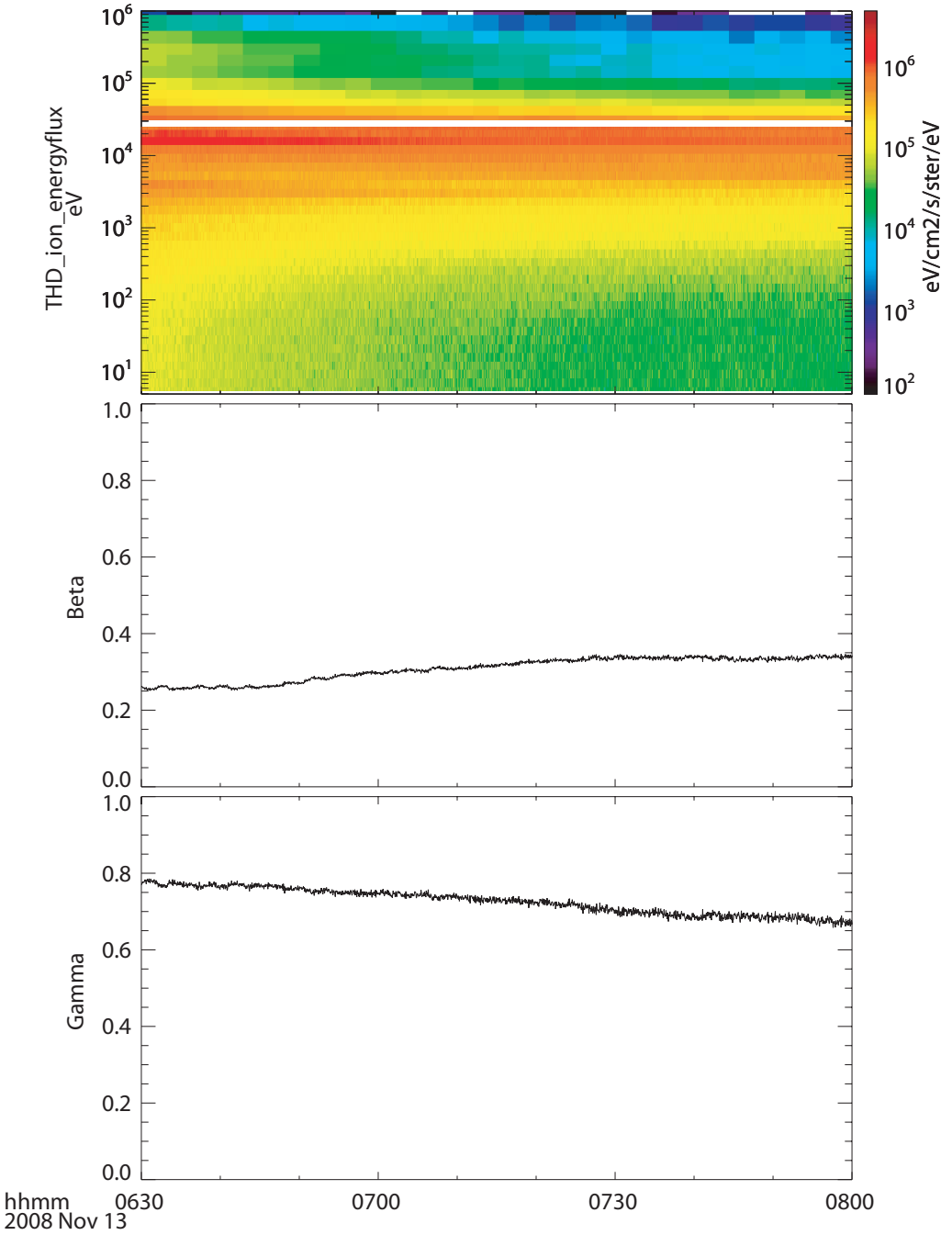

Figure 4.10: From top to bottom, THD ion energy flux spectrogram (measured by the ESA and SST instruments), plasma beta (ratio of thermal pressure to magnetic pressure) measured, and Γ, a parameter that indicates the threshold for the mirror instability is met when it is less than 0.

bounce resonance, as these features may not always be observed (*Southwood and Kivelson*, 1981; *Yang et al.*, 2010). However, we do stress that there is no change in the overall ion population that could explain the time dependent wave activity observed by THD (Figure 4.6).

Finally, the drift bounce resonance mechanism is not consistent with the correlation between solar wind dynamic pressure fluctuations and ULF wave power observed on the ground (Figure 4.3c). To summarize, the polarization of the observed waves, the lack of any time variation of ion energy flux consistent with time variable wave activity, and the relationship between dynamic pressure fluctuations and ULF wave activity observed on the ground all argue against drift bounce resonance as a viable mechanism for driving ULF waves. We conclude that drift-bounce resonance was not the driver of the 6.5 mHz wave activity for this event.

4.5.2 Compressional waves driven by the drift-mirror instability

The drift-mirror instability can drive ULF waves when the plasma beta, or ratio of thermal to magnetic pressure, is large and there is significant pressure anisotropy (*Hasegawa*, 1969). Several observations of compressional waves that have been attributed to the drift mirror instability have all shown that the plasma beta was greater than one (*Zhu and Kivelson*, 1994; *Korotova et al.*, 2009); in contrast, we observe the plasma beta to be ~ 0.3 throughout the interval, as shown in Figure 4.10b. In Figure 4.10c, we plot the threshold for the mirror instability, Γ, previously used by *Korotova et al.* (2009) to demonstrate that the mirror instability was a driver of ULF waves

$$\Gamma = 1 + \beta_{\perp}(1 - \frac{T_{\perp}}{T_{\parallel}}) < 0 \tag{4.1}$$

where $\beta_{\perp}$ is for the thermal pressure perpendicular to the background magnetic field, $T_{\perp}$ is the perpendicular temperature, and $T_{\parallel}$ is the parallel temperature (*Southwood and Kivelson*, 1993). For the entire interval when we observe the 6.5 mHz perturbation, Γ is well above 0, closer to 0.8; this is significantly larger than Γ reported in previous studies of waves driven

by the drift-mirror instability, demonstrating that the mirror instability could not be driving the 6.5 mHz fluctuation (*Korotova et al.*, 2009).

Waves driven by the drift mirror instability ought to have strong perturbations in the transverse magnetic field components near the magnetic equator and weak or non-existent perturbations in the field-aligned magnetic field (*Cheng and Lin*, 1987). In some cases, the compressional perturbations may occur at the magnetic equator as a second harmonic of the transverse perturbations (*Takahashi et al.*, 1990). However, we observe significant perturbations in the field-aligned magnetic field near the magnetic equator and comparatively small or non-existent perturbations in the transverse components both at 6.5 mHz and at lower/higher frequencies (Figure 4.6). Finally, like the drift bounce resonance mechanism, the drift-mirror instability mechanism is not consistent with the correlation between solar wind dynamic pressure fluctuations and ULF wave power. We conclude that the drift-mirror instability was not the driver of the 6.5 mHz wave activity for this event.

4.5.3 Magnetopause surface waves

Surface waves driven by velocity shear at the magnetopause can be observed as monochromatic, compressional perturbations in the magnetosphere (e.g., *Fujita et al.*, 1996; *Agapitov et al.*, 2009; *Hartinger et al.*, 2011). In these cases, a probe located near the magnetopause or in the magnetosheath may observe the signature of the surface wave activity in the form of multiple magnetopause crossings. In this event, THC is located in the magnetosheath and does not observe surface wave signatures, as was the case in previous magnetosheath observations that have been linked with ULF wave activity in the magnetosphere (e.g., *Agapitov et al.*, 2009; *Hartinger et al.*, 2011); however, this evidence alone does not preclude the possibility that a surface wave is present, as the boundary undulations may have too small an amplitude for THC to observe. The amplitude of a surface mode would be expected to decay monotonically with increasing distance from the magnetopause (*Chandrasekhar*, 1961). In this event, the wave amplitude is higher at a probe (THD) that is further from the magnetopause than another probe (THA) during part of the interval, inconsistent with

a surface wave. Finally, there should be some net energy flux tailward for a magnetopause surface wave (*Junginger*, 1985); during several parts of the interval of interest in this event, there is extremely weak or non-existent tailward energy flux (Figure 4.7). We conclude that magnetopause surface waves were not the driver of the 6.5 mHz wave activity for this event.

4.5.4 Compressional waves directly driven by monochromatic dynamic pressure fluctuations

Monochromatic fluctuations in the solar wind have been directly linked to compressional ULF wave in the magnetosphere with the same frequency, with typical frequencies that are comparable to or less than 2 mHz (e.g., *Kepko and Spence*, 2003; *Viall et al.*, 2009). In this event, there is evidence of fluctuations in the solar wind dynamic pressure at $\sim 2mHz$ that may be driving ULF waves of the same frequency in the magnetosphere. However, fluctuations at higher frequencies in the magnetosphere do not appear to be directly correlated with monochromatic fluctuations in the solar wind (Figure 4.6). Furthermore, it is unlikely that monochromatic fluctuations in the solar wind could generate the persistent nodal structures observed by THA and THD. Finally, a frequency of 6.5 mHz is above expected frequencies for quasi-static driving of the magnetosphere by solar wind dynamic pressure fluctuations (*Kepko and Spence*, 2003). We conclude that dynamic pressure fluctuations are not directly driving the 6.5 mHz ULF waves observed at THD and THA, although broadband dynamic pressure fluctuations provide a source of energy for these waves.

4.6 Global mode driven by broadband dynamic pressure fluctuations

Using geomagnetic activity indices and observations in the solar wind, magnetosheath, magnetosphere, and on the ground, we identified an interval favorable for observing a global mode on 13 Nov 2008 from 0625 to 0745 UT. The criteria we used for selecting the interval was the availability of in situ and ground observations in nearly the same local time

sector and in a radial alignment, a stable magnetopause location (based on steady, northward IMF and no large changes in solar wind dynamic pressure), the ability to identify a single driver of ULF waves (broadband dynamic pressure fluctuations), and no significant transient ULF wave activity. We used data from the THEMIS probes and on the ground to identify the properties of ULF waves during this interval. Using these data, we examined the possibility that these waves could be generated by several mechanisms which are known to produce monochromatic fluctuations in the Pc5 frequency range: drift-bounce resonance, drift-mirror instability, magnetopause surface waves, and monochromatic fluctuations in the solar wind. Having eliminated these mechanisms as potential drivers of the monochromatic wave activity, we now examine the global mode mechanism as a means of generating these waves.

4.6.1 Expected global mode features

It is expected that global modes should have field-aligned magnetic field perturbations and east-west electric field perturbations that are 90 degrees out of phase, as observed in this event (Figure 4.7) (*Waters et al.*, 2002). These perturbations were dominant for much of the event, consistent with a wave standing primarily in the radial direction. Global modes should also exhibit a distinct nodal structure throughout their radial extent, as expected for a radially standing wave and as was observed in this event (Figure 4.8c). Finally, dynamic pressure fluctuations are strongly correlated with ULF wave activity in the magnetosphere, suggesting that they could provide a source of energy for wave activity (Figure 4.3c). However, dynamic pressure fluctuations exhibit a broadband frequency spectrum above 2 mHz, yet compressional magnetic field perturbations in the magnetosphere are monochromatic (Figure 4.6). The global mode mechanism provides a ready explanation for this discrepancy. *Wright and Rickard* (1995) showed that drivers with a broad frequency spectrum can excite global modes at discrete frequencies; these global modes can act as reservoirs of energy, maintaining a stable spatial structure even when the rate that energy is supplied by the driver varies in time. Based on these lines of evidence, and the evidence eliminating the possibility for other typical sources of wave activity that have compressional magnetic field

perturbations, we conclude that the 6.5 mHz fluctuation observed at THA and THD was a global mode.

4.6.2 Coupling between global mode and shear Aflvén waves

In certain cases, standing fast mode waves can couple to shear Alfvén waves. For this to occur, the global mode must match the standing Alfvén wave frequency at some location in the magnetosphere (*Kivelson and Southwood*, 1985; *Allan et al.*, 1986b; *Wright and Rickard*, 1995). Additionally, *Kivelson and Southwood* (1985) showed that global modes are evanescent through some of their radial extent before they couple to shear Alfvén waves at the location where the global mode frequency matches the standing Alfvén wave frequency. *Zhu and Kivelson* (1989) and others have shown that the energy transported to a standing Alfvén wave from a global mode depends on the distance between the point where the global mode becomes evanescent and the point where the frequencies are matched. We have presented evidence in Figure 4.9 that standing Alfvén waves were excited near the plasmapause. In Figure 4.11, we examine the relationship between these Alfvén waves and the global mode using qualitative comparisons with the numerical model of a cavity mode (a type of global mode) from *Zhu and Kivelson* (1989); the qualitative results of this model can also be applied to other global modes, such as waveguide modes (*Wright*, 1994; *Rickard and Wright*, 1994). Details of the model implementation are given in Appendix A.

In Figure 4.11a, we show the magnetic field z perturbation (blue), associated with the cavity mode, and the electric field x perturbation (red), associated with Alfvén waves, generated from the model. One cavity eigenfrequency is shown for a case where the Alfvén speed varies as $distance^{\frac{-3}{2}}$, which is expected for a dipole magnetic field and density variations as in *Carpenter and Anderson* (1992). The nodal structure of the cavity mode is seen in the outer region, and it rapidly decreases with decreasing radial distance at the same location as the Alfvén wave activity is sharply peaked ($\sim$ 6.8 Re). Based on earlier models, the amplitude of the b_z perturbation ought to rapidly decrease at radial distances smaller than the location of the turning point (which is at a larger distance than the resonance location)

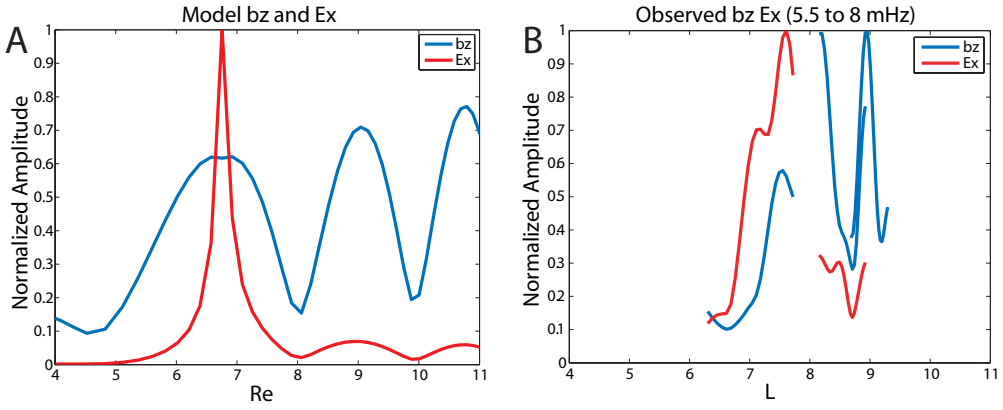

Figure 4.11: A: The z component of the magnetic field perturbation (blue) and x component of the electric field perturbation (red) for a global mode generated using the *Zhu and Kivelson* (1989) 1D model. The x axis indicated distance from the inner model boundary. One eigenfrequency is shown for a case where the Alfvén speed varies as $distance^{\frac{-3}{2}}$, which is expected for a dipole magnetic field and density variations as in *Carpenter and Anderson* (1992). B: The same as A, but for observations from THA, THD, and THE between 0625 and 0745 UT. These data are plotted versus L, or radial distance.

(*Kivelson and Southwood*, 1985, 1986); however, there is a small increase in amplitude at a lower radial distance in this case that is due to the model inaccurately estimating the solution to the wave equation near the resonance location. In this case, very small variations in the assumed solution at the singularity led to noticeable variations in the solution away from the singularity.

In Figure 4.11b, we show observations of the magnetic field z perturbations in the 5.5 to 8 mHz frequency band (blue) and electric field x perturbations in the same frequency band from THA, THD, and THE, normalized in the same manner as in Figure 4.8. In particular, the magnetic field perturbations from each probe are all normalized to the maximum value observed by all three probes during the entire interval (i.e., only one number is used for normalization), and the same is done for the electric field perturbations (note that we have excluded the electric field data from THA because of contamination). Qualitatively similar results are seen between the model and observations; namely, nodal structure from the magnetic field z component in the outer region where the electric field perturbations are weak and strongly enhanced radial electric field perturbations in the inner region where the

global mode frequency matches the standing Alfvén wave frequency. This, combined with the radially inward energy transfer observed in the outer region (Figure 4.7), suggests that a global mode is driving shear Alfvén waves during this event. We note the observations show narrower magnetic field peaks than the numerical model; more recent models have shown similarly narrow peaks (e.g., *Waters et al.*, 2002). Furthermore, the observations show a broader peak in the radial electric field than the model. This is likely caused by the use of an unrealistically high ionospheric conductivity in the model as well as the existence of a weaker than normal density gradient when the observations were made (due to the highly structured plasmapause region); both effects would tend to broaden the peak where the FLR is located (*Mann*, 1997).

The model should only be used for qualitative comparisons because we have not included the sharp changes in plasma mass density at the plasmapause. Such sharp changes can play an important role in coupling between global modes and shear Alfvén waves (e.g., *Zhu and Kivelson*, 1989). In particular, the frequency of standing Alfvén waves changes rapidly at the plasmapause, which can in turn lead to a large range of different frequencies being excited over a small radial distance, perhaps explaining the broad range of frequencies seen by THE as it crosses the plasmapause (Figure 4.9c, *Lin et al.* (1986)). A plausible scenario to explain the coupling between global modes and shear Alfvén waves at the plasmapause in such cases could include the frequency of the fundamental and perhaps additional harmonics of a cavity mode all matching standing Alfvén wave frequencies near the sharp density gradient. Alfvén waves would then be excited at one or more frequencies over a small radial distance and phase mix (e.g., *Mann et al.*, 1995). This would lead to enhancements in wave power at a broad range of frequencies at the plasmapause that are similar to the global mode frequency or frequencies, rather than exactly matching the discrete frequencies of the global mode. Finally, we note that there may be small differences between the data shown in Figure 4.11b, which was measured in the moving spacecraft frame, and data transformed to a stationary frame. These small differences are discussed in Section 4.4.5, and they will not affect the qualitative comparison with the model shown in Figure 4.11a.

4.6.3 Cavity or waveguide mode

Throughout this study we refer to the standing fast mode waves that THA and THD observe as a global mode. In this section, we discuss the relevance of models of two types of global modes, cavity and waveguide modes, to our observations. We emphasize that whether the observations are better described as cavity or waveguide modes, the main conclusions of this paper remain unchanged: broadband dynamic pressure fluctuations can excite global modes (whether cavity or waveguide modes) outside the plasmasphere and in the Pc5 frequency range, and these global modes can in turn excite standing Alfvén waves.

Cavity models treat the magnetosphere as a closed system, with energy only allowed to leak into the ionosphere. In these models, cavity modes have discrete azimuthal wave numbers and extend to all azimuthal locations (e.g., *Kivelson and Southwood*, 1985). In the present study, we do not have enough observations to conclude that the global mode is present at all azimuthal locations. Also, the spacecraft configuration is not ideal for estimating the azimuthal wave number (due to their small azimuthal separation and rapid motion through spatial structures - see section 4.4.4). However, the monochromatic compressional magnetic field perturbations, polarization, and nodal structure are all consistent with cavity mode theory.

Several authors have proposed that the flank magnetosphere is better described as a waveguide than a cavity, as energy leaks into the tail, leading to dispersion and wave modes with a continuum of azimuthal wave numbers. In our event we did not observe significant tailward energy transfer (Figure 4.7, panel 7), nor were our observations consistent with a broad frequency spectrum that was previously attributed to dispersion in the flank waveguide (*Mann et al.*, 1998). However, these observations do not preclude the possibility that the observations are of a waveguide mode. The THEMIS probes used in the present study were not in an ideal, azimuthally separated configuration to observe dispersion as in *Mann et al.* (1998). Furthermore, if the observations are not very remote from the region on the magnetopause where driving is strongest, the THEMIS probes would observe a waveguide mode with low azimuthal wave number. The waveguide mode observations would be identical

to those expected for a cavity mode, although energy would be propagating away from the location of the THEMIS probes and down the waveguide, inconsistent with cavity mode theory (e.g., *Wright*, 1994).

The observations that we have presented could be consistent with either a cavity mode or a waveguide mode with low azimuthal wave number. Although we lack the observations to definitively categorize the global mode as either a cavity or waveguide mode, we find that waveguide mode theory is an appealing description of the manner in which global modes can be excited in the outer magnetosphere (i.e., outside the plasmasphere), in that it includes the possibility that wave energy can leak into the magnetotail and allows for a continuum of azimuthal wave numbers.

4.6.4 Global mode boundaries and frequency

We note that the frequency of the global mode was in the Pc5 band, and that it was observed at large L shells ($L > 7$), where Pc5 FLRs are often observed. Examination of the electron density profiles inferred from spacecraft potential reveals that the plasmapause was located at $L \sim 7$ when the global mode was observed, and that THE was inside the plasmasphere whereas THD and THA were outside the plasmasphere (Figure 4.9a). We do not have the data coverage to identify the exact location of the inner boundary of the cavity. However, our observations strongly suggest that the plasmapause is the inner boundary, as the wave amplitude is significantly lower at THE compared to THD and THA (Figure 4.9b).

It is more difficult to determine the outer boundary of the cavity, due to a lack of observations near the magnetopause. Some models and simulations of global modes have assumed or showed that the magnetopause can function as an outer boundary, whereas a few others have extended the outer boundary to the bow shock (e.g., *Samson et al.*, 1992; *Claudepierre et al.*, 2009). In Figure 4.12, we show data from THB (solar wind), THC (magnetosheath), and THD and THA (magnetosphere) which suggest that the global mode may extend into the magnetosheath. The top four panels of Figure 4.12, from top to bottom, are the high pass filtered ($frequency > 1mHz$) solar wind dynamic pressure

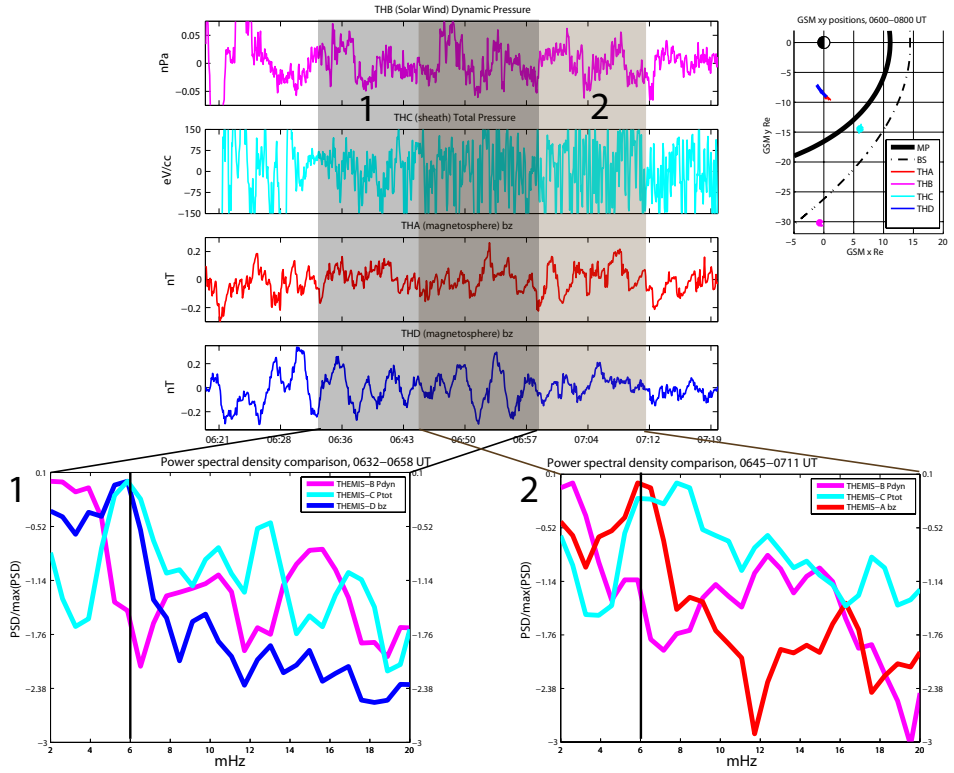

Figure 4.12: On the top, from top to bottom, traces of the high pass filtered ($frequency > 1mHz$) solar wind dynamic pressure observed by THB, total pressure observed by THC, compressional magnetic field observed by THA, and compressional magnetic field observed by THD. The two numbered, shaded areas correspond to intervals for Fourier analysis shown in the bottom two insets. The first inset shows a comparison between PSDs for the compressional magnetic field perturbations observed by THD (dark blue), total pressure fluctuations observed by THC (light blue), and solar wind dynamic pressure fluctuations observed by THB (pink), all normalized to their respective maximum values; a black line denotes 6 mHz. The second inset is the same as the first but for the second interval and using THA (red) instead of THD.

measured at THB, total pressure (thermal and magnetic) perturbations measured at THC, and compressional magnetic field perturbations measured at THA and THD. The 6.5 mHz signal corresponding to the global mode is seen most clearly when THD is passing through an anti-node from $\sim 0630 - 0655$ and when THA is passing through an anti-node from $\sim 0645 - 0715$. A 6.5 mHz signal can also be seen in the magnetosheath (THC, second panel) most clearly from $\sim 0630 - 0650$, yet no 6.5 mHz signal is evident in the solar wind (top panel).

We selected two intervals for Fourier analysis to test whether there is a persistent signal in the magnetosheath related to the global mode that THD and THA observe. The intervals correspond to periods when each probe was passing through an anti-node and most clearly observed the 6.5 mHz signal (see Figure 4.8). We used a 512 point (26 minute) FFT window for this analysis. In inset 1 of Figure 4.12, the PSD for the solar wind dynamic pressure fluctuations, magnetosheath total pressure fluctuations, and compressional magnetic field perturbations observed by THD are shown for the first interval. Each trace has been normalized to the maximum PSD. Both compressional magnetic field perturbations in the magnetosphere and total pressure fluctuations in the magnetosheath have a distinct peak in PSD at 6 mHz (a negligible difference from 6.5 mHz when considering the precision of this Fourier analysis), yet there is no peak at this frequency in the solar wind. Inset 2 of Figure 4.12 shows data in a similar manner to inset 1 from a later interval, except that data from THA is shown instead of THD. During this later interval, the total pressure perturbations observed at THC have a broader frequency spectrum, but they are still enhanced above background levels near 6.5 mHz and overlap with the peak that THA observes (corresponding to the global mode). We conclude that there is a persistent ~ 6.5 mHz signal in the magnetosheath that is likely related to the global mode signature at THA and THD.

To our knowledge, this is the most direct evidence ever reported of global modes extending into the magnetosheath. We cannot say with certainty, however, that the global mode extends into the magnetosheath, as the global mode may be observable yet evanescent in the magnetosheath. As such, we cannot determine whether the outer boundary for the global mode is the magnetopause or the bow shock; this lack of a constraint on the outer boundary

location has implications for any theoretical estimates of the global mode frequency, as we shall discuss.

We can obtain an estimate of the fundamental global mode frequency using a time of flight calculation (transit time for a fast mode wave from one boundary of the cavity to the other and back again)

$$f^{-1} = 2Re \int_{L_i}^{L_o} \frac{dL}{V_{fm}} \tag{4.2}$$

where f is the frequency, Re is an Earth radius, L_i is the location of the inner boundary, L_o is the location of the outer boundary, and V_{fm} is the speed of a fast mode wave (*Takahashi et al.*, 2010). This calculation requires many assumptions, as we cannot definitively constrain the location of the inner and outer boundary and we lack observations of magnetic field, density, and temperature in a large region of the flank magnetosphere. We present two sets of assumptions that lead to different estimates of the fundamental frequency below.

In the first estimate, we assume the inner boundary at the plasmapause ($L_i \sim 7$ based on observation), the outer boundary at the flank magnetopause ($L_o \sim 17$, according to the *Shue et al.* (1997) model), the temperature constant throughout the cavity, the only ion species is protons, the magnetic field varies as a dipole, and the electron density varies as $L^{-4.5}$ (based on the empirical model of *Carpenter and Anderson* (1992)). Using observations at THD during the global mode observation, we find that the Alfvén speed is $\sim 1300\frac{km}{s}$ (at $\sim$ 0700 UT, $L \sim 8$) when assuming pure hydrogen or $\sim 1000\frac{km}{s}$ when assuming 5% oxygen, the sound speed is $600\frac{km}{s}$, and the fast magnetosonic speed is $\sim 1400\frac{km}{s}$ or $\sim 1200\frac{km}{s}$, depending on ion composition. Finally, we assume that the fundamental is a quarter wavelength mode, as previously reported by *Mann et al.* (1999) and *Claudepierre et al.* (2009). To use this assumption, we must divide the fundamental frequency from equation 4.2, which assumes a half-wavelength fundamental mode, by 2. With these observations and assumptions, we find that the frequency of the fundamental global mode is 3.8-4.5 mHz. A larger fraction of heavy ions in the plasma, contributions from the colder, denser plasma of the low latitude boundary layer, and an inner displacement of the inner boundary or outer displacement of the outer boundary would all significantly decrease the estimated fundamental frequency.

These calculations are consistent with our observations if we assume that the 6.5 mHz global mode is a harmonic. Our observations suggest that it is a harmonic, based on the observed nodal structure (Figure 4.11). The separation between the two nodes observed by THD and THA is between 0.75 and 1 Re, while the cavity that we have assumed is 10 Re wide. This does not necessarily imply that the global mode is a tenth harmonic, since several studies have showed that the separation between nodes in an inhomogenous medium is highly irregular (e.g., *Zhu and Kivelson*, 1989; *Waters et al.*, 2002). Furthermore, the fact that we observe a frequency that is roughly double our estimated fundamental frequency does not necessarily imply that we are observing the first harmonic for two reasons: one is the considerable uncertainty in the estimated frequency, and the second is the fact that harmonics are not necessarily integer multiples of the fundamental frequency in an inhomogeneous medium (*Allan and McDiarmid*, 1993). However, the small separation between nodes, when compared to the size of the cavity, is somewhat unexpected given that the estimated fundamental frequency is lower than but within a factor of two of the frequency we observe, suggesting either a first or at most a second harmonic (*Allan and McDiarmid*, 1993). This suggests that either the nodal structure is highly irregular (i.e., very small nodal separation in this region compared to elsewhere in the cavity) or at least one of the assumptions contained in the time-of-flight calculation is not valid. These concerns remain if we assume a half-wavelength mode as the fundamental mode rather than a quarter-wavelength mode.

One major assumption that we have made in the time-flight-calculation which may be invalid is the location of the outer boundary. In the second estimate of the fundamental frequency, we assume that the global mode is not bounded by the magnetopause and extends into the magnetosheath, as suggested by data shown in Figure 4.12. Due to the large number of assumptions that must be made to calculate the fundamental frequency in this case, we do not attempt an estimate in the same manner as our first suggested scenario. We rely instead on the results shown in *Harrold and Samson* (1992), which demonstrated that global modes that extend into the magnetosheath can have frequencies on the order of 1 mHz for typical plasma and magnetic field parameters. A fundamental frequency on the order of 1

mHz is consistent with our observations for the same reasons described for the first scenario, assuming that the global mode we observe is a harmonic of the fundamental. However, this scenario allows for the observed global mode to be a higher order harmonic than the previous scenario, as the fundamental frequency would be much lower than 3.8-4.5 mHz.

4.6.5 Relationship between global mode and lower frequency waves

Both THD and THA observe perturbations at lower frequencies than 6.5 mHz. We attempted to identify the source of these waves and their relationship to the 6.5 mHz signal. As mentioned previously, it is likely that waves below 2 mHz are being directly driven by solar wind dynamic pressure fluctuations of comparable frequency. It is more difficult to identify the source of the waves between 2 and 6.5 mHz. These waves have frequencies of several mHz and are associated with enhanced east-west magnetic and radial electric field perturbations (e.g., Figure 4.6, panels 2 and 5) during at least the latter part of the interval, all of which are consistent with standing shear Alfvén waves (e.g., *Lee and Lysak*, 1989). If these are standing Alfvén waves, they may be unrelated to the 6.5 mHz global mode. A broadband driver, such as solar wind dynamic pressure fluctuations, can excite a continuum of standing Alfvén waves throughout the entire magnetosphere without the presence of a global mode (*Dungey*, 1967). Thus, it is possible that the broadband solar wind fluctuations are driving Alfvén waves at frequencies that are set by the local field line resonance frequency as well as a global mode at the 6.5 mHz frequency (frequency set by the magnetospheric cavity properties).

There are some features of the wave activity between 2 and 6.5 mHz that cannot be easily explained by standing Alfvén waves. In particular, there are strong z component perturbations between 2 and 6.5 mHz observed by THD between $\sim$ 0630 and 0700 UT that are not observed by THA (Figure 4.6, panels 3 and 6). Similarly, there are strong z component perturbations between 2 and 6.5 mHz observed by THA after 0730 UT that are not observed by THD (Figure 4.6, panels 3 and 6). Standing Alfvén waves driven by the solar wind are not typically associated with strong perturbations in the z component.

Furthermore, we can rule out other potential drivers of ULF wave activity with strong z component perturbations between 2 and 6.5 mHz for the same reasons that we ruled them out for the 6.5 mHz global mode. In particular, the ambient plasma conditions do not support the drift mirror instability or the drift-bounce resonance mechanisms, and the z perturbations at THD (inner probe) are much larger than at THA (outer probe) for at least part of the interval, precluding the possibility of direct driving by a magnetopause surface wave or monochromatic fluctuations in the solar wind.

These z perturbations could, however, be evidence for a global mode. An immediate question is what is the relationship between these z perturbations, the Alfvén wave activity, and the 6.5 mHz global mode. Unfortunately, further analysis of the polarization properties and spatial structure of this lower frequency wave activity to confirm the presence of a global mode in the same manner as for the 6.5 mHz fluctuations is complicated for several reasons: the 6.5 mHz signal is also present, Alfvén waves are also present, and the intervals of time in which the lower frequency signal is clearly observed are too short for detailed analysis (i.e., appropriate filtering or isolation of the signal in the frequency domain is not possible). However, it is possible that the 6.5 mHz global mode is a harmonic of a lower frequency global mode. This hypothesis is supported by the observations of large amplitude standing Alfvén wave perturbations at the plasmapause by THE, which have their peak power at a lower frequency than 6.5 mHz (Figure 4.9c). This lower frequency global mode could be driving Alfvén waves at the same frequency at the plasmapause.

4.7 Summary

Unlike previous observations of global (cavity/waveguide) modes outside the plasmasphere, this study reports on observations of a global mode in the absence of other wave modes. This facilitates wave mode identification, as the small amplitudes observed ($\sim 200pT$, $0.8\frac{mV}{m}$) could easily have been obscured by other wave activity that can occur at similar locations with higher amplitudes, such as compressional waves driven by the drift-mirror instability (e.g., *Korotova et al.*, 2009). Furthermore, we have presented evidence of coupling between

a global mode and shear Alfvén waves; in particular, we have shown radially inward energy transfer from the global mode to the plasmapause, where shear Alfvén waves in the same frequency range as the global mode are observed. Finally, we have shown that monochromatic global mode waves can be generated outside the plasmasphere at the flank of the magnetosphere, despite the fact that substantial dispersion is expected from tailward propagation (*Rickard and Wright*, 1995).

Our observations suggest that global modes are a viable mechanism for converting energy from fluctuations in the solar wind to monochromatic fluctuations in the Pc5 frequency band in the magnetosphere, even if those external fluctuations are broadband. Our results can help explain the propensity of monochromatic, Pc5-band ground pulsations to develop over a wide range of latitudes in the absence of a monochromatic solar wind driver (*Wright and Rickard*, 1995). Moreover, a monochromatic global mode is required in order to generate monochromatic, radially localized Alfvén waves via FLR. Our results, therefore, lend observational credence to the global mode driver model of FLRs localized at mid to high latitudes, at least during the particular conditions (e.g., IMF northward) during which this event occurred (*Samson and Rostoker*, 1972; *Walker et al.*, 1979).

We have not shown the relationship between a monochromatic global mode and a monochromatic standing Alfvén wave directly in this study, as we observed standing Alfvén waves with a range of frequencies that overlapped the global mode frequency; we attributed this range of frequencies to the sharp density gradient at the plasmapause. However, we have shown that monochromatic global modes can at least drive standing Alfvén waves over a frequency range that includes the global mode frequency; we expect that monochromatic Alfvén waves would be observed when driven by global modes in regions with smaller, smoother density gradients.

This event was selected from 3-4 similar events that occurred over a span of several months during intervals when geomagnetic activity was low, only one potential driver of ULF waves was expected to be present (to facilitate wave mode identification), and spacecraft conjunctions were ideal. In Chapter 5, we will conduct a more systematic search for global mode events, and investigate the properties of an event ensemble to further examine the role

that global modes play in energy transfer in the Earth's magnetosphere.

CHAPTER 5

Statistical study of global modes outside the plasmasphere

Global modes can generate large-scale, monochromatic ULF wave activity in the Earth's magnetosphere; they exhibit a monochromatic frequency spectrum even in the presence of a driver with a broadband frequency spectrum. There is evidence from ground-based observations, numerical models, and MHD simulations that suggests the global mode mechanism is an important means of generating monochromatic ULF waves. However, direct observations of global modes are limited to a few case studies due to unique challenges associated with unambiguously detecting them in situ. In this study, we use electric field, magnetic field, and plasma data from multiple THEMIS spacecraft as well as ground based observations to identify an ensemble of global modes in a region outside of the nominal plasmapause location. We use this ensemble to obtain a lower bound of 1.0% for the occurrence rate of global modes in the 3 to 20 mHz frequency range in the Earth's magnetosphere. We also find that global modes are more likely to occur in the noon local time sector and at radial distances of less than 7.5 Re. The ion foreshock is an important source of energy for global modes with frequencies greater than 10 mHz, and the occurrence of all global modes generally increases with increasing solar wind flow speed and decreasing solar wind dynamic pressure.

5.1 Introduction

In Chapter 4 we described the importance of global modes as a mechanism for driving localized, monochromatic ULF wave activity. We demonstrated this using a case study of a global mode in the Pc5 (2-7 mHz) frequency range. In this chapter, we further explore the

Event	Location (MLT)	Frequency (mHz)	Driver
Kivelson et al., [1997]	Pre-Noon	24	Ion foreshock waves
Mann et al., [1998]	Noon, Dawn	2.5	Broadband Pressure Fluctuations
Eriksson et al., [2006]	Noon	6.8, 27	Broadband Pressure Fluctuations
Hartinger et al., [2012]	Dawn	6.5	Broadband Pressure Fluctuations

Figure 5.1: The properties of global modes found from previous in situ observations outside of the plasmasphere.

importance of global modes using a statistical study. We shall focus on the region outside of the plasmasphere for this study because of the important role ULF waves may play in radiation belt dynamics and because of the wider availability of electric field data in this region (electric field measurements tend to be complicated by electrostatic wake effects in the plasmasphere - see Appendix B.2).

An overview of previous case studies of global modes that used in situ observations outside the plasmasphere is shown in Figure 5.1. We only include case studies that specifically studied global modes, not studies that suggested global modes as one possible explanation for ULF wave observations. The location, frequency, and driving mechanism are shown for each event. All of the previous observations outside the plasmasphere were located in the dawn or noon local time sectors. Three of the four had frequencies in the Pc5 frequency range. These three events were also driven by dynamic pressure fluctuations with a broadband frequency spectrum. The other event was driven by waves originating in the ion foreshock and had a frequency of 24 mHz, which overlapped the expected frequency spectrum of the driver. These observations suggest that the noon and dawn local time sectors are best for observing global modes, and that typical global mode frequencies outside of the plasmasphere fall in the Pc5 and Pc4 range (2-22 mHz). MHD simulations and numerical models in dipole geometries have also shown that global modes can be generated with these frequencies (*Lee and Lysak*, 1989; *Claudepierre et al.*, 2009).

All previous global mode studies that relied on in situ observations were case studies. There has not been a study that quantified the occurrence of global modes or that studied

them in a systematic manner using in situ data. The THEMIS mission is ideal for this purpose, owing to the availability of electric field, magnetic field, and plasma data, as well as multi-point spacecraft observations near the magnetic equator and ground magnetometer observations. All of these sources of data can be used to identify global modes using multiple lines of evidence, motivated by previous models and observations (e.g., *Waters et al.*, 2002).

In this chapter, we identify a large number of global mode events using THEMIS data and examine their properties. In section 5.2, we describe the instrumentation used in this study. Sections 5.3, 5.4 and 5.5 will be devoted to developing and implementing criteria that can be used to identify global modes while excluding other types of wave activity. Section 5.6 will be devoted to examining this ensemble of global modes and comparing with previous models and observations. Finally, we summarize our results in section 5.7.

5.2 Instrumentation

Much of the instrumentation used in these studies has already been described in Chapter 4, section 4.2; in particular, the THEMIS fluxgate magnetometer (FGM), electric field instrument (EFI), electrostatic analyzer (ESA), and solid state telescope (SST). We note here that the sensitivity of the fluxgate magnetometer outside of 5 Re is 12 pT and the sensitivity of the electric field instrument for measuring ULF signals is $0.2\frac{mV}{m}$.

We shall also use ground magnetometer data from the THEMIS ground based network (*Russell et al.*, 2008), Canadian Array for Realtime InvestigationS of Magnetic Activity (CARISMA) (*Mann et al.*, 2008), Geophysical Institute Magnetometer Array (GIMA) (*Galbraith et al.*, 2008), United States Geologic Survey network (*Love and Finn*, 2011), Magnetometer Array for Cusp and Cleft Studies (MACCS) (http://space.augsburg.edu/maccs/about.html), Athabasca University THEMIS UCLA Magnetometer Network (AUTUMN) (*Connors et al.*, 2009), and Canadian Magnetic Observatory Network (CANMON) (http://www.geomag.nrcan.gc.ca).

In Chapter 4 and Appendix B, we discussed sources of contamination for EFI and how contaminated intervals can be identified on a case by case basis. This study requires a routine method for identifying and removing contaminated intervals for the purposes of processing

a large amount of data. To that end, we developed quality control flags designed to identify contaminated intervals by comparing the electric field measured by the short and long EFI booms (in the spin plane) in the frequency domain. These flags are described in Appendix B, section B.2.

5.3 Automatic event selection

For the initial, automatic selection of global mode events, we selected an interval for analysis that began on 01 February 2008 and ended on 01 April 2010, and we used data from two THEMIS probes, THA and THE. This choice of interval was motivated by several factors. Our event selection criteria required electric field data, and these data were not available routinely before January 2008, motivating the choice to begin on 01 February 2008. The apogee of the THEMIS orbit precesses around the Earth on a timescale of about 13 months; thus, two full precessions around the Earth are included in the selected interval. We chose to end our analysis on 01 April 2010 because the THEMIS orbits changed significantly then, with two probes leaving Earth orbit and the three other probes decreasing their typical spatial separations. These new configurations were not ideal for several tests we conducted to validate the automatic global mode selection. Finally, we chose to use THA and THE because they spend more time in the magnetosphere than THB and THC, and THD's orbit is very similar to THE, so it does not provide much additional data coverage.

The automatic global mode selection is based on observations from a single spacecraft. In order to obtain high quality data for these observations, we require fast survey data (see Appendix B). This effectively excludes half of the THEMIS data set. We also exclude data that are typically in the plasmasphere by restricting our analysis to observations made at distances greater than 5 Re from the Earth. Our choice to exclude intervals in the plasmasphere was motivated by the presence of cold plasma wake effects in the EFI data in that region as well as the desire to focus on a region where global modes that are more effective in influencing the radiation belts (due to their locations and lower frequencies which are comparable with electron drift frequencies) are more likely to be generated. Finally, we

require that the probe is in the magnetosphere when making the observations; we make this determination using density and particle flux perpendicular to the background magnetic field from the ESA instrument. To impose these restrictions, we load THEMIS position data and data from the ESA instrument for all fast survey intervals. We require that the probe is at a distance greater than 5 Re, in region of density less than 5 particles per cm^3 (this condition also further restricts the chances of being in the plasmasphere), and in a region with perpendicular flux (integrated over ESA energies) less than $2x10^7$ particles per second per cm^2 for an interval of at least 85 minutes for data to be considered in our analysis.

Shown in Figure 5.2A, 5.2B, and 5.2C is the total fast survey data coverage in the GSM xy plane, in number of hours, for THA, THE, and both probes combined, respectively. THA samples slightly larger radial distances than THE during part of the interval, as shown by the differences between Figures 5.2A and 5.2B at larger radial distances. The uneven data coverage shown in 5.2A and 5.2B is due to the orbits of both probes changing slightly during the the interval as well as the changing criteria determining when fast survey data would be transmitted to the ground. Figure 5.2C shows that when data from both probes are combined, nearly all 1 Re by 1 Re pixels have at least 10 hours of fast survey data, indicating that there is ample data available for the present study.

In the following sections, we shall describe how we use this fast survey data to identify global modes in the frequency domain using multiple Fast Fourier Transform (FFT) windows. Figure 5.2D, 5.2E, and 5.2F are for the number of FFT windows that were ultimately used to identify global modes. Although THA has a similar amount of fast survey data to THE, there are far fewer FFT windows available to identify global modes. This discrepancy is due to the systematically worse measurement of ULF electric field perturbations by THA (see Appendix B.2); we do not use data from intervals with contaminated electric field data in our study. Although the useable data coverage, shown in Figure 5.2F, is not completely uniform, there are at least 20 FFT windows available to identify global modes in most 1 Re by 1 Re pixels; this is sufficient for the present study.

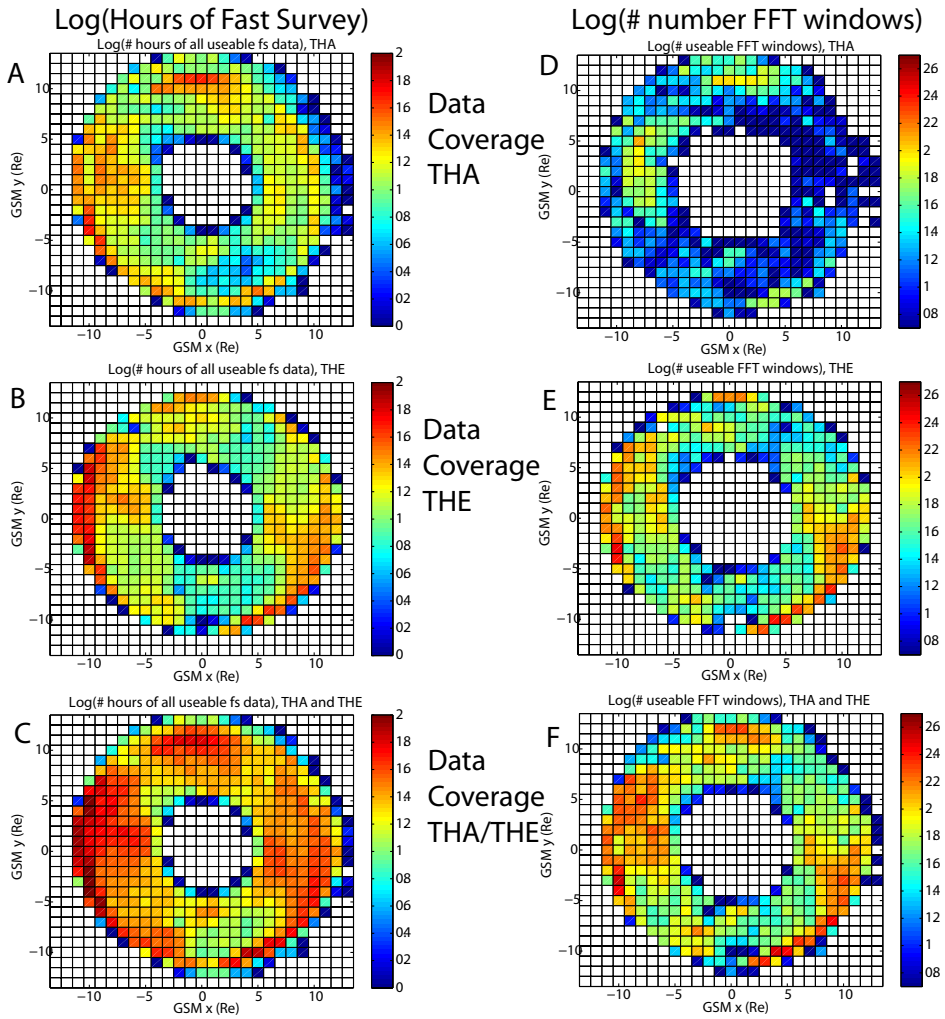

Figure 5.2: A) Log (base 10) of the number of hours of fast survey data outside of 5 Re and inside of the magnetopause in the GSM xy plane for THA. B) The same as A, but for THE. C) The same as A, but for THA and THE combined. D) Log (base 10) of the number of FFT windows that can be used to identify global modes for THA. E) Same as D but for THE. F) Same as D but for THA and THE combined.

5.3.1 Types of global modes to be selected

We discussed expected observational features of global modes in Chapter 4, section 4.1.2. These included perturbations in the east-west electric field and parallel magnetic field with a ~ 90 degree phase difference in time and nodal structure throughout their radial extent (*Waters et al.*, 2002). We must further elaborate on the differences between different types of global modes to motivate our event selection criteria and to discuss potential sources of bias in preferentially detecting certain types of global modes. We now discuss the difference between cavity modes and waveguide modes.

Cavity models treat the Earth's magnetosphere as a closed system with energy being lost to the boundaries of the cavity. In these models, a periodic boundary condition is imposed in the azimuthal direction, leading to the quantization of the azimuthal wave vector. These cavity mode solutions behave similarly to radially standing fast mode waves. However, *Samson et al.* (1992), motivated by observations of field line resonances with anti-sunward directed phase velocities, noted that a more realistic model of the magnetosphere would allow fast mode waves to propagate out of the magnetosphere and through the magnetotail. In these models, the flank magnetosphere would be treated like a waveguide rather than a cavity; energy from the solar wind could then excite waveguide modes on the dayside that propagate tailward.

Unlike in cavity models of the Earth's magnetosphere, in waveguide models the azimuthal wave vector can take a continuum of values. *Wright* (1994) examined dispersion associated with waveguide modes in a simplified model where the density and background magnetic field, and thus the Alfvén speed, were uniform. Perfectly reflecting boundary conditions are imposed in the radial and field-aligned directions, quantizing the wave vectors in those directions. However, no boundary condition is imposed in the direction along the waveguide, and a continuum of values for the wave vector is possible. *Wright* (1994) assume a solution of the form

$$e^{i\omega t \pm \vec{k}\cdot\vec{r}}, k_x = \pm\frac{n\pi}{x_n}, k_z = \pm\frac{m\pi}{z_m}, n, m = 1, 2, 3... \tag{5.1}$$

where x is the radial direction, y is along the waveguide, z is along the background field, k is

the wave vector, ω is the wave frequency, and x_m is the width of the waveguide in the radial direction. They also obtain the fast mode dispersion relation and phase and group velocities along the waveguide (y direction)

$$\omega^2 = v_a^2(k_x^2 + k_y^2 + k_z^2) \tag{5.2}$$

$$v_{ph-y} = \frac{\omega}{k_y} = \frac{k}{k_y} v_a \tag{5.3}$$

$$v_{g-y} = \frac{\partial \omega}{\partial k_y} = \frac{k_y}{k} v_a \tag{5.4}$$

A disturbance in this waveguide can be decomposed according to wave vector. Waveguide modes with $v_{g-y} = v_a$ originating from a disturbance in the center of the waveguide will travel most quickly down the waveguide, traveling a distance y_0 and arriving at point O (Figure 5.3) in time

$$t = t_0 \equiv \frac{y_0}{v_a} \tag{5.5}$$

At later times, waveguide modes at point O will have wave vectors and frequencies determined by

$$k_y^2(y_0, t) = \frac{k_x^2 + k_y^2}{\frac{t^2}{t_0^2} - 1} \tag{5.6}$$

$$\omega^2(y_0, t) = (k_x^2 + k_z^2) v_a^2 (1 + \frac{1}{\frac{t^2}{t_0^2} - 1}) \tag{5.7}$$

In the long time limit, these become

$$k_y \to 0, \omega^2 \to (k_x^2 + k_z^2) v_a^2 \tag{5.8}$$

where the frequency is analogous to the $k_y = 0$ cavity mode; cavity modes need not have $k_y = 0$, but this simple model shows that in the long time limit the flank waveguide solution will be identical to a $k_y = 0$ cavity mode. In other words, dispersion in this simplified flank waveguide is such that in short times after an initial disturbance, waves observed at an arbitrary point down the waveguide will appear like traveling fast mode waves. In the long

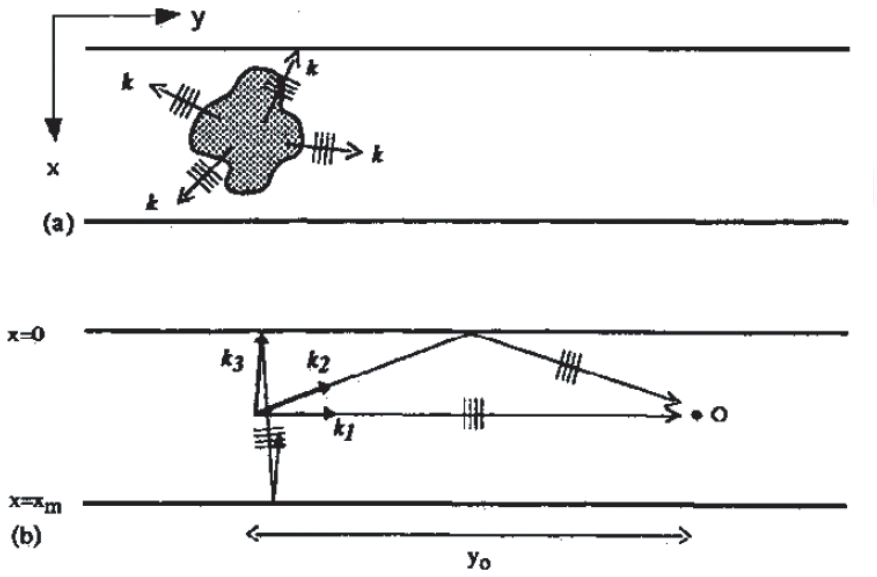

Figure 5.3: A schematic depiction of dispersion in the flank waveguide. An impulse at one end of the waveguide (could be analagous to subsolar point) can be decomposed according to the y component of the wave vector. Perturbations observed at an arbitrary point further down the waveguide would first appear like fast mode waves propagating down the waveguide; at later times, they would appear like radially standing fast mode waves. From *Wright* (1994).

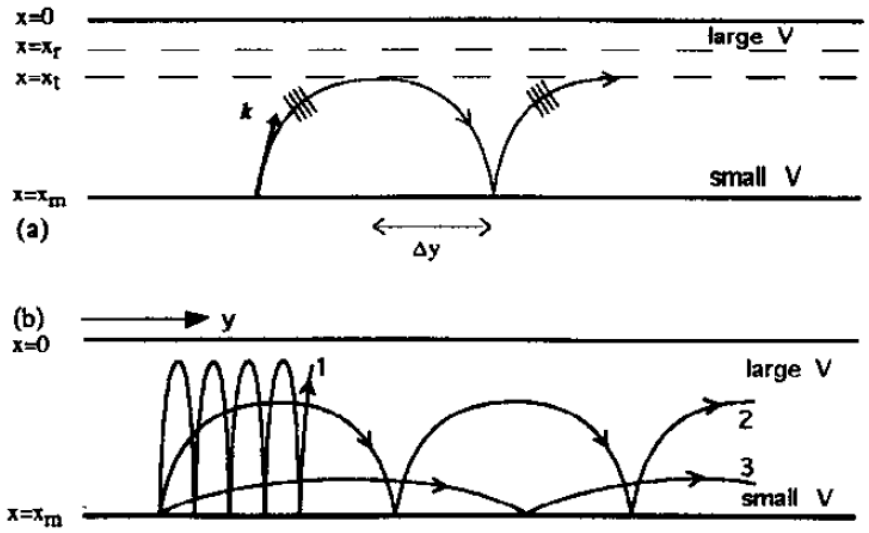

Figure 5.4: On the top, a schematic showing how ray paths are expected to bend in an inhomogeneous waveguide, where the Alfvén speed decreases monotonically with increasing distance from the inner boundary. On the bottom, ray paths for three waveguide modes with different k_y. From *Wright* (1994).

time limit, they will appear more like radially standing fast mode waves, similar to cavity modes. We note here that for both waveguide modes and cavity modes, lower values of k_y lead to more rapidly growing wave activity (*Kivelson and Southwood*, 1985, 1986; *Wright*, 1994). Cavity mode studies in box and cylindrical geometries showed that the peak growth occurred for azimuthal wave numbers of approximately 3 (*Kivelson and Southwood*, 1986; *Allan et al.*, 1986b)

Wright (1994) also examined a more realistic model for the Earth's inhomogeneous magnetosphere by allowing the Alfvén speed to decrease monotonically with distance from the inner boundary. In these cases, ray paths bend as they penetrate into the inner magnetosphere region and are eventually reflected at an inner location that depends, among other things, on the azimuthal wave vector of the waveguide mode. This situation is shown in Figure 5.4; lower k_y modes have reflection points at distances further from the boundary and thus can penetrate deeper into the magnetosphere.

When a more realistic representation of the Earth's magnetosphere than the model of *Wright* (1994) is used, resonant mode coupling may occur between the compressional waveg-

uide mode and shear Alfvén waves via field line resonance. *Wright* (1994) suggested that waveguide modes with $ky \rightarrow 0$ ought to be most important for driving field line resonance for two reasons. One is that ω is nearly independent of k_y for small k_y, allowing for coherent driving of shear Alfvén waves for a range of different driving conditions; in other words, different waveguide frequencies may be excited for different driving conditions, but all drivers should have a range of frequencies in common that correspond to the low k_y limit. Another reason is that the low k_y modes linger at a particular MLT for a longer time due to their propagation direction (and velocity) being more radial than azimuthal, allowing them to drive field line resonances at fixed locations over several wave cycles. They may also be more likely to drive field line resonances at lower radial distances since they penetrate deeper into the inner magnetosphere (see Figure 5.4). Lower k_y cavity modes are also more effective at driving shear Alfvén waves, with the peak coupling occurring with azimuthal wave numbers of 3 (*Kivelson and Southwood*, 1986; *Allan et al.*, 1986b).

Rickard and Wright (1995) modeled waveguide modes excited by a pulse on the magnetopause and showed synthetic satellite data at a variety of points in the waveguide. They noted that the z component of magnetic field perturbations is never smooth and monochromatic, generally exhibits a reduction in period over time, and decays in amplitude with increasing distance from the magnetopause. They concluded that the best place to observe waveguide modes is near the magnetopause, but that even then a satellite will not observe a monochromatic signal. It is thus difficult to unambiguously identify waveguide modes or differentiate them from ambient noise.

To summarize the above discussion, cavity models treat the magnetosphere as a closed system whereas waveguide models treat the magnetosphere as being open. Waveguide modes should generally be more difficult to observe than cavity modes, because they do not exhibit monochromatic signals. However, in the long time limit, waveguide modes with large k_y will exit the magnetotail whereas waveguide modes with small k_y will remain. These small k_y waveguide modes are more effective at driving FLR and are observationally similar to cavity modes. When only the low k_y modes are present, the observed wave activity would exhibit a monochromatic rather than a broadband frequency spectrum. We shall design our event

selection criteria to identify cavity mode signatures, because it is difficult to discriminate the broadband frequency spectrum expected for a superposition of waveguide modes (which have a broad k_y spectrum) from noise. However, these criteria will be effective at identifying waveguide modes with low k_y, which are important to study because of their effectiveness in driving FLR (cavity modes with low k_y are also more effective at driving FLR). We note here that a limitation of this study is the inability to identify waveguide modes with large k_y or a superposition of waveguide modes with both large and small k_y.

5.3.2 Data products used for event selection

For all fast survey intervals greater than 85 minutes where a probe is located at a distance greater than 5 Re and is within the magnetosphere, we require several data products to conduct the tests to identify global modes. First, we obtain EFI, FGM, ESA, and SST data directly from the THEMIS website (http://themis.ssl.berkeley.edu/index.shtml) and apply the latest calibrations and corrections using the software package distributed by the THEMIS science team. We remove any gaps in these data sets and interpolate all data sets to the same time resolution, 3 seconds.

Second, we check the quality of the electric field data in the spin plane using quality control flags described in Appendix B, section B.2. If the data are contaminated, we exclude it from our analysis. We obtain the component along the spin axis using the $E \cdot B = 0$ approximation when the normal of the spin plane is at a large angle to the background magnetic field direction (as in the last chapter).

Third, we high-pass filter (frequency $>$ 2 mHz) the electric and magnetic field data, and we rotate these data into the field-aligned coordinate (FAC) system used in Chapter 4 in which z is along the background magnetic field, y points eastward, and x completes the right-hand orthogonal set pointing radially outward. Having done this, we compute the power spectral density (PSD) of each component of the magnetic and electric field data using a 26 minute Fast Fourier Transform (FFT) window with a $\frac{3}{4}$ overlap between windows; a Hanning window is applied to the data before conducting the FFT. We also compute the

cross phase and coherence between the z component of the perturbation magnetic field and y component of the perturbation electric field. These are the components that are expected to be associated with global modes (*Waters et al.*, 2002).

Fourth, we compute the thermal pressure using ESA and SST ion and electron data and magnetic pressure using FGM data. We compute the ratio of the thermal to the magnetic pressure, β. We also high pass filter the thermal and magnetic pressures, compute the cross phase between them, and compute the total pressure perturbation. We then compute the noise threshold associated with the thermal pressure perturbation as a function of frequency and time using Poisson counting statistics from the original ESA and SST measurements. Finally, we compute the PSD for the thermal, magnetic, and total pressure perturbations.

The final data products used in our automatic selection procedure include the PSD of each FAC component of the electric and magnetic field, the cross phase between the electric field y and magnetic field z component, the coherence between the electric field y and magnetic field z component, β, the cross phase between the thermal and magnetic pressure perturbations, the thermal pressure noise threshold, the thermal pressure PSD, the magnetic pressure PSD, and the total pressure PSD.

5.3.3 Event selection methodology

Global modes, whether they are cavity modes or waveguide modes with low k_y, are observationally similar to radially standing fast mode waves. As such, they ought to have electric field y and magnetic field z components that are 90 degrees out of phase (*Chi and Russell*, 1998; *Waters et al.*, 2002). Furthermore, they ought to have thermal and magnetic pressure perturbations that are in phase (e.g., *Song et al.*, 1994). Finally, if they are being observed at a location remote from a FLR, they ought to have primarily compressional magnetic field perturbations and east-west electric field perturbations (*Waters et al.*, 2002). Our initial, automatic event selection criteria were motivated by these features and designed to select intervals with perturbations consistent with radially standing fast mode waves.

We conduct tests in the frequency domain using the data products described in section

5.3.2. There is a limit to the accuracy of Fourier analysis in capturing the true nature of time variable wave activity in space plasmas (e.g., *Paschmann and Daly*, 2000), but this accuracy can be increased by using multiple FFT windows. To reduce the chances of selecting events which may match our global mode selection criteria due to the uncertainty inherent in the Fourier analysis (e.g., noise with a broadband frequency spectrum), we require our criteria to be met at the same frequency for at least 4 consecutive FFT windows. Despite the window overlap, the first and last of the 4 FFT windows contain practically independent measurements due to the suppression of the signal at the edge of each by application of the Hanning window.

We only consider the 3 to 20 mHz frequency band for this analysis. The lower frequency cutoff at 3 mHz was chosen to exclude ULF wave events which may not be global modes but instead are waves directly driven by the solar wind; we return to this point in section 5.5.3. The upper frequency cutoff was chosen because of the decreasing precision of our 26 minute FFT window in identifying spectral features at higher frequencies. These tests could be repeated at higher frequencies with a smaller window, or with a different signal processing technique such as wavelet analysis (provided care was taken in comparing results obtained at different frequencies), but we leave that as a topic for future work. The 3-20 mHz frequency band is appropriate for this study because several previous observations, simulations, and models of global modes in this region found frequencies falling within or very close to this frequency range (*Lee and Lysak*, 1989; *Claudepierre et al.*, 2009, see Figure 5.1).

To select an event, we require first that the electric field y and magnetic field z perturbations are above the noise thresholds of each instrument and have a coherence greater than or equal to 0.7 for four consecutive FFT windows. We also require that the absolute value of the cross phase between them be greater than 45 or less than 135 degrees. These criteria, when met, suggest the presence of an electromagnetic wave that has a radially standing component (*Chi and Russell*, 1998).

We next determine whether the wave activity is a fast mode using separate tests for the $\beta < 0.5$ and $\beta \geq 0.5$ cases. We used different event selection criteria for intervals with $\beta < 0.5$ and intervals with $\beta \geq 0.5$ because wave modes with compressional magnetic field

perturbations which appear like global modes, such as mirror mode waves, are more likely to occur during intervals with $\beta \geq 0.5$ (*Hasegawa*, 1969). Furthermore, in the $\beta < 0.5$ case, thermal pressure perturbations generated by a fast mode may be below the detection capability of ESA and SST (there should be no fast mode thermal pressure perturbation if $\beta = 0$), requiring additional tests that do not use any information about these pressure perturbations.

5.3.4 High Beta event selection

The relationship between the thermal, magnetic, and total pressure perturbations has been modeled for a variety of different wave modes in the Earth's magnetosphere, including the drift-mirror mode (*Hasegawa*, 1969; *Pokhotelov et al.*, 1985), shear Alfvén (toroidal mode, *Southwood*, 1977), compressional Alfvén (poloidal mode, *Southwood*, 1977), and the drift-compressional Alfvén (*Pokhotelov et al.*, 1985). In all of these cases, the thermal pressure perturbation ought to be out of phase with the magnetic pressure perturbation. In some of these cases, the total pressure perturbation ought to be negligible, whereas in other cases (e.g., drift mirror mode), there may be a total pressure perturbation that is non-negligible but less than the magnetic or thermal pressure perturbation. These relationships have been confirmed through observation (e.g., *Baumjohann et al.*, 1987).

In contrast to these wave modes, the fast mode ought to be associated with significant (exceeding both the magnetic and thermal pressure perturbation) total pressure perturbations and thermal and magnetic perturbations that are in phase (*Song et al.*, 1994). We seek to discriminate fast wave modes from all other wave modes. We determine whether the wave is a fast mode or not at a given frequency and time using two tests. If either test succeeds, we count wave activity at that frequency and time as a fast mode. We recognize that not requiring that events pass both tests is a less strict criteria for event selection; however, we found that too many potential global mode events were removed if we used these strict criteria. Our methodology was thus designed to automatically identify many events, some of which will be culled through additional rounds of testing described in sections 5.4 and 5.5.

The first test is designed to accommodate intervals when there is a thermal pressure perturbation above the noise threshold of the ESA and SST instruments. It is meant to check whether thermal pressure perturbations are in phase with magnetic pressure perturbations, as expected for the fast mode. If the total pressure perturbation is greater than the magnetic pressure perturbation, suggesting that any thermal pressure perturbation must be in phase with the magnetic pressure perturbation, the test is passed. Additionally, if the cross phase between the thermal and magnetic pressure is less than 90 degrees, the test is passed.

These two cases, although seemingly redundant, are meant to account for the limitations of cross-spectral analysis and the instrumentation of THEMIS to avoid missing fast mode events. In particular, the absolute accuracy of the measurement of the thermal pressure perturbation is questionable in some cases (e.g., in the presence of a significant population of cold ions below the detection threshold of ESA), leading to misleading results when making the comparison between the total pressure perturbation, which includes the contribution from thermal pressure, and the magnetic pressure perturbation. Additionally, when a signal is observed close to the noise threshold of the particle detectors on THEMIS, thermal pressure perturbations may not be readily detectable or coherent with magnetic pressure perturbations, leading to misleading results when using the cross-phase spectrum. Our objective in using both parts of this test was to reduce the effect of either limitation in identifying fast mode events.

The second test is designed to accommodate intervals when the thermal pressure perturbation is below the noise threshold of the ESA and SST instruments. In these cases, we first check if the magnetic pressure perturbation is greater than our estimate of the noise inherent in the thermal pressure perturbation measurement; if that is true, a non-fast mode wave such as a compressional Alfvén mode ought to generate a detectable thermal pressure perturbation (*Southwood*, 1977). We compare the total pressure perturbation to the sum of the magnetic pressure perturbation and the thermal pressure noise. If the former is greater than or equal to the latter, we conclude that there was no thermal pressure perturbation present that offset the magnetic pressure perturbation, and the total pressure perturbation was significant (i.e., not due to statistical fluctuations in the thermal pressure perturbation

measurement) and consistent with a fast mode wave event.

In Figure 5.5, we show an example interval where $\beta \geq 0.5$. The electric field data were uncontaminated during the beginning of the interval, as indicated by the ULF electric field quality control flag in the top panel (Appendix B.2). Plasma β is shown in the second panel, and it is above 0.5 for the entire interval. ULF perturbations are seen in both the electric field z (black) and magnetic field y (pink) components in the third panel. The fourth panel shows the cross phase between these two components. The dynamic cross phase spectrum has been masked at frequencies/times where the signal is below the noise threshold of either EFI or FGM, the coherence between the two perturbations is less than or equal to 0.7, and the cross phase between the two perturbations is less than 45 degrees or greater than 135 degrees. It has also been masked during times when the electric field data are contaminated (note the correspondence between large periods of missing data in this panel and the quality control flag in the top panel). This mask would be the same for either the $\beta \geq 0.5$ or $\beta < 0.5$ cases.

A further mask is applied to the data in the fourth panel that removes all frequencies/times that did not pass the fast mode tests, resulting in the data in the fifth panel. One interval is found where there is at least 4 consecutive FFT windows at a constant frequency where data remains unmasked, as indicated by the box. These data have been automatically identified as a global mode, as indicated by the flag in the sixth (bottom) panel. Further demonstration that these data are consistent with the global mode event selection criteria is shown in the smaller time range in the inset. In the top panel, wave activity is shown with the electric field y (pink) and magnetic field z (black) perturbations 90 degrees out of phase. In the bottom panel, the total (black), thermal (green), and magnetic (blue) pressure perturbations are shown. They are all in phase and the total pressure changes, as expected for a fast mode wave.

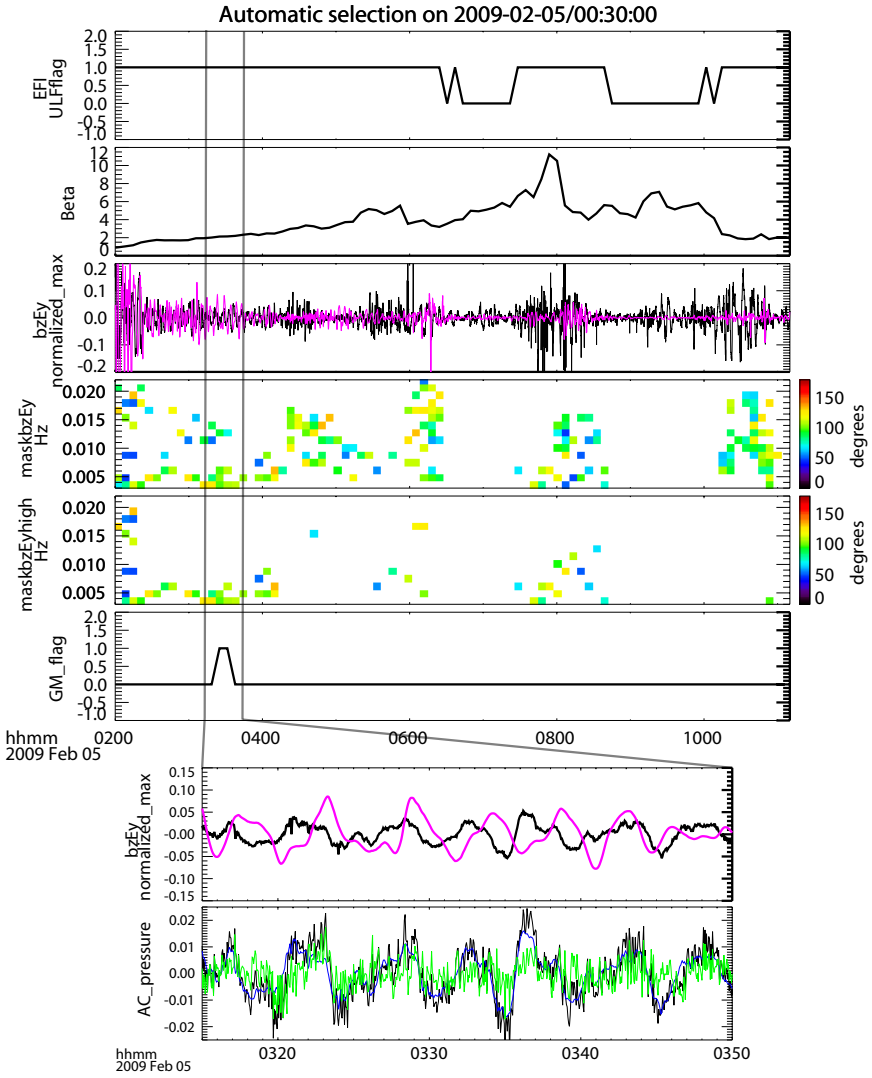

Figure 5.5: From top to bottom, flag for contaminated electric field data (1=uncontaminated,0=contaminated), β, the magnetic field z (black) and electric field y (pink) perturbations normalized to their respective maximum values, the cross phase between these perturbations masked where the signal is below the noise threshold and the perturbations are not coherent (coherence ≤ 0.7) and their cross-phase is not between 45 and 135, the same cross phase but with an additional mask where none of the tests for high beta fast modes are satisfied, and the flag for global modes (1=global mode, 0 otherwise). Black boxes mark frequencies/times where at least 4 consecutive FFT windows met the criteria for automatic selection of global modes. In the inset, the magnetic field z (black) and electric field y (pink) perturbations and the total (black), thermal (green), and magnetic (blue) pressure perturbations for a shorter interval (marked off by black lines).

5.3.5 Low Beta event selection

We found that the automatic fast mode selection criteria outlined in the previous section identified very few global mode events during low β intervals. This was likely due to very low signal to noise ratios for the thermal pressure perturbation measurement caused by the near absence of thermal pressure perturbations in low β fast mode waves. Despite our efforts to account for these effects using two tests described in the previous section, no events can be identified with these tests during intervals when the noise threshold of the thermal pressure perturbation measurement exceeds the magnetic pressure perturbation. Because of this limitation, we developed a test that was independent of the thermal pressure measurement, motivated by previous wave mode identification efforts (*Song et al.*, 1994). We only implemented this test for intervals when $\beta < 0.5$.

In low β plasmas, only the fast mode and Alfvén mode are expected to be present. The Alfvén mode is expected to have primarily transverse magnetic field perturbations near the magnetic equator. This is true for most Alfvén waves that are expected to be driven by the solar wind and through drift-bounce resonance (*Southwood et al.*, 1969; *Southwood*, 1974). To test whether this is true, we compute the ratio of the sum of the x and y component of the magnetic field PSD to the z component. If this number is less than 1 for any FFT window/frequency, we conclude the measurement in that FFT window/frequency is consistent with fast mode wave activity. There are some cases where this test will incorrectly identify compressional Alfvén waves as fast mode waves, due to the fact that Alfvén waves can sometimes be associated with significant magnetic field compressions (e.g., *Southwood*, 1977). These exceptions will be identified using additional tests in section 5.5.

We also use the $\beta \geq 0.5$ tests for $\beta < 0.5$ intervals. If any of the tests are passed, we conclude that the measurement is consistent with fast mode wave activity. If none are passed, we conclude that the measurement is not a fast mode. We re-iterate here that not requiring that events pass all tests is a less strict criteria for event selection. Our motivation for using these less strict criteria was that too many potential global mode events were removed if we required that all tests were passed. We designed our methodology to first automatically

identify many events and subsequently to remove non-global mode events using the additional tests described in sections 5.4 and 5.5.

In Figure 5.6, we show an example interval where $\beta < 0.5$. The electric field data were uncontaminated for the entire interval. Plasma β is shown in the top panel, and it is below 0.5 for the entire interval. ULF perturbations are seen in both the electric field z (black) and magnetic field y (pink) components in the second panel, where each perturbation has been normalized to its respective maximum value. The third panel shows the cross phase between these two components. The dynamic cross phase spectrum has been masked at frequencies/times where the signal is below the noise threshold of either EFI or FGM, the coherence between the two perturbations is less than or equal to 0.7, and the cross phase between the two perturbations is less than 45 degrees or greater than 135 degrees. This mask would be the same for either the $\beta \geq 0.5$ or $\beta < 0.5$ cases.

The next panel shows the result of the fast mode tests for both the $\beta < 0.5$ and the $\beta \geq 0.5$ cases; a mask is applied to the data in the third panel that removes all frequencies/times that did not pass any of the fast mode tests, resulting in the cross phase spectrum in the fourth panel. Two intervals are found where there are at least 4 consecutive FFT windows at a constant frequency where data remains, as indicated by the boxes. These data have been automatically identified as a global mode, as indicated by the flag in the sixth (bottom) panel. To show the effect of the additional test for the $\beta < 0.5$ case, we show another dynamic cross phase spectrum in the fifth panel; a further mask is applied to the data in the third panel that removes all frequencies/times that did not pass any of the fast mode tests for the $\beta \geq 0.5$ case. The test designed for identifying fast mode waves during $\beta < 0.5$ intervals was not conducted. As a result, one of the global mode events was not identified.

Further demonstration that these events are consistent with the global mode event selection criteria is shown in the smaller time range in the inset, which is for the second event. There is clear wave activity and the electric field y (pink) and magnetic field z (black) perturbations appear to be 90 degrees out of phase for much of the interval in the top panel. In the bottom panel, the total (black), thermal (green), and magnetic (blue) pressure perturbations are shown. They are all in phase and the total pressure changes as expected for

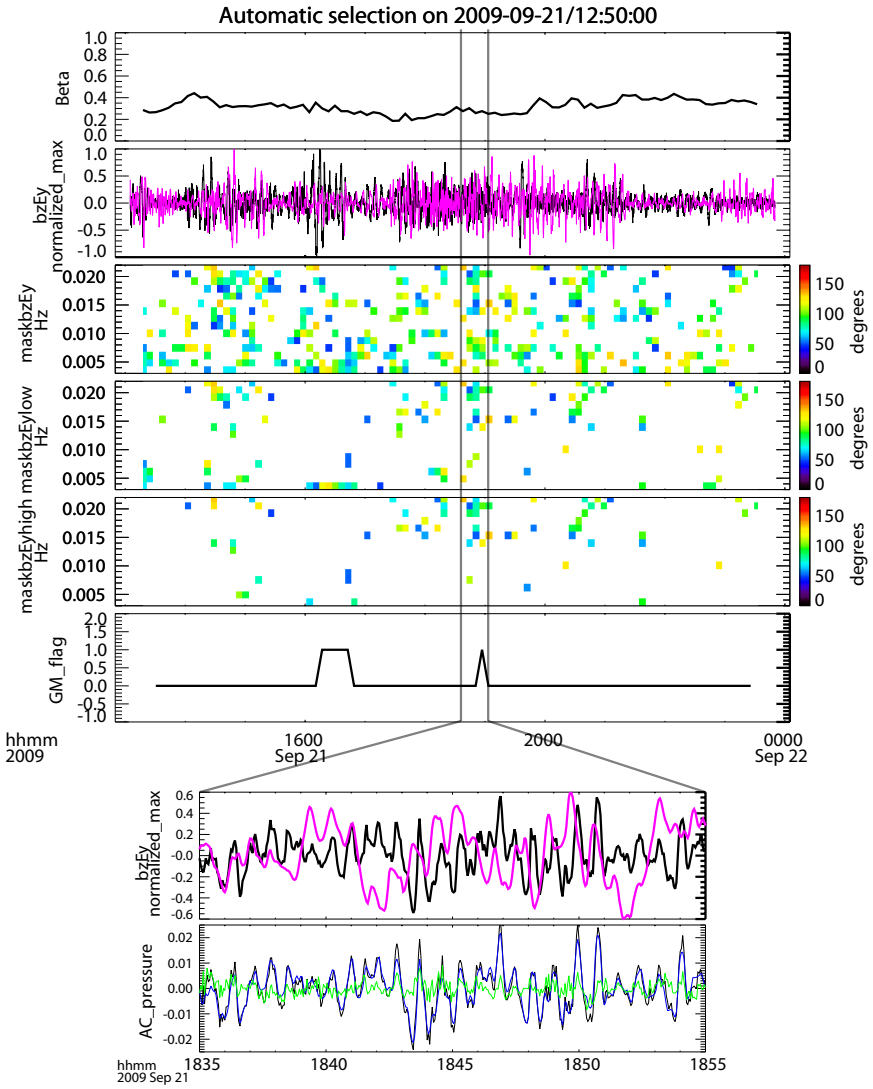

Figure 5.6: From top to bottom, β, the magnetic field z (black) and electric field y (pink) perturbations normalized to their respective maximum values, the cross phase between these perturbations masked where the signal is below the noise threshold and the perturbations are not coherent (coherence ≤ 0.7) and their cross-phase is not between 45 and 135, the same cross phase but with an additional mask where none of the tests for low and high beta fast modes are satisfied, the same as the previous except only tests for high beta fast modes are considered, and the flag for global modes (1=global mode, 0 otherwise). Black boxes mark frequencies/times where at least 4 consecutive FFT windows met the criteria for automatic selection of global modes. In the inset, the magnetic field z (black) and electric field y (pink) perturbations and the total (black), thermal (green), and magnetic (blue) pressure perturbations for a shorter interval (marked off by black lines).

a fast mode wave.

5.3.6 Results of Automatic Selection

Using the automatic global mode selection criteria, we found 524 global mode events; 171 were identified by THA and 353 were identified by THE. Many of these events were not distinct in that there was another global mode event identified using the FFT window before or after the time that the global mode was event was identified.

The location of each event is shown in Figure 5.7A. Most events were identified near pre-noon and noon, consistent with earlier global mode case studies (see Figure 5.1). In Figure 5.7B, only events with $\beta < 0.5$ are shown. In Figure 5.7C, only events with $\beta \geq 0.5$ are shown. Most of the events in the latter category were identified on the night side. The events were likely located in the plasma sheet, where β is expected to be greater than 0.5. We shall explore these data in greater detail, including obtaining occurrence rates, after culling non-global mode events with further tests in the text two sections.

5.4 Data reduction I - Spectral Analysis

Our objective in this section and the next section is to identify and remove events from the automatically selected event list that should not be identified as global modes. In this section we apply tests based on only the electric field y and magnetic field z perturbations. We require events that can unambiguously be identified as global modes, and thus seek to remove events where either the electric or magnetic perturbation exhibits a broadband frequency spectrum. To remove the events with a broadband frequency spectrum, we conducted two tests: an automated examination of the power spectrum computed for each perturbation for each global mode event and a visual inspection of each signal and the associated cross phase, coherence, and power spectral densities.

To conduct either test, we first removed non-unique events from our analysis. We defined a unique global mode event as one that does not occur within 15 minutes of another global

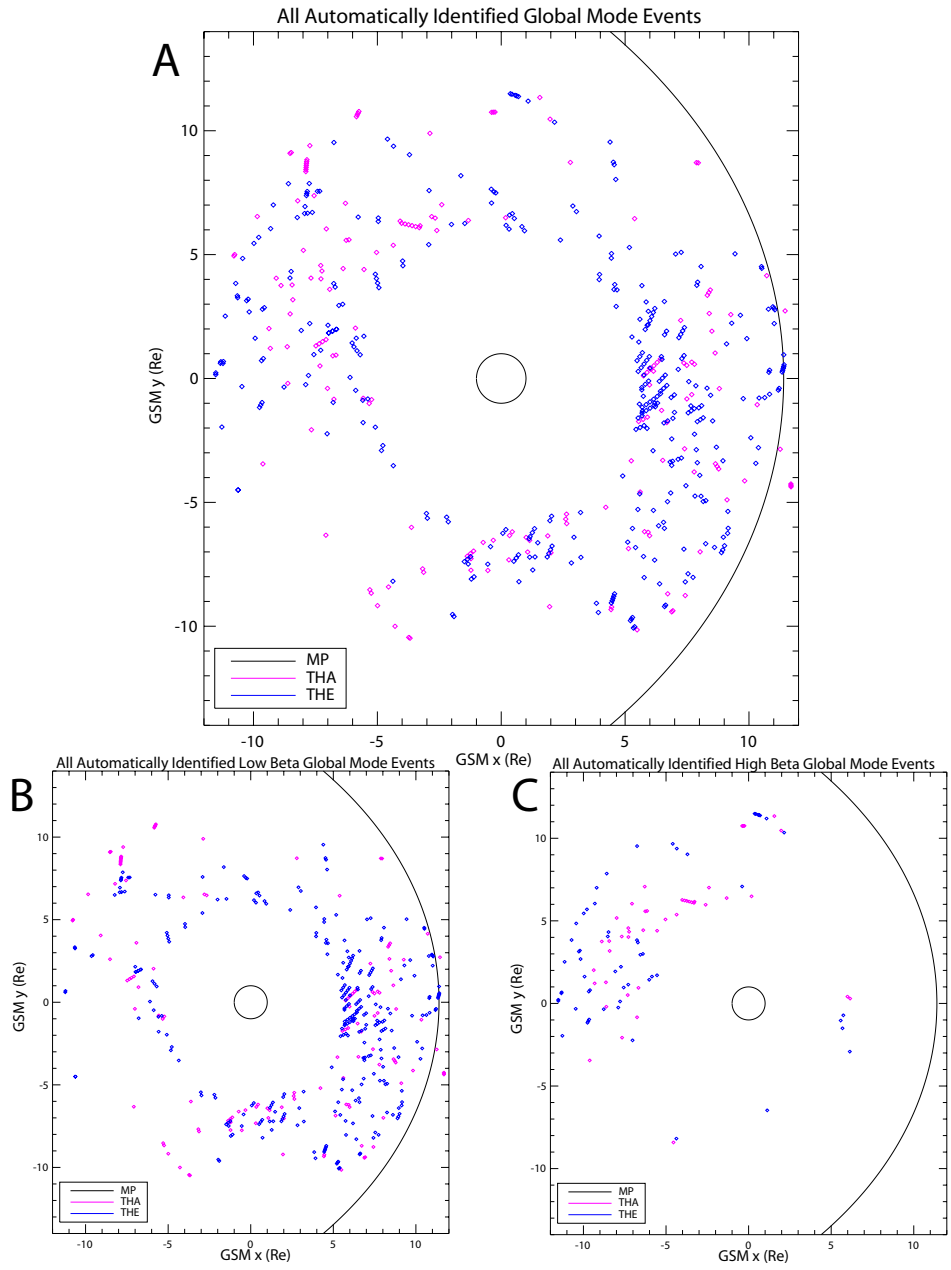

Figure 5.7: A) All global mode events that were automatically selected by THA (pink) or THE (blue). B) All global mode events that were automatically selected by THA or THE when $\beta < 0.5$. C) All global mode events that were automatically selected by THA or THE when $\beta \geq 0.5$.

mode event, and thus must be separated from other events by at least two consecutive FFT windows. For a given unique event which included several non-unique global mode events, we only examined the event that occurred first for the automated test, but we examined the entire duration which included all non-unique events for visual inspection.

5.4.1 Common power spectral density peaks

For each unique event, we analyzed the power spectral density for the magnetic field z and electric field y perturbations obtained during the automatic selection described in section 5.3.2. We searched for distinct power spectral density peaks in both perturbations, which would be expected to be observed for a radially standing fast mode wave. We required that these peaks be located within 1.3 mHz (the precision of our Fourier analysis) of each other and within 1.3 mHz of the frequency of the automatically identified global mode.

To facilitate the automatic identification of power spectral density peaks, we first modeled the original power spectrum using a least squares fit to a power law, and we subtracted this trend from the original spectrum. Next, we compute the first derivative of the power spectral density with respect to frequency using a numerical method (3 point, Lagrangian interpolation). We define a peak as a point where the first derivative is 0; if a point has a derivative that is 0 or positive and is followed by a point with a negative derivative, we identify it as a peak.

An event passes this test for common spectral peaks if peaks are identified for both the electric field y and magnetic field z perturbation, these peaks are within 1.3 mHz of each other, and these peaks are within 1.3 mHz of the frequency of the automatically identified global mode.

5.4.2 Visual Inspection

We visually inspected all unique, automatically identified global mode events to verify that the common spectral peak test removed events that should not be identified as global modes while retaining events that should be identified as global modes. To do this, we inspected

both the original signals and the associated cross phase, coherence, and dynamic power spectral densities. We also inspected the power spectrum used for the common spectral peak test.

Overall, the common spectral peak test tended to remove events that exhibited a broadband frequency spectrum, as expected. However, there were some events that had a broadband frequency spectrum which passed the test because the spectrum was spiky and distinct peaks were mistakenly identified. We removed such events from our analysis during the visual inspection. There were also some events that did not pass the test because the time chosen for analysis did not include a clear, monochromatic signal for either the electric or magnetic field perturbation; however, a later or earlier time would have included such monochromatic signals. We made this determination by inspecting the original signals, power spectral densities, and coherence and cross phase spectra. In these cases, we selected a different time and repeated the automatic test; if the test was passed we retained the event for subsequent analysis. Finally, there were a few events where the original frequency identified as a global mode was not the frequency that corresponded to the largest power spectral density or the most monochromatic signal. In these cases, we selected an appropriate frequency for the global mode and repeated the test; if the test was passed we retained the event for subsequent analysis. When selecting either a different frequency or time for the event, we also verified that the new frequency/time satisfied the global mode criteria used for automatic selection.

In Figure 5.8, we show results from the common spectral peak test for the second automatically identified event from Figure 5.6. The magnetic field z (black) and electric field y (pink) perturbations are shown in Figure 5.8A. After visually inspecting this event in the manner described above, we determined that the FFT window at 18:47 had the clearest, most monochromatic wave activity in both the electric and magnetic field perturbations. We show the PSD (background trend subtracted) at this time for both components in Figure 5.8B. They share a common spectral peak with each other and with the frequency that we identified as having characteristics associated with global modes at 19 mHz, as indicated by the green line. They also share a common peak at 4 mHz, but wave activity at this

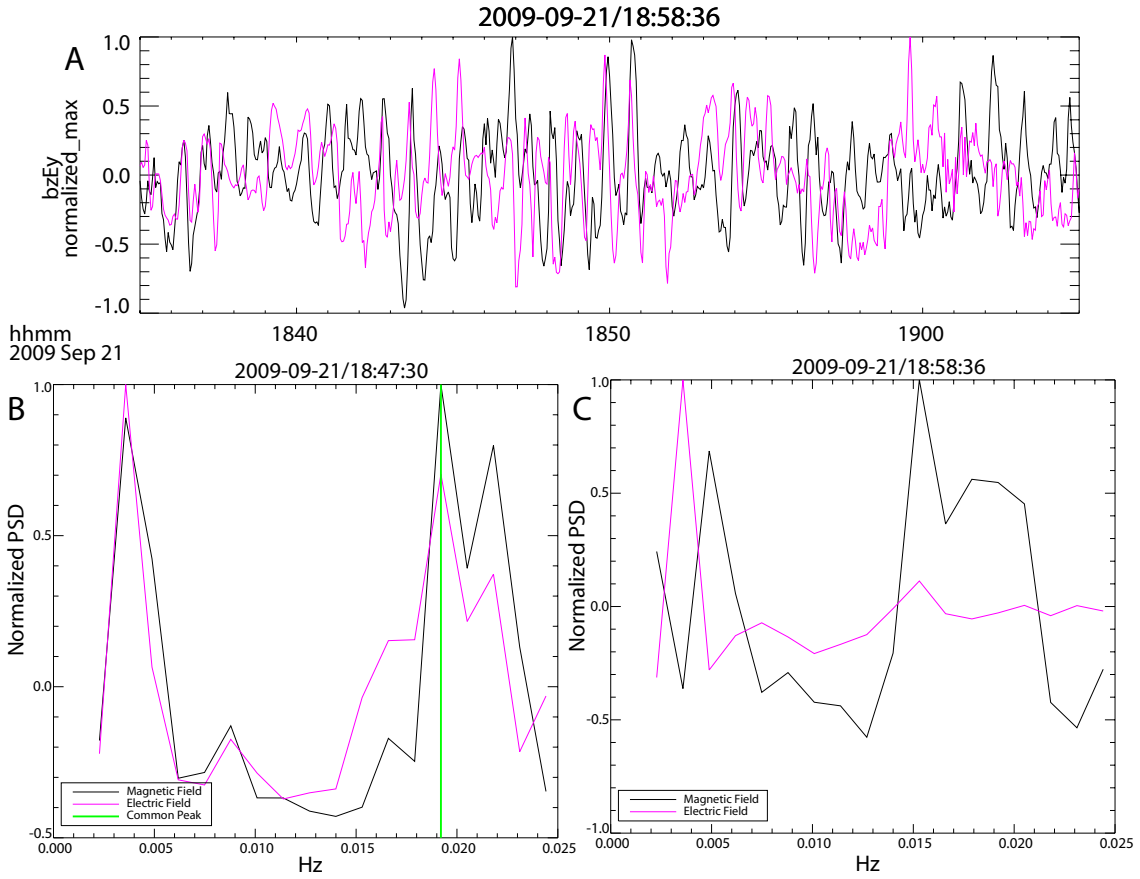

Figure 5.8: A) Magnetic field z (black) and electric field y (pink) perturbations observed during the second automatically identified global mode event in Figure 5.6. B) The power spectral density with background trend (power law) removed for the magnetic field z (black) and electric field y (pink) perturbations at 18:47:30 UT, a time chosen with visual inspection. A green line indicates a frequency with a common spectral peak. Clear peaks at 4 mHz were not chosen as common spectral peaks because wave activity at this frequency did not meet the global mode selection criteria. C) The power spectral density with background trend (power law) removed for the magnetic field z (black) and electric field y (pink) perturbations for the FFT window at 18:58:36 UT, the original, automatically chosen time.

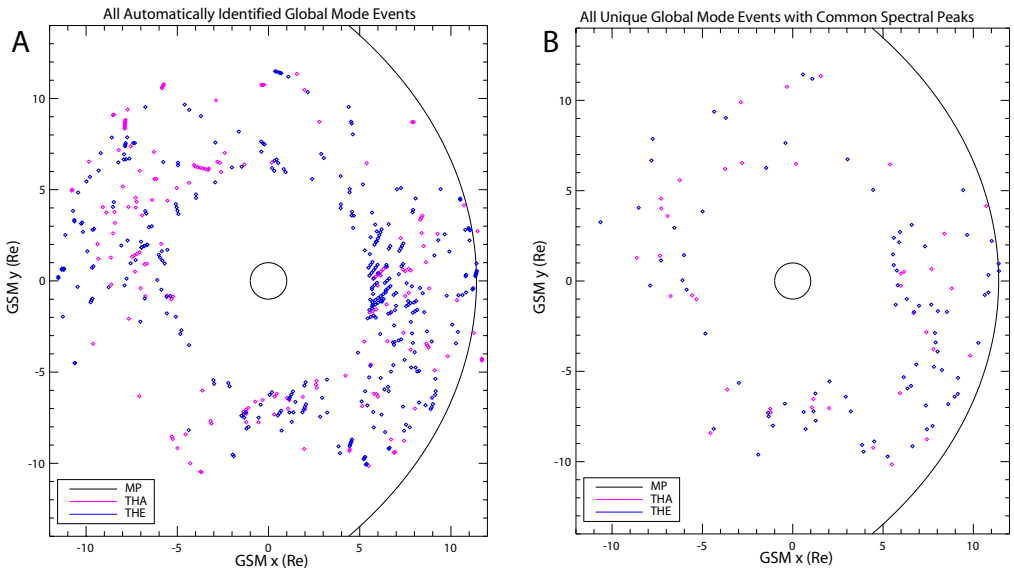

Figure 5.9: A) All global mode events that were automatically selected by THA or THE (reproduced from Figure 5.7A for reference). B) All unique global mode events with common spectral peaks.

frequency does not satisfy our global mode criteria and thus it does not pass the common spectral peak test. Finally, In Figure 5.8C, we show the same data as Figure 5.8B, but for an FFT window at the original, automatically selected time of 18:58 UT. The wave activity was not as clear at this time, and the spectra do not pass the common spectral peak test. This highlights the importance of the process of visual inspection to avoid removing events that have features that are consistent with global modes, but that are not necessarily clearly identifiable as monochromatic electric and magnetic field perturbations for the entire automatically selected interval (which could include many non-unique, automatically identified events).

During the process of visual inspection, we manually selected appropriate time ranges for each unique event, which could include several automatically identified global mode events. We will use these time ranges and the frequency associated with each global mode for the tests in the next section.

At the end of this visual inspection and automatic comparison between power spectral density peaks, we had identified a subset of 119 unique events that passed the common spectral peak test out of 524 automatically selected events (including non-unique events).

Thirty-eight were identified by THA and 81 were identified by THE. The global distribution of events is shown in Figure 5.9. Figure 5.9A is identical to Figure 5.7A and shows all automatically selected events (unique and non-unique) for reference. Figure 5.9B shows only unique events that passed the common spectral peaks test.

5.5 Data reduction II - Further tests

The purpose of this section is to examine the 119 events identified in the previous section in greater detail. All of these events share the common features: phase differences between the electric field y and magnetic field z perturbations that are close to 90 degrees, coherence between these perturbations that is greater than 0.7, a signal above the noise threshold of both EFI and FGM, and electric and magnetic field perturbations with a common peak in power spectral density (indicating a monochromatic wave).

In Chapter 4, sections 4.1.3 and 4.5, we discussed sources of wave activity that were not global modes that shared some of the observational signatures of global modes. Briefly, these included waves driven by resonant interactions with ring current ions, waves driven by the drift-mirror instability, waves directly driven by monochromatic solar wind dynamic pressure fluctuations, and magnetopause surface waves. In this section, we discuss several tests which can be used to further discriminate global mode events from these other sources of ULF wave activity.

5.5.1 Phase between thermal and magnetic pressure perturbation

We expect fast mode waves to generate perturbations in the total pressure, whereas Alfvén waves and mirror mode waves should not. In a homogeneous medium, shear Alfvén waves do not generate a perturbation in the total pressure, magnetic pressure, or thermal pressure. In the inhomogeneous magnetosphere, they may generate a perturbation in the magnetic pressure and thermal pressure, but not in the total pressure (*Southwood*, 1977; *Denton and Vetoulis*, 1998; *Denton et al.*, 2003). Previous studies have attempted to discriminate between fast mode waves and these other wave sources using the phase difference between

the thermal pressure perturbation and magnetic pressure perturbation (*Song et al.*, 1994). We have already used this technique in the automatic selection of global mode events, and we required that events that occurred during intervals where $\beta \geq 0.5$ meet the expected criteria for fast mode waves. However, we used less strict criteria for events where $\beta < 0.5$, and we did not necessarily require that the thermal and magnetic pressure perturbations be in phase, or that there was a significant total pressure perturbation. Here, we conduct a similar test for all events using the more precisely determined frequencies and times from section 5.4.2. Our objective is to remove events that occurred during intervals with $\beta < 0.5$ that may not be fast mode wave events.

Using the frequencies and times for global mode events selected in section 5.4.1 and the cross phase between the magnetic and thermal pressure perturbation, we calculated the mean of the absolute value of the phase difference between these perturbations. If the mean phase difference was less than 90 degrees, we concluded that the wave activity was a fast mode, consistent with a global mode. If the mean phase difference was greater than or equal to 90 degrees, we concluded that it was not a fast wave mode. If the thermal pressure perturbation was below the noise threshold or the thermal and magnetic pressure perturbations were not coherent (coherence < 0.7), we did not conduct the test.

In Figure 5.10A, we show an example of an event that passed the fast mode, or phase difference, test during a period when $\beta < 0.5$. In this case, the thermal pressure perturbation (green) was small but above the noise threshold. The magnetic pressure perturbation (blue) was in phase with the thermal pressure, causing a total pressure (black) perturbation that was larger in amplitude than either the thermal or magnetic pressure perturbations. In Figure 5.10B, we show another event that occurred during a $\beta < 0.5$ interval; however, this event failed the test, since the thermal pressure perturbation was not in phase with the magnetic pressure perturbation. This event was previously reported by *Takahashi et al.* (2011), and it is a poloidal mode standing Alfvén wave that was likely driven by wave-particle interactions with ring current ions. This type of ULF wave shares many observational features with global modes when observed near the magnetic equatorial plane by a single spacecraft. For this reason, the fast mode test was critical for removing such events during $\beta < 0.5$ intervals

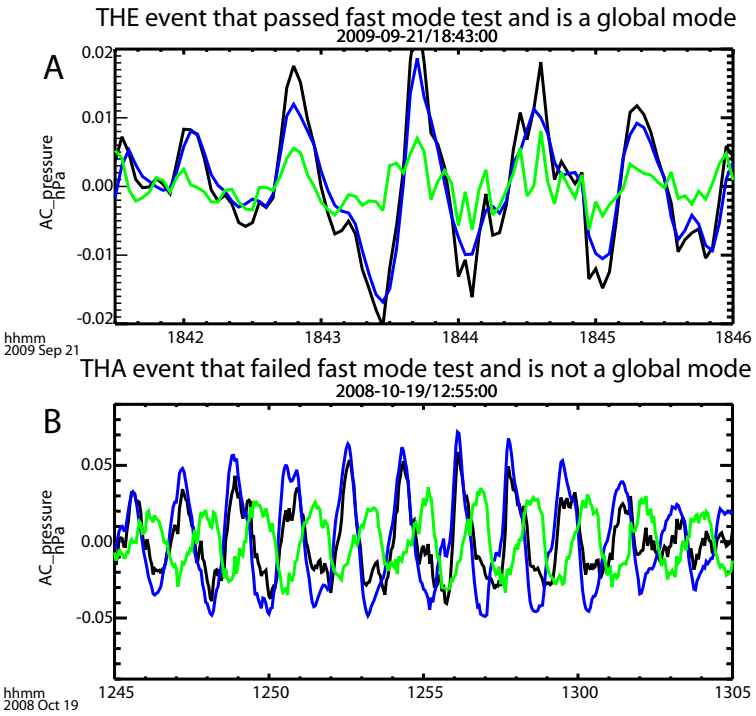

Figure 5.10: A) An event that passed the fast mode test; the small thermal pressure perturbation (green) is in phase with the magnetic pressure perturbation (blue), leading to a larger overall total pressure perturbation (black). B) An event that did not pass the fast mode test; the thermal pressure perturbation (green) is not in phase with the magnetic pressure perturbation (blue), leading to a smaller overall total pressure perturbation (black).

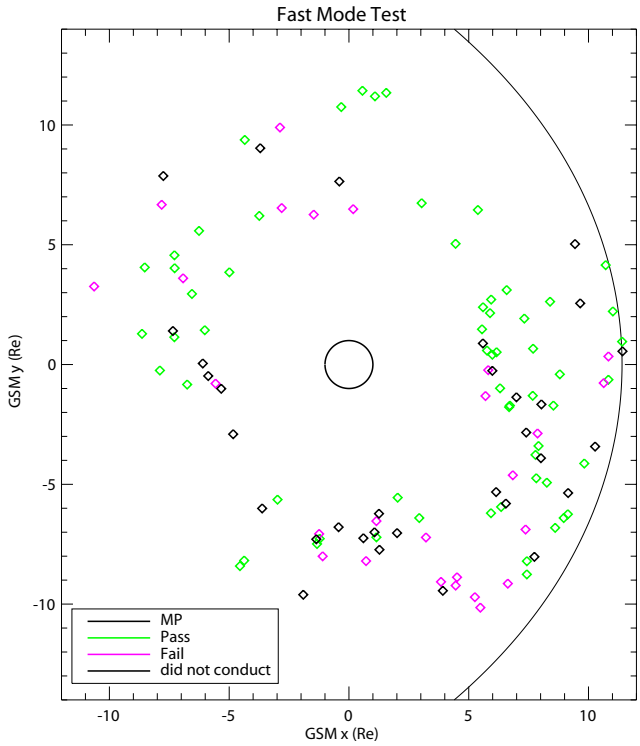

Figure 5.11: The same events as in Figure 5.9B color coded according to whether they passed the fast mode test (green) or failed the test (pink). Black points are events where the test could not be conducted

(they would automatically be removed using the more strict selection criteria of $\beta \geq 0.5$ intervals, see section 5.3.4).

The results of all fast mode tests are shown in Figure 5.11, where events are color coded green if they passed the test, pink if they did not pass the test, and black if the test could not be conducted. There were 32 events where the test could not be conducted, 61 where the event was identified as a fast mode (passed the test), and 26 events that were not identified as a fast mode.

5.5.2 Signal coherence for spatially separated probes

We expect global modes to exhibit coherent wave activity over large spatial scales (*Waters et al.*, 2002). Unlike standing Alfvén waves, which have radial spatial extents of roughly 0.5 Re when energy is provided by a monochromatic driver (*Mann*, 1997; *Yeoman et al.*, 1997) and exhibit a continuum of frequencies as radial distance changes (*Anderson et al.*, 1989),

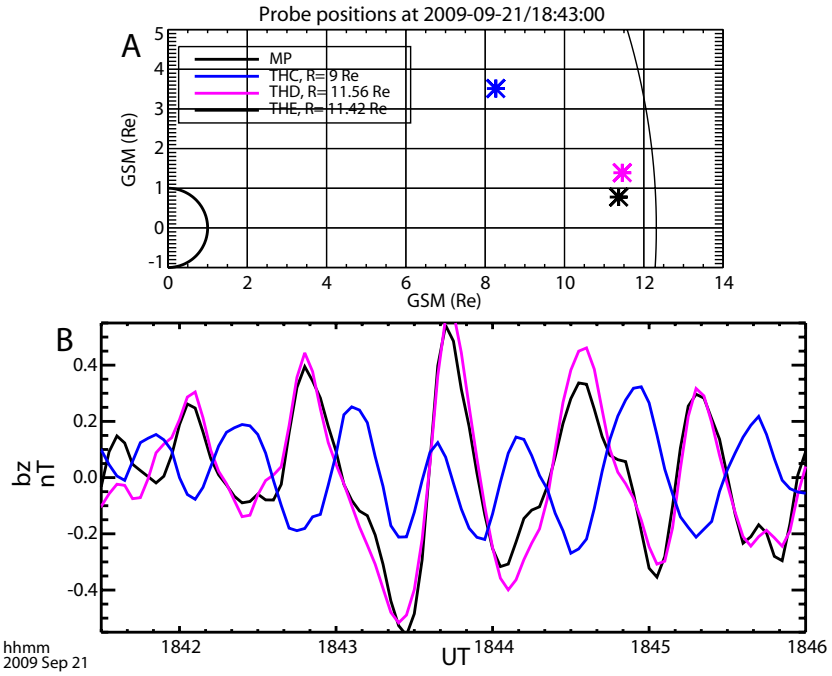

Figure 5.12: The same event as in Figure 5.10A. A) Positions of the THEMIS spacecraft in the GSM xy plane. B) Magnetic field z perturbation observed at each spacecraft.

global modes ought to have coherent signals at the same frequency over several Re in radial distance. Thus, a test that examines the coherence between signals observed at spatially separated spacecraft could be used to identify global modes (*Anderson and Engebretson*, 1995).

For each unique global mode event identified in section 5.4.1, we determined if at least one of the other four THEMIS probes was located at a radial distance greater than 1 Re from the observing probe and within the magnetosphere. We computed the coherence between the magnetic field z perturbations observed by each spatially separated pair of probes. If any of them had a coherence greater than 0.7, we consider the signal to be globally coherent, consistent with a global mode.

An example of one event that passed this test is shown in Figure 5.12; this is the same event presented in Figure 5.10A. There are three THEMIS probes in the noon local time sector, as indicated in Figure 5.12A, which shows their positions in the GSM xy plane. THD (blue) and THE (black) are very close to together and observe nearly the same magnetic field z perturbation, as shown in Figure 5.12B. These signals have a coherence close to 1, but this

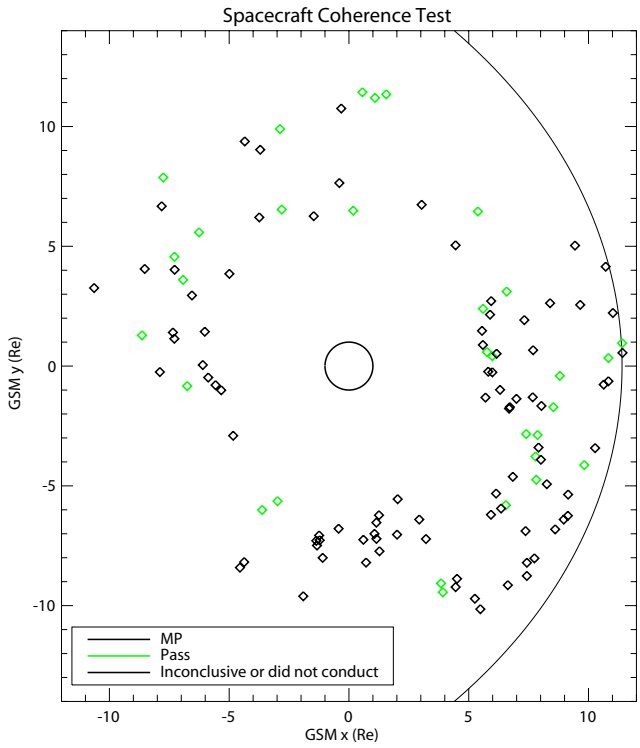

Figure 5.13: The same events as in Figure 5.9B color coded green if they passed the spacecraft coherence test or black if the test was inconclusive or could not be conducted.

evidence does not meet the criteria of the test, as the spacecraft are less than one Re apart in radial distance. THC (pink) is located at a distance greater than 1 Re from THE, and it observes a very similar signal to THD and THE, with the exception of a higher frequency component not evident at THD and THE. The coherence between the signals observed by THE and THC is well above 0.7 in the frequency band and time span of the global mode event, so this event passes the test.

In Figure 5.13 we show the global distribution of unique global mode events color coded green if they passed the spacecraft coherence test and black if the test was inconclusive or could not be conducted. There were 31 events where spatially separated ($>$ 1 Re) spacecraft observed coherent b_z signals, 15 events where spatially separated spacecraft did not observe coherent signals (although in some cases they were very widely separated, by as much as approximately 10 Re, and may not have been within the cavity/waveguide supporting the global mode), and 73 events where there was no spacecraft with data available at a distance $>$ 1 Re (within the magnetosphere) to conduct the test.

There are several caveats when applying these tests; most importantly, it is possible for spatially separated probes to be within the extent of a global mode, yet not observe coherent signals because one probe is located at a node of the radial standing wave structure. Thus we did not use this test to exclude events from our database.

5.5.3 Spectral peaks in common with solar wind

We chose to examine wave activity with frequencies above 3 mHz in the present study partly because these frequencies are higher than what is typically expected for direct driving of magnetospheric ULF waves by solar wind fluctuations. The magnetosphere is not expected to respond to the solar wind quasi-statically at these frequencies (e.g., *Kepko and Spence*, 2003). There is some observational evidence, however, that the solar wind can directly drive ULF waves in the magnetosphere with frequencies as high as 5 mHz (*Viall et al.*, 2009). Since this falls within the range of frequencies examined in this the study, we conducted a test to estimate how many global mode events in the frequency range between 3 and 5 mHz could be directly driven.

There were 14 events where THA and THE identified a global mode with a frequency between 3 and 5 mHz while another THEMIS probe (either THB or THC) was located in the pristine solar wind (i.e., not in the ion foreshock, magnetosheath, or magnetosphere). We performed a 52 minute FFT on the solar wind density, solar wind dynamic pressure, and the b_z perturbation associated with the magnetospheric global mode. Unlike *Viall et al.* (2009), we did not correct for time delays or errors that could arise due to spatial structures in the solar wind. These effects were negligible since the THEMIS solar wind monitors were located close to the Earth in all cases; significantly closer than the WIND spacecraft used in *Viall et al.* (2009). Time delays due to the propagation of the solar wind from THEMIS spacecraft to the subsolar point were typically less than 1 minute, which is very small compared to the size of the 52 minute FFT window we use for these comparisons.

We performed a least squares fit to a power law function for each power spectrum, and then subtracted this power law from the original spectrum to more clearly identify

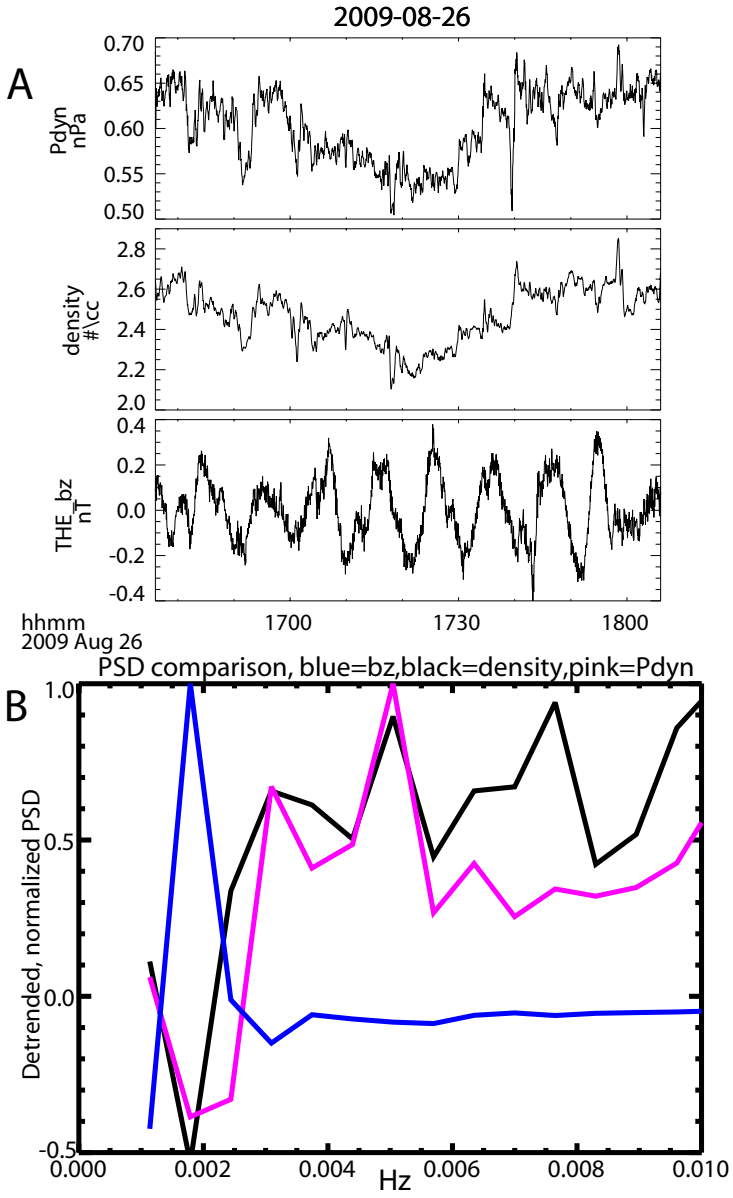

Figure 5.14: A) From top to bottom, solar wind dynamic pressure and density measured by THC and the magnetic field z perturbation measured by THE in the magnetosphere. B) A comparison between the power spectral densities, which have been detrended and normalized to their respective maximum values. Blue is for the magnetic field z perturbation measured by THE, pink is for the solar wind dynamic pressure measured by THC, and black is for the solar wind density measured by THC.

peaks. Finally, we determined whether the event was directly driven by comparing the power spectra of the three signals. If either the solar wind dynamic pressure or density had a common spectral peak with the magnetic perturbation (peaks within 1.3 mHz of each other as determined by visual inspection, same as in section 5.4), we identified that event as directly driven.

Figure 5.14 shows the results of one test. In Figure 5.14A, the top panel is for the solar wind dynamic pressure and density as measured by THC, which is approximately 15 Re upstream of the subsolar point during this event. There does not appear to be any monochromatic wave activity. In contrast, the bottom panel of Figure 5.14A shows monochromatic magnetic field z perturbations observed by THE, which is located in the magnetosphere and close to the subsolar point, near noon. The power spectral density comparison between these three signals is shown in Figure 5.14B, where the power law has been subtracted and the PSD has been normalized to the respective maximum values for comparison. The solar wind signals have a broadband frequency spectrum, whereas the magnetospheric signal has a sharp peak near 2 mHz; thus, we conclude that this signal was not directly driven by the solar wind. We note that this 2 mHz signal was one of only 3 events in our database with a frequency below our chosen lowest frequency of 3 mHz; the original frequency recorded during the automatic selection was indeed above 3 mHz, but it was lowered to 2 mHz during the process of visual inspection (see section 5.4.2).

We found 3 cases out of 12 (or 25% of cases) where there was a peak in power spectral density in both the b_z perturbation and either the solar wind dynamic pressure or density fluctuations. The results of all the tests are shown in Figure 5.15, where global mode events are color coded green if no common peak was found, pink if a common peak was found, and black if the test was not conducted. All three events that were directly driven (that failed the test), were located on the dayside, as expected for directly driven waves (*Takahashi and Ukhorskiy*, 2007; *Viall et al.*, 2009).

When doing a similar type of comparison, *Viall et al.* (2009) found that 54% of events with ULF wave activity with frequency between 0.5 and 5 mHz in the magnetosphere were concurrent with a peak at the same frequency in the solar wind. Our results are not in

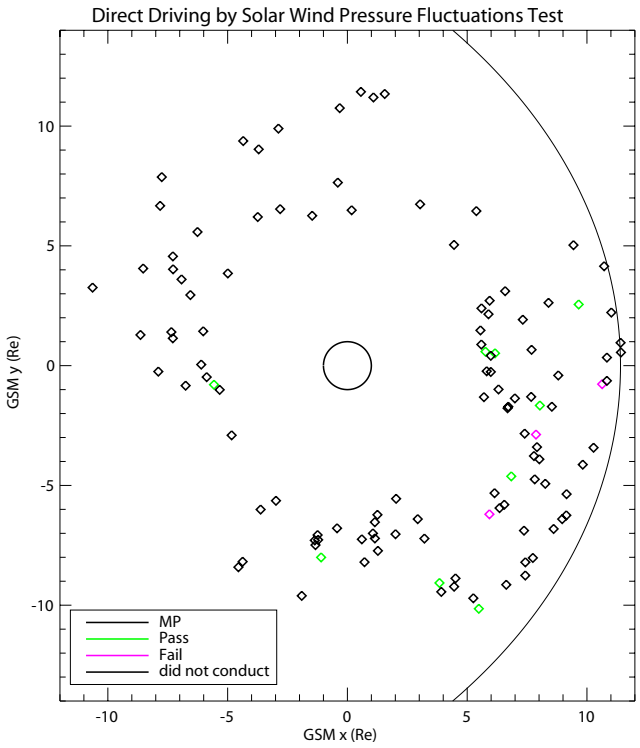

Figure 5.15: The same events as in Figure 5.9B color coded according to whether they passed the solar wind direct driving test (green - likely were not directly driven) or failed the test (pink - likely were directly driven). Black points are events where the test was not be conducted

variance with *Viall et al.* (2009) for three reasons. *Viall et al.* (2009) restricted their analysis to the dayside magnetosphere where clear cases of directly driven waves should be most prevalent, whereas our study covers all local time sectors where the occurrence rate of clearly identifiable directly driven waves could be lower. A second reason is that the number reported by *Viall et al.* (2009), 54%, includes comparisons between all frequencies in the range between 0.5 and 5 mHz. The solar wind may be less effective at directly driving ULF waves at frequencies above 3 mHz when compared to the range between 0.5 mHz and 3 mHz; thus, the occurrence rate for directly driven waves may be lower than 54% at frequencies above 3 mHz, consistent with our result, and higher at frequencies below 3 mHz. Finally, we note that the events that were compared to the solar wind fluctuations all satisfied the global mode automatic selection criteria (section 5.3) and were thus a small subset of all ULF wave events; it is not immediately clear how this source of bias may affect our estimate of the occurrence rate of directly driven waves, but it may be possible that directly driven waves are less likely to satisfy these criteria.

We note that our sample size is limited and our estimate of the occurrence rate of directly driven waves in our ensemble of global mode events may change if more events between 3 and 5 mHz with a solar wind monitor were identified. However, even if our estimate of the occurrence rate of directly driven waves were significantly increased, it would not affect the main results of this study. There are only a few other events (36) with wave frequencies less than 5 mHz. With the present occurrence rate of directly driven waves, 9 additional events would be directly driven, a small fraction of the total number of events. If our estimate of the occurrence rate were changed significantly and doubled to be consistent with *Viall et al.* (2009), there would be 18-19 additional directly driven events, which is still a small fraction of the total number of events (119).

5.5.4 Frequency vs. latitude on ground

One of the original motivations for the development of global mode theory was the ground observation of monochromatic signals with the same frequency at a wide range of magnetic

latitudes corresponding to a wide range of radial distances in the magnetosphere (*Samson and Rostoker*, 1972). This was unexpected, since different radial distances have different characteristic standing Alfvén wave frequencies; a constant frequency at a wide range of latitudes suggests that some mechanism, such as global modes, imposes a frequency selection. The examination of data from a latitudinal chain of ground magnetometers is thus a natural way to test for the presence of global modes.

Global modes generate standing Alfvén waves via FLR that may be detected using ground magnetometers at one or more locations (*Zhu and Kivelson*, 1989; *Mathie and Mann*, 2000). It is also possible for them to generate a signal on the ground at a location remote from any FLR; however, it will be weaker (*Kivelson and Southwood*, 1988; *Lee*, 1996). In contrast to global modes, other sources of ULF wave activity, such as standing Alfvén waves, are not expected to exhibit monochromatic signals with constant frequency over a wide range of latitudes. For example, *Takahashi et al.* (2011) reported a giant pulsation event that was a fundamental poloidal mode driven by interactions with ring current ions; this pulsation, like other giant pulsations, was only observed at a narrow range of latitudes. Toroidal mode standing Alfvén waves driven by monochromatic surface waves also do not typically extend over a wide range of latitudes (e.g., *Hartinger et al.*, 2011). Toroidal mode Alfvén waves directly driven by a source of energy with a broadband frequency spectrum can extend over a wide range of latitudes but have different frequencies at different latitudes (*Samson and Rostoker*, 1972).

We conducted tests using ground magnetometers located in Canada and Alaska. The locations of these stations are shown in Figure 5.16. Before conducting this test, we determined whether the magnetic local time of the THEMIS probe observing the global mode fell within the range of the local time of eastern Canada and western Alaska. We then computed the coherence between the spacecraft magnetic field z perturbation and the east-west component of the magnetic field perturbation observed by all ground stations. Finally, we calculated the mean coherence at the frequency and time corresponding to the global mode observation. If stations that were separated by more than 5 degrees in magnetic latitude and less than 20 degrees in longitude each had signals that were coherent with the signal

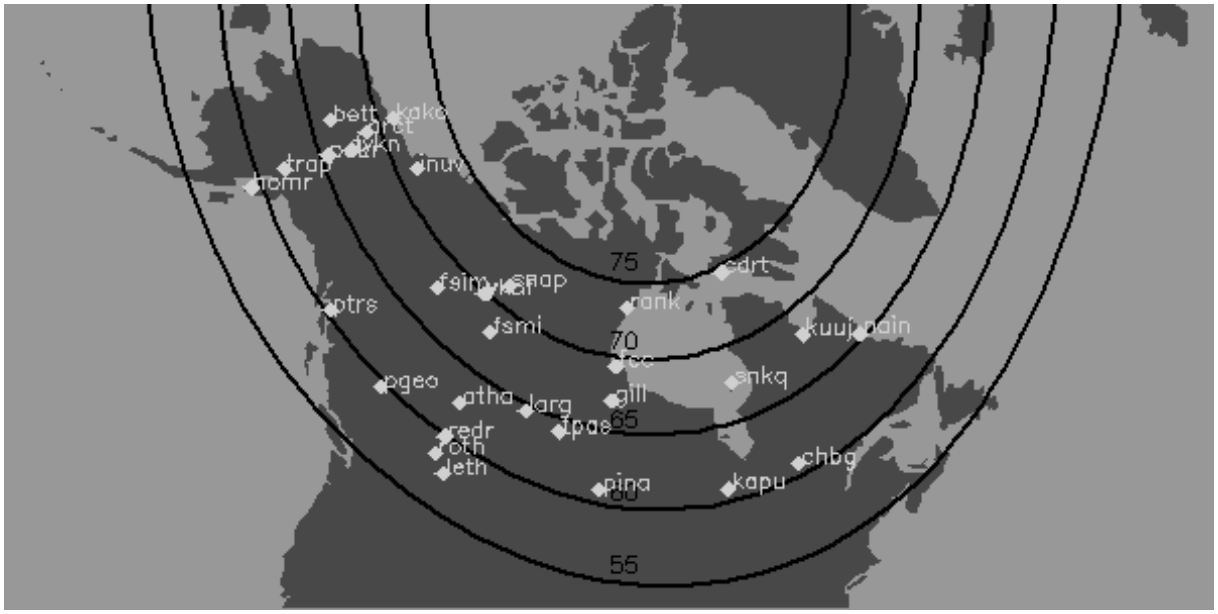

Figure 5.16: The locations of ground magnetometer stations used in this study. Lines of constant magnetic latitude are shown for reference.

observed at THEMIS (coherence > 0.7 at the global mode frequency), the event passed the test.

We show an example event that passed the ground magnetometer coherence test in Figure 5.17. From top to bottom, the magnetic field z perturbation from THA and the east-west magnetic field perturbations from the FSMI, ATHA, REDR. and LETH ground magnetometer stations are shown. These stations are in a latitudinal chain and are only separated by a few degrees in longitude. They have magnetic latitudes that range from 57 degrees to 67 degrees, or, equivalently, the dipole magnetic field lines that intersect the stations cross the equatorial plane at distances that range from 3.5 to 7 Re. A signal is evident at all 4 stations with very nearly the same frequency as the signal at THA; vertical black lines are shown for a few wave cycles to enable comparison between the phase of the signal at THA and at the stations. There are some phase differences that likely arise due to additional wave activity that is unrelated to the global mode and unique to each stations location; however, these small shifts are far too small to account for the frequency shift that would be expected between 57 and 67 degrees in magnetic latitude if a continuum of Alfvén waves were being observed, which ought to be on the order of 10 mHz (*Lee and Lysak*, 1989).

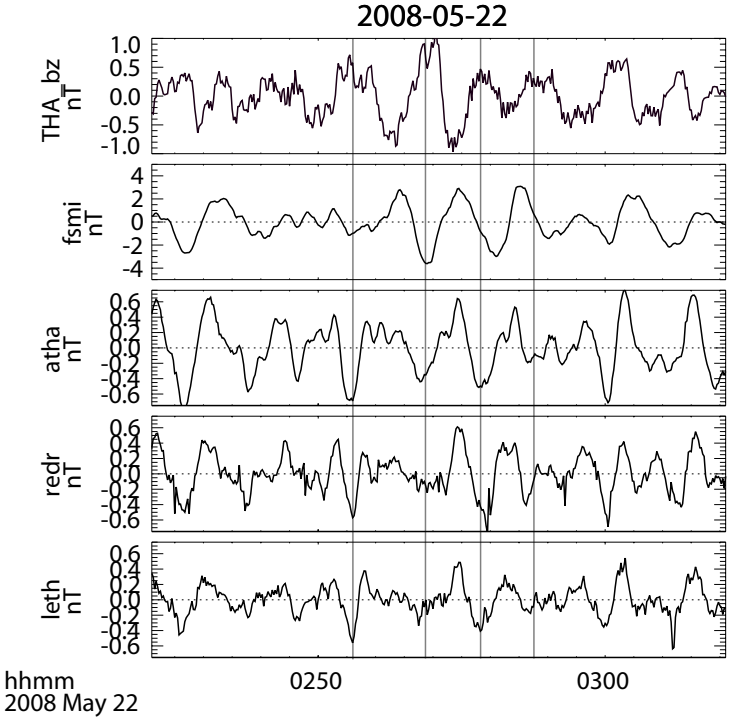

Figure 5.17: An example event passed the ground magnetometer coherence test. From top to bottom, the magnetic field z perturbation from THA and the east-west magnetic field perturbations from the FSMI, ATHA, REDR. and LETH ground magnetometer stations.

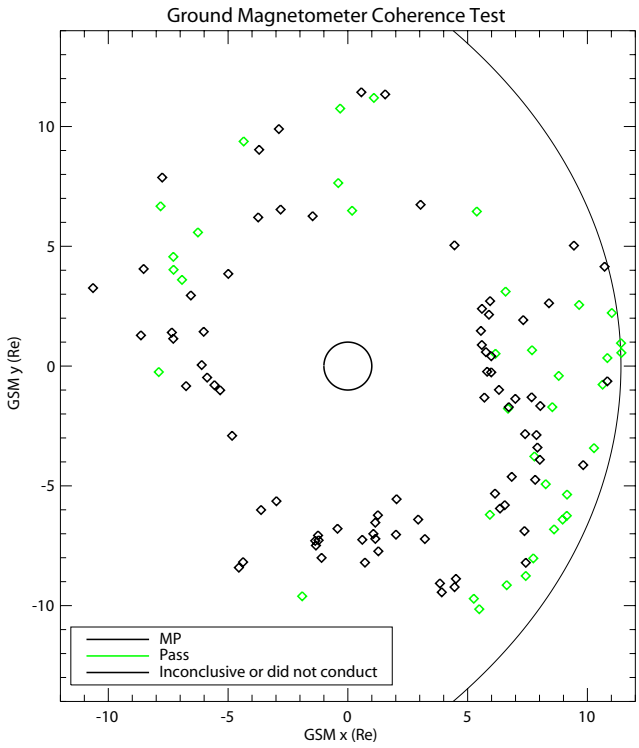

Figure 5.18: The same events as in Figure 5.9B color coded green if they passed the ground magnetometer coherence test or black if the test was inconclusive or could not be conducted.

The signals from all of the stations shown exceeded the coherence threshold with the THA signal (> 0.7 at the global mode frequency), so the test was passed.

In Figure 5.18 we show the distribution of unique global mode events color coded green if they passed the ground magnetometer coherence test and black if the test was inconclusive or could not be conducted. There were 38 events where magnetometers in North America with a separation in magnetic latitude of at least 5 degrees and a separation in longitude of less than 20 degrees observed coherent signals (east-west magnetic field perturbations). There were 50 total events where North America was conjugate to the global mode observation; thus, ground observations, when available, confirmed the in situ global mode observation 76% of the time. There were 81 events that did not pass the ground magnetometer test; 12 events because the signals and station locations did not meet the criteria for the test and 69 events because North America was not conjugate to the spacecraft location (i.e., the test could not be conducted).

5.5.5 Summary of test results

In this section, we conducted four tests which can be used to discriminate global mode events from these other sources of ULF wave activity. One test used thermal and magnetic pressure perturbations to determine whether wave activity was consistent with fast mode waves; this was done in the same manner as described in section 5.3 but using the start and stop times and frequencies that may have been modified after visual inspection of each event (see section 5.4). Events that failed this test likely made it through the automatic selection process because of the separate, less strict selection criteria for intervals with $\beta < 0.5$, and they can immediately be discarded from the database. A second test examined coherence in the b_z perturbations observed at spatially separated spacecraft; we cannot discard events that failed this test because of the possibility that probes could be located at nodes of the global mode, or may be located far outside the global mode region (e.g., outside of the boundaries of the cavity or far away from the energy source). A third test compared PSD from solar wind dynamic pressure and density perturbations to b_z perturbations in the magnetosphere; the three events that failed this test can immediately be discarded, and we estimate that there are few other events in our database that are directly driven. We do not use this test as supporting evidence for interpreting an event as a global mode, because there are many other types of wave activity that would also be expected to pass this test. Finally, a fourth test examined spatially separated ground magnetometers for coherent signals; events that failed this test cannot be discarded because of the uncertainties involved in observing fast mode wave signatures on the ground (*Kivelson and Southwood*, 1988).

In Figure 5.19, we divide our data into 3 categories:

1. Events that failed either the first (fast mode) or third (solar wind) test and are not considered global mode events.

2. Events for which the first (fast mode) test could not be conducted, the third test was not failed (solar wind), and neither of the other two tests (ground magnetometer, spacecraft coherence) were passed are considered ambiguous.

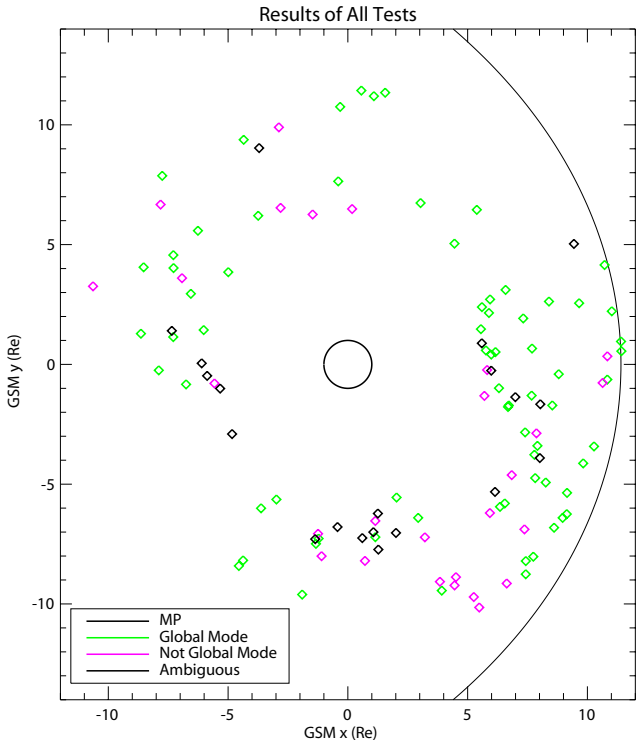

Figure 5.19: The same events as in Figure 5.9B color coded according to whether they are considered global modes (green), are not considered global modes (pink), or are ambiguous (black)

3. Events that did not fail any of the tests and passed at least one of the tests, excluding the third test (solar wind), and are considered global mode events.

Out of 119 events, there were 27 events that were not considered global mode events (pink in Figure 5.19), 20 that were considered ambiguous (black in Figure 5.19), and 72 that were considered global mode events (green in Figure 5.19).

5.6 Global mode properties: statistical results

In sections 5.3, 5.4, and 5.5 we identified global mode events using an automatic selection technique followed by both automatic and visual culling techniques to obtain a list of 72 global mode events. All of these events meet the following criteria at a specific frequency for at least 4 consecutive FFT windows (an equivalent time span of 26 minutes):

1. Electric field data uncontaminated, so the cross-phase between the electric and magnetic field perturbation is trustworthy.

2. Electric field y and magnetic field z perturbations have a coherence greater than or equal to 0.7.

3. The absolute value of the cross-phase between these two perturbations is greater than 45 or less than 135 degrees, suggesting a radially standing fast mode wave.

4. These two perturbations exhibit a monochromatic frequency spectrum and have a common spectral peak.

5. Wave activity is consistent with fast mode MHD waves. If $\beta < 0.5$, we require that either the magnetic field perturbation is compressional or there is a significant total pressure perturbation (or, equivalently, that the thermal and magnetic pressure perturbations are in phase). If $\beta \geq 0.5$, we require that there is a significant total pressure perturbation.

We conducted additional tests to further eliminate other types of ULF wave activity from our global mode event list. After conducting these tests (see section 5.5) and requiring that no tests are failed and at least one test is passed, we are confident that nearly all non-global mode events were removed, with the exception of a few events that may be directly driven by solar wind dynamic pressure fluctuations at the lowest frequencies we considered (< 5 mHz).

We can obtain a normalized occurrence rate for global modes in different regions and under different driving conditions by finding the percentage of time that global modes occurred in that region/during those conditions. The total amount of observation time is defined using all FFT windows that could potentially be identified as a global mode. We exclude all FFT windows during contaminated EFI intervals. We also exclude the first two FFT windows at the beginning of every interval and the last FFT window at the end of every interval due to the requirement that four consecutive FFT windows meet the global mode criteria. Finally, since 75% of each FFT window overlaps another FFT window, we count each 26 minute FFT window as being equivalent to 6.5 minutes. The total observation time, defined in this manner, including both THA and THE, is 135.07 days.

We define the total duration of global mode events using the start and stop times for each individual global mode event, which were determined both automatically and visually (see section 5.4). The total global mode observation time from all 72 events is 1.35 days. We define the overall occurrence rate of global modes as the total global mode observation time divided by the total observation time, 1.0%. We can estimate how this occurrence rate may change if we repeated our observations and used the same event selection methodology during other 26 month intervals with similar driving conditions. We must also assume that the same sources of systematic bias would be present in the new sets of observations. From case to case, we would then expect the number of observed global mode events to be well represented by the Poisson distribution. The standard deviation for the number of observed events can then be represented as the square root of 72 (the number of global mode events), 8.49. Assuming that the average duration of global mode events is 1.35 days divided by 72 events, or 0.0188 days, we can obtain a range for the expected occurrence rate of global

mode events, from $\frac{1.35-0.0188*72}{135.07} * 100 = 0.881\%$ to $\frac{1.35+0.0188*72}{135.07} * 100 = 1.12\%$.

This is an estimate of the random counting error associated with our global mode observations; we re-iterate that it does not include sources of systematic error. One potential source of systematic error is the presence of a few events in our database that are directly driven by solar wind dynamic pressure fluctuations and are not global modes, as discussed in section 5.5.3. We found earlier that about 25% of events with $3 \lesssim frequency < 5$ mHz could be directly driven, and that about 9 events may still remain in our database that are directly driven. These events could not be identified and removed because the necessary data (solar wind monitor) was not present to conduct the test. Assuming that none of these events were removed by the other 3 tests described in section 5.5, our database would only consist of 63 global events. In this case, the total global mode observation time would be approximately $1.35 - .0188 * 9 = 1.18$ days, and the lower bound on the occurrence rate would be closer to 0.87%.

It likely that the true normalized occurrence rate is closer to 1.0% than to 0.87%, since events that appear to be directly driven may also be global modes. It is possible for a global mode to appear as a directly driven wave if the global mode frequency matches the frequency present in the solar wind. We cannot at present discriminate between events that are truly directly driven and events that are global modes driven by solar wind fluctuations with a monochromatic frequency spectrum. As such, we may be unduly lowering the normalized occurrence rate by removing 9 additional events.

To our knowledge, this is the first attempt to estimate the occurrence rate for global modes using in situ observations. There are several limitations of our methodology; in particular, the inability to detect waveguide modes with high k_y, the inability to discriminate global modes from other wave activity in some instances, and the inability to detect global modes when the spacecraft is located in a node of either the electric or magnetic field perturbation associated with the global mode. We should thus regard 1.0% as a lower bound for the true occurrence rate of global modes.

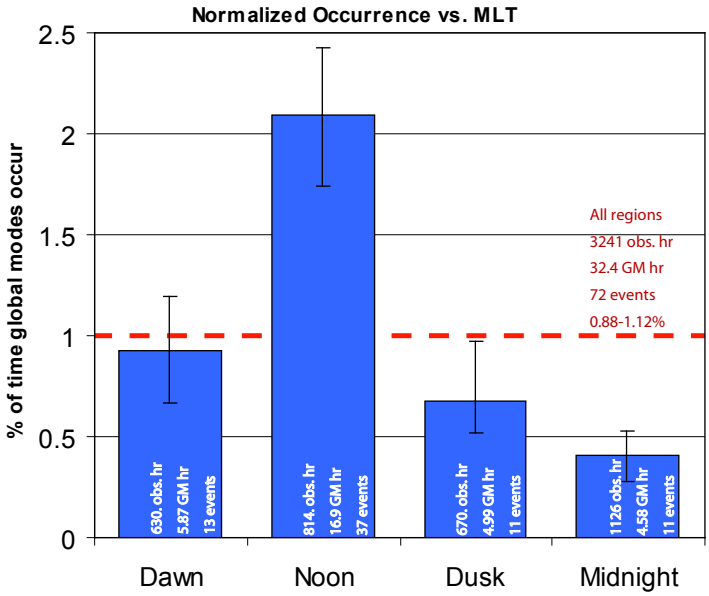

Figure 5.20: The occurrence rate of global mode events vs. MLT.

In the following sections, we examine the properties of global modes using normalized occurrence rates that depend on spatial position and driving conditions. We also examine whether the frequency of global modes varies as a function of spatial position or driving condition. We compare our results to earlier models, simulations, and observations of global modes.

5.6.1 Favored locations of global modes

Shown in Figure 5.2D, 5.2E, and 5.2F, respectively, are the FFT windows included in the total observation time for THA, THE, and both THA and THE, respectively. THA contributes much less observation time than THE, because of the presence of larger quantities of contaminated electric field data (see Appendix B.2). Figure 5.2F indicates that some local time sectors and radial distances are better covered than others, suggesting that the apparent clustering of global mode events at different locations shown in, for example, Figure 5.19, may be misleading. For this reason, we will examine normalized occurrence rates at different locations.

Shown in Figure 5.20 is the occurrence rate in different local time sectors, defined in the

same manner as the normalized global occurrence rate. The total observation time (hours), total global mode observation time (hours), total number of global mode events, and range for the occurrence rate are shown for each local time sector and defined in the same manner as for the calculation of the global occurrence rate. The global occurrence rate is shown as a line in red for reference. Global modes are far more abundant at noon compared to all other local time sectors. They are the least abundant at midnight. The dawn and dusk local time sectors have an intermediate occurrence rate.

There are three likely reasons for the local time asymmetry in the global mode occurrence rate. One is that the primary energy sources for global modes are located in the noon sector. This would be consistent with previous observations that suggest that the ion foreshock and solar wind dynamic pressure are important drivers of global modes (see Figure 5.1). Generally, the ion foreshock and solar wind dynamic pressure fluctuations are most effective at driving ULF waves in the noon local time sector (*Takahashi et al.*, 1981, 1984; *Takahashi and Ukhorskiy*, 2007).

The second reason for the local time asymmetry of the occurrence rate is the biasing of our study with regard to observing low k_y waveguide modes. At local noon, assuming a transient wave energy source that is symmetric with respect to the noon meridian, a superposition of waveguide modes which are propagating both eastward and westward would be observed. This superposition would be similar to a single $k_y = 0$ waveguide mode that would be observed at all times before and after the energy source is removed; thus, the observational signature would be identical to a monochromatic, radially standing fast mode wave and would be detected during our event selection. In other local time sectors, a superposition of wave modes with a continuum of k_y would be observed that changes as a function of time, as shown in Equation 5.7 (*Wright*, 1994); further away from noon, a signature that is similar to a monochromatic, radially standing fast mode wave would be less likely to be generated or observed (*Rickard and Wright*, 1995). Thus, our event selection methodology, designed to detect radially standing fast mode waves, is biased to detect global modes close to the noon local time sector.

A third reason for the local time asymmetry is that the magnetospheric cavity/waveguide

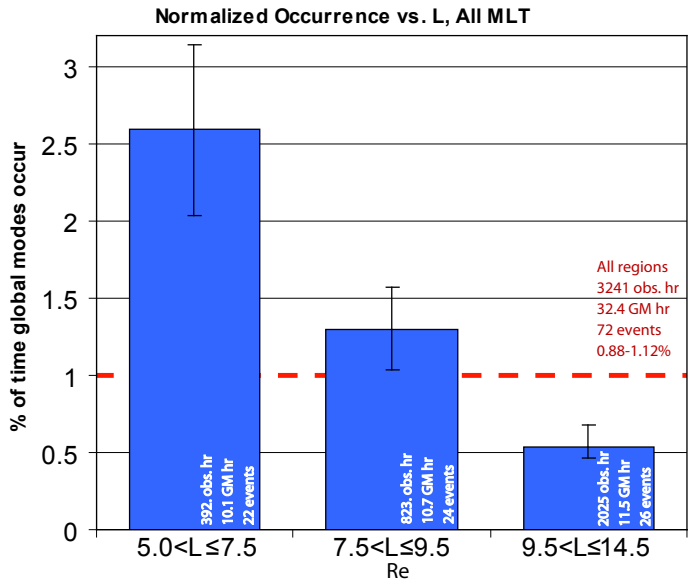

Figure 5.21: The occurrence rate of global mode events vs. L, presented in the same manner as Figure 5.20.

may not be able to sustain global modes equally well in different local time sectors. This could explain the relatively low occurrence rate for global modes on the nightside, where there is no fixed outer boundary such as the magnetopause to reflect and trap fast mode wave energy. Indeed, it is surprising that any radially standing fast mode waves exist in this local time sector, as fast mode wave energy would be expected to rapidly escape into the magnetotail.

In Figure 5.21 we examine the occurrence rate of global modes as a function of L, or the radial distance at which a dipole magnetic field line crosses the magnetic equatorial plane (*McIlwain*, 1966). All global modes were observed between L of 5.9 and 12.3 Re. The occurrence rate for global modes is highest for low L ($5.9 < L \leq 7.5$) at 2.6%, lower for moderate L ($7.5 < L \leq 9.5$) at 1.3%, and lowest for high L ($9.5 < L \leq 12.3$) at 0.54%.

There are two related reasons for the dependence of global mode occurrence rate on L. One is that higher L values are closer to the magnetopause, where wave activity with a broadband frequency spectrum is commonly observed due to transient magnetopause perturbations or the presence of waveguide modes with a continuum of k_y, which appear as wave activity with a broadband frequency spectrum (*Rickard and Wright*, 1995). Both of these types of

wave activity would tend to obscure monochromatic, radially standing global modes, making it more difficult to identify events in this region. Also, waveguide modes with low k_y are expected to have their turning points at lower L values than waveguide modes with high k_y, as shown in Figure 5.4 and discussed in section 5.3.1. Thus, only lower k_y waveguide modes would be observed at low L values, whereas a continuum of k_y values would be observed at higher L values. These low k_y waveguide modes are more likely to be identified during the event selection process. To summarize, lower L values are better for identifying global modes because only monochromatic waveguide modes ($k_y \sim 0$ rather than a continuum of k_y values) are present and there are fewer sources of obscuring wave activity.

We also examined the occurrence rate of global modes versus geomagnetic latitude (dipole). We did not find any significant dependence on geomagnetic latitude, but we attribute this to the narrow range of latitudes that THEMIS samples near the magnetic equator. We expect that if the data coverage extended to regions with significant distances from the magnetic equator, there would be a reduction in the occurrence rate of global modes observed at off-equatorial latitudes due to the trapping of fast mode wave energy near the magnetic equator (*Lee*, 1996).

5.6.2 Favored driving conditions for global modes - geomagnetic activity

We obtained hourly geomagnetic activity indices and solar wind data from OMNIweb for use in computing occurrence rates for different driving conditions. The solar wind data were time-referenced to the subsolar magnetopause.

We examined the dependence of the occurrence rate of global modes on the Kp and AE indices, and we found no strong relationships. However, the observation interval occurred during solar minimum, when the nominal level of geomagnetic activity is expected to be lower. We note that out of 72 events, only 3 occurred during intervals when Kp was greater than or equal to 4 and only 15 occurred during intervals when AE was greater than or equal to 200 nT. This suggests a preference of global modes for lower geomagnetic activity, as suggested by *Kivelson et al.* (1997), but we do not regard it as conclusive evidence because

of a lack of observations during intervals with higher geomagnetic activity.

5.6.3 Favored driving conditions for global modes - solar wind flow speed

We next examine the dependence of global mode occurrence rate on solar wind flow speed. We expect that the occurrence rate should generally increase with increasing solar wind flows speed. One reason is that surface waves generated by flow shear instabilities, a potential energy source for global modes, should increase in amplitude at higher solar wind flow speed. Another reason is the change in the nature of the boundary condition at the magnetosheath at high solar wind speed, which can effectively energize global modes (*Mann et al.*, 1999). Figure 5.22A shows the dependence on the occurrence rate of global modes on solar wind flow speed. Figure 5.22B and 5.22C show the data coverage for the different solar wind flow speed ranges in Figure 5.22A. It is clear from these panels that data coverage is not uniform for different solar wind conditions. The dependence on solar wind velocity ought to be most important in the dawn and dusk local time sectors. To avoid any source of bias due to the data coverage changing between the low and high solar wind speed cases, we separated the data into two local time regions before computing the occurrence rate.

The first region included the dawn and dusk sectors ($3 < MLT \leq 9$ or $15 < MLT \leq 21$). Data for this region is shown in the left two bars in Figure 5.22A; the occurrence rate increases from 0.7% to 1.3% as the solar wind velocity increases from $263 < v_{sw} \leq 450$ to$450 < v_{sw} \leq 751$, as expected. The second region included the noon and midnight sectors ($9 < MLT \leq 15$ or $21 < MLT$ or $MLT \leq 3$). Data for this region is shown in the right two bars in Figure 5.22A; here, the occurrence rate does not increase as significantly from low to high solar wind speed. It increases from 1.0% to 1.4%, but this change could be within the error due to there being a small number of events at higher solar wind speed. We conclude that solar wind flow speed affects the occurrence rate of global modes, but the effect is mostly evident in the flank magnetosphere.

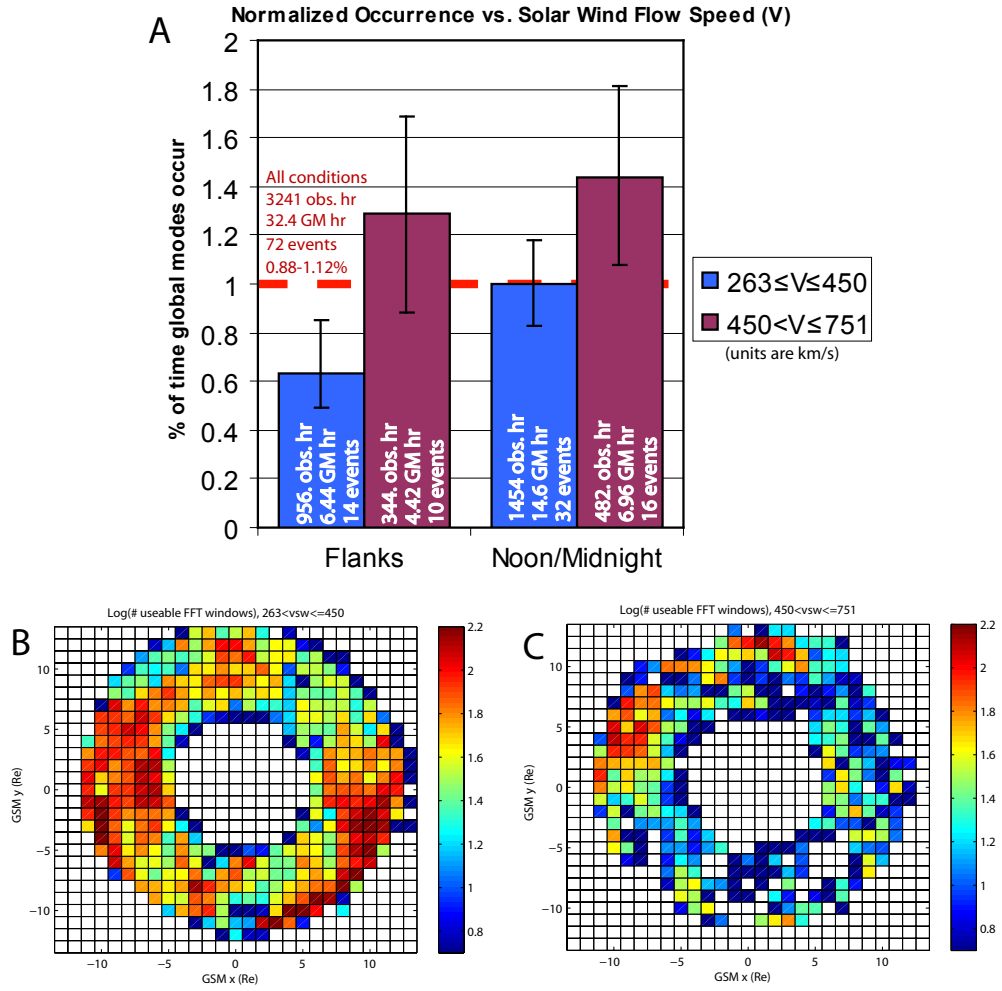

Figure 5.22: A) The occurrence rate of global mode events vs. solar wind flow speed. The left two bars are for data that includes the dawn and dusk magnetic local time sectors, and the right two bars are for data that includes the noon and midnight local time sectors B) Data coverage for intervals when $263 < v_{sw} \leq 450$. C) Data coverage for intervals when $450 < v_{sw} \leq 751$.

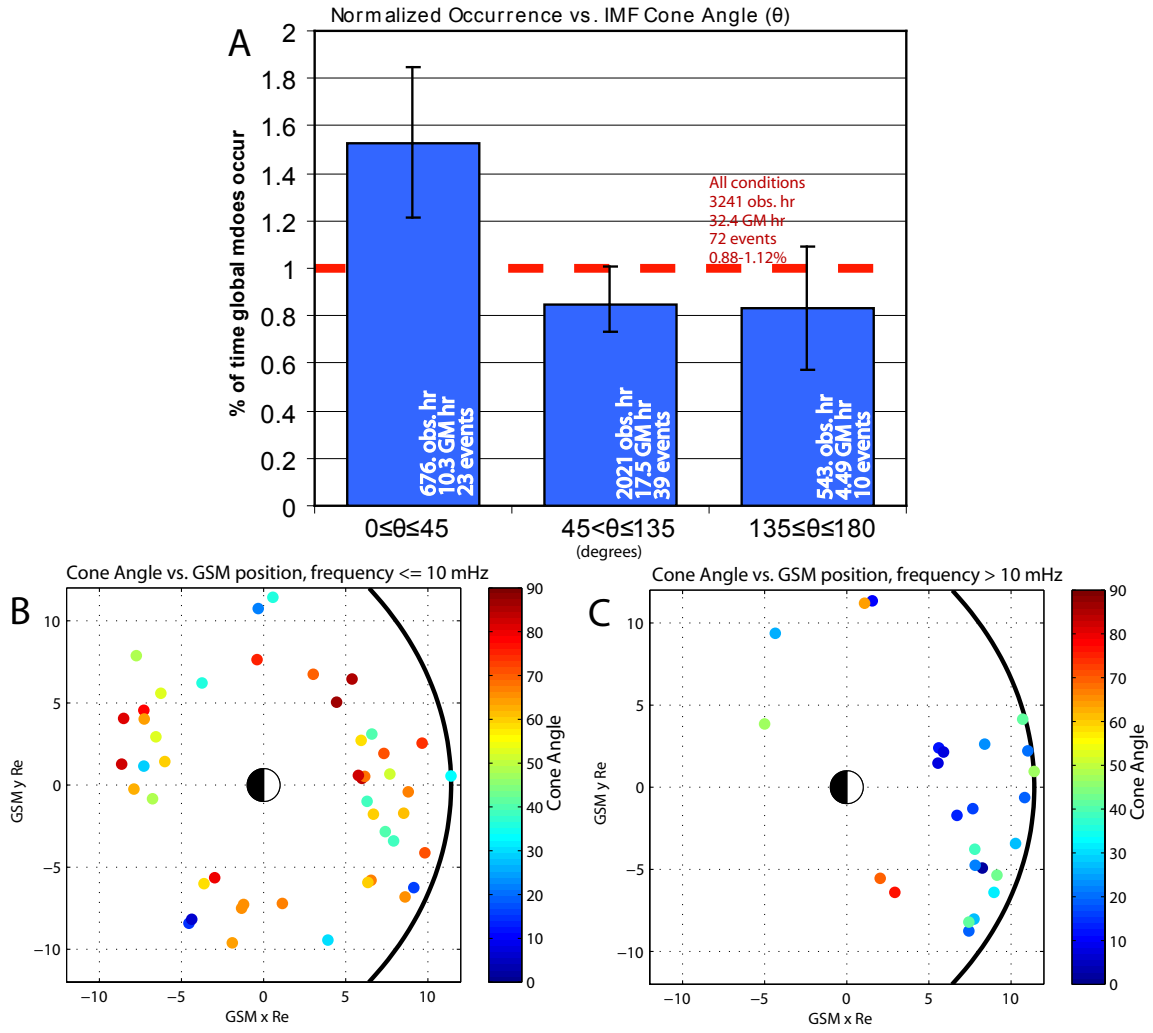

Figure 5.23: A) The occurrence rate of global mode events vs. IMF cone angle. B) The cone angle of global mode events with frequencies less than or equal to 10 mHz versus GSM xy position. To focus on differences between radial and perpendicular (to Earth-Sun line) IMF, we apply the transformation $\theta \rightarrow |180 - \theta|$ when the cone angle is larger than 90 degrees. C) The same but for frequencies greater than 10 mHz

5.6.4 Favored driving conditions for global modes - IMF cone angle

The ion foreshock is an important source of ULF waves in the dayside magnetosphere, particularly during intervals of radial IMF (*Troitskaya et al.*, 1971; *Fairfield et al.*, 1990; *Engebretson et al.*, 1991; *Clausen et al.*, 2009; *Eastwood et al.*, 2011). Waves originating in the ion foreshock have been suggested as a driver for global modes (*Kivelson et al.*, 1997; *Takahashi et al.*, 2010). Because the ion foreshock is most effective at generating ULF waves in the magnetosphere during intervals of radial interplanetary magnetic field (IMF), we examine the dependence of the global mode occurrence rate on IMF cone angle. Cone angle values close to 0 or 180 are associated with radial IMF and, as a result, intervals of strong driving of magnetospheric ULF waves (*Troitskaya et al.*, 1971). They would also be expected to be associated with a higher occurrence of global modes, if the ion foreshock is an energy source for the global modes. This relationship should be strongest in dayside magnetosphere and at frequencies in the Pc3 and Pc4 frequency range, which are locations in the magnetosphere and frequencies consistent with driving by ULF waves or transient events such as hot flow anomalies generated in the ion foreshock (*Takahashi et al.*, 1981, 1984; *Eastwood et al.*, 2011).

Figure 5.23A shows the occurrence rate of global modes versus cone angle. There is a preference for global modes to occur during intervals of low cone angle ($0 < coneangle \leq 45$ degrees when compared to higher values of cone angle. This trend becomes more evident when the cone angle is plotted versus position for each event and sorted by frequency. In Figure 5.23B, the cone angle is plotted for all events with frequencies less than or equal to 10 mHz. Here, we only want to differentiate between cases when the IMF is radial and cases when the IMF is perpendicular to the Earth-Sun line; we thus transform all cone angles greater than 90 degrees according to $\theta \rightarrow |180 - \theta|$. There is no clear relationship between cone angle and global mode occurrence here, with all events spread throughout the magnetosphere and displaying a wide range of cone angles.

The situation is different in Figure 5.23C, where the cone angle is plotted for all events with frequencies greater than 10 mHz. First, most of the events with frequencies greater

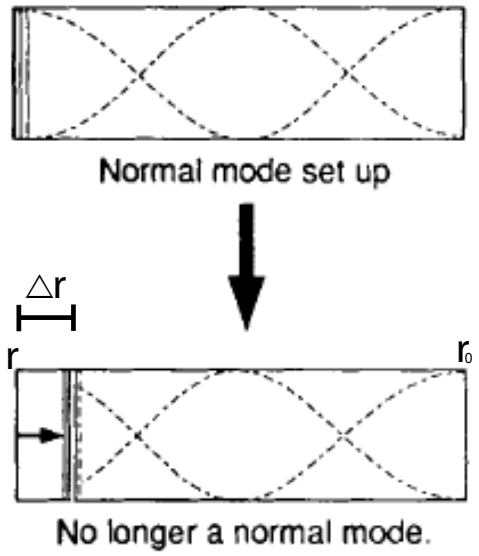

Figure 5.24: The frequency of normal modes present in an organ pipe changes when the dimensions of the pipe change (while the sound speed is held fixed). Taken from *Kivelson et al.* (1997).

than 10 mHz are clustered near pre-noon and noon, in contrast to Figure 5.23B. Second, all events in this cluster occurred when the cone angle was either close to 0 or close to 180 degrees. This evidence strongly suggests that the ion foreshock is the most important source of energy for global modes with frequencies greater than 10 mHz near the noon local time sector. It is consistent with the identified ion foreshock driver in the *Kivelson et al.* (1997) case study in which the wave activity, like the events in Figure 5.23C, had a frequency above 10 mHz. This evidence is also consistent with earlier observations of magnetospheric ULF waves driven by ULF waves in the ion foreshock occurring most often at these locations and frequencies (*Takahashi et al.*, 1981, 1984).

5.6.5 Favored driving conditions for global modes - solar wind dynamic pressure

Solar wind dynamic pressure fluctuations are an important energy source for ULF waves in the Earth's magnetosphere (e.g., *Kepko et al.*, 2002; *Takahashi and Ukhorskiy*, 2007). As shown in Figure 5.1, they have been linked to global modes in several case studies. We thus expect solar wind dynamic pressure to affect the occurrence of global modes.

Dynamic pressure fluctuations can provide energy for global modes, but they can also

preclude their occurrence. *Kivelson et al.* (1997) noted that cavity modes, a type of global mode, require a cavity with stable dimensions, plasma parameters, and magnetic field configuration to grow. They made an analogy with an organ pipe, showing that if the length of the organ pipe changes significantly while the sound speed in the pipe remains the same, the organ pipe will no longer be able to support the normal mode that was present in the original pipe configuration. Figure 5.24 is taken from *Kivelson et al.* (1997), and it shows this situation. Global modes in the magnetosphere are affected when the dimensions of the magnetosphere change just as the organ pipe is affected. Solar wind dynamic pressure plays an important role in determining the dimensions of the magnetosphere; in particular, the magnetopause location (*Shue et al.*, 1997).

Changes in solar wind dynamic pressure that are comparable to global mode periods can drive global modes (e.g., *Claudepierre et al.*, 2009), but they can also preclude their occurrence if the fluctuations are large enough that they cause a significant change in the dimensions of the magnetospheric cavity. We demonstrate this with a 1D model of a fast mode wave standing in between two perfectly reflecting boundaries, one of which is the magnetopause. The inner boundary is at location r_0 and the outer boundary is at the magnetopause location, r. The fast magnetosonic speed, v_{fm} is uniform everywhere. The fundamental frequency of the standing fast mode wave is then

$$f = \frac{v_{fm}}{2(r - r_0)} \tag{5.9}$$

When the outer boundary is displaced by an amount Δr, the frequency changes by an amount

$$\Delta f = \frac{-v_{fm}\Delta r}{2(r - r_0)(r - r_0 + \Delta r)} \tag{5.10}$$

We show how these locations and displacements are defined in Figure 5.24 which is similar to the 1D model of the fast mode apart from the boundary conditions. Equation 5.10 shows that the larger the displacement of the boundary, the larger the frequency change. It also shows that an inner, or negative, displacement of the boundary increases the frequency whereas an outer displacement reduces the frequency, consistent with the fast mode transit

time decreasing or increasing as the boundary location changes. The absolute value of the frequency change can be compared to the original cavity frequency using

$$\frac{f}{|\Delta f|} = \frac{r - r0}{\Delta r} \tag{5.11}$$

In order for the change in frequency to be significant when compared to the original frequency, the displacement of the outer boundary must be large when compared to the original cavity size, $r - r_0$. The relationship between the the frequency and change in frequency is similar in form to the expression for the quality factor, Q, of the cavity. Q is a measure of the response of the cavity to an external energy source, or the ratio of the time-averaged energy in the cavity to the energy loss per cycle (*Jackson*, 1998). Values of Q that are much higher than 1 indicate that the cavity is effective at storing energy from an external energy source, whereas values close to or less than 1 indicates that it is not effective at storing energy and any natural modes will be rapidly damped.

Equation 5.11 does not give an exact relationship between Δr and the Q of the cavity in this 1D model, because damping has not been included in the model and the timescale on which the change occurs has not been considered. For example, if the fundamental period is significantly shorter than the timescale on which the boundary location changes, Q may still be very high. Nevertheless, it indicates two of the most important quantities to consider, $r - r0$ and Δr, when estimating the dependance of global mode occurrence on boundary location changes. When the displacement is small compared to the original cavity size, Q ought to be larger and the cavity ought to be more effective at storing energy.

This 1D model can be used to estimate how the occurrence rate of global modes ought to depend on changes in the boundary location in the magnetosphere due to solar wind dynamic pressure, with the understanding that other factors, such as the inner boundary condition, can also play a role in determining their occurrence. We consider the magnetopause location as the outer boundary and the equatorial ionosphere as the inner boundary ($r_0 = 1Re$). Using the *Shue et al.* (1997) empirical model, the magnetopause location at the subsolar

point when the z component of the IMF is 0 is

$$r = 11.4P^{\frac{-1}{6.6}} \tag{5.12}$$

where P is the solar wind dynamic pressure. In order to use Equation 5.11, we also require an estimate for the displacements of the outer boundary due to dynamic pressure. *Takahashi and Ukhorskiy* (2007) showed the instantaneous measurements (1 minute) of solar wind dynamic pressure and the amplitude of solar wind dynamic pressure fluctuations in the Pc5 frequency band are extremely well correlated. Using Figure 14 in that paper, we find the relationship between them is given by

$$\delta P(Pc5) = .084P^{.95} \tag{5.13}$$

Using Equations 5.12, 5.13, and 5.11, we find the dependence of $\frac{r-r0}{\Delta r}$ on the solar wind dynamic pressure based on the 1D model for global mode frequencies in the mHz range (Pc5). Figure 5.25A shows how $\frac{r-r0}{\Delta r}$ changes as a function of solar wind dynamic pressure as a black line. In the absence of other effects, increasing the dynamic pressure will decrease $\frac{r-r0}{\Delta r}$, or render the magnetospheric cavity/waveguide less effective at sustaining global modes. As $\frac{r-r0}{\Delta r}$ decreases, the energy supplied to global modes by dynamic pressure fluctuations will increase, as indicated by Equation 5.13; these two effects may both be important but one will tend to decrease the occurrence of global modes whereas the other will increase the occurrence.

Q can be directly measured using power spectra. For a spectral peak corresponding to a global mode, Q is defined as the frequency with peak power divided by the full width at half maximum of the peak (*Jackson*, 1998). For each global mode event, we computed the power spectra for the magnetic field z perturbation when the spectral peak was most clearly defined. Here, we used the full time resolution available during fast survey, 0.125 seconds, and an FFT window of length 34 minutes to decrease noise in the power spectra (*Paschmann and Daly*, 2000). As in section 5.4, we fit a power law to the spectrum to remove the background trend and more clearly identify the spectral peak. Finally, we used

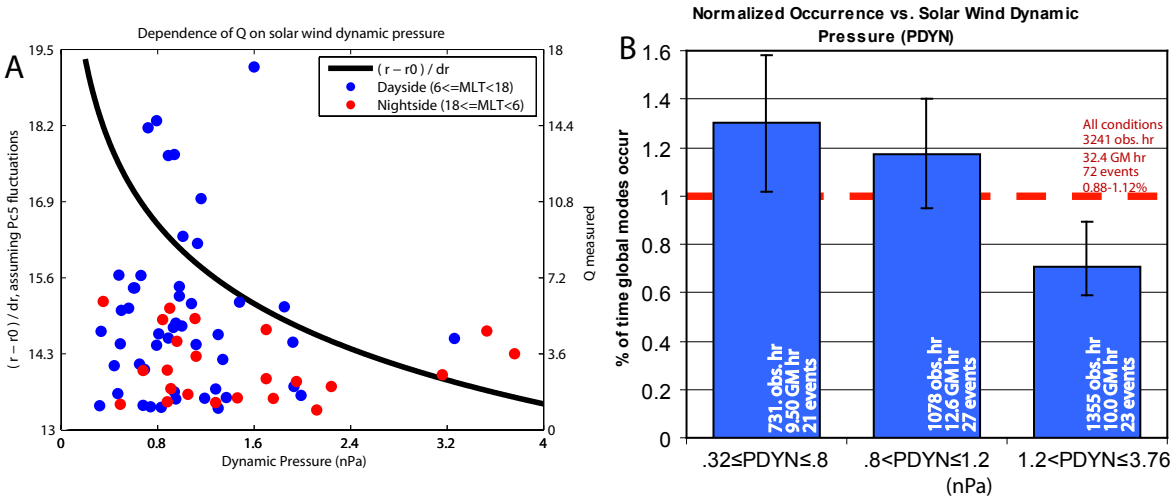

Figure 5.25: A) The dependance of $\frac{r-r_0}{\Delta r}$ and Q on solar wind dynamic pressure. B) The occurrence rate of global mode events vs. Solar wind dynamic pressure.

the data in the immediate vicinity of the peak to produce a least squares fit to a Gaussian function. We used the output of this fit to compute the full width at half-maximum, peak frequency, and Q.

We show our measured values of Q in Figure 5.25A, with events on the dayside as blue points and events on the nightside as red points. Q appears to generally decrease from low to high solar wind dynamic pressure. The trend is most clear for dayside events, where the relation between displacements of the magnetopause boundary and solar wind dynamic pressure ought to be most significant. Clearly, there are other factors besides the solar wind dynamic pressure that are important in determining Q, as there is a large amount of scatter in these data. We note that these Q values are consistent with earlier measurements of Q for global modes (e.g., *Kivelson et al.*, 1997; *Goldstein et al.*, 1999, Q= 10, 4.4, respectively).

Figure 5.25B shows the occurrence rate of global modes as a function of solar wind dynamic pressure. There is no significant difference between the occurrence in the first two bins, but the occurrence rate is significantly lower in the higher bin ($1.2 < P \leq 3.76$ nPa) compared to lower values of solar wind dynamic pressure. This is the opposite trend from what is expected for magnetospheric ULF waves that are directly driven by solar wind dynamic pressure fluctuations; the amplitude of these waves should and does increase as the

amplitude of the dynamic pressure fluctuations increases (*Takahashi and Ukhorskiy*, 2007). However, this trend is expected for global modes if the effect of $\frac{r-r0}{\Delta r}$ (or Q) decreasing with increasing dynamic pressure is more important than the increase in the energy supplied to global modes.

The reduction in the occurrence rate at higher values of the dynamic pressure may also be partially caused by a biasing for intervals when global modes can be unambiguously identified. The presence of ULF wave activity, whether directly driven monochromatic ULF waves or waves with a broadband frequency spectrum, may be obscuring global modes during intervals when solar wind dynamic pressure fluctuations have larger amplitudes.

5.6.6 Favored frequencies for global modes

The frequency of global modes depends on the properties of the magnetospheric cavity/waveguide. Cavity size will affect the frequency; for example, larger cavities will tend to have lower frequencies (Equation 5.9). The plasma conditions inside the cavity/waveguide also affect frequency; for example, a significant population of heavy ions will decrease the frequency. Boundary conditions can also affect the frequency (*Mann et al.*, 1999). It is also important to note that more than one type of cavity/waveguide mode is possible; the equatorial ionosphere, plasmapause, magnetopause, and bow shock have all been proposed as potential cavity/waveguide mode boundaries, leading to a number of possible cavities, each having its own distinct frequency. Proposed and observed global mode frequencies have ranged from $\lesssim 1$ mHz to tens of mHz.

In light of this wide range of predictions for global mode frequency, it is difficult to predict exactly what trend, if any, is expected when an ensemble of global mode observations at a range of radial distances and magnetic local times is examined. We have already demonstrated in Figure 5.23 that global modes with frequencies above 10 mHz are preferentially driven by the ion foreshock in the pre-noon and noon local time sectors. This is consistent with some reports from MHD simulations and observations of cavity mode frequencies in that region (*Kivelson et al.*, 1997; *Claudepierre et al.*, 2009). However, these are not the

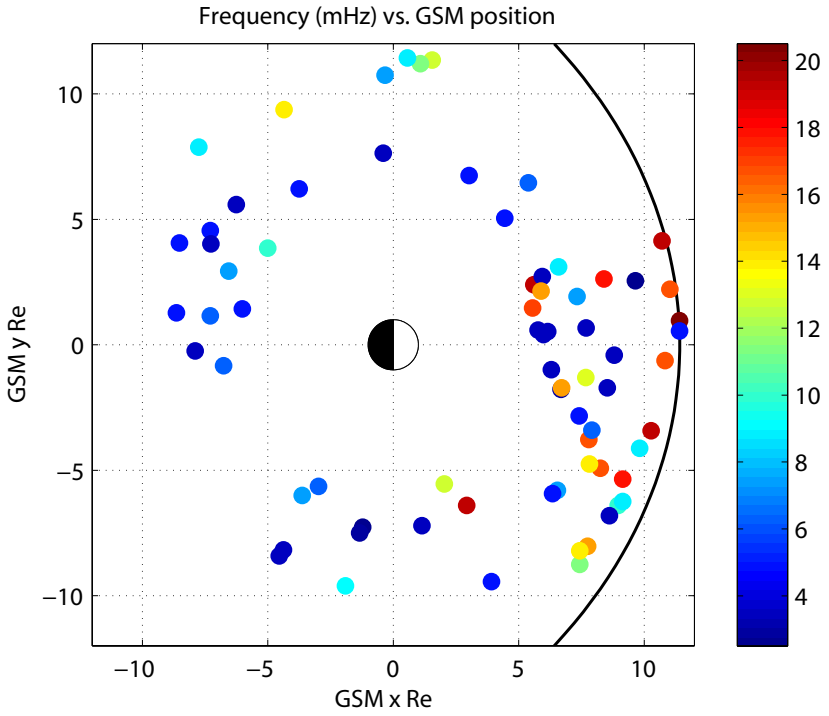

Figure 5.26: The position of each global mode event in the GSM xy plane. The global mode frequency (mHz) is indicated in color.

only global mode frequencies that can be excited in that region, as evidenced by Figure 5.23B. The ion foreshock is only effective at driving global modes in that region when the driving frequency spectrum from the ion foreshock overlaps with one or more of the accessible global mode frequencies in the magnetosphere (*Wright*, 1994). These frequencies could correspond to only a subset of possible cavity/waveguides in the dayside magnetosphere; the cavity/waveguides corresponding to the lower frequency global modes that were found on the dayside may not be effectively driven by the ion foreshock.

Figure 5.26 shows the frequency of all global mode events vs. position in the GSM xy plane. Apart from the clustering of higher frequency ($10 < f \lesssim 20$ mHz) global modes on the dayside, there are no immediately obvious trends. The lower frequency ($3 \lesssim f \leq 10$ mHz) global modes occur at all local times and radial distances. Notably, they do not have decreasing frequencies with increasing radial distance. This trend would be expected for standing Alfvén waves, which nominally have decreasing frequencies with increasing radial

distances in this region (outside of the plasmasphere). The absence of this trend is supporting evidence that our methodology has selected global mode events rather than standing Alfvén waves.

The lack of a clear trend with respect to radial distance or magnetic local time or a preference for specific frequencies suggests that there is significant variability in the properties of magnetospheric cavities/waveguides. This is reasonable when considering the variability expected in, for example, the magnetopause location or the distribution of plasma mass density from event to event. We note here that we only searched for events in the frequency range $3 \lesssim f \lesssim 20$ mHz, and thus we cannot comment on global mode frequencies outside of that range, such as the ULF waves that are often observed on the ground at discrete frequencies below 3 mHz (*Samson et al.*, 1991).

To summarize, global modes with frequencies between 10 and 20 mHz occur almost exclusively on the dayside. Global modes with frequencies in the range $3 \lesssim f \leq 10$ mHz occur at all local times and radial distances considered in this study ($5 < r \lesssim 13$ Re), with no clear trends evident.

5.7 Summary

In this chapter, we used data from multiple THEMIS spacecraft to identify 72 global mode events. Our event selection criteria were designed to use magnetic field, electric field, and plasma data from a single spacecraft as well as multi-spacecraft and ground observations to identify these global modes while excluding other ULF wave modes. We used this ensemble to obtain a lower bound of 1.0% for the occurrence rate of global modes in the Earth's magnetosphere. We also find that global modes are more likely to occur in the noon local time sector and at radial distances of less than 7.5 Re. The ion foreshock is an important source of energy for global modes with frequencies greater than 10 mHz, and the occurrence of all global modes generally increases with increasing solar wind flow speed and decreasing solar wind dynamic pressure.

Our database of 72 events consists of many events with very low wave amplitudes com-

pared to other typical sources of wave activity, perhaps explaining why so few global modes have been observed in the past. For example, the events shown in Figure 5.12 and Figure 5.25 had magnetic field perturbations of $\lesssim$ 500 pT. These small amplitude waves, despite lasting for many wave cycles and having coherent electric and magnetic field perturbations, would not be readily noticeable when examining a time series with other, larger amplitude ULF wave modes. We note here that our study may be biased to observe lower amplitude global modes, because both electric and magnetic field perturbations observed by the probe must be above the noise threshold to detect the global mode. Since the spatial locations of electric field nodes (weakest signals) correspond to the locations of magnetic field anti-nodes (strongest signals) and vice versa, it is possible that global modes will never be detected at peak amplitude locations using the observational criteria in this study.

Global modes, regardless of whether they have low amplitudes, can play an important role in driving standing Alfvén waves, as shown in previous models and the results of Chapter 4. They may also play an important role in accelerating radiation belt electrons either directly or indirectly via the standing Alfvén waves. Studying the importance of global modes in both cases is an important topic for future work.

CHAPTER 6

Conclusions

Ultra Low Frequency (ULF) waves are an important mechanism for energy transfer in the Earth's magnetosphere, interacting with a variety of different plasma populations and other plasma wave modes. The solar wind is an important energy source for ULF waves, and there are many pathways through which solar wind energy can drive wave activity. In this thesis, two case studies and two statistical studies were presented to demonstrate the manner in which energy is transferred from the solar wind to magnetospheric ULF waves. We focused on three aspects of energy transfer: the role of the plasmasphere in modulating ULF wave energy transfer, field line resonance, and global modes. This thesis has accomplished four main tasks:

1. Quantified the difference in Pc5 ULF wave power between the plasmasphere and trough region.

2. Provided further validation of the field line resonance paradigm, meeting the criteria for definitive proof described by *Glassmeier et al.* (1999)

3. Demonstrated that global modes are a valid mechanism for converting energy from fluctuations in the solar wind with a broadband frequency spectrum to monochromatic shear Alfvén waves in the magnetosphere, outside the plasmasphere, and in the Pc5 frequency band.

4. Placed a lower bound on the occurrence rate for global modes outside of the plasmasphere.

Chapter 2 discussed a statistical study examining the effect of the plasmasphere on ULF wave energy transfer. We concluded in this chapter that the plasmasphere has an

important effect on ULF wave energy transfer in the Pc5 frequency band; in particular, we quantified the difference in wave power spectral density inside and outside the plasmasphere, finding it to be as much as an order of magnitude for both electric and magnetic field perturbations. This effect had not previously been observed in situ, and these observations complement models that have shown the importance of the plasmasphere in modulating ULF wave activity and motivate future models (e.g., *Zhu and Kivelson*, 1989). We proposed that the difference in power spectral density is caused by the reflection of fast mode waves incident on the plasmapause from the outer magnetosphere or the fact that the range of frequencies accessible to standing Alfvén is typically above the Pc5 frequency range in the plasmasphere. Determining which of these reasons best explains these differences by comparing with models and making more detailed observations of wave polarization is a topic for future work.

Chapter 3 discussed a field line resonance case study. This was the first study to make an observation of the electromagnetic energy flux near the magnetic equator and at the FLR location, and we concluded that FLR is a viable mechanism for converting isotropic electromagnetic energy transfer to field-aligned electromagnetic energy transfer, meeting the criteria for the validation of the FLR paradigm described by *Glassmeier et al.* (1999). We also estimated the energy flux into the ionosphere and the Joule dissipation rate, which we find to be comparable. Future work could include better quantifying the energy transfer from the magnetic equator to the ground by including incoherent scatter radar (to better estimate energy lost through Joule dissipation) and low Earth orbiting satellites (to estimate energy lost through the field-aligned acceleration of electrons).

Chapter 4 and Chapter 5 discussed the role of global modes in ULF wave energy transfer. Chapter 4 showed with a case study that the global mode mechanism can convert energy from solar wind dynamic pressure fluctuations with a broadband frequency spectrum to monochromatic ULF wave activity in the magnetosphere; in particular, standing Alfvén waves at the plasmapause. This is the first study to show this conversion and energy transfer. It is important because the wave frequency was in the Pc5 frequency band, a suitable frequency for radiation belt interactions, and the observation region was outside the plasmapause, where evidence for global modes has been more controversial (*Waters et al.*,

2002).

Chapter 5 further explored the role of global modes in ULF wave energy transfer through a statistical study. Using an ensemble of 72 events, we estimated a lower bound for the normalized occurrence rate of global modes of 1%, and identified the typical spatial locations, frequencies, and driving conditions for global modes. This was the first time attempted statistical study of global modes using in situ data, and it is an important first step in quantifying the importance of global modes relative to other ULF wave modes in the context of energy transfer. Future work will include case studies drawn from this ensemble that are similar to the one presented in Chapter 4, but for different driving mechanisms and in different locations of the magnetosphere, to better understand what factors affect the spatial extent, duration, and amplitude of global modes. Using these case studies, we will be able to better quantify biases associated with our statistical study. In particular, we can determine whether the typical global mode signal strength at nodes is below the noise thresholds of the THEMIS fields instruments, and better estimate the limitations of THEMIS in detecting global modes. We will also use these case studies and MHD simulations to estimate an upper bound for the occurrence rate of global modes, by more closely examining which solar wind conditions preclude the existence of global modes (as in Chapter 5, Section 5.6.5). Additional work will determine how important global modes are relative to other energy transfer mechanisms in the Earth's magnetosphere. One example will be to study whether large amplitude Alfvén waves can routinely be generated by standing fast mode waves with smaller amplitudes ($< 1\frac{mV}{m}$), as shown for a single case study in Chapter 4.

APPENDIX A

Global mode numerical model

Following *Zhu and Kivelson* (1988), the Earth's magnetosphere is modeled as a box (Figure A.1). The background magnetic field is in the z direction, and two perfectly reflecting boundaries in z correspond to the northern and southern ionosphere, leading to the quantization of the parallel wave number, k. Periodic boundary conditions are imposed in the y direction corresponding to the east-west direction in the Earth's magnetosphere, leading to the quantization of the azimuthal wave number, λ. The solutions are assumed to have both oscillating and decaying time dependence corresponding to a complex frequency, ω. The perturbations have the form

$$e^{i\lambda y}e^{ikz}e^{-i\omega t} \tag{A.1}$$

Finally, the Alfvén speed varies in the x direction corresponding to the radial direction in Earth's magnetosphere.

The same strategy as *Zhu and Kivelson* (1988) is used in solving the linearized MHD equations in the box geometry. The MHD equations are combined into one differential equation for b_z, the compressional magnetic field perturbation. An initial value is assumed, the differential equation is Laplace transformed in time, and a driving term, b_0, is left resulting in the following expression

$$\frac{d}{dx}[\frac{1}{\frac{\omega^2}{v_a^2}-k^2}\frac{db_z}{dx}]+[\frac{\frac{\omega^2}{v_a^2}-k^2-\lambda^2}{\frac{\omega^2}{v_a^2}-k^2}]b_z=b_0(x,\omega) \tag{A.2}$$

Green's function formalism is used to convert this expression into a homogeneous equation

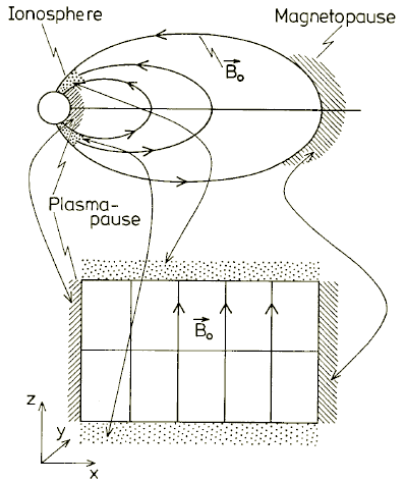

Figure A.1: The Earth's dipole field modeled as a box. Source: (*Glassmeier et al.*, 1999)

and solve for the eigenmodes of the system,

$$\frac{d}{dx}\left[\frac{1}{\frac{\omega^2}{v_a^2}-k^2}\frac{dG}{dx}\right]+\left[\frac{\frac{\omega^2}{v_a^2}-k^2-\lambda^2}{\frac{\omega^2}{v_a^2}-k^2}\right]G=\delta(x-x') \tag{A.3}$$

which can in turn be used to construct a solution appropriate for an arbitrary driver.

$$b_z(x,\omega)=\int_a^b G(x,x',\omega)b_0(x',\omega)dx' \tag{A.4}$$

$$b_z(x,t)=\frac{1}{2\pi}\int_F b_z(x,\omega)e^{-i\omega t}d\omega \tag{A.5}$$

However, the eigenmode solutions to the homogeneous equation can themselves be used to infer many of the properties of energy transfer via ULF waves in the Earth's magnetosphere. There are two classes of solution to the homogeneous equation, purely oscillating normal modes and slowly decaying quasi-eigenmodes (*Zhu and Kivelson*, 1988). Normal modes are obtained if the equation is not singular in the spatial range of interest; quasi-eigenmodes are obtained if there is a singularity. Physically, normal modes correspond to a case in which the condition for FLR is not met within the boundary of the box, and the quasi-eigenmodes correspond to a case in which an FLR does occur.

In order to obtain the final solutions given in Equations A.4 and A.5, the Green's function in Equation A.3 must first be obtained. I use the same technique as *Zhu and Kivelson* (1989) to solve this expression. First, I select a test frequency, ω. I then determine the location of the singularity for that frequency. Since I am solving for the quasi-eigenmodes, this will be inside the boundaries of the box model. I then use the method of Frobenius to obtain a power series solution that can be used to approximate the solution to equation A.3 near the singularity. Two solutions are obtained,

$$R(x) = (x - x_\omega)^2 + \frac{\lambda^2 (x - x_\omega)^4}{8} + \dots \tag{A.6}$$

$$S(x) = \frac{\lambda^2 R(x) \ln(x - x_\omega)}{2} + 1 - \frac{\omega^2 (x - x_\omega)^3}{3} + \dots \tag{A.7}$$

$$x_\omega = \frac{k^2}{\omega^2} \tag{A.8}$$

These solutions are obtained assuming that the Alfvén speed varies as $\frac{1}{x}$, but they can be modified to accommodate other functions.

The approximate solution contains a logarithmic term that is multi-valued at the singularity. *Zhu and Kivelson* (1988) outline a technique to make it single valued. A branch cut is made in the complex x-plane so that as the real part of $x - x_\omega$ goes from negative to positive values (i.e., the singularity is crossed), the following transformation occurs

$$\ln(x - x_\omega) \rightarrow \ln(x - x_\omega) + i2\pi\tau \tag{A.9}$$

$$\tau = +1, Im(x_\omega) < 0 \tag{A.10}$$

$$\tau = -1, Im(x_\omega) > 0 \tag{A.11}$$

Using this technique, the solution is obtained on either side of the singularity.

For the next step, the solution is numerically integrated from just before the singularity to the lower boundary of the box at $x = a$ and from just after the singularity to the upper boundary of the box at $x = b$ using a Runge-Kutta technique. The following boundary

conditions must be satisfied at $x = a, b$ for the quasi-eigenmode

$$G'(a) = AR'(a) + BS'(a) = 0 \tag{A.12}$$

$$G'(b) = AR'(b) + BS'(b) = 0 \tag{A.13}$$

If the boundary conditions can be satisfied, appropriate A and B can be computed and the solution G is obtained from the numerical integration. If the boundary conditions can't be satisfied, a new test frequency is chosen and the above procedure is repeated.

Using these techniques, the quasi-eigenfrequencies/eigenmodes for a given Alfvén speed profile can be obtained. The technique can be generalized to non-monotonic Alfvén speed profiles (*Zhu and Kivelson*, 1989). The step by step summary for obtaining the quasi-eigenmode solutions is given below.

1. Select test frequency.
2. Find location of singularity.
3. Approximate solution near singularity.
4. Make S single-valued and obtain separate solutions appropriate for either side of the singularity.
5. Integrate one solution to the lower boundary and one to the upper boundary to get the full solution.
6. Check whether boundary conditions can be enforced with this solution. If they can be enforced, G is obtained by computing the coefficients of R and S. If they can't be enforced, select a new test frequency and repeat 2-6.

APPENDIX B

Quality control for the THEMIS Electric Field Instrument (EFI)

The instantaneous phase of ULF waves observed by the THEMIS probes is of primary interest for these studies. In particular, the phase difference between the east-west electric and field-aligned magnetic perturbation and the phase differences between spatially separated probes. However, measurements of ULF electric field fluctuations by EFI can potentially be contaminated by spurious, non-geophysical electric fields (*Bonnell et al.*, 2008). The sources of these fields include electrostatic wakes generated by the motion of the spacecraft through cold plasma (e.g., the plasmasphere) and asymmetric illumination of EFI booms caused by, for example, passage through the shadow of the spacecraft (*Mozer*, 1973). These spurious electric fields may affect the measurement of both the amplitude and phase of geophysical electric field fluctuations such as global modes. Furthermore, they may affect spatially separated THEMIS probes in different ways. These effects will confound any attempt to identify global modes. We thus identify and remove from our analysis intervals where contamination is significant.

EFI measures the electric field in the spin plane using the voltage difference between two spherical probes at either end of a 49.6 m boom and two spherical probes at either end of a 40.4 m boom. These spinning spacecraft frame electric fields are sampled 32 times per spin and both the long and the short boom electric fields can be fit separately to a model of the form

$$A + B\cos\psi + C\sin\psi \tag{B.1}$$

using a least squares method, where ψ is the spin phase relative to the Sun pulse (when

the Sun sensor is pointed at the Sun) and A, B, and C are the fit parameters. The fit parameters are then used to compute the electric field in other, non-spinning coordinate systems. This fitting procedure is routinely done on board the spacecraft, and during some intervals, referred to as "slow survey," only the fit parameters for the longer boom are returned to the ground. However, during other intervals known as "fast survey," the voltage differences and electric fields in the spinning frame for both the short and long booms are returned to the ground.

The most direct technique to identify possible sources of contamination for the electric field measurement is to inspect the voltage or electric fields measured in the spinning spacecraft frame when fast survey data are available. In the presence of a geophysical electric field that varies on a timescale much greater than one spin period (3 seconds), the waveforms should appear sinusoidal. Wake electric fields or asymmetric illumination of the booms will cause deviations from sinusoidal behavior (see Section B.1 or *Bonnell et al.* (2008) for examples). However, the presence of these effects does not necessarily preclude the use of EFI data. Non-geophysical spikes in the waveforms corresponding to, for example, shadowed intervals are routinely removed onboard and a model fit is made to the remaining data. The quality of the model fit can then be inspected visually.

A further test can more directly determine how strongly any non-geophysical effects are contaminating the ULF electric field measurement. The short EFI boom is more strongly affected by asymmetric illumination and wake electric fields due to the voltage probes' closer proximity to the spacecraft. A comparison between the electric fields measured by the short and long booms can be used to determine the quality of the electric field measurement; if the wave electric fields measured by the short and long boom are very similar in amplitude and phase, it is less likely (although technically still possible) that spurious electric fields are significantly affecting the measurement of geophysical ULF electric fields.

If only slow survey data are available, it still may be possible to check for contamination by comparing the EFI electric field with the electric field measured by ESA and FGM using the MHD approximation

$$\overrightarrow{E} = -\overrightarrow{v} \times \overrightarrow{B} \tag{B.2}$$

where $\overrightarrow{E}$ is the electric field, $\overrightarrow{v}$ is the either the electron or ion velocities measured by ESA, and $\overrightarrow{B}$ is the magnetic field measured by FGM. This comparison is only possible when ULF velocity perturbations are measured by ESA. This may not always be the case, as ESA itself is subject to several sources of contamination which cannot be removed during slow survey, and the ULF perturbations may be below ESA's detection threshold. Agreement between the ion and electron moment velocities is one indicator that the ESA instrument is effectively measuring ULF velocity perturbations. Major sources of contamination, such as penetrating radiation, affect the electron or ion flux measurements differently (*McFadden et al.*, 2008b); agreement between the two measurements suggests that contamination does not significantly affect either measurement. Visual inspection of the energy flux spectrograms separately can also be used to check for contamination. If contamination is not significantly affecting the measurement of the velocity, the vxB electric field can be directly compared with the EFI electric field to check its validity.

We inspected the quality of the electric field data for the three THEMIS probes in the magnetosphere during the event described in Chapter 4. We found that both the phase and the amplitude of THA's measurement of the electric field were seriously contaminated for the entire interval described in the paper due to both boom shadowing and electrostatic wake effects. THD and THE data were useable for much of the interval. Figures and analysis showing the tests we conducted and the intervals with trustworthy data are shown in Section B.1.

B.1 EFI quality control for 13 November 2008 event

In the following four figures, we inspect the quality of the electric field data. In the first three figures, we examine each probe individually. In the last figure, we compare data from the three probes. In all of these figures, we use Despun Sun-L (DSL) coordinates, in which z is along the spin axis of the satellite, y is normal to z and the spacecraft-sun direction, and x completes the right-handed orthogonal set.

The measurement of geophysical electric fields for this interval is systematically much

worse for THA compared to THD and THE. THD and THA are in close proximity for a large period of time and are on nearly the same orbit, so it is highly unlikely that these differences are caused by localized differences in plasma composition or temperature leading to, for example, electrostatic wake properties differing between the two probes; this could not be the case for the entire interval. Observationally, THA appears much more strongly affected by shadowing than THD or THE. This suggests a systematic difference between the probes with regard to the effect of asymmetric illumination which would cause a poorer measurement of geophysical electric fields; this difference is likely due to THAs spin axis being oriented differently than THD or THE, causing the booms to spend a larger portion of each spin in the spacecraft's shadow. THD and THE are also affected by spurious electric fields during some intervals. These effects become more pronounced when the geophysical electric field is weak (allowing effects from non-geophysical sources to dominate the measurement).

Figure B.1 is for THA. Figure B.1a shows, from top to bottom, the high pass filtered ($frequency > 1mHz$) DSL x component measured by the long boom (green), short boom (blue), and onboard using the long boom (black), and the same for the DSL y component. Only the long boom is used to compute the electric field on board during THEMIS slow survey intervals, but during fast survey intervals both are available. There are slight differences between the black line and green line because of calibration factors that have been applied on the ground using the THEMIS software package. Red boxes indicated areas for spot checking the quality of the electric field measurement. Figure B.1b shows the same information as B.1a, but only for the interval from $\sim 0406 - 0410$ UT. Note that the two DSL x traces for the short and long boom do not agree, suggesting that the electric field measurement is contaminated. The red box indicates an interval for analysis of the electric field in the spinning frame. Figure B.1c shows, from top to bottom, the electric field measured by the long boom (black) and corresponding spin fit (blue), and the same for the short boom for the boxed interval indicated in B.1b. There are significant deviations from sinusoidal behavior in both panels, with large spikes indicating intervals where a voltage probe was in the shadow of the spacecraft and non-sinusoidal behavior (the slope of the line appears linear) indicating the presence of asymmetric electrostatic wake electric fields. The model

is primarily fitting the non-geophysical phenomena, providing a reason for the disagreement seen in B.1b. Figure B.1d is the same as B.1a, but only for the interval from $\sim 0445 - 0500$. There is poor agreement in phase and amplitude between the short boom and long boom in the DSL x component. This is relevant to the present study, as both measurements are required to infer properties of the cavity mode. Figure B.1e shows, from top to bottom, the electric field measured by the long boom (black) and corresponding spin fit (blue), and the same for the short boom for the boxed interval indicated in B.1d. The wake electric fields are weaker for this interval compared to B.1c, but shadowing is still important and the behavior is markedly non-sinusoidal, causing large deviations between the data and model fit to a sine wave; these in turn cause the discrepancies between the long and short boom seen in B.1d.

Figure B.1f shows a comparison between the electric field from EFI and vxB (FGM and ESA) for the third boxed interval in B.1a (0813-0827). Included are, from top to bottom, a comparison between DSL x velocity measured by ESA electron detector (black) and ESA ion detector (red), the same for DSL y, a comparison between DSL x electric field from EFI (blue), vxB with electrons (black), and vxB with ions (red), and the same for the DSL y component. The fact that the electron and ion velocities agree in the top two panels suggest that the vxB approximation is trustworthy for this interval. The fact that neither the phase nor the amplitude agree between vxB and the EFI electric field suggest that the EFI measurement of the electric field is not trustworthy. Based on all of these data, we conclude that the THEMIS-A electric field measurement by EFI is not useable for the present study.

Figure B.2 is for THD. Figure B.2a shows, from top to bottom, the high pass filtered ($frequency > 1mHz$) DSL x component measured by the long boom (green), short boom (blue), and onboard using the long boom (black), and the same for the DSL y component. Only the long boom is used to compute the electric field on board during THEMIS slow survey intervals, but during fast survey intervals both are available. There are slight differences between the black line and green line because of calibration factors that have been applied on the ground using the THEMIS software package. Red boxes indicated areas for spot checking the quality of the electric field measurement. Figure B.2b is the same as in B.2a, but only for the interval from $\sim 0418 - 0450$ UT. Note that the two DSL x traces for

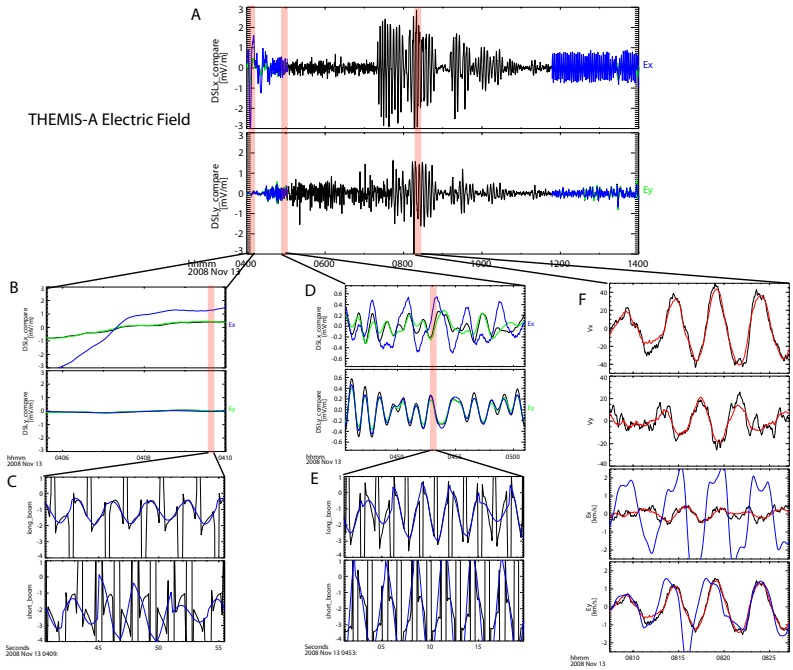

Figure B.1: A) From top to bottom, the high pass filtered ($frequency > 1mHz$) DSL x component measured by the long boom (green), short boom (blue), and onboard using the long boom (black), and the same for the DSL y component. B) The same as in A, but only for the interval from $\sim 0406 - 0410$ UT. C) From top to bottom, the electric field measured by the long boom (black) and corresponding spin fit (blue), and the same for the short boom for the boxed interval in B. D) The same as in A, but only for the interval from $\sim 0445 - 0500$. E) From top to bottom, the electric field measured by the long boom (black) and corresponding spin fit (blue), and the same for the short boom for the boxed interval indicated in D. F) A comparison between the electric field from EFI and vxB (FGM and ESA) is shown for the third boxed interval in A (0813-0827). From top to bottom, a comparison between DSL x velocity measured by ESA electron detector (black) and ESA ion detector (red), the same for DSL y, a comparison between DSL x electric field from EFI (blue), vxB with electrons (black), and vxB with ions (red), and the same for the DSL y component.

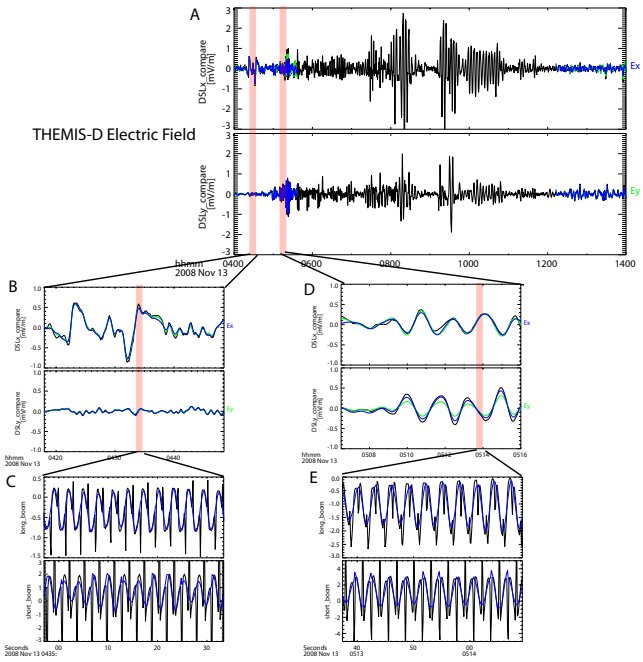

Figure B.2: A) From top to bottom, the high pass filtered ($frequency > 1mHz$) DSL x component measured by the long boom (green), short boom (blue), and onboard using the long boom (black), and the same for the DSL y component. B) The same as in A, but only for the interval from $\sim 0418 - 0450$ UT. C) From top to bottom, the electric field measured by the long boom (black) and corresponding spin fit (blue), and the same for the short boom for the boxed interval indicated in B. D) The same as in A, but only for the interval from $\sim 0506 - 0516$. E) From top to bottom, the electric field measured by the long boom (black) and corresponding spin fit (blue), and the same for the short boom for the boxed interval indicated in D.

the short and long boom agree well (compare with THEMIS-A), suggesting that the electric field measurement is not contaminated. The red box indicates an interval for analysis of the electric field in the spinning frame. Figure B.2c shows, from top to bottom, the electric field measured by the long boom (black) and corresponding spin fit (blue), and the same for the short boom for the boxed interval indicated in B.2b. Large spikes indicate intervals where a voltage probe was in the shadow of the spacecraft these spikes are removed onboard before fitting to a sine wave. The model is primarily fitting geophysical electric fields, leading to the agreement in B.2b. Figure B.2d shows the same information as Figure B.2a, but only for the interval from $\sim 0506 - 0516$. There is good agreement in phase and amplitude between the short boom and long boom in the DSL x and y components (compare to THA).

Figure B.2e shows, from top to bottom, the electric field measured by the long boom (black) and corresponding spin fit (blue), and the same for the short boom for the boxed interval indicated in B.2d. The spikes are removed as in B.2c, leading to the agreement in B.2d.

Unfortunately, we can find no interval where the ESA data can be used to compute vxB to compare with EFI in the same manner as Figure B.1. However, we note that the data is trustworthy during the fast survey interval (ends at $\sim$ 0620 UT), and there is no reason to expect that contamination will increase for the interval used in the paper (0625-0745 UT), based on the fact that the ambient plasma conditions as measured by ESA and electron density as inferred by spacecraft potential are not significantly changing (if they were, electrostatic wake effects could be come important) and the angle the spin-axis makes with the ecliptic does not change significantly (if it did, boom shadowing effects could become important). Based on all of these data, we conclude that the THEMIS-D electric field measurement by EFI is useable for the present study.

Figure B.3 is for THE. Figure B.3a shows, from top to bottom, the high pass filtered ($frequency > 1mHz$) DSL x component measured by the long boom (green), short boom (blue), and onboard using the long boom (black), and the same for the DSL y component. Only the long boom is used to compute the electric field on board during THEMIS slow survey intervals, but during fast survey intervals both are available. There are slight differences between the black line and green line because of calibration factors that have been applied on the ground using the THEMIS software package. Red boxes indicated areas for spot checking the quality of the electric field measurement. Figure B.3b is the same as B.3a, but only for the interval from $\sim 0554 - 0611$ UT. The two DSL x traces for the short and long boom agree well (compare with THEMIS-A), suggesting that the electric field measurement is not contaminated however, this will be shown to be untrue in B.3c. The red box indicates an interval for analysis of the electric field in the spinning frame. Figure B.3c shows, from top to bottom, the electric field measured by the long boom (black) and corresponding spin fit (blue), and the same for the short boom for the boxed interval indicated in B.3b. During this period, THEMIS-E is in the plasmasphere and generates an electrostatic wake, evidenced by the non-sinusoidal traces. The model is primarily fitting non-geophysical phenomena.

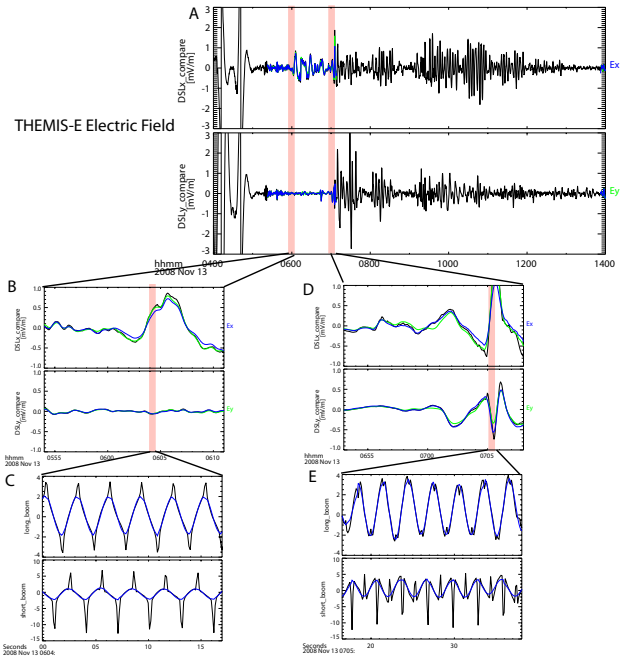

Figure B.3: A) From top to bottom, the high pass filtered ($frequency > 1mHz$) DSL x component measured by the long boom (green), short boom (blue), and onboard using the long boom (black), and the same for the DSL y component. B) The same as in A, but only for the interval from $\sim 0554 - 0611$ UT. C) From top to bottom, the electric field measured by the long boom (black) and corresponding spin fit (blue), and the same for the short boom for the boxed interval indicated in B. D) The same as in A, but only for the interval from $\sim 0653 - 0708$. E) From top to bottom, the electric field measured by the long boom (black) and corresponding spin fit (blue), and the same for the short boom for the boxed interval indicated in D.

However, the electrostatic wake appears to affect both the long and short booms in a similar manner, leading to the agreement in B.3b; both booms are measuring non-geophysical electric fields. D) The same as in B.3a, but only for the interval from $\sim 0653 - 0708$. There is good agreement in phase and amplitude between the short boom and long boom in the DSL x and y components (unlike THA). Figure B.3e shows, from top to bottom, the electric field measured by the long boom (black) and corresponding spin fit (blue), and the same for the short boom for the boxed interval indicated in B.3d. The spikes are removed prior to the model fit, and no wake effects are present, leading to the agreement in B.3d.

Unfortunately, we can find no interval where the ESA data can be used to compute vxB to compare with EFI for THE. However, we note that the data is trustworthy near the end of the fast survey interval ($\sim$ 710 UT and later), and we do not expect electrostatic wake or boom shadowing effects to become more prevalent after this time. Based on all of these data, we conclude that the THEMIS-E electric field measurement by EFI is useful near this time.

Figure B.4 shows a comparison of the DSL x measurement of the electric field for all probes. From top to bottom, the high pass filtered ($frequency > 1mHz$) DSL x component measured by the long boom (green), short boom (blue), and onboard using the long boom (black) for THEMIS-A, THEMIS-D, and THEMIS-E are shown. Note that THE is at perigee near 0445, and the large fluctuations before 0500 are artifacts of the high pass filtering. The largest discrepancies between the short and long boom can be seen in the THEMIS-A measurements in the top panel. Measurements of the electric field by the short and long boom for THEMIS-D and THEMIS-E tend to agree much better. Although there are some intervals where the amplitude differs by as much as 0.1 and 0.2 $\frac{mV}{m}$ for THD and THE (particularly when the overall electric field perturbations, and likely the geophysical portion of the electric field measurement, have small amplitude), the phase is very similar, unlike THA. We note that the DSL x component in this region is pointed in a similar direction to the field-aligned y coordinate (east-west) used to identify the cavity mode in the paper. THD and THE electric field data should thus be reliable for this study (excluding the intervals where THE is experiencing electrostatic wake effects).

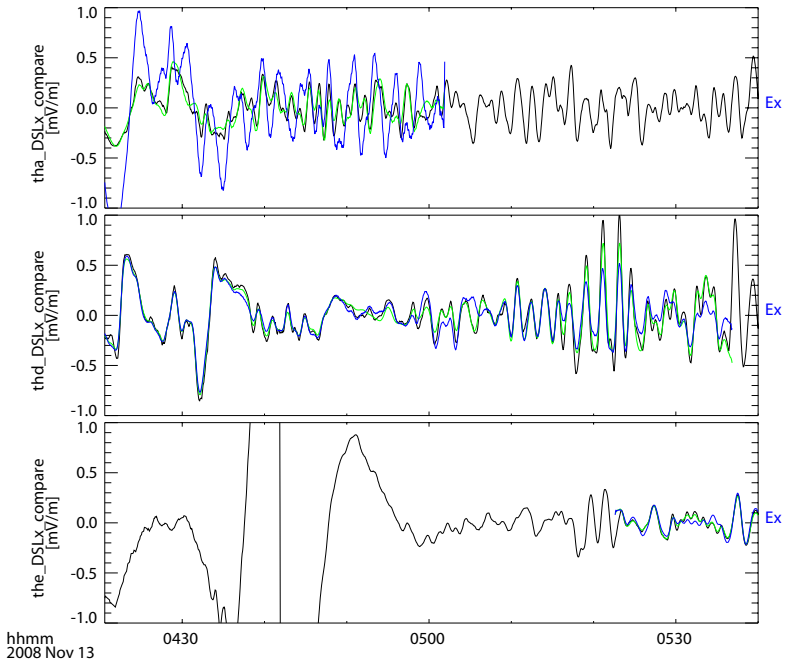

Figure B.4: From top to bottom, the high pass filtered ($frequency > 1mHz$) DSL x component measured by the long boom (green), short boom (blue), and onboard using the long boom (black) for THEMIS-A, THEMIS-D, and THEMIS-E.

B.2 Routine EFI quality control

We require a method for routinely identifying intervals with contaminated electric field data. As in the previous sections, we can identify contaminated intervals using a comparison between the electric field measured by the short boom and the long boom (e.g., in Figure B.4). Generally speaking, the measurement of the DC electric field is more affected by sources of contamination. Since we do not want to remove intervals of high quality AC electric field measurements, we will only compare the AC fields measured by the short and long booms. Here, we define AC signals as having frequencies above 3 mHz.

We developed four flags based on the comparison of the short and long boom electric fields: one is based on the phase difference between the short and long boom measurement of the DSL x component of the electric field, one for the DSL y component, one for the ratio of the amplitude of the short boom measurement to the long boom measurement of the electric field in the spin plane, and one for the overall data quality. If any of the first three flags

indicate low quality data, the final flag indicates that the data is contaminated.

To compute these flags, we first subtracted the DC electric field from both the short and long boom measurements (frequency < 2 mHz). Next, we used a 512 point FFT window to compute the power spectral density of the DSL x and y components for both the short and long boom. We also computed the cross phase between the short and long boom for both the DSL x and y components. Finally, we computed the noise threshold of the instrument assuming a sensitivity of $0.2\frac{mV}{m}$ (*Bonnell et al.*, 2008), and excluded all data below the noise threshold when computing the quality control flags.

We can only compute the quality control flags during intervals where fast survey data is available and when there is a ULF signal above the noise threshold of the instrument. For these reasons, we classify THEMIS electric field data in following four categories: slow survey, fast survey with no signal, fast survey with contaminated signal, fast survey with clean signal. We only use data in the second and fourth category for the analysis in Chapter 5.

To compute the flag based on the phase difference between the short and long boom measurement of the DSL x component of the electric field, we take the average of the absolute value of the cross phase between the short and long boom measurement in the 3 to 20 mHz frequency band, excluding all data below the noise threshold. If no data is above the noise threshold, we classify that particular FFT window as having no signal. We compute the flag based on the phase difference between the short and long boom measurement of the DSL y component of the electric field in the same manner. Both flags are numbers between 0 and 180 degrees; if the data are high quality, the flags should be close to 0.

To compute the flag based on the ratio of the amplitude of the short boom measurement to the long boom measurement of the electric field in the spin plane, we first compute a quantity proportional to the RMS amplitude of the electric field perturbation in the spin plane by taking the square root of the sum of the DSL x and y power spectral densities. We then take the ratio of the RMS amplitudes measured by the short and long boom, excluding all data below the noise threshold. If no data is above the noise threshold, we classify that

particular FFT window as having no signal. This flag indicates high quality data when it is close to 1.

Finally, we compute the overall quality control flag by using thresholds for the values of the first three flags. Our criteria for high quality data are as follows: DSL x cross phase flag is less than 30 degrees, DSL y cross phase flag is less than 30 degrees, RMS amplitude ratio flag is between .625 and 1.6. If all three of these criteria are met, the last quality control flag is 1 and indicates uncontaminated data. Otherwise, it is 0 and indicates contaminated data.

We computed quality control flags for each FFT window used in the study described in Chapter 5. The interval studied included all fast survey intervals occurring at distances from the Earth greater than 5 Re and inside the magnetopause. THA and THE were both used for the interval from 01 February 2008 to 01 April 2010. In Figure B.5, we show the occurrence rate of contaminated electric field data for THA; the occurrence rate is defined as the number of fast survey FFT windows with a contaminated signal divided by the sum of the number of FFT windows with both contaminated and uncontaminated signals (intervals with no signal above the noise threshold are excluded). In Figure B.6, we show the same occurrence rate for THE. It is clear from these figures that most of the contaminated data occurs on the dayside, likely coincident with regions of increased cold plasma which can cause electrostatic wakes. The electric fields measured by THA are more likely to be contaminated than for THE. This is likely due to systematic differences in the solar aspect angle for both probes. Lower solar aspect angles will lead to longer duration boom shadowing intervals and hence a higher chance of contaminated data. However, we do not have a definitive explanation for the systematic differences between THA and THE. Finding the source of these differences is a topic for future work.

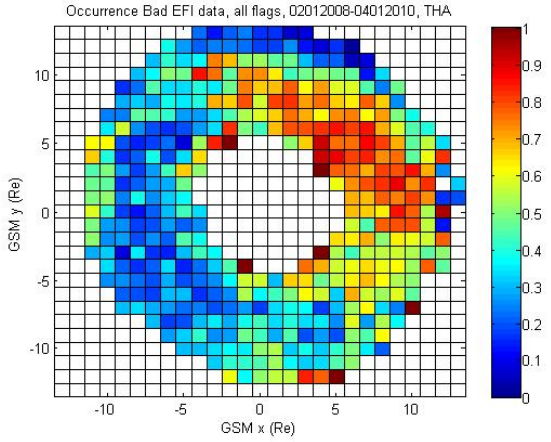

Figure B.5: Occurrence rate of contaminated electric field data for THA

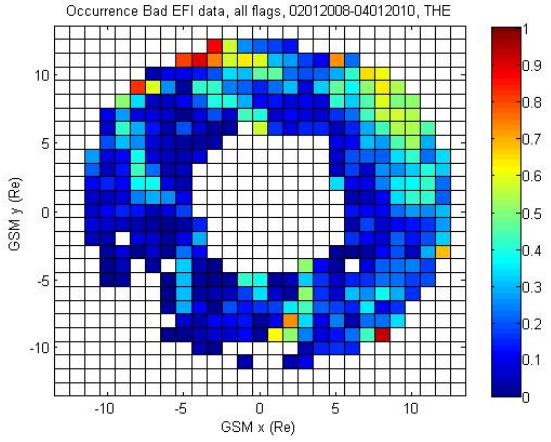

Figure B.6: Occurrence rate of contaminated electric field data for THE

APPENDIX C

Signal processing

We employ several standard signal processing techniques to both characterize ULF wave activity and verify the quality of THEMIS electric field data in this thesis. We describe these techniques in this section.

C.1 Subtraction of background fields

The presence of slowly varying trends in the time domain can obscure the presence of wave activity. It can also adversely affect the analysis of wave activity in the frequency domain if the trends have timescales that are comparable to the window used for, e.g., Fourier analysis. We subtract such trends before conducting Fourier analysis or visually inspecting AC signals in the time domain.

There are several methods for removing background trends from data. One method is to model the background trend; for example, using the *Tsyganenko* (1989) model or a third order polynomial fit to represent the Earth's magnetic field. Such a method can work well for studies where the background trend is well constrained. However, we had trouble using this method for much of the work in this thesis, due to the large variability of the Earth's magnetic field at the wide range of radial distances and magnetic local times considered in each study; no single model fit the data well at all times, and there was often a non-negligible (i.e., significant enough to affect Fourier analysis and visual inspection of traces) DC trend remaining after subtracting each model we tried.

A second method is to obtain the DC trend using a low pass filter; this trend can then be subtracted from the original signal. This two step method is equivalent to using a high pass

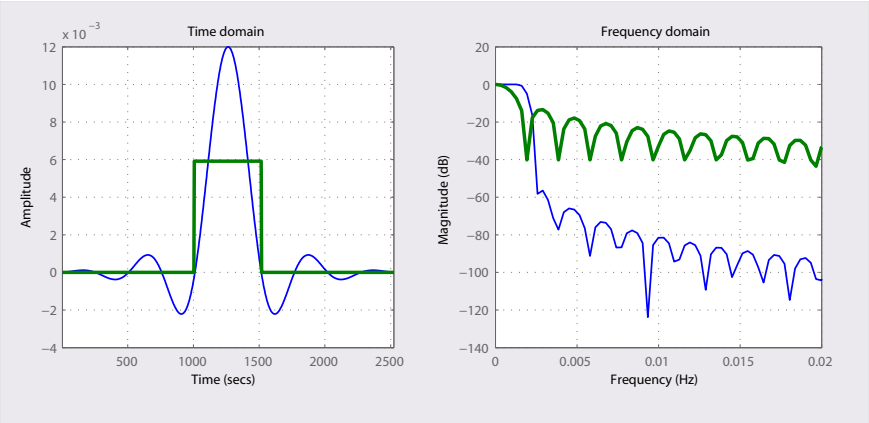

Figure C.1: A comparison between the FIR filter used to pass frequencies below 2 mHz (blue) and a boxcar filter (green). The filters are shown in the time domain on the left and the filter response is shown in the frequency domain on the right.

filter, but we found that it had fewer drawbacks than using a high pass filter alone (e.g., it did not affect the phase spectrum). It has advantages and disadvantages that are unique to each low pass filter chosen.

When using this technique, we convolve a low pass finite impulse response (FIR) filter with the original signal in the time domain to compute the background trend. This filter was constructed using Bessel functions, and the upper cutoff could be adjusted for analysis of different wave frequencies. This filter had advantages over other filters, such as a boxcar, in that the side band is smaller and thus only frequencies close to or below the cutoff frequency are passed by the filter. A comparison between a 500 second (f $<$ 2 mHz) boxcar window and the FIR filter designed to pass frequencies below 2 mHz is shown in Figure C.1; the filters are shown in the time domain on the left and the response of the filters is shown in the frequency domain on the right. Although the main lobe is not as wide for the boxcar filter (right), it is clear that the power transferred at frequencies $\gtrsim$ 3 mHz is much larger for the boxcar filter. The FIR filter constructed from Bessel functions is thus better at filtering data, provided that signal frequencies near the upper frequency cutoff of the filter are not examined.

Using several tests with synthetic data, we found that this filter and method of subtraction

did not alter the phase or amplitude of the original signal provided we restricted our analysis to signal frequencies that were well above the upper frequency cutoff of the filter. For example, if we set the upper frequency cutoff of the low pass filter to 2 mHz, computed the background trend using the filter, and then subtracted this trend from the original signal, we would restrict our analysis of the AC signal to frequencies above 3 mHz.

C.2 Fourier analysis

We use a fast Fourier transform (FFT) to obtain information about ULF signals in the frequency domain. We typically use a Hanning window when performing the FFT. The choice of window affects the resolution in frequency space, the stability of the spectrum (i.e., if different segments of a signal are examined, the reproducibility of the spectrum), and the leakage of signal power between different frequencies (*Bloomfield*, 1976). The Hanning window removes some of the information contained at the beginning and end of the signal, but reduces the leakage between frequencies, particularly from low to high frequencies, when compared to the rectangular window.

The length of the FFT window determines the resolution in frequency (*Bloomfield*, 1976). We use a variety of different window sizes, depending on the signal frequencies of interest, and these are specified in each chapter.

There are many different normalization conventions used for FFT analysis (*Paschmann and Daly*, 2000), often leading to confusion when comparing results between different studies. Although the normalization convention does not affect the results of any chapter in this thesis, we will now detail our convention for completeness.

We used the same normalization convention as *Brautigam et al.* (2005), for ease of comparison with the results in that study in Chapter 2. With their convention, the power spectral density in terms of the discrete Fourier transform is defined as follows

$$P(f) = \frac{2}{W \triangle f} \left| \sum_{k=0}^{N-1} x(k) w_k e^{-i2\pi f k \Delta t} \right|^2 \tag{C.1}$$

$$W = N \sum_{k=0}^{N-1} w_k^2 \tag{C.2}$$

where P is the power spectral density (PSD), f is the frequency, N is the number of data points in the FFT window, Δ t is the sampling time, t is discrete time and equals $k\Delta$ t, T is the length of the FFT interval and equals $N\Delta$ t, f is the discrete frequency step $\frac{1}{T}$, x is the signal, w is the windowing function, and W is the normalization constant determined from the window.

An equivalent RMS amplitude at a given frequency, assuming that wave activity is steady, can be obtained from the PSD using the following equation

$$A(f) = \sqrt{\frac{W \Delta f P(f)}{2}} \tag{C.3}$$

C.3 Cross spectral analysis

Cross spectral analysis is a useful tool for determining various wave properties, including polarization and spatial extent (using multi-point observations) (*Means*, 1972; *Paschmann and Daly*, 2000). Following the analysis of *Paschmann and Daly* (2000) for simplicity sake (since they only considered two 1D signals rather than 3D signals, which would lead to a spectral matrix as in *Means* (1972)), the cross spectral density (CSD) between two 1D signals $u[j]$ and $v[j]$, with corresponding FFT coefficients $\tilde{u}[n]$ and $\tilde{v}[n]$, is

$$G_{uv}[n] = \frac{2N}{f_s} \tilde{u}^*[n] \tilde{v}[n] \tag{C.4}$$

where * denotes the complex conjugate. This can be divided into real and imaginary parts

$$G_{uv}[n] = C_{uv}[n] + iQ_{uv}[n] \tag{C.5}$$

The PSD is a then a special case of the CSD,

$$S_u[n] = G_{uu}[n] \tag{C.6}$$

Using these definitions, the cross phase between the two signals, Φ_{uv} is

$$\tan(\Phi_{uv}[n]) = \frac{Q_{uv}[n]}{C_{uv}[n]} \tag{C.7}$$

and the coherence between the two signals, $\gamma^2_{uv}[n]$, is

$$\gamma^2_{uv}[n] = \frac{|G_{uv}[n]|^2}{S_u[n]S_v[n]} \tag{C.8}$$

In order to obtain a meaningful coherence spectrum, G_{uv}, S_u, and S_v must be calculated using an averaging method in the frequency domain (e.g., two adjoining frequency bins are averaged). Otherwise, $\gamma^2_{uv}[n]$ will equal 1 at all frequencies.

Bibliography

Agapitov, O., K.-H. Glassmeier, F. Plaschke, H.-U. Auster, D. Constantinescu, V. Angelopoulos, W. Magnes, R. Nakamura, C. W. Carlson, S. Frey, and J. P. McFadden (2009), Surface waves and field line resonances: A THEMIS case study, *Journal of Geophysical Research (Space Physics)*, *114*(A13), A00C27, doi:10.1029/2008JA013553.

Alfvén, H. (1945), Magneto-hydrodynamic waves and sunspots. I, II, *Monthly Notices of the Royal Astronomical Society*, *105*, 3.

Allan, W. (1982), Phase variation of ULF pulsations along the geomagnetic field-line, *Planetary and Space Science*, *30*, 339–346, doi:10.1016/0032-0633(82)90039-3.

Allan, W., and D. R. McDiarmid (1993), Frequency ratios and resonance positions for magnetospheric cavity/waveguide modes, *Annales Geophysicae*, *11*, 916–924.

Allan, W., E. M. Poulter, and S. P. White (1986a), Hydromagnetic wave coupling in the magnetosphere - Plasmapause effects on impulse-excited resonances, *Planetary Space Science*, *34*, 1189–1200, doi:10.1016/0032-0633(86)90056-5.

Allan, W., S. P. White, and E. M. Poulter (1986b), Impulse-excited hydromagnetic cavity and field-line resonances in the magnetosphere, *Planetary Space Science*, *34*, 371–385, doi:10.1016/0032-0633(86)90144-3.

Anderson, B. J. (1993), Statistical studies of Pc 3-5 pulsations and their relevance for possible source mechanisms of ULF waves, *Annales Geophysicae*, *11*, 128–143.

Anderson, B. J., and M. J. Engebretson (1995), Relative intensity of toroidal and compressional Pc 3-4 wave power in the dayside outer magnetosphere, *Journal of Geophysical Research*, *100*, 9591–9604, doi:10.1029/95JA00132.

Anderson, B. J., M. J. Engebretson, and L. J. Zanetti (1989), Distortion effects in spacecraft observations of MHD toroidal standing waves - Theory and observations, *Journal of Geophysical Research*, *94*, 13,425–13,445, doi:10.1029/JA094iA10p13425.

Anderson, R. R., D. A. Gurnett, and D. L. Odem (1992), CRRES plasma wave experiment, *Journal of Spacecraft and Rockets*, *29*, 570–573, doi:10.2514/3.25501.

Auster, H. U., K. H. Glassmeier, W. Magnes, O. Aydogar, W. Baumjohann, D. Constantinescu, D. Fischer, K. H. Fornacon, E. Georgescu, P. Harvey, O. Hillenmaier, R. Kroth, M. Ludlam, Y. Narita, R. Nakamura, K. Okrafka, F. Plaschke, I. Richter, H. Schwarzl, B. Stoll, A. Valavanoglou, and M. Wiedemann (2008), The THEMIS Fluxgate Magnetometer, *Space Science Reviews*, *141*, 235–264, doi:10.1007/s11214-008-9365-9.

Baker, D. N., S. Kanekal, J. B. Blake, B. Klecker, and G. Rostoker (1994), Satellite anomalies linked to electron increase in the magnetosphere, *Eos Transactions*, *75*, 401–405, doi:10.1029/94EO01038.

Baumjohann, W., N. Sckopke, J. Labelle, B. Klecker, and H. Luehr (1987), Plasma and field observations of a compressional Pc 5 wave event, *Journal of Geophysical Research*, *92*, 12,203–12,212, doi:10.1029/JA092iA11p12203.

Berube, D., M. B. Moldwin, and M. Ahn (2006), Computing magnetospheric mass density from field line resonances in a realistic magnetic field geometry, *Journal of Geophysical Research (Space Physics)*, *111*(A10), A08206, doi:10.1029/2005JA011450.

Bloomfield, P. (1976), *Fourier analysis of time series: an introduction*, John Wiley and Sons.

Bonnell, J. W., F. S. Mozer, G. T. Delory, A. J. Hull, R. E. Ergun, C. M. Cully, V. Angelopoulos, and P. R. Harvey (2008), The Electric Field Instrument (EFI) for THEMIS, *Space Science Reviews*, *141*, 303–341, doi:10.1007/s11214-008-9469-2.

Boyd, T. J. M., and J. J. Sanderson (2003), *The Physics of Plasmas*, Cambridge University Press.

Brautigam, D. H., G. P. Ginet, J. M. Albert, J. R. Wygant, D. E. Rowland, A. Ling, and J. Bass (2005), CRRES electric field power spectra and radial diffusion coefficients, *Journal of Geophysical Research (Space Physics)*, *110*(A9), A02214, doi:10.1029/2004JA010612.

Carpenter, D. L., and R. R. Anderson (1992), An ISEE/Whistler model of equatorial electron density in the magnetosphere, *Journal of Geophysical Research*, *97*, 1097–1108, doi: 10.1029/91JA01548.

Chandrasekhar, S. (1961), *Hydrodynamic and hydromagnetic stability*, Oxford: Clarendon.

Chen, L., and A. Hasegawa (1974), A Theory of Long-period Magnetic Pulsations, 1. Steady State Excitation of Field Line Resonance, *Journal of Geophysical Research*, *79*, 1024–1032, doi:10.1029/JA079i007p01024.

Cheng, C. Z., and C. S. Lin (1987), Eigenmode analysis of compressional waves in the magnetosphere, *Geophysical Research Letters*, *14*, 884–887, doi:10.1029/GL014i008p00884.

Chi, P. J., and C. T. Russell (1998), Phase skipping and Poynting flux of continuous pulsations, *Journal of Geophysical Research*, *103*, 29,479–29,492, doi:10.1029/98JA02101.

Claudepierre, S. G., M. Wiltberger, S. R. Elkington, W. Lotko, and M. K. Hudson (2009), Magnetospheric cavity modes driven by solar wind dynamic pressure fluctuations, *Geophysical Research Letters*, *36*, L13101, doi:10.1029/2009GL039045.

Claudepierre, S. G., M. K. Hudson, W. Lotko, J. G. Lyon, and R. E. Denton (2010), Solar wind driving of magnetospheric ULF waves: Field line resonances driven by dynamic pressure fluctuations, *Journal of Geophysical Research*, *115*(A14), A11202, doi: 10.1029/2010JA015399.

Clausen, L. B. N., T. K. Yeoman, R. C. Fear, R. Behlke, E. A. Lucek, and M. J. Engebretson (2009), First simultaneous measurements of waves generated at the bow shock in the solar wind, the magnetosphere and on the ground, *Annales Geophysicae*, *27*, 357–371, doi: 10.5194/angeo-27-357-2009.

Connors, M., C. T. Russell, I. Schofield, K. Hayashi, D. Boteler, I. Asudeh, and R. Irwin (2009), AUTUMN/STEP and POLARIS EHB: Spanning Canada With Research Magnetometers, *AGU Spring Meeting Abstracts*, p. A7.

Daly, R. A., and W. J. Hughes (1985), The effect of hydromagnetic waves on the shape of the plasmapause boundary, *Journal of Geophysical Research*, *90*, 537–542, doi: 10.1029/JA090iA01p00537.

Damiano, P. A., A. N. Wright, R. D. Sydora, and J. C. Samson (2007), Energy dissipation via electron energization in standing shear Alfvén waves, *Physics of Plasmas*, *14*(6), 062,904, doi:10.1063/1.2744226.

Darrouzet, F., D. L. Gallagher, N. André, D. L. Carpenter, I. Dandouras, P. M. E. Décréau, J. de Keyser, R. E. Denton, J. C. Foster, J. Goldstein, M. B. Moldwin, B. W. Reinisch, B. R. Sandel, and J. Tu (2009), Plasmaspheric Density Structures and Dynamics: Properties Observed by the CLUSTER and IMAGE Missions, *Space Science Reviews*, *145*, 55–106, doi:10.1007/s11214-008-9438-9.

Denton, R. E., and G. Vetoulis (1998), Global poloidal mode, *Journal of Geophysical Research*, *103*, 6729–6740, doi:10.1029/97JA03594.

Denton, R. E., M. R. Lessard, and L. M. Kistler (2003), Radial localization of magnetospheric guided poloidal Pc 4-5 waves, *Journal of Geophysical Research*, *108*, 1105, doi: 10.1029/2002JA009679.

Dungey, J. W. (1955), Electrodynamics of the Outer Atmosphere, in *Physics of the Ionosphere*, p. 229.

Dungey, J. W. (1963), Hydromagnetic waves and the ionosphere, in *The Ionosphere*, edited by A. C. Stickland, p. 230.

Dungey, J. W. (1967), Hydromagnetic Waves, in *Physics of Geomagnetic Phenomena*, edited by S. Matsushita & W. H. Campbell, p. 913.

Eastwood, J. P., S. J. Schwartz, T. S. Horbury, C. M. Carr, K.-H. Glassmeier, I. Richter, C. Koenders, F. Plaschke, and J. A. Wild (2011), Transient Pc3 wave activity generated by a hot flow anomaly: Cluster, Rosetta, and ground-based observations, *Journal of Geophysical Research*, *116*(A15), A08224, doi:10.1029/2011JA016467.

Elkington, S. R., M. K. Hudson, and A. A. Chan (2003), Resonant acceleration and diffusion of outer zone electrons in an asymmetric geomagnetic field, *Journal of Geophysical Research (Space Physics)*, *108*, 1116, doi:10.1029/2001JA009202.

Engebretson, M., K.-H. Glassmeier, M. Stellmacher, W. J. Hughes, and H. Lühr (1998), The dependence of high-latitude Pc5 wave power on solar wind velocity and on the phase of high-speed solar wind streams, *Journal of Geophysical Research*, *103*, 26,271–26,384, doi:10.1029/97JA03143.

Engebretson, M. J., N. Lin, W. Baumjohann, H. Luehr, and B. J. Anderson (1991), A comparison of ULF fluctuations in the solar wind, magnetosheath, and dayside magnetosphere. I - Magnetosheath morphology. II - Field and plasma conditions in the magnetosheath, *Journal of Geophysical Research*, *96*, 3441–3464, doi:10.1029/90JA02101.

Eriksson, P. T. I., L. G. Blomberg, S. Schaefer, and K.-H. Glassmeier (2006), On the excitation of ULF waves by solar wind pressure enhancements, *Annales Geophysicae*, *24*, 3161–3172, doi:10.5194/angeo-24-3161-2006.

Fairfield, D. H. (1971), Average and unusual locations for the earth's magnetopause and bow shock., *Journal of Geophysical Research*, *76*, 6700–6716, doi:10.1029/JA076i028p06700.

Fairfield, D. H., W. Baumjohann, G. Paschmann, H. Luehr, and D. G. Sibeck (1990), Upstream pressure variations associated with the bow shock and their effects on the magnetosphere, *Journal of Geophysical Research*, *95*, 3773–3786, doi:10.1029/JA095iA04p03773.

Fok, M.-C., J. U. Kozyra, A. F. Nagy, and T. E. Cravens (1991), Lifetime of ring current particles due to Coulomb collisions in the plasmasphere, *Journal of Geophysical Research*, *96*, 7861–7867, doi:10.1029/90JA02620.

Fraser, B. J., J. L. Horwitz, J. A. Slavin, Z. C. Dent, and I. R. Mann (2005), Heavy ion mass loading of the geomagnetic field near the plasmapause and ULF wave implications, *Geophysical Research Letters*, *320*, L04102, doi:10.1029/2004GL021315.

Fujita, S., K. H. Glassmeier, and K. Kamide (1996), MHD waves generated by the Kelvin-Helmholtz instability in a nonuniform magnetosphere, *Journal of Geophysical Research*, *101*, 27,317–27,326, doi:10.1029/96JA02676.

Galbraith, J., M. Heavner, and D. Wilkinson (2008), The Geophysical Institute Magnetometer Array: Making Real-Time Geophysical Measurements Available for Operational Space Weather Needs, *AGU Fall Meeting Abstracts*, p. A1546.

Glassmeier, K.-H. (1980), Magnetometer array observations of a giant pulsation event, *Journal of Geophysics Zeitschrift Geophysik*, *48*, 127–138.

Glassmeier, K. H., H. Volpers, and W. Baumjohann (1984), Ionospheric Joule dissipation as a damping mechanism for high latitude ULF pulsations - Observational evidence, *Planetary and Space Science*, *32*, 1463–1466, doi:10.1016/0032-0633(84)90088-6.

Glassmeier, K.-H., C. Othmer, R. Cramm, and et al. (1999), Magnetospheric Field Line Resonances: A Comparative Planetology Approach, *Surveys in Geophysics*, *20*, 61–109, doi:10.1023/A:1006659717963.

Goldstein, J., M. K. Hudson, and W. Lotko (1999), Possible evidence of damped cavity mode oscillations stimulated by the January, 1997 magnetic cloud event, *Geophysical Research Letters*, *26*, 3589–3592, doi:10.1029/1999GL003636.

Greenwald, R. A., and A. D. M. Walker (1980), Energetics of long period resonant hydromagnetic waves, *Geophysical Research Letters*, *7*, 745–748, doi:10.1029/GL007i010p00745.

Hardy, D. A., M. S. Gussenhoven, R. Raistrick, and W. J. McNeil (1987), Statistical and functional representations of the pattern of auroral energy flux, number flux, and conductivity, *Journal of Geophysical Research*, *92*, 12,275–12,294, doi:10.1029/JA092iA11p12275.

Harrold, B. G., and J. C. Samson (1992), Standing ULF modes of the magnetosphere - A theory, *Geophysical Research Letters*, *19*, 1811–1814, doi:10.1029/92GL01802.

Hartinger, M., M. B. Moldwin, V. Angelopoulos, K. Takahashi, H. J. Singer, R. R. Anderson, Y. Nishimura, and J. R. Wygant (2010), Pc5 wave power in the quiet-time plasmasphere and trough: CRRES observations, *Geophysical Research Letters*, *370*, L07107, doi:10.1029/2010GL042475.

Hartinger, M., V. Angelopoulos, M. B. Moldwin, K.-H. Glassmeier, and Y. Nishimura (2011), Global energy transfer during a magnetospheric field line resonance, *Geophysical Research Letters*, *38*, L12101, doi:10.1029/2011GL047846.

Hasegawa, A. (1969), Drift mirror instability of the magnetosphere., *Physics of Fluids*, *12*, 2642–2650, doi:10.1063/1.1692407.

Hasegawa, H., M. Fujimoto, T.-D. Phan, H. Rème, A. Balogh, M. W. Dunlop, C. Hashimoto, and R. TanDokoro (2004), Transport of solar wind into Earth's magnetosphere through rolled-up Kelvin-Helmholtz vortices, *Nature*, *430*, 755–758, doi:10.1038/nature02799.

Hsu, T.-S., and R. L. McPherron (2007), A statistical study of the relation of Pi 2 and plasma flows in the tail, *Journal of Geophysical Research*, *112*(A11), A05209, doi:10.1029/2006JA011782.

Hudson, M., R. Denton, M. Lessard, E. Miftakhova, and R. Anderson (2004), A study of Pc-5 ULF oscillations, *Annales Geophysicae*, *22*, 289–302, doi:10.5194/angeo-22-289-2004.

Jackson, J. D. (1998), *Classical Electrodynamics, 3rd Edition*, John Wiley and Sons, Inc.

Jacobs, J. A., Y. Kato, S. Matsushita, and V. A. Troitskaya (1964), Classification of Geomagnetic Micropulsations, *Journal of Geophysical Research*, *69*, 180–181, doi:10.1029/JZ069i001p00180.

Johnson, M. H., and J. Kierein (1992), Combined release and radiation effects satellite (CRRES) - Spacecraft and mission, *Journal of Spacecraft and Rockets*, *29*, 556–563, doi:10.2514/3.55641.

Junginger, H. (1985), Poynting vector as a diagnostic of hydromagnetic wave structure, *Journal of Geophysical Research*, *90*, 4155–4163, doi:10.1029/JA090iA05p04155.

Junginger, H., G. Haerendel, and F. Melzner (1985), A statistical study of wave Poynting vectors measured during long-period magnetospheric pulsations at geostationary orbit, *Journal of Geophysical Research*, *90*, 8301–8307, doi:10.1029/JA090iA09p08301.

Kangas, J., A. Guglielmi, and O. Pokhotelov (1998), Morphology and physics of short-period magnetic pulsations, *Space Science Reviews*, *83*, 435–512.

Kepko, L., and H. E. Spence (2003), Observations of discrete, global magnetospheric oscillations directly driven by solar wind density variations, *Journal of Geophysical Research*, *108*, 1257, doi:10.1029/2002JA009676.

Kepko, L., H. E. Spence, and H. J. Singer (2002), ULF waves in the solar wind as direct drivers of magnetospheric pulsations, *Geophysical Research Letters*, *29*(8), 1197, doi:10.1029/2001GL014405.

Kivelson, M., M. Cao, R. McPherron, and R. Walker (1997), A possible signature of magnetic cavity mode oscillations in ISEE spacecraft observations, *JOURNAL OF GEOMAGNETISM AND GEOELECTRICITY*, *49*(9), 1079–1098.

Kivelson, M. G., and D. J. Southwood (1985), Resonant ULF waves - A new interpretation, *Geophysical Research Letters*, *12*, 49–52, doi:10.1029/GL012i001p00049.

Kivelson, M. G., and D. J. Southwood (1986), Coupling of global magnetospheric MHD eigenmodes to field line resonances, *Journal of Geophysical Research*, *91*, 4345–4351, doi:10.1029/JA091iA04p04345.

Kivelson, M. G., and D. J. Southwood (1988), Hydromagnetic waves and the ionosphere, *Geophysical Research Letters*, *15*, 1271–1274, doi:10.1029/GL015i011p01271.

Kivelson, M. G., J. Etcheto, and J. G. Trotignon (1984), Global compressional oscillations of the terrestrial magnetosphere - The evidence and a model, *Journal of Geophysical Research*, *89*, 9851–9856, doi:10.1029/JA089iA11p09851.

Kivelson, M. G. & Russell, C. T. (Ed.) (1995), *Introduction to Space Physics*, Cambridge University Press.

Kokubun, S., R. L. McPherron, and C. T. Russell (1976), Ogo 5 observations of Pc 5 waves - Ground-magnetosphere correlations, *Journal of Geophysical Research*, *81*, 5141–5149, doi:10.1029/JA081i028p05141.

Korotova, G. I., D. G. Sibeck, V. Kondratovich, V. Angelopoulos, and O. D. Constantinescu (2009), THEMIS observations of compressional pulsations in the dawn-side magnetosphere: a case study, *Annales Geophysicae*, *27*, 3725–3735, doi:10.5194/angeo-27-3725-2009.

Kouznetsov, I., and W. Lotko (1995), Radial energy transport by magnetospheric ULF waves: Effects of magnetic curvature and plasma pressure, *Journal of Geophysical Research*, *100*, 7599–7612, doi:10.1029/94JA02293.

Lee, D.-H. (1996), Dynamics of MHD wave propagation in the low-latitude magnetosphere, *Journal of Geophysical Research*, *101*, 15,371–15,386, doi:10.1029/96JA00608.

Lee, D.-H., and R. L. Lysak (1989), Magnetospheric ULF wave coupling in the dipole model - The impulsive excitation, *Journal of Geophysical Research*, *94*, 17,097–17,103, doi:10.1029/JA094iA12p17097.

Lee, D.-H., and K. Takahashi (2006), MHD Eigenmodes in the Inner Magnetosphere, in *Magnetospheric ULF Waves: Synthesis and New Directions*, *Washington DC American Geophysical Union Geophysical Monograph Series*, vol. 169, edited by K. Takahashi, P. J. Chi, R. E. Denton, & R. L. Lysak, p. 73.

Lee, D.-H., M. K. Hudson, K. Kim, R. L. Lysak, and Y. Song (2002), Compressional MHD wave transport in the magnetosphere 1. Reflection and transmission across the plasmapause, *Journal of Geophysical Research (Space Physics)*, *107*, 1307, doi: 10.1029/2002JA009239.

Lemaire, J. F., and K. I. Gringauz (1998), *The Earth's Plasmasphere*, Cambridge University Press.

Lin, N. G., L. J. Cahill, M. J. Engebretson, M. Sugiura, and R. L. Arnoldy (1986), Dayside pulsation events near the plasmapause, *Planetary Space Science*, *34*, 155–181, doi: 10.1016/0032-0633(86)90112-1.

Liu, J., V. Angelopoulos, D. Sibeck, T. Phan, Z. Y. Pu, J. McFadden, K. H. Glassmeier, and H. U. Auster (2008), THEMIS observations of the dayside traveling compression region and flows surrounding flux transfer events, *Geophysical Research Letters*, *35*, L17S07, doi: 10.1029/2008GL033673.

Love, J. J., and C. A. Finn (2011), The USGS Geomagnetism Program and Its Role in Space Weather Monitoring, *Space Weather*, *9*, S07001, doi:10.1029/2011SW000684.

Mann, I. R. (1997), On the internal radial structure of field line resonances, *Journal of Geophysical Research*, *102*, 27,109–27,120, doi:10.1029/97JA02385.

Mann, I. R., A. N. Wright, and P. S. Cally (1995), Coupling of magnetospheric cavity modes to field line resonances: A study of resonance widths, *Journal of Geophysical Research*, *100*, 19,441–19,456, doi:10.1029/95JA00820.

Mann, I. R., G. Chisham, and S. D. Bale (1998), Multisatellite and ground-based observations of a tailward propagating Pc5 magnetospheric waveguide mode, *Journal of Geophysical Research*, *103*, 4657–4670, doi:10.1029/97JA03175.

Mann, I. R., A. N. Wright, K. J. Mills, and V. M. Nakariakov (1999), Excitation of magnetospheric waveguide modes by magnetosheath flows, *Journal of Geophysical Research*, *104*, 333–354, doi:10.1029/1998JA900026.

Mann, I. R., D. K. Milling, I. J. Rae, L. G. Ozeke, A. Kale, Z. C. Kale, K. R. Murphy, A. Parent, M. Usanova, D. M. Pahud, E.-A. Lee, V. Amalraj, D. D. Wallis, V. Angelopoulos, K.-H. Glassmeier, C. T. Russell, H.-U. Auster, and H. J. Singer (2008), The Upgraded CARISMA Magnetometer Array in the THEMIS Era, *Space Science Reviews*, *141*, 413–451, doi:10.1007/s11214-008-9457-6.

Mathie, R. A., and I. R. Mann (2000), Observations of Pc5 field line resonance azimuthal phase speeds: A diagnostic of their excitation mechanism, *Journal of Geophysical Research*, *105*, 10,713–10,728, doi:10.1029/1999JA000174.

McFadden, J. P., C. W. Carlson, D. Larson, M. Ludlam, R. Abiad, B. Elliott, P. Turin, M. Marckwordt, and V. Angelopoulos (2008a), The THEMIS ESA Plasma Instrument and In-flight Calibration, *Space Science Reviews*, *141*, 277–302, doi:10.1007/s11214-008-9440-2.

McFadden, J. P., C. W. Carlson, D. Larson, J. Bonnell, F. Mozer, V. Angelopoulos, K.-H. Glassmeier, and U. Auster (2008b), THEMIS ESA First Science Results and Performance Issues, *Space Science Reviews*, *141*, 477–508, doi:10.1007/s11214-008-9433-1.

McIlwain, C. E. (1966), Magnetic Coordinates, *Space Science Reviews*, *5*, 585–598, doi:10.1007/BF00167327.

McPherron, R. L. (2005), Magnetic Pulsations: Their Sources and Relation to Solar Wind and Geomagnetic Activity, *Surveys in Geophysics*, *26*, 545–592, doi:10.1007/s10712-005-1758-7.

Mead, G. D., and D. H. Fairfield (1975), A quantitative magnetospheric model derived from spacecraft magnetometer data, *Journal of Geophysical Research*, *80*, 523–534, doi:10.1029/JA080i004p00523.

Means, J. D. (1972), Use of the Three-Dimensional Covariance Matrix in Analyzing the Polarization Properties of Plane Waves, *Journal of Geophysical Research*, *77*, 5551–5559, doi:10.1029/JA077i028p05551.

Mills, K. J., A. N. Wright, and I. R. Mann (1999), Kelvin-Helmholtz driven modes of the magnetosphere, *Physics of Plasmas*, *6*, 4070–4087, doi:10.1063/1.873669.

Mills, K. J., A. W. Longbottom, A. N. Wright, and M. S. Ruderman (2000), Kelvin-Helmholtz instability on the magnetospheric flanks: An absolute and convec-

tive instability approach, *Journal of Geophysical Research*, *105*, 27,685–27,700, doi: 10.1029/1999JA000289.

Moldwin, M. B., L. Downward, H. K. Rassoul, R. Amin, and R. R. Anderson (2002), A new model of the location of the plasmapause: CRRES results, *Journal of Geophysical Research (Space Physics)*, *107*, 1339, doi:10.1029/2001JA009211.

Mozer, F. S. (1973), Analysis of Techniques for Measuring DC and AC Electric Fields in the Magnetosphere, *Space Science Reviews*, *14*, 272–313, doi:10.1007/BF02432099.

Newton, R. S., D. J. Southwood, and W. J. Hughes (1978), Damping of geomagnetic pulsations by the ionosphere, *Planetary and Space Science*, *26*, 201–209, doi:10.1016/0032-0633(78)90085-5.

Ni, B., Y. Shprits, M. Hartinger, V. Angelopoulos, X. Gu, and D. Larson (2011), Analysis of radiation belt energetic electron phase space density using THEMIS SST measurements: Cross-satellite calibration and a case study, *Journal of Geophysical Research*, *116*(A15), A03208, doi:10.1029/2010JA016104.

Obayashi, T., and J. A. Jacobs (1958), Geomagnetic Pulsations and the Earth's Outer Atmosphere, *Geophysical Journal International*, *1*, 53–63, doi:10.1111/j.1365-246X.1958.tb00034.x.

Olson, J. V. (1999), Pi2 pulsations and substorm onsets: A review, *Journal of Geophysical Research*, *104*, 17,499–17,520, doi:10.1029/1999JA900086.

Ozeke, L. G., I. R. Mann, and I. J. Rae (2009), Mapping guided Alfvén wave magnetic field amplitudes observed on the ground to equatorial electric field amplitudes in space, *Journal of Geophysical Research*, *114*(A13), A01214, doi:10.1029/2008JA013041.

Paschmann, G., and P. W. Daly (2000), *Analysis Methods for Multi-Spacecraft Data*, ESA Publications Division.

Plaschke, F., K.-H. Glassmeier, H. U. Auster, O. D. Constantinescu, W. Magnes, V. Angelopoulos, D. G. Sibeck, and J. P. McFadden (2009), Standing Alfvén waves at the magnetopause, *Geophysical Research Letters*, *36*, L02104, doi:10.1029/2008GL036411.

Pokhotelov, O. A., V. A. Pilipenko, and E. Amata (1985), Drift anisotropy instability of a finite-beta magnetospheric plasma, *Planetary Space Science*, *33*, 1229–1241, doi: 10.1016/0032-0633(85)90001-7.

Radoski, H. R. (1971), A note on the problem of hydromagnetic resonances in the magnetosphere, *Planetary Space Science*, *19*, 1012–1013, doi:10.1016/0032-0633(71)90152-8.

Rae, I. J., E. F. Donovan, I. R. Mann, F. R. Fenrich, C. E. J. Watt, D. K. Milling, M. Lester, B. Lavraud, J. A. Wild, H. J. Singer, H. Rème, and A. Balogh (2005), Evolution and characteristics of global Pc5 ULF waves during a high solar wind speed interval, *Journal of Geophysical Research*, *110*(A9), A12211, doi:10.1029/2005JA011007.

Rae, I. J., C. E. J. Watt, F. R. Fenrich, I. R. Mann, L. G. Ozeke, and A. Kale (2007), Energy deposition in the ionosphere through a global field line resonance, *Annales Geophysicae*, *25*, 2529–2539.

Rickard, G. J., and A. N. Wright (1994), Alfven resonance excitation and fast wave propagation in magnetospheric waveguides, *Journal of Geophysical Research*, *991*, 13,455, doi: 10.1029/94JA00674.

Rickard, G. J., and A. N. Wright (1995), ULF pulsations in a magnetospheric waveguide: Comparison of real and simulated satellite data, *Journal of Geophysical Research*, *100*, 3531–3537, doi:10.1029/94JA02935.

Russell, C. T., P. J. Chi, D. J. Dearborn, Y. S. Ge, B. Kuo-Tiong, J. D. Means, D. R. Pierce, K. M. Rowe, and R. C. Snare (2008), THEMIS Ground-Based Magnetometers, *Space Science Reviews*, *141*, 389–412, doi:10.1007/s11214-008-9337-0.

Samson, J. C., and G. Rostoker (1972), Latitude-Dependent Characteristics of High-Latitude

Pc 4 and Pc 5 Micropulsations, *Journal of Geophysical Research*, *77*, 6133–6144, doi: 10.1029/JA077i031p06133.

Samson, J. C., R. A. Greenwald, J. M. Ruohoniemi, T. J. Hughes, and D. D. Wallis (1991), Magnetometer and radar observations of magnetohydrodynamic cavity modes in the earth's magnetosphere, *Canadian Journal of Physics*, *69*, 929–937.

Samson, J. C., B. G. Harrold, J. M. Ruohoniemi, R. A. Greenwald, and A. D. M. Walker (1992), Field line resonances associated with MHD waveguides in the magnetosphere, *Geophysical Research Letters*, *19*, 441–444, doi:10.1029/92GL00116.

Sarris, T. E., W. Liu, K. Kabin, X. Li, S. R. Elkington, R. Ergun, R. Rankin, V. Angelopoulos, J. Bonnell, K. H. Glassmeier, and U. Auster (2009), Characterization of ULF pulsations by THEMIS, *Geophysical Research Letters*, *36*, L04104, doi:10.1029/2008GL036732.

Schunk, R. W., and A. F. Nagy (2004), *Ionospheres*, Cambridge University Press.

Shue, J.-H., J. K. Chao, H. C. Fu, C. T. Russell, P. Song, K. K. Khurana, and H. J. Singer (1997), A new functional form to study the solar wind control of the magnetopause size and shape, *Journal of Geophysical Research*, *102*, 9497–9512, doi:10.1029/97JA00196.

Sibeck, D. G., and V. Angelopoulos (2008), THEMIS Science Objectives and Mission Phases, *Space Science Reviews*, *141*, 35–59, doi:10.1007/s11214-008-9393-5.

Singer, H. J., W. P. Sullivan, P. Anderson, F. Mozer, P. Harvey, J. Wygant, and W. McNeil (1992), Fluxgate magnetometer instrument on the CRRES, *Journal of Spacecraft and Rockets*, *29*, 599–601, doi:10.2514/3.25506.

Song, P., C. T. Russell, and S. P. Gary (1994), Identification of low-frequency fluctuations in the terrestrial magnetosheath, *Journal of Geophysical Research*, *99*, 6011–6025, doi: 10.1029/93JA03300.

Southwood, D. J. (1974), Some features of field line resonances in the magnetosphere, *Planetary and Space Science*, *22*, 483–491, doi:10.1016/0032-0633(74)90078-6.

Southwood, D. J. (1977), Localised compressional hydromagnetic waves in the magnetospheric ring current, *Planetary Space Science*, *25*, 549–554, doi:10.1016/0032-0633(77)90061-7.

Southwood, D. J., and M. G. Kivelson (1981), Charged particle behavior in low-frequency geomagnetic pulsations. I Transverse waves, *Journal of Geophysical Research*, *86*, 5643–5655, doi:10.1029/JA086iA07p05643.

Southwood, D. J., and M. G. Kivelson (1993), Mirror instability. I - Physical mechanism of linear instability, *Journal of Geophysical Research*, *98*, 9181–9187, doi:10.1029/92JA02837.

Southwood, D. J., J. W. Dungey, and R. J. Etherington (1969), Bounce resonant interaction between pulsations and trapped particles, *Planetary and Space Science*, *17*, 349, doi:10.1016/0032-0633(69)90068-3.

Stewart, B. (1861), On the Great Magnetic Disturbance Which Extended from August 28 to September 7, 1859, as Recorded by Photography at the Kew Observatory, *Royal Society of London Philosophical Transactions Series I*, *151*, 423–430.

Takahashi, K., and B. J. Anderson (1992), Distribution of ULF energy (f is less than 80 mHz) in the inner magnetosphere - A statistical analysis of AMPTE CCE magnetic field data, *Journal of Geophysical Research*, *971*, 10,751, doi:10.1029/92JA00328.

Takahashi, K., and A. Y. Ukhorskiy (2007), Solar wind control of Pc5 pulsation power at geosynchronous orbit, *Journal of Geophysical Research (Space Physics)*, *112*(A11), A11205, doi:10.1029/2007JA012483.

Takahashi, K., R. L. McPherron, E. W. Greenstadt, and C. A. Neeley (1981), Factors controlling the occurrence of Pc 3 magnetic pulsations at synchronous orbit, *Journal of Geophysical Research*, *86*, 5472–5484, doi:10.1029/JA086iA07p05472.

Takahashi, K., R. L. McPherron, and T. Terasawa (1984), Dependence of the spectrum of Pc 3-4 pulsations on the interplanetary magnetic field, *Journal of Geophysical Research*, *89*, 2770–2780, doi:10.1029/JA089iA05p02770.

Takahashi, K., R. W. McEntire, C. Z. Cheng, and L. M. Kistler (1990), Observation and theory of Pc 5 waves with harmonically related transverse and compressional components, *Journal of Geophysical Research*, *95*, 977–989, doi:10.1029/JA095iA02p00977.

Takahashi, K., S.-i. Ohtani, W. J. Hughes, and R. R. Anderson (2001), CRRES observation of Pi2 pulsations: Wave mode inside and outside the plasmasphere, *Journal of Geophysical Research*, *106*, 15,567–15,582, doi:10.1029/2001JA000017.

Takahashi, K., R. E. Denton, R. R. Anderson, and W. J. Hughes (2006), Mass density inferred from toroidal wave frequencies and its comparison to electron density, *Journal of Geophysical Research*, *111*(A10), A01201, doi:10.1029/2005JA011286.

Takahashi, K., J. Bonnell, K.-H. Glassmeier, V. Angelopoulos, H. J. Singer, P. J. Chi, R. E. Denton, Y. Nishimura, D.-H. Lee, M. Nosé, and W. Liu (2010), Multipoint observation of fast mode waves trapped in the dayside plasmasphere, *Journal of Geophysical Research*, *115*(A14), A12247, doi:10.1029/2010JA015956.

Takahashi, K., K.-H. Glassmeier, V. Angelopoulos, J. Bonnell, Y. Nishimura, H. J. Singer, and C. T. Russell (2011), Multisatellite observations of a giant pulsation event, *Journal of Geophysical Research*, *116*(A15), A11223, doi:10.1029/2011JA016955.

Tamao, T. (1965), Transmission and coupling resonance of hydromagnetic disturbances in the non-uniform Earth's magnetosphere, *Tohoku University, Science Reports, Series 5, Geophysics(2)*, *17*, 43–72.

Troitskaya, V. A., T. A. Plyasova-Bakunina, and A. V. Gul'Elmi (1971), The connection of Pc2-4 pulsations with the interplanetary magnetic field., *Akademiia Nauk SSSR Doklady*, *197*, 1312–1314.

Tsyganenko, N. A. (1989), A magnetospheric magnetic field model with a warped tail current sheet, *Planetary and Space Science*, *37*, 5–20, doi:10.1016/0032-0633(89)90066-4.

Viall, N. M., L. Kepko, and H. E. Spence (2009), Relative occurrence rates and connection

of discrete frequency oscillations in the solar wind density and dayside magnetosphere, *Journal of Geophysical Research*, *114*(A13), A01201, doi:10.1029/2008JA013334.

Walker, A. D. M., R. A. Greenwald, W. F. Stuart, and C. A. Green (1979), STARE auroral radar observations of Pc 5 geomagnetic pulsations, *Journal of Geophysical Research*, *84*, 3373–3388, doi:10.1029/JA084iA07p03373.

Waters, C. L., K. Takahashi, D.-H. Lee, and B. J. Anderson (2002), Detection of ultralow-frequency cavity modes using spacecraft data, *Journal of Geophysical Research*, *107*, 1284, doi:10.1029/2001JA000224.

Williams, D. J. (1983), The earth's ring current: Causes, generation, and decay - /Tutorial Lecture/, *Space Science Reviews*, *34*, 223–234, doi:10.1007/BF00175279.

Wright, A. N. (1994), Dispersion and wave coupling in inhomogeneous MHD waveguides, *Journal of Geophysical Research*, *99*, 159–167, doi:10.1029/93JA02206.

Wright, A. N., and G. J. Rickard (1995), A numerical study of resonant absorption in a magnetohydrodynamic cavity driven by a broadband spectrum, *Astrophysical Journal*, *444*, 458–470, doi:10.1086/175620.

Wygant, J. R., P. R. Harvey, D. Pankow, F. S. Mozer, N. Maynard, H. Singer, M. Smiddy, W. Sullivan, and P. Anderson (1992), CRRES electric field/Langmuir probe instrument, *Journal of Spacecraft and Rockets*, *29*, 601–604, doi:10.2514/3.25507.

Wygant, J. R., A. Keiling, C. A. Cattell, M. Johnson, R. L. Lysak, M. Temerin, F. S. Mozer, C. A. Kletzing, J. D. Scudder, W. Peterson, C. T. Russell, G. Parks, M. Brittnacher, G. Germany, and J. Spann (2000), Polar spacecraft based comparisons of intense electric fields and Poynting flux near and within the plasma sheet-tail lobe boundary to UVI images: An energy source for the aurora, *Journal of Geophysical Research*, *105*, 18,675–18,692, doi:10.1029/1999JA900500.

Yang, B., Q.-G. Zong, Y. F. Wang, S. Y. Fu, P. Song, H. S. Fu, A. Korth, T. Tian, and H. Reme (2010), Cluster observations of simultaneous resonant interactions of ULF waves

with energetic electrons and thermal ion species in the inner magnetosphere, *Journal of Geophysical Research*, *115*(A14), A02214, doi:10.1029/2009JA014542.

Yeoman, T. K., D. M. Wright, T. R. Robinson, J. A. Davies, and M. Rietveld (1997), High spatial and temporal resolution observations of an impulse-driven field line resonance in radar backscatter artificially generated with the Tromsø heater, *Annales Geophysicae*, *15*, 634–644, doi:10.1007/s00585-997-0634-9.

Zhu, X., and M. G. Kivelson (1988), Analytic formulation and quantitative solutions of the coupled ULF wave problem, *Journal of Geophysical Research*, *93*, 8602–8612, doi:10.1029/JA093iA08p08602.

Zhu, X., and M. G. Kivelson (1989), Global mode ULF pulsations in a magnetosphere with a nonmonotonic Alfven velocity profile, *Journal of Geophysical Research*, *94*, 1479–1485, doi:10.1029/JA094iA02p01479.

Zhu, X., and M. G. Kivelson (1991), Compressional ULF waves in the outer magnetosphere. I - Statistical study, *Journal of Geophysical Research*, *96*, 19,451, doi:10.1029/91JA01860.

Zhu, X., and M. G. Kivelson (1994), Compressional ULF waves in the outer magnetosphere. 2: A case study of Pc 5 type wave activity, *Journal of Geophysical Research*, *99*, 241–252, doi:10.1029/93JA02106.